CO2 reduction using nanostructured metal oxide/catalyst hybrid layers assembled at CIGS photoelectrodes

Julian Guerrero

Université Paris Cité

Université Paris Cité

Ecole doctorale chimie physique et chimie analytique de Paris

Centre ED 388

Laboratoire d'Electrochimie Moléculaire – UMR CNRS 7591

CO_2 reduction using nanostructured metal oxide/catalyst hybrid layers assembled at CIGS photoelectrodes

Par Julian Guerrero

Thèse de doctorat de Electrochimie Moléculaire et Biologique

Dirigée par Negar Naghavi
et Marc Robert

Présentée et soutenue publiquement le 19 décembre 2022

Devant un jury composé de :

Remita HYND, Professeur, Université Paris Saclay, Rapportrice
David TILLEY, Professeur, Université de Zurich, Rapporteur
Encarnacion TORRALBA-PENALVER, Chargée de recherche CNRS, Université Paris-Est Créteil, Examinatrice
Daniel ABOU-RAS, Chargé de recherche, Helmholtz-Zentrum Berlin (HZB), Examinateur
Nathanaelle SCHNEIDER, Chargée de recherche, CNRS – IPVF, Invitée
Marc ROBERT, Professeur, Université Paris Cité, Directeur
Negar NAGHAVI, Directrice de recherche, CNRS – IPVF, Co-directrice

Abstract

Artificial photosynthesis is a promising approach for CO_2 valorization and fuel production. However, in such systems, the conversion efficiency is still too low for industrial applications. To achieve a high solar-to-fuel conversion efficiency, new strategies yielding high photocurrent along with sufficient photo-voltage should be developed. Even though remarkable progresses made since the first photoelectrochemical (PEC) CO_2 reduction cell was reported in 1978, research about PEC CO_2 reduction is still on the early stage of development. Despite tremendous efforts made for the development of PEC CO_2RR cells, the performances remain unsatisfactory, most of the reported PEC photocathodes suffer from low solar conversion efficiency, uncontrolled product selectivity, poor durability, and strong competition between CO_2RR and hydrogen evolution reaction (HER). The loading of the photoelectrode surface with electrocatalysts or molecular catalysts has been shown to be an effective approach to accelerate and regulate the surface reaction kinetics and improve the product selectivity in PEC systems. Therefore, a key topic in the PEC CO_2RR is related to on photoelectrode fabrication and cell design to achieve high energy conversion efficiencies and high selectivity toward target products. Recent advances in photovoltaic on the one hand and in molecular catalysis on the other hand open up new possibilities for improving photo-conversion processes in order to overcome the limitations of PEC systems. The objective of this PhD has been to develop versatile transparent and conductive nanostructured layers integrating molecular catalysts and adaptable to thin film based solar cells for photo-electro-reduction of CO_2. These layers have multiple functionalities: window and protective layers for solar cells and functionalization of photo-electrode for solar to fuel conversion.

To reach this goal, molecular catalysts including earth abundant metals (such as Cobalt) have been integrated to the window layer of high-efficiency Cu(In,Ga)Se_2 based solar cells as a proof of concept. A strong emphasis has been placed on the design and development of the window layers, their integration at the surface of solar cells, and the understanding of the impact of their nanostructure morphology, shape, and composition on the light absorption of the PV cells and on the photoelectrochemical CO_2 reduction process.

First, hybrids ZnO/catalyst layers were prepared by a simple one step electrochemical deposition method on ZnO:Al transparent conducting layers. Three type of nanostructured electrodes have been developed: a hybrid nanoporous structure (NPS) incorporating a molecular catalyst presenting a sponge-like structure at a nanoscale level, nanorod ZnO structures (ZNRs) and 3D nanostructure based on the nanoporous ZnO structure (NPS) grown on ZNRs. Molecular catalysts based on phthalocyanine derivatives have been integrated to these nanostructured layers. Their reactivity and stability in electrochemical CO_2 reduction to CO have been evaluated.

The most efficient combination of catalyst/nanostructure in terms of efficiency, stability and product selectivity have been integrated to the window layer of Copper Indium Gallium Selenide (CIGS) solar cells, resulting in a multilayer device capable of performing PEC reduction of CO_2 at low overpotential while reaching high current densities and maintaining high stability. We showed that the combination of hybrids ZnO with very low concentration of an encapsulated Co-based molecular catalyst inside the oxide layer can lead to a high catalytic response for the reduction of CO_2 into CO (93% selectivity) with large currents (up to ca. 7 mA cm^{-2}). This demonstrates the molecules' highly electrochemically active nature through the oxide layer.

Keywords: *CO_2 reduction, molecular catalyst, cobalt complexes, CIGS solar cell, photoelectrodes, nanomaterials, solar fuels.*

Résumé

La photosynthèse artificielle est une approche prometteuse pour la valorisation du CO_2 et la production de carburants. Cependant, dans ces systèmes, le rendement de conversion est encore trop faible pour les applications industrielles. Pour atteindre un haut rendement de conversion solaire-carburant, de nouvelles stratégies produisant un photo-courant élevé et une tension photoélectrique suffisante doivent être développées. Malgré les progrès remarquables réalisés depuis la première cellule de réduction du CO_2 par voie photoélectrochimique (PEC) en 1978, la recherche sur la réduction du CO_2 par PEC n'en est qu'à ses débuts. Malgré les efforts considérables déployés pour le développement des cellules PEC de réduction du CO_2, les performances restent insatisfaisantes. La plupart des photocathodes PEC rapportées souffrent d'une faible efficacité de conversion solaire, d'une sélectivité des produits incontrôlée, d'une faible durabilité et d'une forte concurrence entre la réduction du CO_2 et la réaction d'évolution de l'hydrogène (HER). Le chargement de la surface des photoélectrodes avec des électrocatalyseurs ou des catalyseurs moléculaires s'est avéré être une approche efficace pour accélérer et réguler la cinétique de la réaction de surface et améliorer la sélectivité du produit dans les systèmes PEC. Par conséquent, un sujet clé de la réaction de réduction du CO_2 par PEC est lié à la fabrication des photoélectrodes afin d'obtenir des rendements de conversion énergétique élevés et une sélectivité élevée pour les produits ciblés. Les progrès récents dans le domaine photovoltaïque d'une part et de la catalyse moléculaire d'autre part ouvrent de nouvelles possibilités pour améliorer les processus de photoconversion afin de surmonter les limites des systèmes PEC. L'objectif de cette thèse a été de développer des couches nanostructurées transparentes et conductrices polyvalentes intégrant des catalyseurs moléculaires et adaptables aux cellules solaires en couches minces pour la photo-électroréduction du CO_2. Ces couches ont des fonctionnalités multiples : couches de fenêtre et de protection pour les cellules solaires et fonctionnalisation de la photo-électrode pour la conversion du soleil en carburant.

Pour atteindre cet objectif, des catalyseurs moléculaires comprenant des métaux abondants (comme le cobalt) ont été intégrés à la couche de fenêtre de cellules solaires à haut rendement à base de Cu(In,Ga)Se2 comme preuve de concept. L'accent a été mis sur la conception et le développement des couches de fenêtre, leur intégration à la surface des cellules solaires et la compréhension de l'impact de la morphologie, de la forme et de la composition de leur nanostructure sur l'absorption de la lumière par les cellules photovoltaïques et sur le processus de réduction photoélectrochimique du CO_2.

Tout d'abord, des couches hybrides ZnO/catalyseur ont été préparées par une méthode simple de dépôt électrochimique en une étape sur des couches conductrices transparentes ZnO:Al. Trois types d'électrodes nanostructurées ont été développés : une structure hybride nanoporeuse (NPS) incorporant un catalyseur moléculaire présentant une structure de type éponge à l'échelle nanométrique, des structures de ZnO nanorod (ZNRs) et une nanostructure 3D basée sur la struc-

ture de ZnO nanoporeuse (NPS) cultivée sur des ZNRs. Des catalyseurs moléculaires (phthalocyanines, porphyrines) ont été intégrés aux couches nanostructurées. Leur réactivité et leur stabilité dans la réduction électrochimique du CO_2 en CO ont été évaluées.

La combinaison la plus efficace de catalyseur/nanostructure en termes d'efficacité, de stabilité et de sélectivité du produit a été intégrée à la couche de fenêtre des cellules solaires au séléniure de cuivre, d'indium et de gallium (CIGS), ce qui a donné lieu à un dispositif multicouche capable d'effectuer la réduction PEC du CO2 à un faible surpotentiel tout en atteignant des densités de courant élevées et en maintenant une grande stabilité. Nous avons montré que la combinaison de ZnO hybride avec une très faible concentration d'un catalyseur moléculaire à base de Co encapsulé à l'intérieur de la couche d'oxyde peut conduire à une réponse catalytique élevée pour la réduction du CO_2 en CO (93% de sélectivité) avec des courants importants (jusqu'à environ 7 mA cm^{-2}). Ceci démontre la nature hautement active électrochimiquement des molécules à travers la couche d'oxyde.

***Mots-clefs** : Réduction du CO_2, catalyseur moléculaire, complexes de cobalt, cellule solaire CIGS, photoélectrodes, nanomatériaux.*

Résume de la thèse

Le carbone est l'épine dorsale de la vie sur Terre. Nous sommes faits de carbone, nos civilisations, nos économies, nos maisons, nos moyens de transport sont construits sur du carbone. Nous avons besoin de carbone, mais ce besoin est également lié à l'un des problèmes les plus graves auxquels nous sommes confrontés aujourd'hui : le changement climatique mondial.

Le dioxyde de carbone est présent naturellement dans l'atmosphère terrestre à la suite d'éruptions volcaniques, de feux de forêt naturels et de la respiration des plantes et des animaux. Dans la nature, la concentration de CO_2 est régulée par l'activité géologique et les organismes photosynthétiques qui utilisent la photosynthèse pour convertir le CO_2 et l'eau en sucres. Ce sont des éléments clés du cycle naturel du carbone qui contrôle le niveau de CO_2 dans l'atmosphère terrestre et donc la température de surface de la planète. Cependant, en raison des émissions anthropiques, le niveau de CO_2 dans l'atmosphère augmente de manière significative, dépassant la capacité de séquestration naturelle et rompant l'équilibre du cycle du carbone, ce qui entraîne un réchauffement climatique. Depuis le début de la révolution industrielle, lorsque les hommes ont commencé à brûler massivement des combustibles fossiles, les concentrations de dioxyde de carbone dans l'atmosphère sont passées d'environ 280 ppm à plus de 420 ppm, soit la concentration la plus élevée depuis deux millions d'années. Selon l'indice annuel des gaz à effet de serre (AGGI) du laboratoire de surveillance mondiale de la « National Oceanic and Atmospheric Administration » (NOAA), l'abondance de CO_2 dans l'atmosphère a augmenté en moyenne de 1,88 ppm par an au cours des 42 dernières années (1979-2021), le taux de croissance a atteint 2,4 ppm par an au cours de la dernière décennie (2011-2021) et l'augmentation annuelle du CO_2 de 2021 à 2022 est de 2,60 ppm3.

Afin de répondre à ces préoccupations, la communauté scientifique s'est réunie pour trouver des solutions. Des efforts considérables ont été déployés pour mettre au point une série de technologies permettant de réduire les émissions, de capturer, d'utiliser et de stocker efficacement le carbone. La réduction des émissions nécessite un coût social et économique et des accords internationaux. Le piégeage et le stockage du carbone nécessitent des emplacements souterrains ou sous le plancher océanique à grande échelle, dans des bassins sédimentaires appropriés, et la construction des installations de piégeage et de stockage du carbone peut entraîner des coûts sociaux tels

que des facteurs juridiques et réglementaires. La transformation du CO_2 en carburants est ensuite présentée comme une solution écologique. La réaction de réduction convertit le CO_2 en éléments constitutifs du carbone, tels que le monoxyde de carbone (CO), qui peuvent être utilisés dans des processus industriels ou pour la synthèse de produits chimiques plus précieux. Un processus artificiel de recyclage du CO_2 peut donc contribuer à atténuer les émissions de CO_2 à long terme.

Inspirée de la nature, la réduction du CO_2 par l'énergie solaire, également appelée photosynthèse artificielle, permet de capter l'énergie de la lumière solaire au moyen de matériaux absorbant la lumière et de convertir les molécules de CO_2 en molécules dérivées du carbone, en stockant l'énergie solaire dans des liaisons chimiques. La réduction photocatalytique (PC) et la réduction photoélectrocatalytique (PEC) du CO_2 sont deux approches représentatives pour réaliser la photosynthèse artificielle. Cependant, le CO_2 étant l'une des molécules les plus stables sur le plan thermodynamique, la réaction de réduction du CO_2 (CO_2RR) n'est pas seulement un processus exigeant sur le plan énergétique et thermodynamique, mais elle doit également relever de grands défis cinétiques en raison de la grande stabilité et de l'inertie de cette molécule. L'efficacité et la commercialisation à grande échelle des systèmes CO_2RR sont encore considérablement limitées par leur faible sélectivité catalytique, leur lenteur cinétique et les surpotentiels élevés nécessaires.

En général, pour réussir à réduire le CO_2 grâce à l'énergie solaire, il faut une absorption efficace de la lumière solaire, une séparation et transport des charges avec une faible recombinaison, et une réaction de surface rapide. Les systèmes photocatalytiques (P et PEC partagent ces étapes clés. Cependant, par rapport au procédé PC basé sur la suspension de particules, la réduction PEC du CO_2 basée sur les photoélectrodes peut intégrer et optimiser les avantages de la photocatalyse et de l'électrocatalyse. Les systèmes PEC sont assistés par une polarisation externe qui améliore la séparation des charges et l'efficacité de la conversion de l'énergie, cette polarisation supplémentaire pouvant être fournie par de l'électricité renouvelable. Une fois que les porteurs de charge ont atteint la surface, les électrons peuvent réduire le CO_2 en carburants.

Même si des progrès remarquables ont été réalisés depuis que la première cellule de réduction PEC du CO_2 a été signalée en 19786, la recherche sur la réduction du CO_2 par PEC n'en est qu'à ses débuts et des défis techniques importants restent à relever avant que la réduction PEC du CO_2 ne devienne industriellement viable. Malgré les efforts considérables déployés pour le développement des cellules PEC CO_2RR, les performances restent insatisfaisantes, la plupart des photocathodes PEC réimplantées

souffrent d'une faible efficacité de conversion solaire, d'une sélectivité incontrôlée du produit, d'une faible durabilité et d'une forte concurrence entre la CO_2RR et la réaction d'évolution de l'hydrogène (HER). Le chargement de la surface de l'électrode avec des électro-catalyseurs ou des catalyseurs moléculaires s'est avéré être une approche efficace pour accélérer et réguler la cinétique de la réaction de surface et améliorer la sélectivité du produit dans les systèmes PEC. Par conséquent, l'un des principaux sujets de la PEC CO_2RR est la fabrication de la photoélectrode et la conception de la cellule afin d'obtenir des rendements de conversion énergétique élevés et des sélectivités élevées pour les produits cibles. Dans cette thèse nous présentons les résultats des travaux de recherche sur la conception et la fabrication d'une photoélectrode hautement efficace et sélective pour la réduction du CO_2 par voie photoélectrochimique PEC. Ce travail a été réalisé en combinant l'expertise de l'Institut Photovoltaïque d'Île-de-France (IPVF) dans le domaine des matériaux photovoltaïques, et du Laboratoire d'Électrochimie Moléculaire (LEM) dans le domaine des catalyseurs moléculaires et de la catalyse.

L'objectif principal de cette thèse était le développement de nanostructures transparentes, conductrices et polyvalentes intégrant des catalyseurs moléculaires à base de métaux abondants (comme le cobalt) et leur intégration à des cellules solaires à base de $CuInGaSe_2$ (CIGS) pour la photoélectroréduction du CO_2.

Les matériaux photovoltaïques (PV) à base de chalcopyrite de cuivre (CIGS) sont parmi les photocathodes les plus attrayants pour le développement de cellules photovoltaïques. Dans cette thèse, nous avons étudié l'intégration de catalyseurs moléculaires à base de métaux abondants dans la terre et présentant une grande sélectivité pour la réduction du CO_2 sur les couches de surface d'une cellule solaire CIGS, créant ainsi un dispositif multicouche capable de réaliser la réduction PEC du CO_2 à des surtensions plus faibles et avec une grande stabilité.

Dans cette thèse, nous nous sommes concentrés sur l'électrochimie comme outil principal pour la synthèse et la mesure des performances des électrodes et des photoélectrodes.

La première partie de mon travail, a été dédiée à l'intégration de catalyseurs moléculaires dans des couches hybrides d'oxyde de zinc (ZnO). Le ZnO présente d'excellentes propriétés optiques, une faible toxicité et est largement disponible sur terre. Parmi les avantages spécifiques du ZnO, on peut également souligner la facilité avec laquelle il peut être préparé en haute qualité par des voies en solution. ZnO peut être synthétisé

par voie électrochimique à partir de solutions aqueuses de sels de zinc. En 1996, Izaki et al.,[1] et Peulon et al.,[2][3] ont découvert indépendamment des méthodes pour déposer par électrolyse des films minces de ZnO cristallin à partir de solutions aqueuses de sels de zinc, en utilisant la réduction cathodique. Le dépôt électrochimique est simple et peu coûteux pour la préparation de ZnO de haute qualité. De plus, des films conformes peuvent être facilement produits par électrodéposition sur des substrats de forme compliquée, cette technique permet de concevoir des nanostructures complexes en combinant et en ajustant les conditions de croissance.[4]–[7]

La croissance électrochimique du ZnO permet également de charger des molécules organiques pendant la croissance du film, comme reporté par Yoshida et al.,[8] l'auto-assemblage électrochimique de films minces de ZnO modifiés par des colorants peut être obtenu dans un processus en une étape, en ajoutant des colorants solubles (Eosine) dans le bain électrochimique contenant le sel de zinc. Ils ont obtenu des films minces de ZnO colorés avec des morphologies de surface et des structures cristallographiques différentes. La présence d'additifs dans le bain a un impact significatif sur le mécanisme de croissance local et modifie la forme de l'oxyde de zinc. Dans la plupart des cas, les additifs sont incorporés au dépôt sous forme de structures hybrides organiques-inorganiques, ce qui donne des matériaux hybrides nanoporeux. L'utilisation d'une matrice inorganique poreuse nanostructurée de ZnO permet non seulement l'immobilisation d'une grande quantité de la molécule organique mais aussi la bonne accessibilité des complexes à la solution électrolytique.

Puisque les cellules CIGS sont terminées par une couche de fenêtre en ZnO, qui peut être préparée et modifiée par électrochimie, notre stratégie était d'incorporer un catalyseur moléculaire dans la matrice inorganique de ZnO, résultant en un film hybride avec une activité catalytique.

Nous décrivons la formation de trois différentes nanostructures de ZnO : (i) une couche hybride nanoporeuse d'oxide métallique/catalyseur moleculaire (NPS), (ii) un réseau de nanorods (ZNRs), et (iii) une structure 3D formée par les nanorods couverts par une fine couche hybride nanoporeuse (ZNRs+NPS). Nous présentons comme exemple l'incorporation d'un complexe de cobalt (CoPc3). Cependant, il a été démontré qu'il est facile de changer les catalyseurs moléculaires et d'incorporer différents catalyseurs dès lors que ces derniers sont solubles dans le bain électrochimique utilisé pour l'électrodéposition des couches hybrides de ZnO NPS. L'incorporation des catalyseurs moléculaires a été démontrée par différentes techniques (UV-vis, ICP, XPS, IR). Ces structures présentent une transmission importante de la lumière visible, permettant leur

application dans des dispositifs photovoltaïques. Notre stratégie permet d'incorporer une très faible quantité de catalyseur moléculaire dans les électrodes (1-10 nmol cm^{-2}) et de contrôler celle-ci en faisant varier l'épaisseur de la couche (50 – 1000 nm). D'autres analyses par spectroscopie infrarouge à réflectance totale atténuée (ATR-IR) sur la poudre de CoPc3 et les électrodes hybrides chargées de CoPc3 (ZnO|CoPc3 NPS) indiquent une encapsulation réussie du catalyseur dans la couche. Le résultat de la cartographie EDX révèle une distribution homogène du catalyseur dans l'électrode. En outre, la cartographie de l'élément Co a indiqué qu'il n'y avait pas d'agrégation du cobalt.

Electrolyses à long terme ont été réalisées avec les nanostructures préparées à un potentiel de -2.1 V vs SCE pendant 1h, en atteignant des densités de courant élevées pour la réduction du CO_2 dans un solvant organique (acetonitrile), des valeurs de -2.4 mA cm^{-2} jusqu'à de grandes densités de courant environ -5.0 mA cm^{-2}, ont été obtenues après une série d'optimisations des électrodes. Les produits de réaction ont été étudiés par chromatographie en phase gazeuse (GC), indiquant la production de CO avec une sélectivité supérieure à 95% et une efficacité faradique de 98%. Un seul sous-produit, le H_2, a également été détecté.

Enfin, nous avons montré qu'en combinant une structure de ZnO nanoporeux (NPS) déposée sur des couches de nanorods de ZnO, il est possible d'atteindre pour un potentiel de polarisation de -2.1 V vs SCE, des densités de courant allant jusqu'à -3 mA cm^{-2} en utilisant une très faible quantité de catalyseur (0.73 nmol cm^{-2}).

Compte tenu des bonnes performances des électrodes hybrides ZnO|CoPc3 dans les conditions la réduction electrochimique de CO_2, nous avons alors pensé à intégrer ce matériau comme couche fenêtre d'une cellule solaire CIGS et utiliser celle-ci comme photocathode pour réduire le CO_2 sous irradiation lumineuse en conditions PEC.

Dans un deuxième temps, à l'aide d'un processus d'électrodéposition assisté par la lumière, ces couches hybrides fonctionnelles (ZnO|CoPc3) ont été intégrées à la surface de cellules solaires CIGS à haut rendement comme couche fenêtre et protective. L'accent a été mis sur la modification des couches de fenêtre et la compréhension de l'impact de la morphologie et de la composition de la nanostructure hybride sur l'absorption de la lumière dans les cellules solaires CIGS.

Les photoelectrode (CIGS/CdS/ZnO/AZO/ZnO + ZnO|CoPc3) développées ont été étudiées en photoélectrolyse dans un solvant organique (acetonitrile). Ils ont montré la formation sélective de CO à partir de CO_2 avec une densité de courant élevée (jusqu'à

-7 mA cm^{-2} à -1.7 V vs SCE sous irradiation de lumière visible 100 mW cm^{-2}). Les excellentes performances du dispositif peuvent être expliquées par une combinaison des excellentes propriétés catalytiques de la couche hybride formée par le ZnO et le catalyseur moléculaire CoPc3, et par les effets combinés incluant une haute efficacité de capture de la lumière et un transport de charge rapide entre les couches de la cellule CIGS, permettant aux électrons d'atteindre les centres catalytiques dans la dernière couche, et un taux de réduction rapide du CO_2 sur les sites catalytiques.

Les performances des photoélectrodes CIGS modifiées par la couche hybride (ZnO|CoPc3) ont également été étudiées dans la réduction PEC du CO_2 dans des solutions aqueuses. Des expériences préliminaires ont montré que les électrodes à catalyseur CIGS/CdS/ZnO/AZO/ZnO| CoPc3 peuvent réduire efficacement le CO_2 en CO, avec une densité de courant moyenne de -0.85 mA cm^{-2} à -0,057 V vs RHE et une sélectivité du CO de 87 %.

Cette étude est la première à décrire une cellule CIGS comme constituant d'une photocathode à base moléculaire de réduction du CO_2 dans un solvant organique qui présente des performances exceptionnelles de réduction PEC du CO_2 (haute sélectivité et bonne stabilité) et un photocourant élevé sous illumination. En particulier, notre étude a abouti au premier dispositif CIGS incorporant un catalyseur moléculaire par une méthode autre que l'immobilisation covalente sur la surface. En outre, nous avons également exploré les performances de nos dispositifs dans un système de réduction PEC du CO_2 dans l'eau, obtenant des résultats très encourageants qui ouvrent un certain nombre de possibilités d'amélioration.

Références

[1] M. Izaki, and Omi, T. "Transparent zinc oxide films prepared by electrochemical reaction," *Appl. Phys. Lett.* 1996 68, 2439

[2] S. Peulon, D. Lincot, *Adv. Mater.* **1996**, *8*, 166.

[3] Th. Pauporté, D. Lincot, *Appl. Phys. Lett.* **1999**, *75*, 3817.

[4] T. Yoshida, H. Minoura, *Adv. Mater.* **2000**, 4.

[5] S. Haller, T. Suguira, D. Lincot, T. Yoshida, *Phys. Stat. Sol. (a)* **2010**, *207*, 2252.

[6] Z. Jehl, J. Rousset, F. Donsanti, G. Renou, N. Naghavi, D. Lincot, *Nanotechnology* **2010**, *21*, 395603.

[7] Th. Pauporté, G. Bataille, L. Joulaud, F.J. Vermersch, *J. Phys. Chem. C* **2010**, *114*, 194.

[8] T. Yoshida, M. Tochimoto, D. Schlettwein, D. Wöhrle, T. Sugiura, H. Minoura, *Chem. Mater.* **1999**, *11*, 2657.

General introduction

Carbon is the backbone of life on Earth. We are made of carbon, our civilizations, economies, homes, means of transport are built on carbon. We need carbon, but that need is also interlaced with one of the most serious problems facing us today: global climate change.

Carbon dioxide occurs naturally in the Earth's atmosphere as a result of volcanic eruptions, natural forest fires, plant and animal respiration. In nature, CO_2 concentration has been regulated by geological activity and photosynthetic organisms which use photosynthesis to convert CO_2 and water into sugars. These are key parts of the natural carbon cycle which controls the level of CO_2 in the Earth's atmosphere and hence the surface temperature of the planet.[1] However, owing to the anthropogenic emission, CO_2 level in the atmosphere significantly increases, exceeding the natural sequestration capacity and breaking the carbon cycle balance, thus leading to climate warming.[2] Since the beginning of the Industrial Revolution, when people first started burning massively fossil fuels, carbon dioxide concentrations in the atmosphere have risen from about 280 ppm to more than 420 ppm, the highest concentration in two million years. According to the Annual Greenhouse Gas Index (AGGI) of the National Oceanic and Atmospheric Administration (NOAA) Global Monitoring Laboratory, the atmospheric abundance of CO_2 has increased by an average of 1.88 ppm per year over the past 42 years (1979-2021), the growth rate increased to 2.4 ppm per year during the last decade (2011-2021) and the annual CO_2 increase from 2021 to 2022 was 2.60 ppm.[3]

In order to address these concerns, the scientific community has come together to find solutions. Substantial effort has been made to develop a range of technologies to achieve emission reductions, efficient carbon capture, utilization and storage. Direct emission reduction requires social and economic cost and international accords. The carbon capture and storage requires large scale underground or under seafloor locations suitable sedimentary basins, and building the carbon capture and storage facilities may cause social cost such as legal and regulatory factors. The transformation of CO_2 to fuels is then presented as an eco-friendly solution, the reduction reaction converts CO_2 into carbon building blocks, such as carbon monoxide (CO), which can be used in industrial processes or for the synthesis of more valuable chemicals. Hence an artificial CO_2 recycling process can contribute mitigating CO_2 emission in long term.[4]

Inspired by nature, solar-driven CO_2 reduction, also known as artificial photosynthesis, can capture energy from sunlight by means of light absorbing materials and convert CO_2 molecules into carbon-derived molecules, storing solar energy into chemical bonds. Photocatalytic (PC) and photoelectrocatalytic (PEC) CO_2 reduction are two representative approaches to carry out artificial photosynthesis. However, CO_2 is one of the uttermost thermodynamically stable molecules, the CO_2 reduction reaction (CO_2RR) is not only an energetically demanding and thermodynamically uphill process, but faces also great kinetic challenges due to the high stability and inertness of this molecule. The efficiency and upscaling commercialization of CO_2RR systems are still significantly restricted by their poor catalytic selectivity, slow kinetics, and high overpotentials needed.[5]

In general, a successful solar-driven CO_2 reductions requires efficient sunlight harvesting, charge separation/transport with a low recombination, and a fast surface reaction. PC and PEC systems share these mentioned key steps. However, compared with the particle suspension–based PC process, the photoelectrode-based PEC reduction of CO_2 can integrate and optimize the advantages of both photocatalysis and electrocatalysis. PEC systems are assisted by an external bias that enhances charge separation and energy conversion efficiency, the extra bias could potentially be supplied by renewable electricity. After charge carriers reach the surface, the electrons can reduce CO_2 into fuels.

Even though remarkable progresses made since the first PEC CO_2 reduction cell was reported in 1978,[6] research about PEC CO_2 reduction is still on the early stage of development, significant technical challenges remain to be resolved before PEC CO_2 reduction becomes industrially viable. Despite the tremendous efforts in the development of PEC CO_2RR cells, the performances remain unsatisfactory, most of the reported PEC photocathodes suffer from low solar conversion efficiency, uncontrolled product selectivity, poor durability, and strong competition between CO_2RR and hydrogen evolution reaction (HER).[7] The loading of the electrode surface with electrocatalysts or molecular catalysts has been shown to be an effective approach to accelerate and regulate the surface reaction kinetics and improve the product selectivity in PEC systems.[8] Therefore, a key topic in the PEC CO_2RR focuses on photoelectrode fabrication and cell design to achieve high energy conversion efficiencies and high selectivities toward target products. The present manuscript summarizes the results of the research work on the design and fabrication of a highly efficient and selective photoelectrode for PEC CO_2 reduction. This work was achieved by combining the research

expertise of the Photovoltaic Institute of Île-de-France (IPVF) in photovoltaic materials, and the Molecular Electrochemistry Laboratory (LEM) in molecular catalysts and catalysis. In this thesis we have studied the integration of an earth-abundant metal-based molecular catalysts with high selectivity for CO_2RR on the surface layers of a Copper Indium Gallium Selenide (CIGS) solar cell, creating a multilayer device able to perform PEC reduction of CO_2 at lower overpotentials with high stability.

The present text is organized in five chapters, chapter I is devoted to give a presentation of the context of the thesis project, the main problems and drawbacks found in the PEC CO_2 reduction photoelectrodes reported so far, a brief presentation of the strategy proposed to overcome the challenges and a detailed description of the state of the art. In this thesis, we focused on electrochemistry as principal tool for synthesis and performance measurement of the electrodes and photoelectrodes, we present in chapter II all the experimental setups for the electrodeposition of hybrid structures with a catalytic activity towards CO_2RR and all the characterization techniques applied on these materials, as well as the photovoltaic and electrochemical characterization techniques used with photoelectrodes. The following two chapters summarize the results obtained. Chapter III describe the integration of molecular catalysts into zinc oxide hybrid layers, we present the growth of different nanostructures with a series of optimisation experiments and the characterisation made on these materials. The performance and characterisation of these nanostructures in electrocatalytic CO_2 reduction is also presented and discussed in this chapter. Afterward, chapter IV presents and describes the incorporation of the hybrid catalytic layer on a CIGS solar cell by a light-assisted electrodeposition process, resulting in photoelectrodes with a high catalytic activity towards CO_2RR. Structural and photovoltaics characterization made and the results obtained using this modified CIGS photoelectrodes in a PEC system to reduce CO_2 to CO are presented. Finally, the analysis as well as conclusions and perspectives are summarized in Chapter V.

Contents

Chapter I

Phototelectrochemical (PEC) CO_2 reduction: general aspects

I Photoelectrochemical (PEC) CO_2 reduction: general aspects

I.1 Context

I.1.1 Energetic context: Why CO_2 reduction?

Our society is inherently dependent on reliable and efficient energy sources to run and sustain its activities. Since the beginning of the industrial revolution fossil fuels, upon combustion, have proved to be a consistent energy source. Their importance should not be underestimated, the combustion of coal, oil and natural gas supply close to 90 per cent of our current energy needs and makes much of what we do possible in our lifes.[9] However, fossil fuels pose a fundamental dilemma for our human society, their widespread use comes at a cost the gases emitted during the burning, these gases are strongly implicated as the main drivers of climate change. The massive consumption of fossil fuel results in the significant accumulation of atmospheric carbon dioxide (CO_2) which has a crucial role in global warming phenomenon. In other words, as shown in Figure I.1, CO_2 concentrations are rising mostly because of the fossil fuels that people are burning for energy, it accounts for almost three-quarters of the global emissions.

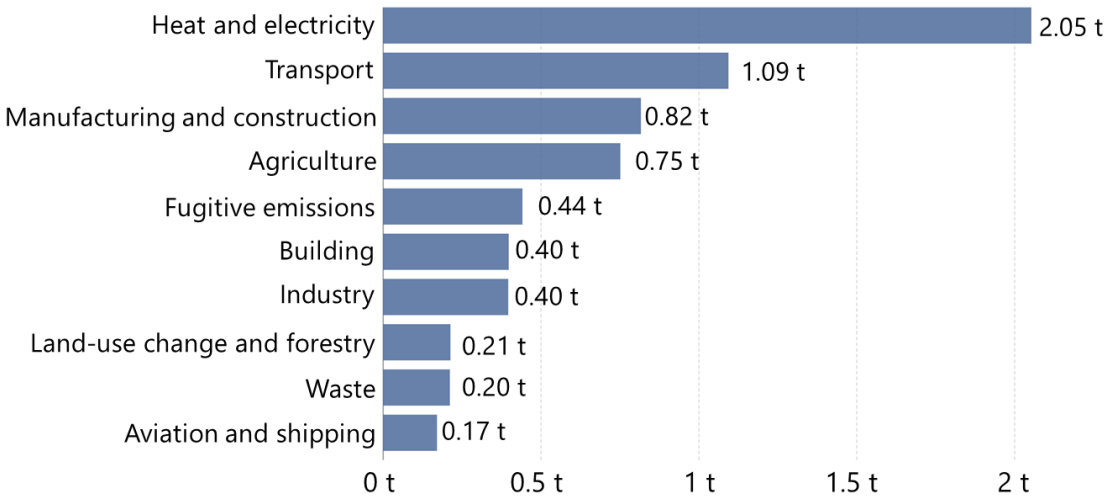

Figure I.1 2019 World greenhouse gas emissions by sector. Source: Our World in Data based on Climate Analysis Indicators Tool (CAIT).[10]

Currently, CO_2 atmospheric concentration is reaching unprecedented values in human history, 36.3 gigatonnes (Gt) in 2021 (Figure I.2), its resulting greenhouse effect is a major factor for climate change. Nevertheless, it will remain difficult to wean our world away from fossil fuels. For all it obvious drawbacks, it remains relatively inexpensive, widely available and readily adaptable to applications large and small, simple and complex.[11] Despite the continuous warning alerts from the scientific community and the climate international agreements, fossil fuels still dominate the global energy consumption. Along with this, there are also important economic consequences since these non-renewable resources are on their way to exhaustion. Thus, it is critical to shift paradigm, develop sustainable and renewable approaches for energy production. In other words, we need to de-fossilize our carbon economy.

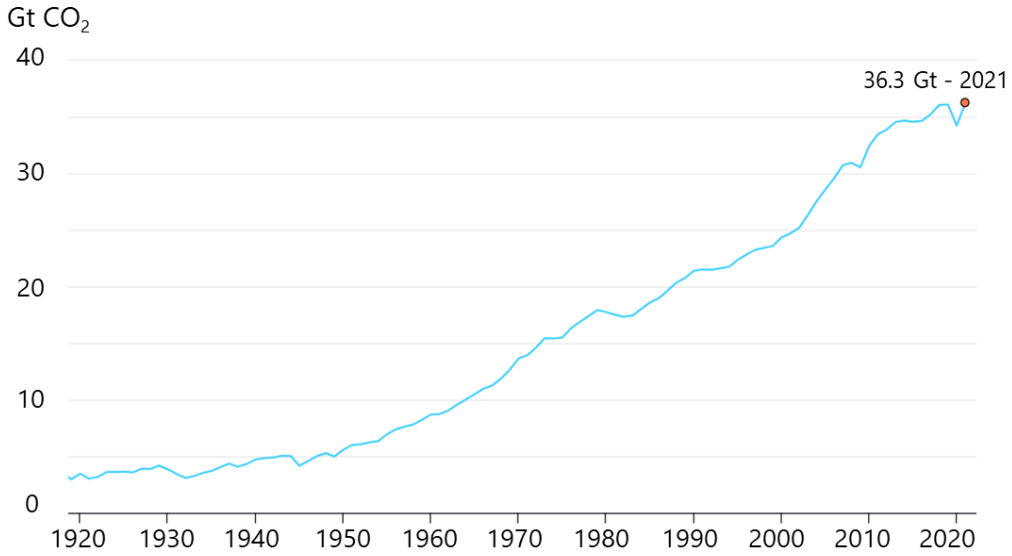

Figure I.2 CO_2 emissions from energy combustion and industrial processes, 1920-2021. Source: *AIE, 2020.*[12]

In response to the challengues, many scientists and engineers have committed to research ways to reduce CO_2 generated by human activities by several approaches, such as direct emission reduction, carbon capture/sequestration and storage, and the conversion of the CO_2 molecule into fuels.[4,13] Direct emission reduction or reduction of carbon intensity in the economy represent a radical approach that requires social and economic cost, keeping the international accord. It pursues the use of alternative fossil-free energy vectors and intrinsically unties energy production from carbon dioxide emissions.[9] The carbon capture and storage (CCS) requires the availability of significant

geological storage capacity, large scale underground or under seafloor locations. Suitable sedimentary basins and building the CCS facilities may cause social cost as well as legal and regulatory factors.[14] CCS may be viewed as a temporary, complementary option toward future sustainable solution. Turning CO_2 to fuels is presented today as the most promising approach. At the same time, CO_2 has been recognized as an inexpensive C1 carbon source, and research efforts are underway to use CO_2 directly in chemical production. The CO_2 catalytic reduction reaction allows to convert CO_2 into fuels. Two promising technologies, corresponding to this path of energy conversion, are electrochemical (EC) and photoelectrochemical (PEC) CO_2 reduction, which could produce gaseous fuel precursors (H_2/CO syngas mixture) or liquid fuels such as formic acid, methanol, methane, or light hydrocarbons, as well as commodity chemicals such as formaldehyde or CO_2-derived polymers from CO_2 recycling,[15,16] offering the possibility to develop a circular zero carbon emission fuel economy, since the required electricity could come from renewable sources such as solar energy. Furthermore, they provide a chemical solution to the intermittency challenge of solar energy, as a large amount of energy can be stored as chemical energy in the CO_2 reduced products, which could be later released.

I.1.2 Conversion of sunlight into fuels - solar fuels

Plant photosynthesis demonstrates the viability of directly converting sunlight into chemical fuels, which involves storing the energy from the incident solar irradiation in the form of chemical bond.[17] Taking inspiration from nature, strategies are burgeoning for the development of chemical processes capable of using sunlight to drive the synthesis of molecular fuels. This fuel production can be achieved through the photocatalytic (PC) or the photoelectrochemical (PEC) reduction of H_2O to H_2 (solar-to-hydrogen conversion) or CO_2 to hydrocarbons (solar-to-hydrocarbon conversion), in some analogy to natural photosynthesis so that it is sometimes referred to as artificial photosynthesis.[18] Since the final target is to use solar light to supply the needed electricity, molecules obtained by these means have been named solar fuels.

Only the CO_2 reduction process will be addressed in the following sections. The strategy developed in this manuscript consists in using solar electricity to convert the CO_2 molecule into fuels through electrochemical processes, with the aim to propose an efficient photoelectrode for PEC CO_2 reduction system.

I.1.3 Photovoltaic (PV) materials for solar fuel production

Among all the renewable resources, solar energy is the most abundant and exploitable one by making available more energy to the Earth for every hour than the total amount of energy humans consume in a year.[19] However, sunlight is intermittent and diffuse. Combining photovoltaic (PV) solar cell technologies that can effectively convert solar energy directly to electrical energy with EC or PEC CO_2 reduction processes that will use this electricity to perform the reactions, provide a chemical solution to the intermittency challenge of the solar energy, resulting in a large storage of electric energy produced by the sunlight in the chemical bonds of the molecules produced upon the CO_2 reduction.

Progress in PEC solar fuels technology has been slow, with remaining challenges in discovery and optimization of materials and design. In contrast to the early-stage character of PEC solar fuels technology, the development and marketing of PV devices for electricity production has become a practical and reliable, source of power throughout the world, despite its intermittence.[20] Considering the commercial success of conventional PV solar cell technologies, their accelerating rate of deployment, and continuing decrease in the cost of solar electricity over the past few years, the scientific community has started thinking more about potential pathways to practical and commercially viable applications of PEC solar energy conversion.

Powering the entire energy process of reducing carbon dioxide or oxidizing water with a photoelectrode requires the semiconductor employed to have a wide band gap and correctly positioned band edges (energy), which limits both the materials that can be employed and the ability of the semiconductor to absorb at solar frequencies available on Earth. An alternative is to connect photovoltaics junctions to PEC systems. PV junctions can have a band gap well-matched to the solar spectrum offering the generation of the voltage required to carry out the desired reaction while capturing a significant portion of the solar spectrum.[21] Heterojunction-based PV devices with suitable band alignment with the addition of dipole layer at junction interface are extensively used now for optimum results, due to their decreased recombination losses at interface and increased band bending.

Various recent PV device were tested as potential candidate for PV applications, being presented as alternative for scalable high efficiency PEC devices. As shown in Figure I.3, highly active photoelectrodes (photocurrent > 10 mA cm^{-2} at short circuit voltage)

such as p-CuO_2,[22,23] p-Si,[24–26] GaN,[27] InP,[28] CuInGaSe (CIGS),[29,30] are the most common reported in recent PEC CO_2 reduction systems. Most of the photoelectrodes showing photocurrent above 10 mA cm^{-2} are based on PV grade light absorbers with buried junctions. Notably, p- or n-Si, III/V based semiconductors, CIS and CIGS achieved the highest reported photocurrent.[31]

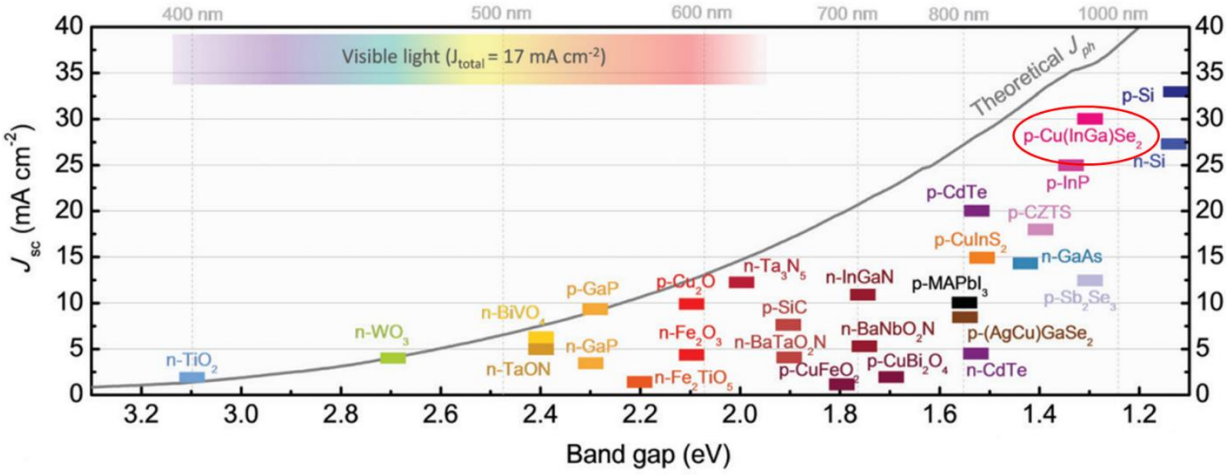

Figure I.3 Reported photocurrent density under short circuit conditions at photoelectrodes in PEC water splitting systems, under standard conditions: 1.5 AM G illumination. Adapted from Kim, J., et al.[31]

The copper chalcopyrite PV materials (i.e., $CuInSe_2$, $CuInS_2$ and $CuInGaSe_2$) are among the most attractive photocathodes for PEC systems. They present narrow and well defined band gaps, which allow for strong absorption of solar radiation in the visible region, presenting band structures which may be easily tailored to specific needs by altering the alloy composition and also have excellent electronic transport properties.[32] Because of these advantages, and the highlighted high photocurrent (ca. 30 mA cm^{-2} Fig. I.3), **we have chosen the $CuInGaSe_2$ PV cells in this work, aiming to develop an efficient PEC CO_2 reduction system.**

I.1.4 Solar fuels systems: PC, PV+EC, PEC configurations

Approaches combining light harvesting photovoltaic and electrochemical components integrated in one device, have aroused considerable interest for applications in CO_2 reduction recently. However, there are several ways to reduce CO_2 with the assistance

of renewable solar energy, this includes solar photovoltaic coupled to electrolyzers, photoelectrochemical and unassisted photocatalytic approaches. These varios approaches are illustrated in Figure I.4 (photocatalysis) Figure I.5 (electrochemical (EC) reduction by an electrolyser with catalysts that drive the necessary conversion reactions powered by a PV device (PV–EC)), Figure I.6 (a fully integrated system where the catalyst is deposited directly on top of the PV material to create a photoelectrochemical (PEC) device).[31,33,34]

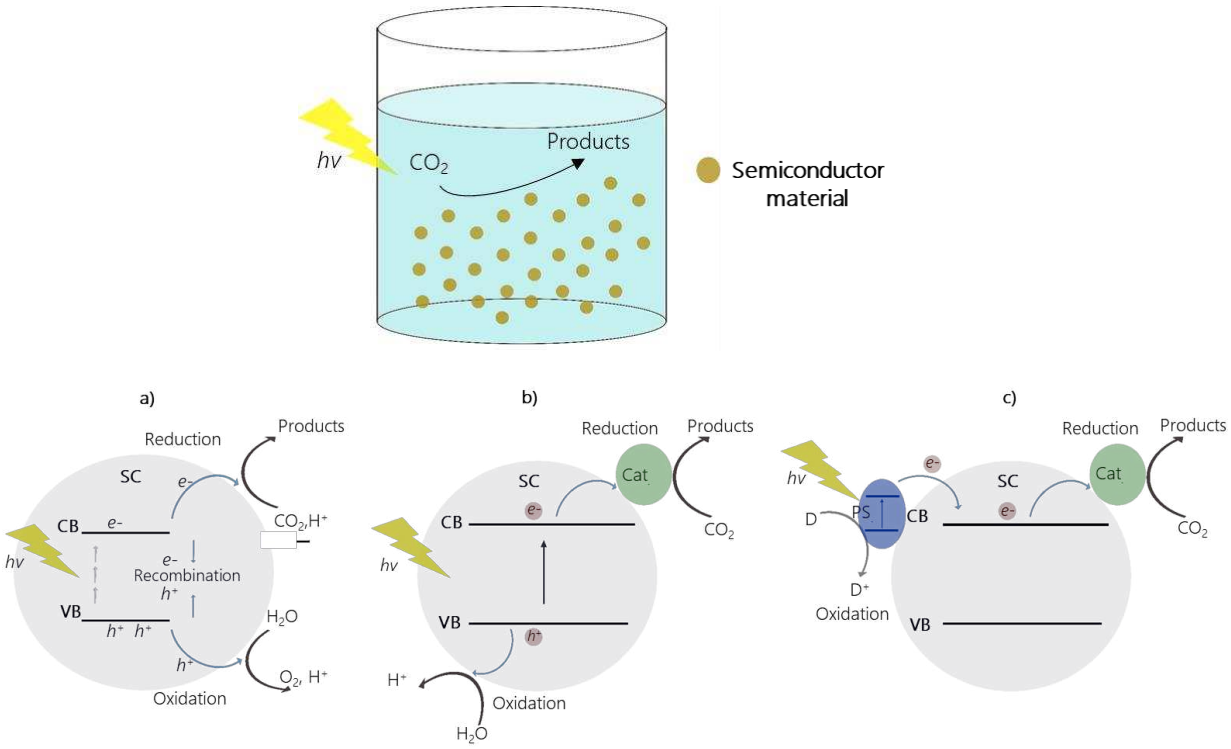

Figure I.4 Unassisted photocatalytic systems using: a) PC in a semiconductor particle. Heterogenized PC system for CO_2 reduction consisting of: b) a semiconductor (SC) particle decorated with a metal complex or metal nanoparticle as co-catalyst, c) a photosensitizer molecule and a co-catalyst immobilized onto the semiconductor particle (SC).

A PEC system can be described as a combination of photocatalytic reduction (PC) and electrocatalytic reduction (EC). It is expected to possess advantages of both approaches to achieve efficient and highly selective conversions of CO_2.[6] In a PEC system, the photoelectrode harvests light to generate electron–hole pairs and only performs a half-cell reaction, while the other half-cell reaction takes place on the counter electrode (that may be with a dark or photosensitive anode). Therefore, the reduction and oxidation products can be spatially separated by an ion-exchange membrane into two

half-cells. The electrode of the PEC system is polarized by an external bias, promoting charge separation through the electric field induced, which usually results in higher conversion efficiency than the PC system. Hence, the photoelectrode-based PEC system for CO_2 photoreduction is considered as a promising approach to achieve high performance.[8] **This is the approach we have selected in this work.**

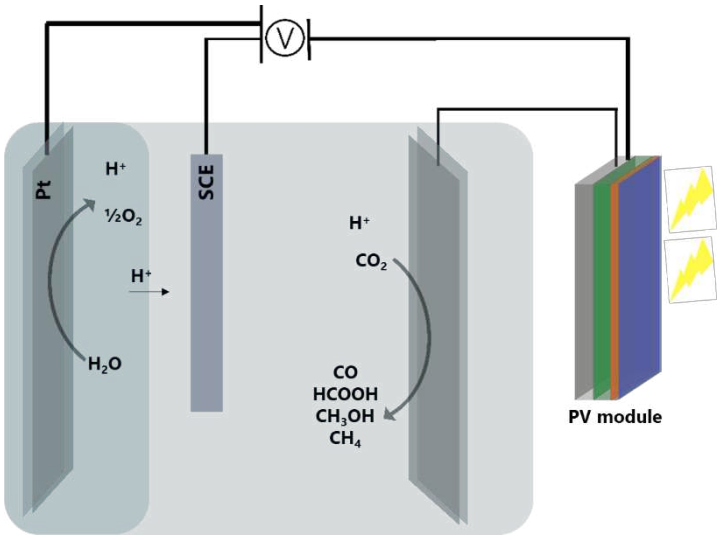

Figure I.5 Schematic representation of a PV-EC devices for production of solar fuels, showing products for electrochemical CO_2 reduction. The external PV cell is connected in series with an electrode which perform the reduction reactions.

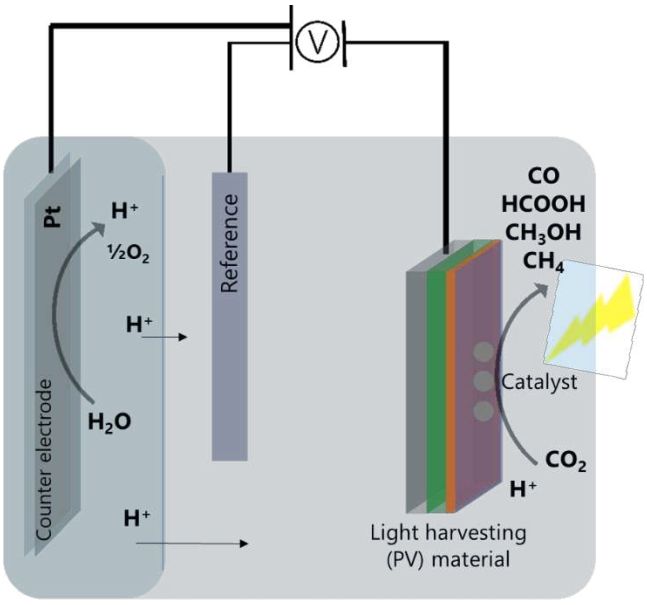

Figure I.6 Illustrative schemes of a PEC CO_2 reduction system using a PV photocathode connected directly to an external bias.

I.1.5 Solar fuels from phototelectrochemical (PEC) CO_2 reduction: current challenges

A photoelectrode in a PEC system consists of a single active device capable of handling the key processes involved in solar fuel generation: absorption of solar photon energy, charge separation and transport, and catalysis at the surface to efficiently use the photogenerated charge carriers to catalysis.[34] In practice, developing a single device to handle all of these functions simultaneously has been challenging. Compared to PV-EC devices, PEC devices are less technologically advanced and mature. PEC devices are still in the early stage of development.[35]

These devices require photon absorber materials that can efficiently harvest solar energy. Development of solar fuels devices begins with identifying and developing appropriate materials for photon capture. There is a wide range of absorber materials that have been investigated, as illustrated in Figure I.3. However, there is currently no single material that fulfils all of the requirements for PEC CO_2 reduction: The PV material must have an appropriate bandgap and band structure to absorb a large portion of the available solar flux and provide a sufficient driving force for the relevant electrochemical reactions. Additionally, it must have good charge transport properties and long-term stability, while ideally consisting of inexpensive, non-toxic and abundant elements.[34]

A semiconductor photoelectrode surface is usually limited by the sluggish reaction kinetics due to the proton coupling multiple electrons involved in the light-driven CO_2 reduction reactions, and poor control of the surface state. Semiconductor surfaces are usually electrocatalytically inert and can hardly interact and activate CO_2 molecules. A common strategy to improve the reaction rate and lower the activation energy or overpotential for CO_2 reduction is to add a catalyst to the light-driven system.

Coupling catalysts with semiconductors can provide more active sites and accelerate the CO_2 reduction kinetics. The loading of surface catalysts can also promote the separation and transportation of photogenerated electron/hole pairs. In some cases, surface co-catalysts can improve the stability of the photoelectrodes consuming rapidly the surface charge carriers.[8] Integration of an electrocatalyst for CO_2 reduction onto the surface of a photoabsorber often improves the performance of the device.

With the expansion of the studies regarding both molecular electrocatalysts for CO_2 reduction,[36–39] and semiconductor materials for solar fuels production,[4,40] there is now

a large number of potential combination of catalysts and absorbers. In the development of hybrid photoelectrodes for PEC CO_2 reduction, the recent studies were mostly focused on noble-metal-based co-catalysts, (e.g., Au, Ag, Pt, Pd, Ru, Rh, Ir, Re) either through direct utilization of noble-metal nanoparticles (NPs) or deposition of noble-metal complexes onto the photocathodes. Considering the cost of noble metal complexes, it is desirable to replace noble metals with abundant transition metals for CO_2 reduction. In this correction, several metals (such as Cu, Co, Zn, and Fe) have been used as NPs or complex catalysts onto photocathodes. With the assistance of such homogeneous molecular catalysts that may provide high catalytic selectivity and efficiency, an overall improvement of the cell performance for PEC CO_2 reduction may be achieved.

When loading a co-catalyst onto a photoelectrode several factors that can influence performance and should be taken into consideration. For example, the loading amount, particle size (in the case of NPs), and dispersion are all important factors. Oversized particles and excessive loading amount may block the incident light from the photoelectrode. In addition, the agglomeration of catalyst particles or complexes can impede the transfer of charge carriers to surface-bonded reactants.[8] Grafting molecular catalyst onto the surface of the electrodes seems to be one of the best strategy to overcome these drawbacks. In general, a good anchoring group should react to form a functionality that is resistant to detachment from the surface, promote charge transfer, be able to withstand the reducing environment during catalysis and be stable to long-term light exposure. Carboxylates and phosphonates are the most widely studied and employed anchoring groups as they bind well to oxide semiconductors.[41]

Semiconductor/catalyst interface is also critical to PEC. Poor interfacial adhesion and inadequate coupling would cause problematic charge transfer across the interface, leading to poor PEC activity and stability. Conventional methods to introduce the catalyst include dropcasting, covalently binding onto the light absorber surface, or physical vapor deposition and electrodeposition onto a protective coating layer. Otherwise, semiconductor catalyst interfaces are usually not sufficiently robust and may gradually disintegrate during prolonged PEC reaction.

To this end, different strategies to enhance the interfacial coupling between semiconductors and catalysts have been studied**. One approach is direct chemical growth**. By introducing the semiconductor material as the substrate into a reaction solution,

catalytic nanostructures may heterogeneously nucleate and grow on its surface. Semiconductor/catalyst interfaces formed by this way are generally very robust and can withstand higher mechanical stresses while protecting from photocorrosion.[42]

Unfortunately, PV materials based in buried junctions, presenting high photocurrent, are generally prone to corrosion and exhibit poor stability in aqueous solution.[34] Adding a catalytic layer to the PV device can improve its stability, acting as both, catalytic and corrosion protection layer. This last must be highly stable, conductive enough and transparent to maintain high light harvesting efficiency. All these mentioned aspects require consideration for the design and application of surface coatings or immobilization of heterogeneous catalysts.

I.1.6 Towards high solar-to-fuel conversion systems: our strategy

Even though, remarkable progresses made since the first PEC CO_2 reduction cell was reported in 1978, research about PEC CO_2 reduction is still on the early stage of development. The majority of published PEC photocathodes suffer from poor durability, low solar conversion efficiency, uncontrolled product selectivity, and strong competition between CO_2RR and hydrogen evolution reaction (HER). Loading a catalyst on the photoelectrode surface has been shown to be an effective approach to accelerate and regulate the surface reaction kinetics and improve the product selectivity in PEC systems. Therefore, the key topic in the PEC CO_2RR still focuses on photoelectrode fabrication to achieve high energy conversion efficiencies and high selectivity toward target products. The catalyst grafting methods proposed so far suffers from poor stability of the binding between the catalyst and the photoelectrode surface.

Given the challenges listed before, there is still a wide range of improvements possible in PEC systems. This manuscript aims to present in detail a new strategy for the development of a hybrid photocathode. We will deposit by electrochemistry a hybrid catalytic layer formed by a metal oxide and a molecular catalyst on top of photoelectrodes.

Using a CIGS PV material as substrate, hybrid metal oxide|molecular catalyst nanostructures can nucleate and grow heterogeneously on its surface by an electrodeposition process that will be describe later. The objective of this approach is to combine the stability offered by the metal oxide layer and the high catalytic activity of the molecular catalyst in a complete photoelectrocatalytic device, without affecting the intrinsic efficiency of the PV layers.

I.2 The difficulty of CO_2 reduction

CO_2 is a stable molecule generally produced by fossil fuel combustion and respiration. Returning CO_2 to a useful state by activation/reduction is a challenging problem, requiring appropriate catalysts and energy input. This poses several fundamental challenges in chemical catalysis, electrochemistry, photochemistry, and semiconductor physics and engineering.[33]

CO_2 is a triatomic molecule with a molecular weight of 44.01 g mol^{-1} and a standard heat of formation ($\Delta_f H°$) of -394 kJ mol^{-1}. At room temperature and atmospheric pressure, it is a gas. At atmospheric pressure it sublimes directly from a solid to a gas at -78 °C.[1] In the molecule carbon (C) and oxygen (O) atoms are held together through bonds formed by sharing electrons and possess strong electrical affinities. The C═O bond has a large bond energy of 750 kJ mol^{-1}, meaning that the dissociation of the C═O bond is a tough procedure and great energy input is required to break this bond. Thus, CO_2 molecule has high stability and inert nature. Additionally, CO_2 is a highly symmetrical nonpolar linear molecule, leading to a rough adsorption and activation process.[2]

Carbon dioxide is the most oxidized form of carbon, hence, the only chemical transformation possible would be to reduce it, that means to transfer electrons to it. The situation becomes very complicated when hydrogen is involved.[43]

I.2.1 Thermodynamic considerations

The CO_2 reduction process has numerous elementary steps. Typically, multiple electrons and protons are involved in the reduction process, and depending on the number of electrons and protons involved in the CO_2RR, there are many possible products including CO, HCOOH, CH_3OH, CH_4, and C_2+ products.[2] The corresponding redox potentials and the Gibbs free energy of the reactions are summarized in the table 1.

Table 1. Apparent standard redox potentials ($E^{0\prime}$) relative to the Standard Hydrogen Electrode (SHE) at pH 7 and the free Gibbs energy of some specific CO_2 conversion reactions.[2,44]

Product	Reaction	$E^{0\prime}$ V vs. SHE	ΔG^{θ} (kJ mol^{-1})
Hydrogen	$2H^+ + 2e^- \rightarrow H_2$	-0.41	237.17
CO_2 anion radical	$CO_2 + e^- \rightarrow \dot{CO}_2^{*-}$	-1.90	-
Formic acid	$CO_2 + 2H^+ + 2e^- \rightarrow HCOOH$	-0.61	269.86
Carbon monoxide	$CO_2 + 2H^+ + 2e^- \rightarrow CO + H_2O$	-0.53	257.38
Formaldehyde	$CO_2 + 4H^+ + 4e^- \rightarrow HCHO + H_2O$	-0.48	528.94
Methanol	$CO_2 + 6H^+ + 6e^- \rightarrow CH_3OH + H_2O$	-0.38	701.87
Methane	$CO_2 + 8H^+ + 8e^- \rightarrow CH_4 + H_2O$	-0.24	818.18
Ethanol	$2CO_2 + 12H^+ + 12e^- \rightarrow C_2H_5OH + 3H_2O$	-0.33	1325.56

However, the actual electrode potentials required to drive these reduction reactions are much more negative than the equilibrium ones. The additional potential that is needed to make the reaction happen will cause an energy loss. The operating overpotential is then used to quantify this loss. It corresponds to the difference between the applied potential at an electrode performing a given reaction, and the standard redox potential of this reaction.

I.2.2 Kinetic considerations

In regards to conversion reactions listed in Table 1, the Gibbs free energy change of these reduction reactions from CO_2 to other products under a standard state is positive ($\Delta G^{\theta}>0$) meaning that the conversion reactions are non-spontaneous. On the other hand, introduction of one or more electrons to reduce CO_2 into any of its reduced forms requires negative potentials as high as -1.90 V vs. SHE in aqueous media at pH 7 for the formation of the radical anion form, $CO_2^{\bullet -}$.[45] This energetic requirement is related to a large barrier due to an internal reorganization to pass from a linear CO_2 molecule to a bent $CO_2^{\bullet -}$ radical anion form and to solvent reorganization. CO_2 electrochemical reduction is mainly controlled by kinetics. Moreover, CO_2 reduction has several possible reaction pathways resulting in poor reaction selectivity. Although some CO_2 reduction reactions have a better than H_2, it is still a kinetically slow process due to the series of multiple proton-coupled electron transfer processes involved in CO_2 reduction.[46]

Since CO_2 reduction kinetics is slow, it is usually accompanied by significant cogeneration of H_2 from hydrogen evolution reaction (HER). Hydrogen production will be most of the time in competition with the generation of the possible CO_2 reduced products. An effective way to enabling the multi-electron, proton, reduction of CO_2 and to avoid the formation of $CO_2^{\bullet-}$ is therefore to first transfer the photoelectron to a known CO_2 reduction electrocatalyst, this last allows to overcome kinetic barriers and to efficiently and selectively reduce CO_2.[36] The use of a catalyst allows to realize the reaction without applying a too large overpotential, creating another reaction pathway with a lower activation barrier. A range of metals have been shown to be effective as heterogeneous electrocatalysts for CO_2 reduction. Moreover, transition-metal complexes with accessible multiple redox states can promote such proton-assisted, multi-electron pathways. Using molecular catalyst makes possible to target specific CO_2 reduction products and avoid competitive hydrogen evolution.

The reduction of CO_2 typically gives CO and/or formic acid (HCO_2H) as products. Among the wide variety of CO_2 reduction products, CO is a gaseous product that requires only two proton−electron transfers, and thus a kinetically feasible choice compared to CH_3OH and CH_4, which require six and eight proton−electron transfers to form one molecule, respectively. **In this work we will focus on the use of molecular catalyst for CO_2 reduction to CO.**

I.3 Molecular catalysts in CO_2 reduction

Molecular catalysis is one of the most promising approach to obtain atom efficient catalysts with exceptional intrinsic activity toward CO_2 reduction.[47] Molecular catalysts can be used to overcoming the thermodynamic barriers of CO_2 reduction, lowering the overpotential by stabilizing the intermediate transition states between the linear CO_2 molecules and the targeted product. CO_2 has several possible binding modes to transition metal complexes, the two main ones being through coordination of the carbon atom, and through coordination of both oxygen atom and carbon atom. The metal can then act as an inner sphere electron transfer agent to activate CO_2 for further transformation. With the choice of various metal centers and ligand structures, molecular catalysts are highly tunable to achieve intended, combined properties such as fast kinetics, product selectivity and long-term stability.[33]

Substantial work has been dedicated to the development of catalysts for CO_2RR, there now exist a range of known molecular electrocatalysts with high selectivity for the CO_2 reduction reaction, including those based on noble (e.g., Ru, Ir, and Re) and transition metals (e.g., Co, Ni, Fe, Mn, and Cu),[37,39,48,49] specially for CO and HCOOH production. More reduced product such as CH_3OH CH_4 are rarer, while C_2 product have never been reported. In this thesis we will be focus on transition metal complexes catalysts.

Motivated by the desire to avoid the use of precious metal-based CO_2 reduction catalysts, earth-abundant metal complexes catalysts such as Fe and Co porphyrins,[50–53] Co quaterpyridines,[54] and Co phthalocyanines,[55–58] shown in Figure I.7 have been reported by our laboratory and other as interesting class of compounds with some noticeable advantages, such as easy accessibility, chemical stability and structural tunability at the molecular level. Moreover, good catalytic performances have been obtained with these molecular catalysts with excellent selectivity, notably for CO,[55] and HCOOH.[59,60] In some cases, CH_3OH[61] and CH_4[62] have been obtained. Some of these complexes have been used in photoelectrochemical CO_2 reduction. Upon immobilisation on light absorbing photocathodes, we can cite as examples Co phthalocyanine,[26] or Co quaterpyridine,[29] bearing phosphonic acid anchoring groups, that have been included in highly efficient photocathodes for PEC CO_2 reduction.

Quaterpyridine metal complexes

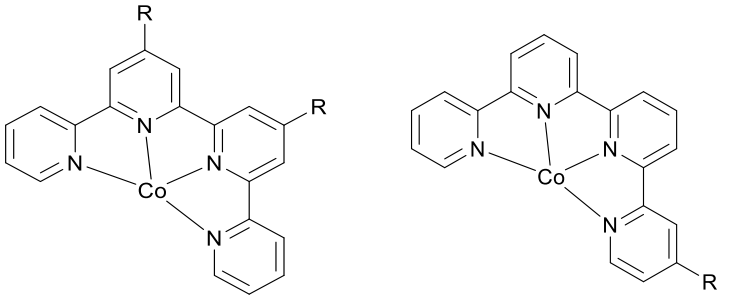

R = Ph-N(Me)$_3^+$, Ph-COOH, etc.

Porphyrin metal complexes

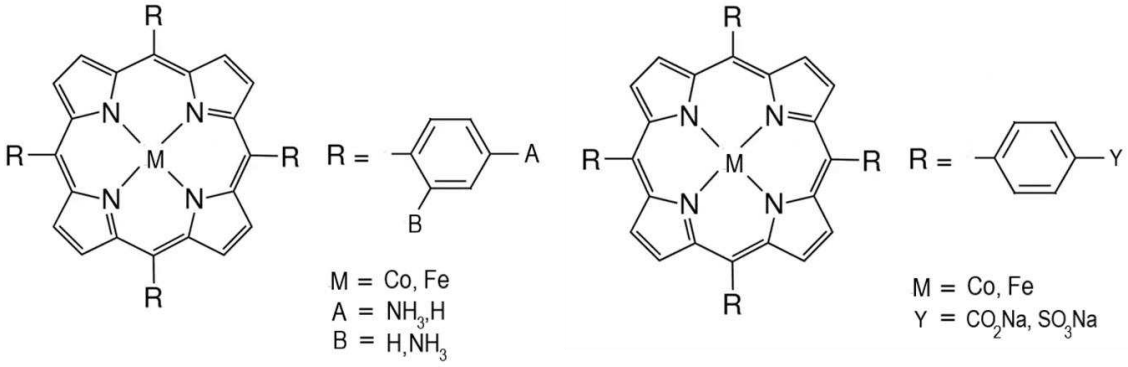

Phthalocyanine metal complexes:

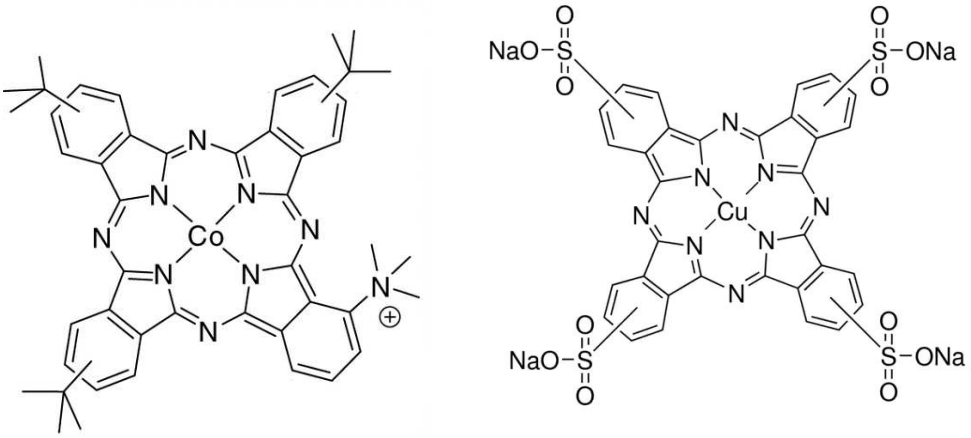

Figure 7 Examples of typical earth-abundant metal based molecular catalysts previously investigated for the electrocatalytic and/or photocatalytic CO_2 reduction.

Among these complexes, cobalt phthalocyanine (CoPc) has been identified as one of the most promising electrocatalysts for CO_2RR owing to its high selectivity and activity

for CO production and its,[55] and also its well-known easy synthesis procedure. Phthalocyanines (Pcs) are principally use in dyes and pigments but Pcs are molecules chemically and thermally stable. The high stability of certain phthalocyanines is one of the essential assets for the technological applications. Some Pcs can be heated up to 500°C under high vacuum without decomposition, they can resist to the action of non-oxidizing acids and bases, they are optically stable and can exhibit good tolerance to high intensity electromagnetic radiation.[63] PCs are also good photosensitizers and good electronic conductors which led them to be used as an active component in dye-sensitized solar cells, as well as in organic solar cells.[64]

The main catalyst used in this manuscript is a water soluble cobalt phthalocyanine bearing four trimethyl ammonium groups, usually referred to with the acronym CoPc3 (Fig. I.8). We have also used a nickel phthalocyanine with tetrasulfonic acid tetrasodium groups and a cobalt tetra-sulphonated phenyl porphyrin CoTSPP.

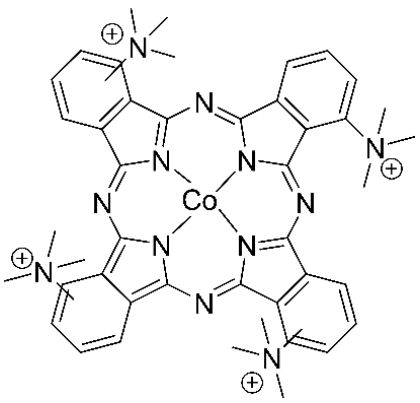

Figure I.8 Phthalocyanine complex, CoPc3 water soluble catalyst, used in this study

I.3.1 Immobilisation/incorporation of molecular Catalysts on electrodes/photoelectrodes

The term "immobilised" is defined here as the use of physical or chemical means to prevent the molecular catalyst from diffusing away from the electrode surface. Catalyst assembled at conductive electrodes are often deposited from an ink containing small quantities of a binder such as Nafion, which provides proton conduction. The immobilisation of molecular catalysts onto the surfaces of photoelectrodes for solar fuel production has been achieved in a variety of manners. In many cases, this requires the chemical modification of the catalyst's ligand structure with appropriate anchoring

groups that allows surface binding in either through a non-covalent or a covalent mode. The choice of these anchoring functions depends mainly on the surface on which catalyst immobilisation is envisioned. Regarding photocathodes, the majority of these surfaces are inorganic semiconductors, including metal oxides and non-oxide group III-V/group IV type semiconductors. To this end, a large number of chemical functions have been described to allow the grafting of photosensitisers and/or catalysts onto metal oxides, including carboxylic acids, phosphonic acids, organosilanes/silatranes, and acetylacetonate or hydroxamate anchoring groups.[65–72] Among these different anchoring moieties, carboxylic acids and phosphonic acids stand out both in terms of being the most widely applied for solar fuel photoelectrodes, specially onto metal oxide surfaces. A recent example is shown in the figure I.9. An important requirement for immobilisation/incorporation of a catalyst onto the semiconductor surface is the stability for long periods of time under catalytic operating conditions. In addition, immobilisation should not hinder the catalytic activity of the complex.

In this terms, we have developed another method relying on the incorporation or encapsulation of the molecular catalyst in the window oxide layer of the photoelectrode by a one-step co-electrodeposition of both the catalyst and the oxide. This allow us to prepare electrodes with self-supported catalyst.[73]

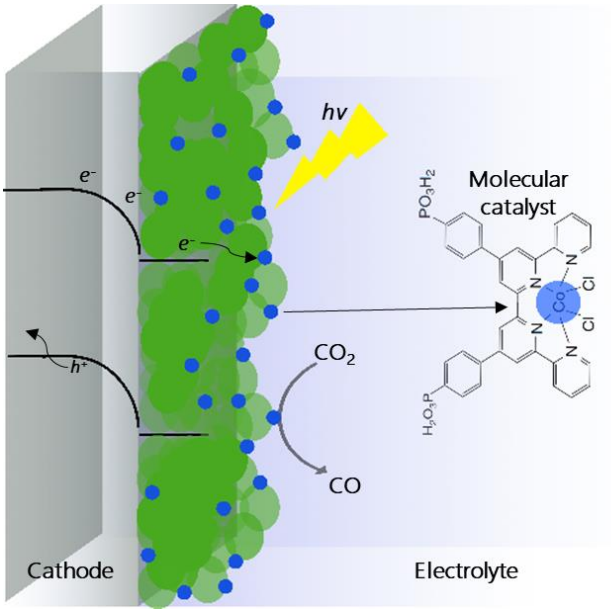

Figure I.9 Schematic illustration of PEC CO_2 reduction hybrid photoelectrode with a covalent linked cobalt quaterpyridine (blue) co-catalyst on a nanoporous TiO_2 layer (green).[29] The catalyst is grafted via two phosphonic acid groups to the TiO_2 window layer covering the photoelectrode (CIGS).

I.4 PEC vs PV systems.

Photoelectrochemical devices enable the transformation of light to energy stored in chemical bonds while photovoltaic devices enable the transformation of light to electricity. The similarities and differences between photo-electrochemical (PEC) and photovoltaic (PV) devices will be discussed in the following sections. The key distinctions between these two systems is that a PEC device contains:

- an electrolyte phase in which ions carry the moving charge
- an electrode-electrolyte interfaces where electrochemical reactions take place

In contrast, a PV cell:

- is a purely solid-state device in which holes or electrons carry the moving charge
- no chemical change occurs

Both PEC and PV devices are designed to harness the energy of hole-electron pairs created by light absorption (typically in a semiconductor or a molecule) by separating them and using them to produce chemical or electrical energy.

The formation of a junction between two materials with an electrochemical potential difference at equilibrium is the critical common point to both PEC and PV devices. The combination of the electric and chemical potential differences across this junction (in different proportions depending on the device) causes holes and electrons to flow in opposite directions, producing the photocurrent. A PV junction is typically based on *p*-*n* homojunction, heterojunction, or *p*-*i*-*n* junction made of doped or intrinsic semiconductors that are also light-absorbing materials. A PEC device junction is typically formed between a semiconductor electrode and an electrolyte, sometimes with an interposed catalyst layer. The light is absorbed either in the semiconductor or in the catalyst.

For a better understanding and to provide us insights for understanding PEC and PV systems, and since this thesis was conducted in two laboratories, one specialized in photovoltaics and the other in electrochemistry and catalysis, it is important to have for each system some description of the fundamentals.

Consequently, in the following sections we will briefly introduce some fundamentals of semiconductors, PEC and PV systems. We will describe the basic working principle

and the reaction mechanism of PEC CO_2 reduction occurring at the solid liquid interface. Finally, we will present some of the more recent PEC CO_2 reduction systems founds in the literature.

I.4.1 Overview of Semiconductor Physics

Semiconductor electronic band structure. The electronic structure of a semiconductor possesses a void energy region where no states are available to promote recombination of an electron and hole produced by photo activation in the solid (Figure I.10). This void region is called the band gap (E_g) and extends from the highest energy level of the electron-occupied valence band (*VB*) to the lowest energy level of the vacant conduction band (*CB*). In metals, these two bands overlap, forming a continuum of states for the electrons. Metals exhibit high electrical mobility due to the lack of a band gap, which enables electrons to move to the available set of delocalized empty orbitals with small activation energy. Semiconductors, on the other hand, have significant energy difference between the two bands, which leads to the valence band being almost completely filled whereas the conduction band is almost vacant.[74] However, electrical mobility can be induced upon exciting the electrons from the *VB* to the *CB*. For that, illumination with photons of energy greater than or equal to E_g is required. The photogenerated electrons from the valence band are excited and promoted to the conduction band, leaving empty states in the valence band, which gets the attributes of positively charged holes.[21]

Intrinsic and extrinsic semiconductors. Typically, Semiconductors are categorized depending on the charge densities of electrons and holes (Figure I.10). At ordinary temperature in a pure semiconductor, some electrons will be promoted to the conduction band by thermal excitation alone. When electrons and holes generated from impurities are much less numerous than thermally generated electrons and holes, they are called intrinsic semiconductors. For intrinsic semiconductors, the densities of electrons and holes are equal. Impurities can be introduced through doping the semiconductors, producing a non-negligible number of electrons and holes. In this case the semiconductor is called extrinsic semiconductor with an excess of either electrons or holes. Introduction of vacancies or impurities possessing a different electronegativity compared to the lattice elements alters the number of charge carriers. Semiconductors

with donor impurities that provide electrons to the lattice are called *n-type* semiconductors with electrons as the majority charge carrier. On the other hand, semiconductors with acceptor impurities that remove electrons from the lattice called are *p-type* semiconductors, using positively charged holes as the majority charge carrier.

Fermi level. Thermodynamically, the Fermi level (E_F) is defined at 0 K as the energy at which the probability of finding an electron is ½. All the energy levels below E_F are occupied by electrons and those above E_F are likely empty at a temperature of 0 K.[75] However, for semiconductors, a more useful working definition is the average electrochemical potential of the electrons in the lattice, since the Fermi level typically lies within the band gap, where electron density is quantum mechanically forbidden.[21] As shown in the figure I.10, for intrinsic semiconductors, where the numbers of electrons and holes are equal, E_F is located at the midpoint of the band gap. For extrinsic semiconductors, E_F is placed slightly below the *CB* for *n-type* semiconductors and slightly above the *VB* for *p-type* semiconductors.[75]

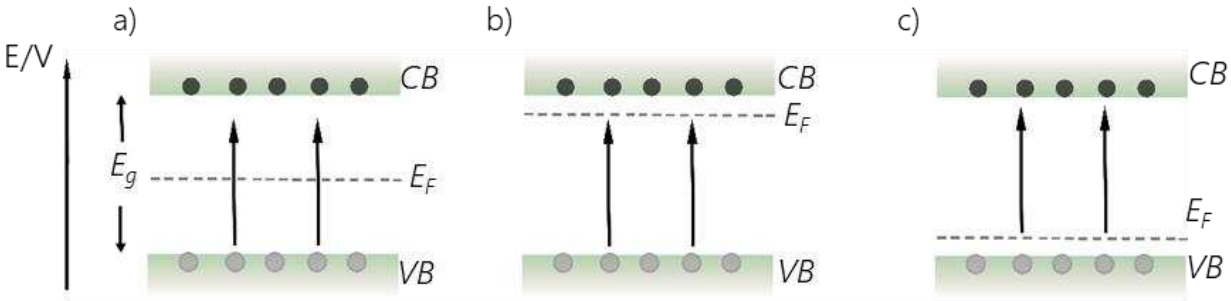

Figure I.10 Energy band representations of a) intrinsic semiconductor, b) extrinsic semiconductor with *n-type* donors and c) extrinsic semiconductor with *p-type* acceptors.

Band bending. When the Fermi level of a semiconductor placed in an electrolyte solution does not match the redox potential of the electrolyte (ΔE_R), electron flow will occur at the semiconductor−electrolyte interface to minimize the difference in the Gibbs free energy of the two different phases. The free energy of a semiconductor (ΔG_{SCr}) can be related to the free energy of an electrolyte ($\Delta G_{electrolyte}$), which is given by the Nernst equation:

$$\Delta G_{electrolyte} = -n.F.\Delta E_R \quad \textbf{(eq. I.1)}$$

Because of the much larger number of electroactive species in the electrolyte than the number of mobile electrons in the semiconductor, E_F changes significantly with electron flow at the interface but E_R remains unchanged. As the ΔG_{SCr} shifts, the *VB* and *CB* energies will shift at the semiconductor–electrolyte interface, keeping the energy difference between the two bands (E_g) the same. The electron flow across the interface creates a space charge region, also called the depletion layer because the majority charge carriers are depleted, near the junction inside the semiconductor. After reaching of equilibrium, the *VB* and *CB* edges in the space-charge region are bent in the band diagram (Figure I.11), indicating a different occupation of energy levels near the interface compared to the bulk material.[21]

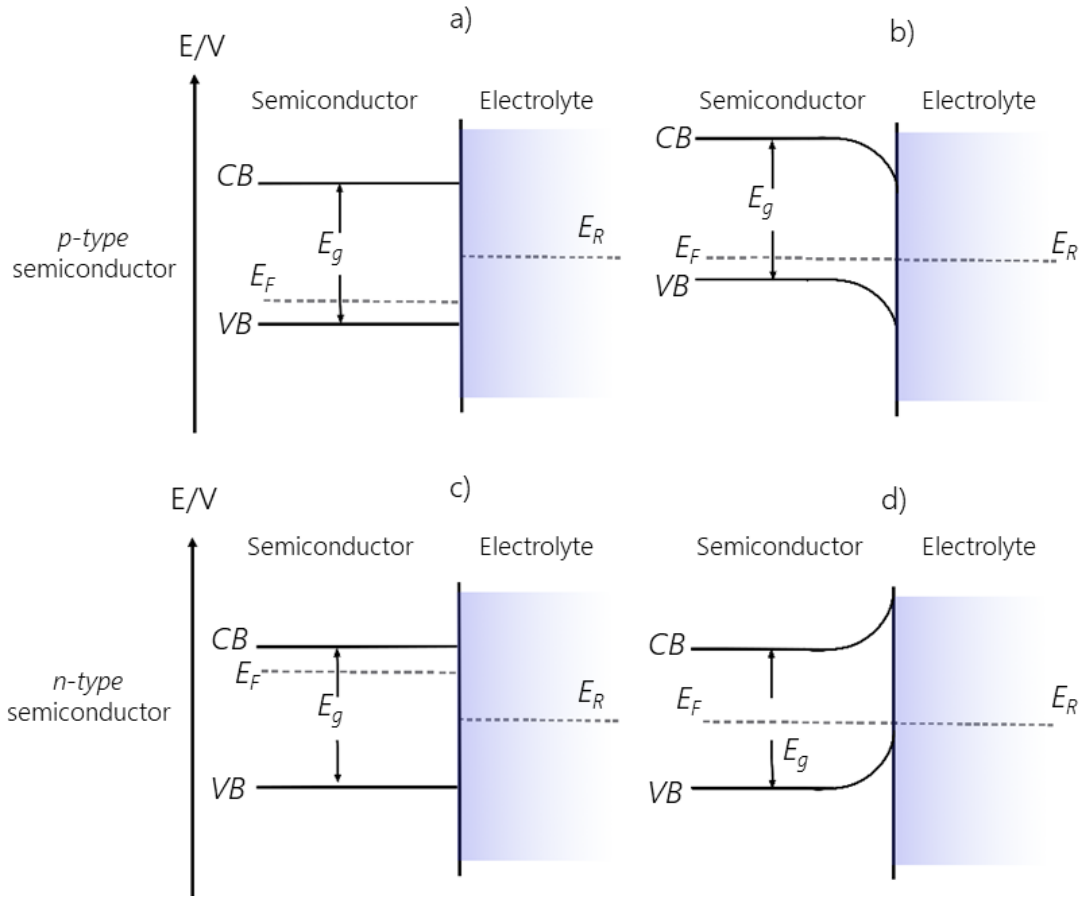

Figure I.11 Band diagrams of *p-type* (a, b) and *n-type* (c, d) semiconductors immersed in an electrolyte before equilibrium (a, c) and at equilibrium (b, d).

The bending is indicative of an electric field that causes electrons and holes to migrate in opposite directions. The charge carrier moving toward the interface can then be used to perform electrochemical reactions. The minority charge carriers are directed toward the semiconductor−electrolyte interface, the nature of this species determines whether an oxidation or reduction reaction is observed at the semiconductor interface. In a *p-type* semiconductor, E_F is located slightly above the *VB*. Therefore, at equilibrium, interfacial electrons flow toward the semiconductor, resulting in an increase in the Fermi level energy and a bandbending gradient that moves *CB* electrons toward the semiconductor interface. The opposite occurs in an *n-type* semiconductor, with electrons flowing from the semiconductor to the solution, lowering the Fermi level energy and forming a potential that moves *VB* holes toward the semiconductor interface.

Consequently, photoreduction reactions will utilize *p-type* semiconductors because electrons will flow down the potential gradient in the conduction band toward the semiconductor electrolyte interface. Photoelectrodes used in PEC CO_2 systems are based on *p-type* semiconductors.

Electron−hole separation under illumination. When a semiconductor absorbs photons with energy $h\nu > Eg$, electrons are promoted from the valence band to vacant states in the conduction band, creating electron–hole pairs. We consider now what happens if the semiconductor is initially in equilibrium with a redox electrolyte in the dark so that the bands are bent as shown in Figure I.11. To utilize the photogenerated electrons and holes effectively in a PEC CO_2 system, which involves multiple steps, the electron−hole pair must be separated in a manner that avoids or at least slows recombination and thus promotes the transfer of the charge carrier to the redox active species at the semiconductor−electrolyte interface. In the absence of an electric field, recombination of the electron−hole pair is a fast process that occurs on a nanosecond time scale by a nonradiative relaxation of excited electrons to the ground state. It is commonly known that the electron−hole recombination limits the electron transfer process at the semiconductor interface since the time scale for electron−hole recombination is faster than the interfacial electron transfers process. Under the effect of the electric field at the interface, the minority carriers (electrons) are swept towards the surface while the holes are pushed to the rear ohmic contact. It follows that, whereas reduction in the dark is prevented by the high barrier for transfer of electrons from the SC to the solution, reduction becomes easy under illumination since electrons are transferred to the solution from the conduction band.[21]

I.4.2 Principles of PEC CO_2RR systems

A typical PEC system for reduction reactions uses a semiconductor photocathode, a reference electrode, and a dark anode in a classical three-electrodes cell (Figure I.13). As mentioned before, PEC CO_2 reduction systems typically use *p-type* semiconductors as the light-harvesting substrate of the photocathode due to the downward band-bending characteristic of p-type semiconductor/electrolyte interface. When a p-type semiconductor photocathode is immersed into the CO_2 saturated electrolyte, a semiconductor-electrolyte interface is formed. The difference of the E_F (or electrochemical potentials) across the interface would induce an electric field and cause the downward band bending of the semiconductor. Upon the light absorption, electron-hole pairs are generated by exciting an electron from the semiconductor valence band to the conduction band and are then separated into free carriers. With many number of holes in the *VB* and few electrons in the *CB*, illumination can effectively increase the electrons in the *CB* and the cathodic current. Driven by the generated electric field, minority charge carriers travel from the inside of semiconductor to the surface and finally are consumed by the surface redox reaction of CO_2 reduction. This process is facilitated by an additional external bias. Meanwhile, holes are forced to pass through the external circuit to the counter electrode and participate in OER to close the reaction loop.[42]

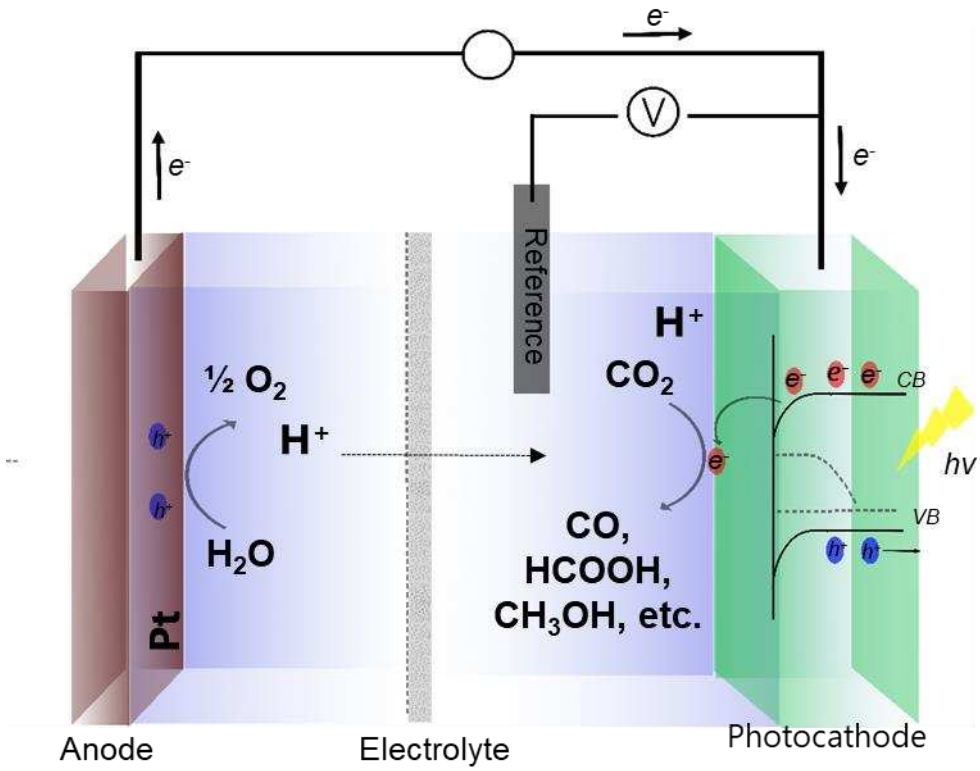

Figure I.13 Schematic illustration of a typical PEC CO_2 reduction system and its working principle in a three-electrodes configuration, with a *p-type* semiconductor photocathode for CO_2 reduction, an anode for H_2O oxidation, and a reference electrode (RE). Adapted from.[7,8,42] For p-type SC used as photocathode, the Fermi level lies close to the *VB* and is typically more positive in potential than the redox potential of the electrolyte, therefore the SC accepts electrons from the solution depleting the SC of majority charge carriers (holes). The net effect is a downward bending of the band in the space charge region. This band bending combined with the associated electric field, enables efficient separation of photoexcited electron–hole pairs, directing electrons toward the electrolyte solution to drive the reduction reaction. Under illumination, the quasi-Fermi energy of electrons (*EF-n*) is raised, enabling electrons to be faster transferred to the redox active species at the semiconductor−electrolyte interface.

I.4.3 PEC CO_2 reduction state of the art

Progress made in CO_2 reduction photocathodes based on earth-abundant transition metal complexes immobilised or incorporated on light-absorbing semiconductors lags far behind that of proton-reducing photocathodes. To date, reported molecular catalyst-based photocathodes performing CO_2 reduction remain scarce, either in organic or aqueous media, and continue to rely largely on precious metal components.

Considering systems operating in aqueous media, among the firsts photoelectrodes modified by a molecular complex reported, we can cite the series of work published by Sato, Morikawa, Arai and co-workers since 2010 using a precious metal Ru-centred metal complexes as molecular catalysts with a InP,[76] Cu_2ZnSnS_4.[77] High selectivity toward formate production were obtained with these systems. However, current density and faradaic efficiency remain low. Later the same group reported a hybrid photocathode that consists of a ruthenium complex catalyst and a p-type semiconductor composed N, Zn co-doped Fe_2O_3, with a multi-heterojunction structure TiO2/N,Zn-Fe_2O_3/Cr_2O_3.[78] The polymeric Ru complex, loaded on the photocathode surface led to a stable small photocurrent of 150 µA cm^{-2} that was exclusive directed to the production of HCOOH, CO, and a small amount of H_2 under 1 sun irradiation at +0.1 V vs RHE. Despite the low current densities reached by this photoelectrode and the poor stability, these studies have been important in paving the way for aqueous PEC CO_2 reduction with molecular based photoelectrodes. One important conclusion is that the mode and method for catalyst immobilisation can play a significant role in determining the end result, regardless of the catalyst's intrinsic performance.

An efficient PEC CO_2 conversion to methanol in a heterogeneous photoelectrocatalyst prepared by covalently binding a Ru(II) metal-organic complex on TiO_2 nanotube arrays, was reported by Liu, J. et al., the shown Ru-Py/TNTAs photocathode tested in PEC CO_2 reduction have shown that 84.8 µmol methanol was produced with 63.9% faradaic efficiency, 62.6 turnover number (TON) and 45% selectivity at −0.9 V under 8 h solar light irradiation.[79] The covalent linking system show better efficiency compared with that without covalent linking, demonstrating carboxyl covalent linking benefits for electron transfer between the metal-organic complex and semiconductor electrode. However, CH_3OH production from CO_2 need to be confirmed with properly labelled studies using $^{13}CO_2$ experiments.

The systems cited above use precious metal molecular catalysts complexes. Systems that uses earth-abundant materials in literature are scarce. In 2020, Pati, et al., have reported the first demonstration where a CIGS electrode combined with an earth abundant cobalt based molecular catalyst was successfully used for PEC CO_2 reduction(Figure I.14).[29] The Co-qPyH molecular catalyst bearing phosphonic acid anchoring groups was grafted on a titanium dioxide upper protective layer of the CIGS cell leading to simultaneously good selectivity (98% CO), activity, and a very low negative overpotential (-0.06 V vs. RHE) under visible-light illumination (100 mW cm^{-2}) in neutral aqueous solution. It corresponds to improved performances when compared with previously

reported molecular hybrid systems, even those including noble metals. One may expect improvement of this system with higher catalyst loading or with nanostructuration of the upper oxide layer.

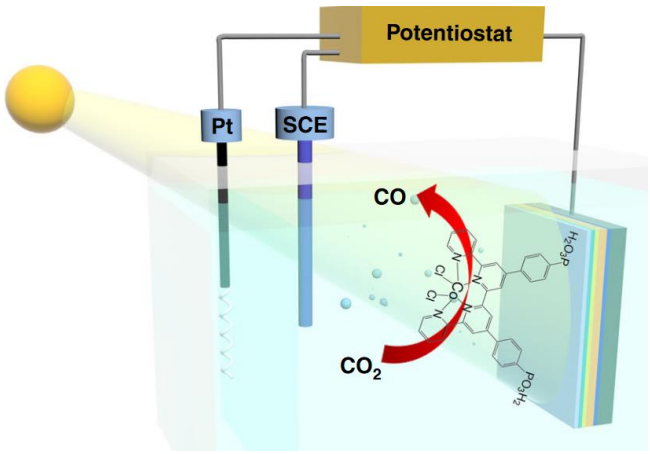

Figure I.14 Illustrative scheme of the PEC CO_2 reduction system reported by Robert, et al.[29] In which a cobalt quaterpyridine complex (Co-qPyH) catalyst bearing phosphonic acid functions is grafted on the TiO_2 window protective layer of a CIGS cell photoelectrode.

Finally, Reisner et al., recently reported a p-type silicon (Si) photoelectrode coated by a mesoporous TiO_2 in which a molecular cobalt phthalocyanine catalyst bearing four phosphonic acid anchoring groups is grafted (Figure I.15), displaying a photocurrent of $-150\ \mu Acm^{-2}$, achieving a high turnover number (TON_{CO} of 939 ± 132) after 12h with 66% selectivity for CO under fully aqueous conditions.[26]

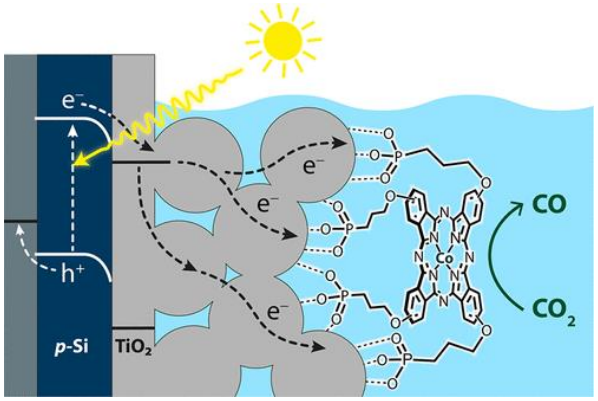

Figure I.15 Schematic representation of a p-type silicon (Si) photoelectrode coated by a mesoporous TiO_2 layer, onto which a molecular cobalt phthalocyanine catalyst bearing four phosphonic acid anchoring groups is grafted. Image from reference.[26]

These two cited work presents a rare example of precious-metal-free based hybrid photoelectrodes for PEC CO_2 reduction. They pave the way for the future development of PEC devices.

Considering systems operating in organic media where enhanced photocathode and/or catalyst stability may be expected, only a few reports exist, most of them including the use of precious metal complexes. For instance, the reported Re-bipyridine catalyst immobilised on a TiO_2 coated Cu_2O photocathode protected by multiple atomic-layer-deposited coatings (Figure I.16), operating in anhydrous acetonitrile (MeCN), has reached Faradaic yields for CO between 80 and 95%. During a 1.5 h test at a highly negative bias potential (-2.05 V vs. Fc+/Fc), the photoelectrode achieved a low turnover for CO of 70.[22]

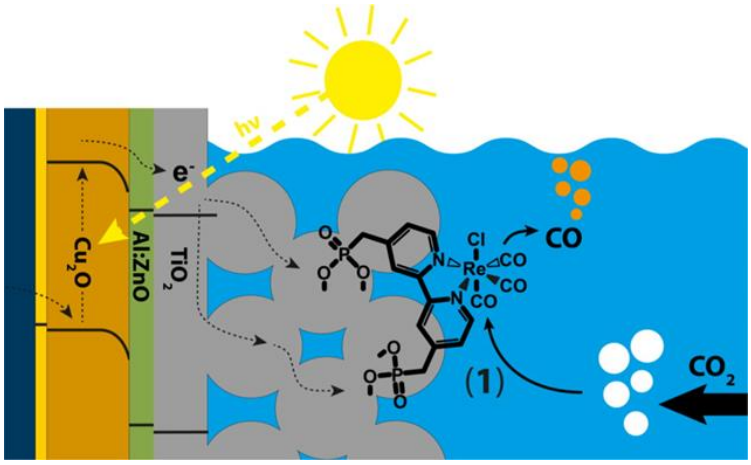

Figure I.16 Schematic representation Cu_2O photocathode coated by a nanostructured TiO_2 scaffold, in which a Re-bipyridine catalyst bearing phosphonic acid anchoring groups is grafted. Image from reference.[22]

Only a few systems employing earth-abundant metal complexes have been used in organic solvents with light-absorbing semiconductor, with the catalyst either dissolved in solution or immobilised at the semiconductor surface. In 2013, Pickett et al. reported CO_2 reduction to CO by Fe porphyrin catalysts in solution, photodriven by a hydrogen terminated *p*-type silicon photoelectrode, operating in dry organic solvents with CF_3CH_2OH as the added proton source. Carbon monoxide was produced with a current efficiency >90% and with a high selectivity over H_2 formation. Photoelectrochemical current density around 3 mA cm^{-2} at -1.1 V vs. SCE were reached in cyclic voltammetry experiments. During a 6 h test at 1.11 V vs. SCE the photoelectrode achieved a turnover for CO of 175.[80] Later, Torralba-Penalver, E., et al., reported the pairing of Si nanowire electrodes (SiNWs) with Mn-bpy catalyst. In this work, three Mn-based bipyridyl tri

carbonyl molecular complexes acting as homogeneous catalysts in MeCN solution led to better properties of nanostructured SiNWs as compared to flat Si electrodes, due to their higher electrochemically active surface area and higher capacity to decouple minority carrier generation and collection.[81] In a similar way, in 2016 D. Wang et al., found that CO_2 reduction in MeCN solutions adding 1-2% of H_2O by a cobalt tris(2-pyridylmethyl)amine catalysts in solution was better at nanostructured SiNW electrodes than planar Si surfaces. Photovoltages of 580 mV and 320 mV were obtained on Si nanowires and a planar Si photoelectrode, respectively.[82] Recently in 2019 Deng and co-workers proposed an easy procedure for coating a metal–organic framework (MOF) on the surface of a TiO_2/Cu_2O photocathode (Figure I.17), which can both prevent photocorrosion and offer active sites for CO_2 reduction, achieving high faradaic efficiency >95% for CO production in 1h electrolysis experiment under visible light irradiation at applied potentials between -1.77 and -1.97 V vs. Fc^+/Fc.[83]

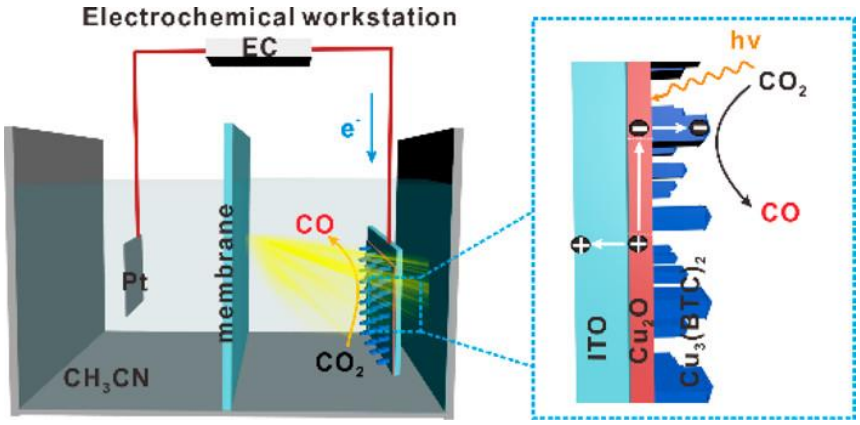

Figure I.17 Schematic illustration for PEC CO_2 reduction in acetonitrile using the hybrid $Cu_2O/Cu_3(BTC)_2$ MOF photocathode. Image from reference.[83]

I.4.4 Summary and Outlook

In summary, the number of examples of molecular catalyst-based photocathodes, especially those based on earth-abundant elements either under aqueous or organic conditions, remains low. One of the biggest hurdles is the search for PV materials that are stable in water during photoelectrolyis. Indeed, none of the photoelectrodes utilised to date are inherently stable and have therefore either been operated under organic conditions where corrosion is somehow slowed down and/or have been coated

with protection layers (commonly TiO_2). However, the majority of reports do not show the stability of their photocathodes beyond 1 h.

Another significant drawback presented by the reported systems is the stability of the linkage between the catalyst and the surface of the photoelectrode. Covalent immobilisation by the mean of phosphonic acid groups or carboxylic groups are so far the most common ways reported to link efficiently the catalyst and the photoelectrode. However, there are still room for improvement since the linkage remains vulnerable to pH changes or negative potentials applied during long-terms electrolysis experiments.

It is thus important that the focus shifts towards finding more stable ways to immobilise molecular catalysts. The lack of progress made for CO_2-reducing photocathodes depicts the difficulties in doing so as a result of issues like stability, efficiency, product selectivity, especially in aqueous conditions, and the fact that most of the efficient molecular catalysts used to date still rely on precious metals. It is important to shift from using noble metals to abundant transition metal.

I.5 Basic concept of solar cells

Solar cell is a key device that converts directly the light energy into usable electrical energy by so-called photovoltaic conversion. The direct conversion of solar radiation into electrical power is known as "the photovoltaic effect". This phenomenon was discovered by A. E. Becquerel in 1839. The most important function of a solar cell is generation of photocurrent and photovoltage. In order to do this, the solar cell must first absorb light from the sun and generate charge carriers. This is possible by using p-n junction in many solar cells.

In fact, the commercial available PV technologies today such as silicon and thin film solar cells, are based on semiconductor materials. The most noticeable PV technologies are the crystalline or multi-crystalline silicon technologies (c-Si) and the thin film based technologies including the cadmium-telluride (CdTe) modules, amorphous silicon modules (a-Si) and copper indium gallium diselenide module (CIGS). The focus of this PhD thesis is on CIGS-based solar cells.

For our main goal of fabricating a highly efficient and selective photoelectrode for PEC CO_2 reduction, we have selected copper indium gallium selenide (CIGS) solar cells as heterojunction material to be used as photocathode. CIGS is a thin film based solar

cell that have achieved certified record cell power conversion efficiencies exceeding 22%.[84]

A brief overview of the semiconductor properties relevant to solar cell operation, which are necessary to understand the operation of *p–n* junction solar cell and a description of the basic principles of *p–n* junction solar cells are given in this chapter. Moreover, we present a short overview of CIGS based heterojunction thin film solar cells. The description of the basic material properties such as crystal properties, Description of the cell technology, starting from the heterojunction formation and the working principle of the cell. This chapter will only briefly cover those scientific issues that are relevant for photovoltaic and catalytic applications. It represents only a small summary of all the vast literature in this field.

I.5.1 Semiconductor (SC)

Inorganic solar cells are based on semiconductor technology and the p-n junction. Typical conducting materials are metals with conductivities greater than 10^3 S/cm, Insulators have a conductivity, smaller than 10^{-8} S/cm; Between these two extremes, semiconductors have a broad range of conductivity. This conductivity is particularly sensitive to temperature, impurities in the material, and light. In semiconducting materials, the conductivity and therefore also the resistivity, (ρ) (in Ω cm) can be tuned to the desired values by changing the amount of impurities, called donor and acceptor dopants.

A semiconductor (SC) is a material where the difference between the valence and the conduction band called the band gap (*Eg*) is a few eV. The bandgap energy depends among other things on the composition of the material and the temperature. For semiconductor materials used in photovoltaic devices, *Eg* is in the range of ~1.1 eV for silicon up to values of ~2.5 eV for III-V compounds.

The semiconductor's properties can be altered by deliberately introducing impurities into the semiconductor material. This is known as doping the material. One method of doping is to introduce impurity atoms known as acceptors near the valence band, which introduces unoccupied energy states. This results in an excess of holes in the material. This type of doping and material is known as *p*-type. Similarly, the other type of doping involves the introduction of impurity atoms, known as donors, just below the conduction band. These donors will contribute excess electrons to the material's

conduction band, causing the doping to become *n*-type. In an undoped semiconductor the fermi level (E_F) is situated in the middle of the band gap. For *n*-type semiconductors E_F is situated closer to the energy of the *CB* and for *p*-type semiconductors closer to the energy of the *VB*.

I.5.2 Basic principles of p–n junction

The *p*-*n* junction is formed by the combination of two different types of semiconductors. There are two types of junctions: heterojunction, which occurs when the two semiconductors are made of different materials, and homojunction, which occurs when the *p*-*n* junction is made of a single material with different doping *p* and *n* (e.g. homojunction Si). An *n*-type material adjacent to a *p*-type material is called a *p*-*n* junction. The basic energy band diagram of the *p*-*n* junction is shown in Figure I.18. In this device an electric field is created across the junction between the two doped regions.

When separate, the n-type and p-type regions are described by thermal equilibrium statistics. After contact, due to the large imbalance in carrier type between the two regions, electrons flow to the left and holes to the right. However, this leaves uncompensated ionized donor and acceptor ions, i.e., a fixed space charge, on either side of the junction. The fixed charge then creates an electric field across the junction (from right to left) that opposes further carrier motion. At equilibrium the net diffusion current across the junction is exactly balanced by the net drift current. Also, the Fermi level on both sides is now equal and the built-in field created by the fixed space charge leads to an energy barrier (*qVbi*). The extension of the field in the region surrounding the junction is called the depletion region, or the space charge region (SCR), and the resulting potential after integrating the field in this region is called the built in potential (*Vbi*). *Vbi* is dependent on the band gap and the doping in the respective p-type and n-type side of the junction.

$$qV_{bi} = E_g - kT * \ln(\frac{N_{CB}N_{VB}}{N_A N_D}) \qquad \textbf{(Eq. I.2)}$$

Where *q* is the electron charge, N_{CB} the effective density of states in the conduction band, N_{VB} the effective density of states in the valence band, N_A the density of acceptors and N_D is the density of donors.

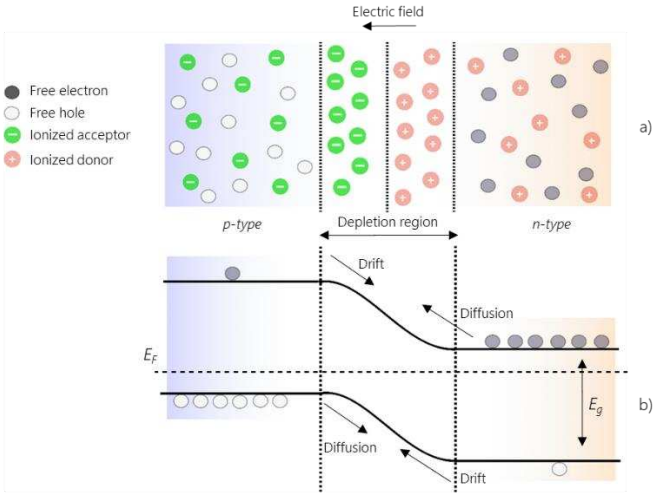

Figure I.18 Scheme of the *p-n* junction: a) formation of the depletion region, the neutral regions, and the electric field originated when the junction is established. b) energy band bending diagram in thermal equilibrium. Adapted from.[85–87]

I.5.3 *p-n* junction under illumination

When a solar cell is illuminated, typically with solar irradiation, photons enter into the structure and exciting the electrons and promoting them from the valence band to the conduction band, creating electron-hole pairs when the energy of the photon is higher than Eg of the *p*-type semiconductor. The number of electron–hole pair is proportional to the light intensity. Without *p-n* junction, these electron-holes recombine. The separation is done by the introduced built in potential in the *p-n* junction. The electrons and holes that drift so that they come in contact with the field in the SCR are separated as the field will move the electrons to the *n*-type side and holes to the *p*-type side of the p-n junction.

This creates a charge separation, which leads to a voltage difference between the two sides, which can drive current through an external load and the charge carriers are circulated through the system (Figure I.18 & I.19).

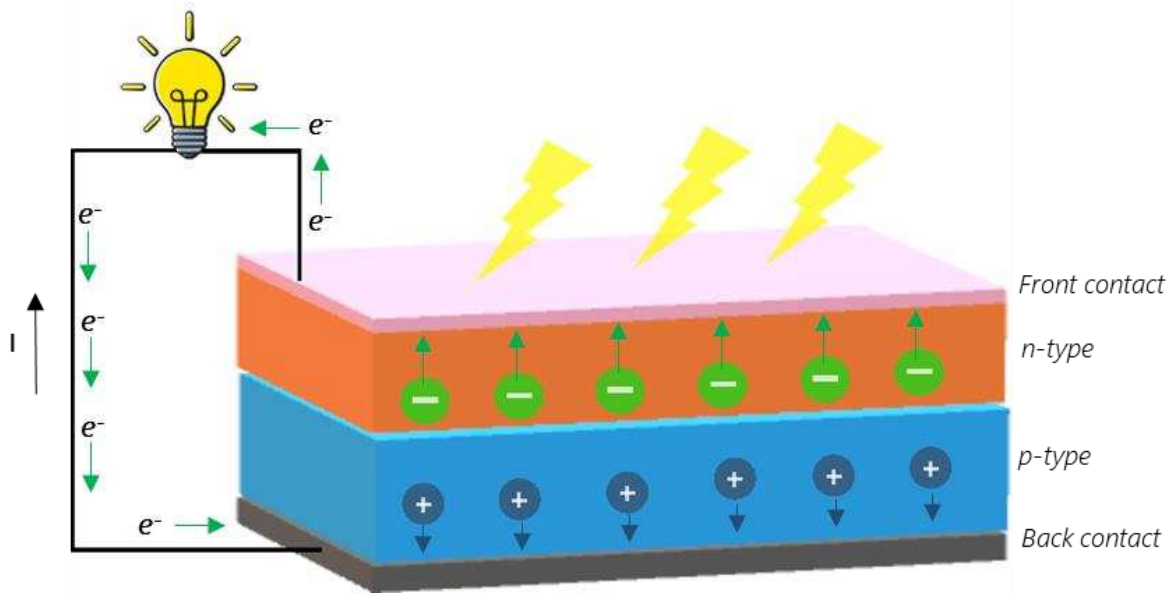

Figure I.19 Schematic operating principle of a PV solar cell under illumination. Adapted from.[85]

I.5.4 Current-voltage characteristics

If one considers a diode at a dark steady state condition at room temperature, just a few, by thermal energy exited, electrons in a diode, will be pulled from the *p*-type material to the *n*-type by the electric field. The barrier of the electric field will at the same time prevent electrons to move in the opposite direction. Thus, only a very small current will flow through the device. However, if an external potential bias is applied the barrier will be lowered. At some point the barrier will be so low that the many electrons in the conduction band at the *n*-type side can start to flow across the junction to the *p*-type side. In the same way, but in the opposite direction, holes from the *p*-type side will cross the junction to the *n*-type side. Both these flows will contribute a large current in the diode at a certain forward bias. This behavior of an ideal diode is described by the diode equation:

$$J = J_0(e^{\frac{qV}{K_B T}} - 1) \qquad \textbf{(eq. I.3)}$$

In a solar cell diode that is subjected to illumination, additional current will flow across the junction as the incoming photons create electron-hole pairs that are separated by the electric field. This current is usually called the photocurrent (J_{ph}). opposing the dark

current (J_{ph}<0). Furthermore, most solar cells are not ideal diodes, which make it necessary to add an ideality factor (A), usually ranging between 1-2, to the denominator of the exponent in Equation I-4. The corresponding J-V characteristic is described by the Shockley diode equation:

$$J = J_0(e^{\frac{qV}{AK_BT}} - 1) - J_{ph} \qquad \textbf{(eq. I.4)}$$

Where k_B is the Boltzmann constant, T is the absolute temperature, q is the electron charge, and V is the voltage at the terminals of the cell, J_o is well known to electronic device engineers as the diode reverse saturation current.

Figure I.20 illustrates a graphical representation of Equation I.4 for a typical solar cell under dark and illuminated conditions. In the typical current-voltage (J-V) curve of a solar cell there are some electrical parameters that are of importance when characterizing a solar cell. The short circuit current (J_{SC}) is one of them. It is defined as the current that flows through a short circuit connected solar cell when no bias is applied. J_{SC} measures the number of photo-excited electrons that reach the contacts. It decreases as Eg increases because fewer photons have enough energy to form electron-hole pairs. J_{SC} should ideally be equal to the light-induced photocurrent J_{ph}. Another important parameter is the open circuit voltage (V_{OC}), which is where the forward bias diffusion current equals J_{ph}.

Setting J to zero in Equation I.4 gives the ideal value:

$$V_{oc} = \frac{AK_BT}{q}\ln\left(\frac{J_{ph}}{J_0} + 1\right) \qquad \textbf{(eq. I.5)}$$

Because J_0 is affected by the properties of the semiconductor material, Equation I.5 shows that so is V_{OC}. As Equation I.2 shows, V_{OC} is dependent on V_{bi} and thus the band gap through J_0. Therefore, as J_{SC} decreases V_{OC} increases with increasing *Eg*, and there is a trade-off between those two parameters.

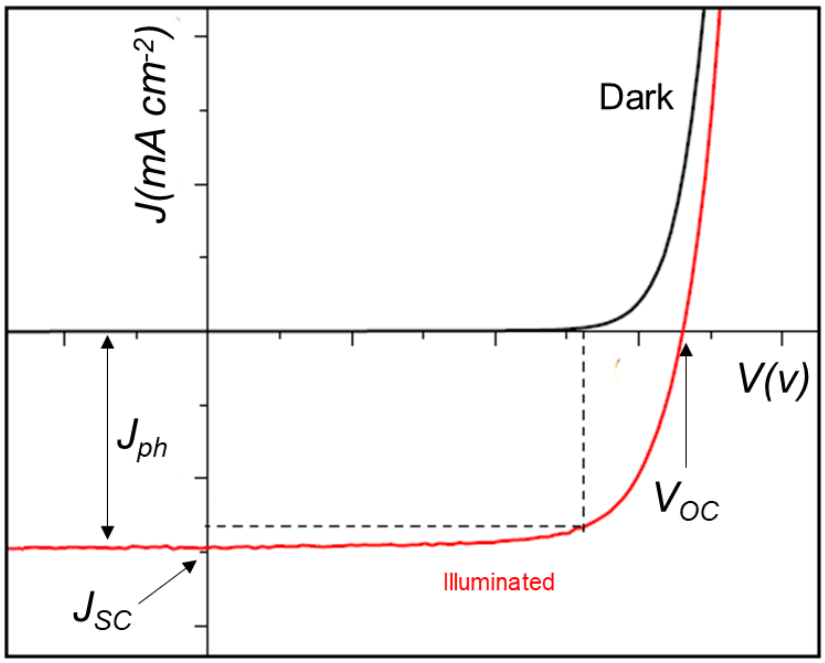

Figure I.20 Current–voltage (J-V) characteristic curves of a PV cell under illumination and darkness.

The J-*V* characteristic is used to calculate the conversion efficiency (η) of the solar cell, which is the ratio of the maximum electrical power produced P_M (in absolute value) to the incident power received by the cell P_{in}.

$$\eta = \frac{P_M}{P_{in}} \qquad \textbf{(eq. I.6)}$$

The maximum power point (P_M) is the point where the output power ($P_{out} = J \times V$) of the solar cell is at its maximum. The current and voltage at this point are defined as J_M and V_M, respectively. The measure of how close the product $J_{SC} \times V_{OC}$ is to P_M is another important parameter and is called the fill factor (FF). This parameter is defined as:

$$FF = \frac{J_m V_m}{J_{sc} V_{oc}} = \frac{P_{max}}{J_{sc} V_{oc}} \qquad \textbf{(eq. I.7)}$$

Graphically, the *FF* represents the ratio of the actual maximum obtainable power, represented by the grey box (Figure I.21), to the product of J_{SC} and the V_{OC}, represented

by the blue box (Figure. I.21). It is a measure of the resistances in the solar cell, represented by squareness of J-V curve.

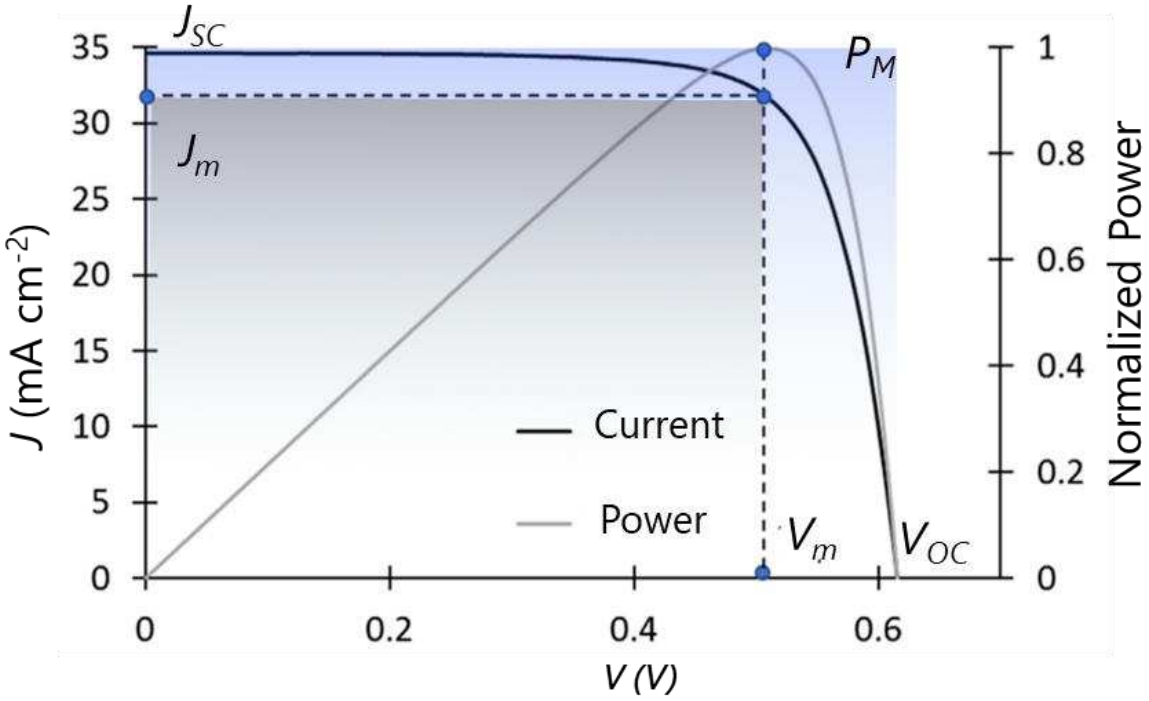

Figure I.21 J-V Curve of a PV cell, showing the main parameters in solar cells: J_{SC}, V_{OC}, P_M, J_m and V_m. Adapted from Riverola, A. et. al. [85]

The FF is affected by the total series resistance (R_s) in the solar cell. Furthermore, it is also influenced by electrical paths that bypass the *p-n* junction, which is gathered in the shunt resistance parameter (R_{sh}). Including these parameters into Equation I.4 results in:

$$J = J_0(e^{\frac{qV-JRs}{AK_BT}} - 1) + \frac{V-R_sJ}{R_{Sh}} - J_{ph} \quad \textbf{(eq. I.8)}$$

The series (R_s) and shunt resistances (R_{sh}) are respectively related to the resistances between the layers and the short circuits in the solar cell. Thus, one or more diodes, more complex, taking into account the phenomena of recombination occurring in the

cell can be added to the equivalent circuit of an ideal solar cell as observed in Figure I.22.

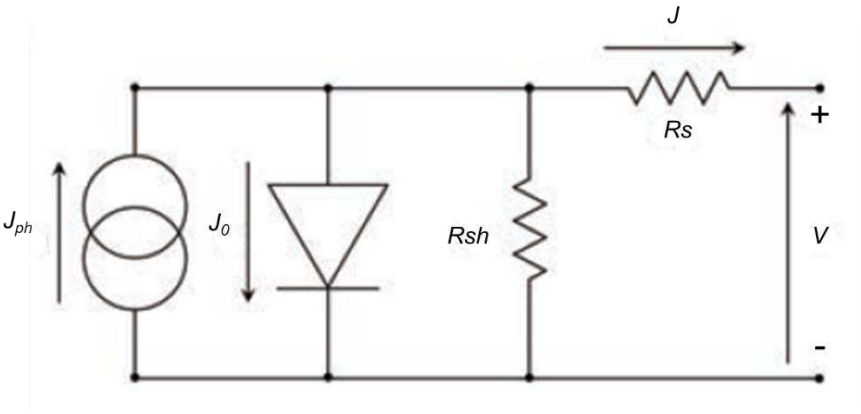

Figure I.22 The equivalent circuit of an ideal solar cell.

As the solar cell purpose is to convert the incoming power of light into electric power, which is defined by the conversion efficiency (η), this later can be written as:

$$\eta = \frac{J_m V_m}{P_{in}} = \frac{J_{sc} V_{oc} FF}{P_{in}} \qquad \textbf{(eq. I.9)}$$

The photovoltaic parameters described are evaluated under standard test conditions: the air mass (AM) 1.5 spectrum with an incident power density of 1000W/m^2 and a temperature of 25 °C.

I.6 CIGS solar cell

The CIGS photovoltaic technology is named from the absorber the called absorber layer, the alloy Cu(In,Ga)Se_2. The first $CuInSe_2$/CdS thin film solar cell was fabricated by Kazmerski et al., in 1976, having a conversion efficiency such as 4.5%.[88] Since then, several number of breakthrough technologies have been developed, alloying with gallium (Ga) such as $CuIn_{1-x}Ga_xSe_2$ (hereafter called CIGS), cation doping and replacing the thick cadmium sulfide, CdS, window layer with a thin CdS layer followed by intrinsic and doped zinc oxide (ZnO) layers.[89] have improved the efficiency. The CIGS alloy is a high-performance absorber material for thin film solar cells since it has direct bandgap

with high absorption coefficient ($1x10^5 cm^{-1}$).[90] Thus, only few micrometers are required to absorb the maximum photons. Also, the thickness of CIGS absorbers are less than c-Si wafer, around a 2 µm thick CIGS absorber film is required for cell fabrication.[91] CIGS is established as an efficient thin-film solar cell technology. These solar cells have attracted great interest of researchers worldwide for their potential to be deposited in flexible substrates and the use in tandem systems. CIGS based thin film solar cell have managed to achieve efficiency above 22% comparable to Si based solar cells.[84]

I.6.1 Material properties

Copper indium selenide (CuInSe2 or CIS) is a ternary *p-type* material belonging to the I–III–VI_2 family. It crystallizes in the tetragonal chalcopyrite structure $CuXY_2$ (X = In, Ga, Al, and Y = Se, S), as shown in Figure I.23. The lattice parameter is related to the In/Ga ratio of c = 56–58 Å (x = 0–1) and a = 1.1–1.15 Å (x = 0–1), which is known as tetragonal distortion that originates from Cu–Se, Ga–Se or In–Se bonds.[92]

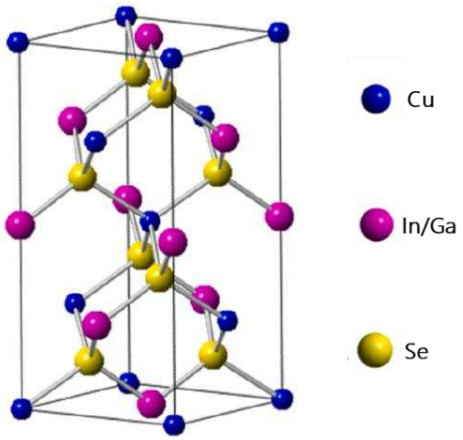

Figure I.23 Crystal structure of tetragonal chalcopyrite CIGS unit cell. Adapted from.[92,93]

$CuInSe_2$ has a bandgap of 1.02 eV and $CuGaSe_2$ 1.68 eV. By varying the stoichiometry of the CuIn1–*x*Ga*x*Se2 compound, i.e. adjusting *x* = Ga/ (In + Ga), the bandgap can be engineered. The bandgap dependence on *x* is of the form *E*g (*x*) = 1.02 + 0.67*x* + 0.11*x* (*x* − 1), but difference between sample can occur and this formula has to be adjusted. The most efficient devices have a Ga content around 0.2–0.3 and thus bandgap energy around 1.1–1.2 eV. The composition is not homogeneous in the absorber and bandgap

engineering is introduced via the variation of the Ga content. Composition grading have a strong impact on the device performance.[84]

Thus as observed on Figure I.24, the system $CuXY_2$ (X = In, Ga, Al, and Y = Se, S) includes a wide range of band-gap energies *Eg* from 1.04 eV in $CuInSe_2$ up to 2.4 eV in $CuGaS_2$, and even 3.7 eV in $CuAlS_2$, thus, covering most of the visible spectrum. All these compounds have a direct band gap, making them suitable for thin film photovoltaic absorber materials.[94] The CIGS p-type layers present a doping level between 10^{16} and 10^{17} cm^{-3}.[95]

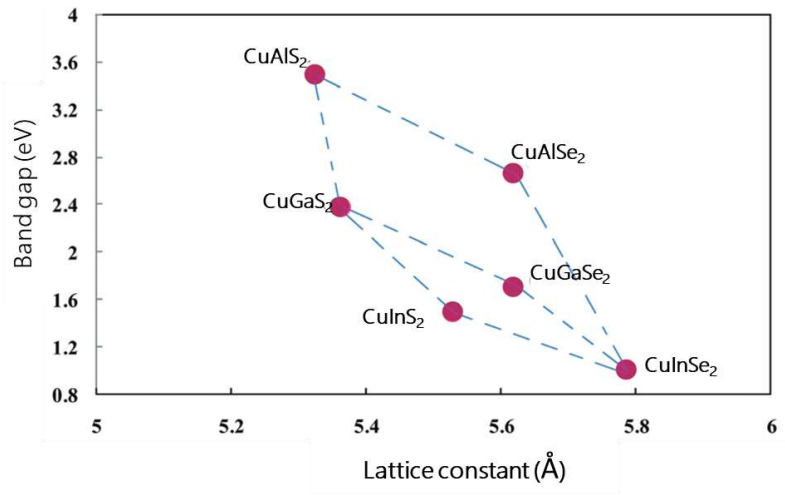

Figure I.24 Correlation between the bandgap and lattice constant a as a function of composition in $Cu(In,Ga)(S,Se)_2$ solid solutions.[93,96]

I.6.2 CIGS device structure

The current state-of-the-art $Cu(In,Ga)Se_2$ (CIGS) solar cells are based on a *p*-*n* heterojunction in which the *p*-type CIGS absorber of 1-2 µm is grown on a metallic contact, i.e. molybdenum. High quality CIGS layers is produced by high-temperature (>500 °C) multi-stage co-evaporation processes. The junction is typically completed by chemical bath deposition of 50 nm thick CdS layer acting as the *n*-side of the junction and sputtering of resistive and transparent conductive oxides, i.e. (50-100 nm) ZnO and 300 nm thick ZnO:Al layers. As ZnO has a band-gap energy of 3.2-3.3 eV it is transparent for the main part of the solar spectrum and therefore is denoted as the window layer of

the solar cell.[96] A schematic structure of a CIGS heterojunction solar cell, is shown in Figure I.25.

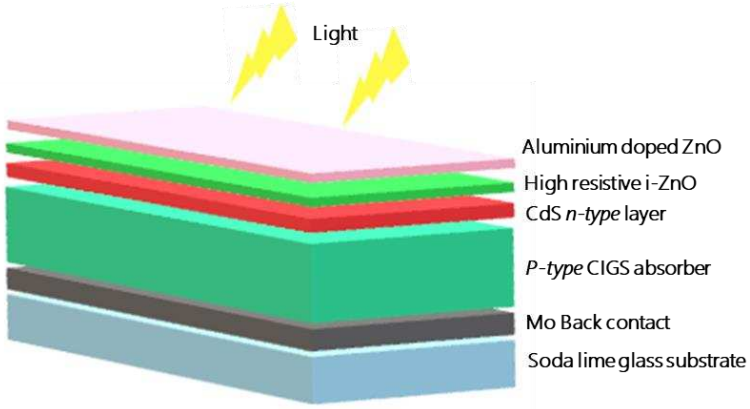

Figure I.25 Schematic layer sequence of a standard ZnO/CdS/Cu(In,Ga)Se2 thin-film solar cell.

Figure I.26 shows the band diagrams of typical CIGS heterojunction solar cells.

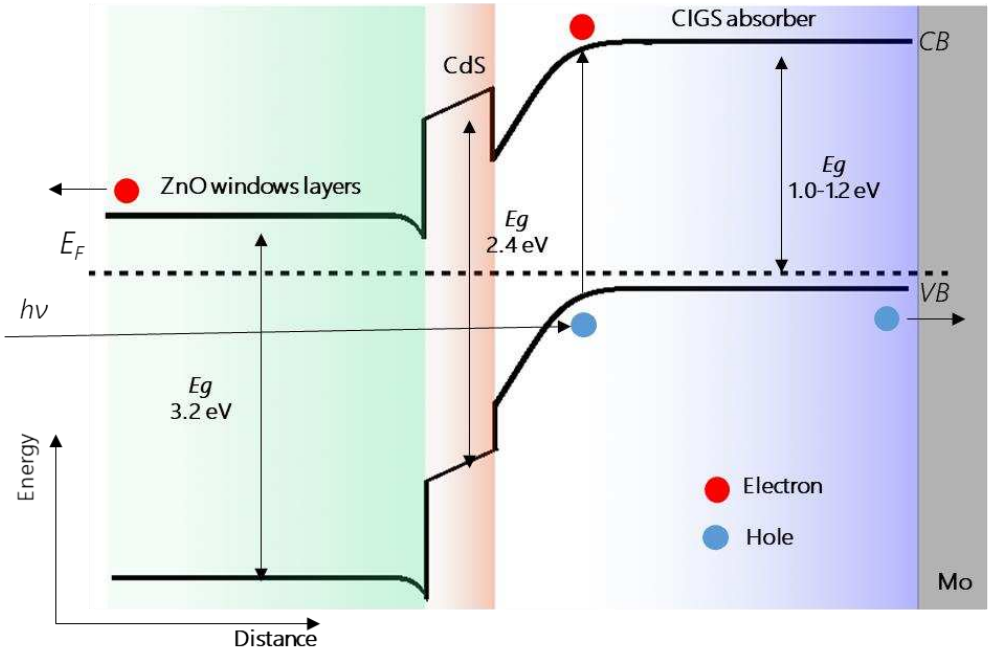

Figure I.26 Band diagram of a standard CIGS solar cell. *CB*: bottom of the conduction band; *VB*: top of the valence band; *Eg*: bandgap. The electrical junction is formed by the contact between the p-type CIGS and n-type CdS/ZnO layers. ZnO transparent conductive oxide (TCO) layers (Eg ≃ 3.2 eV) provide higher conductivity and lower resistivity and act as a window for transmitting the light into the cell and conduct photo-generated current from cell to the external circuit avoiding resistance loss.[97] The *n-type* CdS buffer layer with a wide-gap (Eg ≃ 2.4

eV) transmits light up to 2.4 eV to the *p-type* emitter CIGS absorber where electron–hole pairs are mainly generated. Due to a built-in electric field across the *p–n* junction interface, between CIGS/CdS, electrons within the diffusion length region are swept away from the p-type absorber to the *n-type* buffer layer and collected by the n-type electrode. Similarly, holes are swept away from the n-type layer to the *p-type* layer and collected by the p-type electrode.[93] Adapted from reference.[95] To date, the record efficiencies stand at 23.35 % on a 1 cm^2 cell and 19.64% for a CIGS module.[98]

I.6.3 The Zinc oxide windows layer in the CIGS cell: The key component of our study

In the previous section, we have described the typical CIGS heterojunction solar cell architecture, and its properties. We will focus now on the top layer of the CIGS cell, the ZnO layer, aiming to provide an overview of the strategy proposed in this manuscript, in which a CIGS PV material is used as substrate for deposition of hybrid catalytic layers formed by zinc oxide and a molecular catalyst, by electrochemistry.

An interesting feature in the use of ZnO as window layer is the fact that it can act as front contact collecting electrons from the buffer layer while also letting light pass through to the absorber beneath. The ZnO:Al *n-type* transparent conducting oxide (TCO) offers a highly transparent layer with suitable bandgap (≥ 3.2 eV) that fit perfectly on the diagram band configuration of the CIGS cell as shown in Figure I.26.

Typically, in a CIGS cell the bilayer of ZnO consists of a thin (≃100 nm) intrinsic ZnO layer and a thick (≃300 nm) *n-type* aluminium doped ZnO layer. The intrinsic ZnO is required to provide an isolation between the CdS and Al-doped ZnO (ZnO:Al).[93]

The ZnO presents excellent optical properties, wide availability, and low toxicity. Among the specific advantages of ZnO, one can also highlight the easy growth. ZnO can be synthesized electrochemically from aqueous solutions of zinc salts. In 1996, Izaki et al.[99] and Peulon et al.,[100,101] independently discovered methods to electrodeposit crystalline ZnO thin films from aqueous solution of zinc salts, employing cathodic reduction. Electrochemical deposition is simple and low-cost for the preparation of high quality ZnO. Conformal films can be easily produced by electrodeposition on substrates with a complicated shape and the technique allows the design of complex nanostructures by combining and adjusting the growth conditions.[102–105]

Moreover, the electrochemical growth of the ZnO allows the loading of organic molecules during the film growth. In the end of the 90's Yoshida et al.,[106] reported the electrochemical self-assembly of dye-modified ZnO thin films in a one-step process, by adding water-soluble dyes to the electrochemical bath containing $Zn(NO_3)_2$. They have obtained coloured ZnO thin films with very different surface morphologies and crystallographic structures from the pure ZnO film. The loading of organic molecules into ZnO films was also attempted from an organic molecule and $ZnCl_2$ bath employing cathodic reduction of dissolved molecular oxygen precursor.[107,108] In some cases, surface adsorption of dye molecules hinders crystal growth, leading to formation of porous thin films composed of nano-sized crystallites of ZnO. The use of an inorganic porous nanostructured matrix of ZnO allows the immobilisation of a large amount of the organic molecule and allows good accessibility of the complexes to the electrolytic solution.

Since CIGS cells possess ZnO windows top layers, and this windows layers can be grown and modified by electrochemistry, our strategy was to use these properties to incorporate a molecular catalyst into the ZnO inorganic matrix growing a hybrid ZnO|catalyst film with a catalytic activity. In our case we have focused our work in the CO_2RR.

By introducing the CIGS/CdS/i-ZnO/ZnO stack as the substrate into the reaction solution, co-catalyst nanostructures may heterogeneously nucleate and grow on the surface of ZnO:Al by electrochemistry. Resulting in a photoelectrode coated by a hybrid catalytic and protective ZnO layer.

Before using CIGS cells as a substrate, different ZnO catalytic structures were prepared using ZnO:Al glass-coated electrodes as a substrate, mimicking the top ZnO:Al layer of CIGS cells. A series of experiments were carried out in EC CO_2 reduction, before we started the deposition directly on the CIGS cells. Finally, we have used CIGS/CdS/i-ZnO/ZnO electrodes as substrate and deposited the hybrid catalytic layers on them, followed by a series of experiments to measure the catalytic performance of our electrodes in PEC CO_2 reduction.

Since our strategy consist of electrodeposition and modifications of ZnO layers, at this point of the manuscript, it becomes important to describe and give a general review of the zinc oxide material.

I.6.3.1 Properties of the Zinc Oxide (ZnO)

Zinc oxide is a multifunctional material, which presents unique physical and chemical properties, such as high chemical stability, high electrochemical coupling coefficient, broad range of radiation absorption and high photostability.[109] It is a transparent metal oxide that allows visible light to pass through, making it a perfect candidate for photovoltaics applications (e.g. CIGS solar cells). ZnO is a very promising material for semiconductor device and very attractive for potential use in electronics, optoelectronics and laser technology. Furthermore, ZnO has been reported as a selective photocatalyst for CO_2 reduction to CO,[110–113] and as photoanode for water splitting.[114]

I.6.3.1.1 Crystal Structure

Under ambient conditions, ZnO crystallizes in the thermodynamically stable hexagonal wurtzite structure (Figure I.27). It can be also found in cubic zinc blende structure. This structure can be stabilised only by growth on substrates with cubic structure. At high pressures, upwards of 10 GPa a cubic structure is formed (NaCl lattice), cubic ZnO is an indirect gap semiconductor with a band gap width of Eg = 2.7 eV. The lattice constants for the hexagonal wurtzite structure are a = 3.25Å and c=5.20Å, with their ratio c/a í1.60 being close the ideal value for a hexagonal cell (c/a=1.633).[115] The molar weight of ZnO is 81.38 g mol^{-1} and its volumic weight is 5.6 g cm^{-3}.

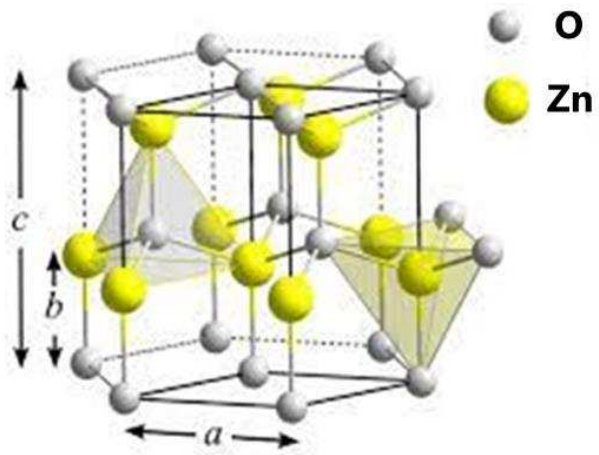

Figure I.27 Representation of the hexagonal wurtzite ZnO crystal structure.

I.6.3.1.2 Optical properties

Zinc oxide is a semiconductor with a wide band gap of 3.3eV when prepared in classical conditions. In the presence of high doping such as Al^{3+} or Ga^{3+} the band gap can be increased. Its transparency is due to its optical band gaps, which is ≥3.3 eV, leading to a transparency for wavelength >360 nm. The doped zinc oxide thin film (ZnO:Al) has a high transmittance up to 1200 nm and a low resistivity, The refractive index of the ZnO is ~2.0 and vary with the wavelength.[116] Moreover, ZnO is also a suitable material for fluorescent displays and field emission displays, due to its strong luminescence in the green–white region of the spectrum.

I.6.3.1.3 Electrical properties

Undoped ZnO with a wurtzite structure is naturally an n-type semiconductor due to the presence of intrinsic defects. The electrical conductivity of zinc oxide can be engineered by doping the material. Extrinsic doping can be achieved by the substitution of group III elements such as Al,[117] Ga[118] or In[119] with Zn sites. ZnO:Al doped present mobility around 30 $cm^2V^{-1}s^{-1}$ and conductivity of ca. 5-6x10^2 Ω cm^{-1}. Doped ZnO can then be used as transparent electric contact in photovoltaics applications.

I.6.3.1.4 Catalytic properties

ZnO has not only been widely investigated in devices; it has also been extensively explored in several catalysis processes including photo-catalysis or water splitting.[109,120,121] Among all the catalytic properties reported, we will be focused in the catalytic activity of ZnO in CO_2RR.

The ZnO is a promising metal oxide catalyst for selective CO_2 reduction to CO production. ZnO- based catalysts have shown high Faradaic efficiencies 80%-90%,[111–113,122–126] making it the prospective candidate for non-noble metal-based catalysts. ZnO catalysts with different morphologies were reported in literature. Nanoporous layers,[111] 2D structures,[110] ZnO, nanoparticles,[127] 3D structures,[124,126–128] and also ZnO hybrid materials[128,129] have been studied and successfully demonstrated as highly active and selective catalysts for CO_2 reduction.

Combining the described catalytic properties of zinc oxide towards CO_2R with those of a molecular catalyst (described previously) in a single hybrid material results in a material that enhances catalytic activity due to a synergistic effect of the two components.

I.6.4 Electrodeposition of ZnO: state-of-the-art

There are several processes for depositing ZnO by using chemical process, such as chemical bath deposition (CBD)/dip coating,[130,130] chemical vapor deposition (CVD)/spray pyrolysis,[131] atomic layer deposition (ALD),[132] sol-gel spin coating,[133] sputtering,[134] hydrothermal synthesis[135] and electrochemical deposition.[100,136] In this manuscript we will only focus on the electrochemical deposition technique.

Electrodeposition is an interesting method. From an economical point of view, it is a low-cost method because the temperature of growth is limited below 100°C and it only requires low electricity consumption. From a material point of view, it allows growth of high quality layers and the geometry of the layer can be controlled by the electrodeposition conditions.

Electrodeposition of zinc oxide is the result of the innovating works of Peulon et al.,[100] and Izaki et al.,[136] in 1996 using cathodic reduction of dissolved oxygen and nitrate ion respectively. Since this, a series of works about the electrochemical deposition of ZnO nanostructure have been reported. We will only focus on the nanostructures obtained by electrodeposition, more specifically, on two interesting geometries: Zinc oxide nanowrods and Zinc oxide nanoporous structures.

I.6.4.1 Zinc oxide nanoporous structures

Depending on several deposition parameters, like the applied voltage, deposition time, charge density and solution precursor, the porosity and morphology of electrodeposited ZnO films may be tuned. Electrodeposited nanostructures can be achieved by co-depositing ZnO with a molecule that will be used as structure directing agent.

For example, it has been reported that the growth rate of ZnO films showing different porosities and morphologies prepared by cathodic electrodeposition was influenced

by sodium laurylsulfate concentration. This surfactant was added to the growth solution, made of aqueous oxygen saturated zinc chloride and other organic acids. If sodium laurylsulfate concentration is high enough, formation and assembly of micelles on the electrode surface could be achieved, allowing the formation of a porous structure, but also leading to a strong increase in the current density and finally, to the growth rate.[137] Besides, the addition of Eosin Y agent into the electrodeposition bath solution was reported. Eosin Y agent allows to deposit crystalline hybrid thin films of ZnO/eosin Y in one-step from an aqueous solution. In particular, the deposition time and the Eosin concentration were optimized to get mesoporous ZnO thin films with large internal surface areas. The addition of eosin Y accelerates the film growth because it catalyses the reduction of O_2 both in its oxidized and reduced forms. The film deposition accompanied with the reduction of eosin Y leads to a formation of unique sponge-like porous crystal of ZnO in which eosin Y molecules were adsorbed.[102,138–141]

Additionally, electrochemical self-assembly of dye-modified ZnO thin films in a one-step process without heat treatment has also been reported for use in dye-sensitized solar cells (DSSCs). The oxide semiconductor can be electrodeposited in the presence of organic dye molecules (e.g. tetra-sulfonated phthalocyanine) to give porous thin films with varying morphology.[102] Later in 2005, Pauporté, T., et al. have reported that ZnO/metal-tetra-sulfonated phthalocyanine (with metal being Ni, Co or Fe) films can be deposited by a simple, one-step method and that the final films are highly loaded with these chromophores. The films present a porous nanostructured morphology. The porosity and the dye loading, was adjusted by controlling the deposition potential. In this work, they demonstrated that almost all the organic molecules present in the films are electrochemically active, paving the way to potential applications in electrochemical devices. Due to the high specific surface area of electrodeposited ZnO thin films, a high amount of the organic molecule can be incorporated and simultaneously the high exposed surface offers the possibility to have high catalytic centers to perform the reaction.

Inspired by these works, we have decided to reproduce the deposition of hybrid nanoporous ZnO layers, this time by incorporating organic molecules with high catalytic activity toward CO_2RR into the porous nanostructured materials. By this mean we were able to create a hybrid transparent catalytic layer that can be also used as protective layer for photoelectrodes.

I.6.4.2 Zinc oxide nanorods structures

ZnO nanorod arrays (NRs) have attracted a lot of interest due to their remarkable physical and chemical properties, in optoelectronics, solar cells, UV photodetectors, and photonic devices.[104] These structures can be easily prepared by electrodeposition thanks to the strong c-axis orientation in the ZnO crystals. The main interest of using nanorod arrays is to enhance the conductivity of electrons. Because the structure is c-axis oriented with a good crystallization, a faster electron transfer is expected. Moreover, ZnO nanorods show high transparency and hardly ever any diffusion which is attributed to both the very high verticality and surface density of the nanorods on such a substrate, making then attractive for photovoltaics applications.

The first ZnO nanorods were reported in 1996 by Lincot et co-workers.[100] They not only showed that cathodic electrodeposition of ZnO is possible but that controlled modifications in the film properties can be obtained. The layers' morphology can be varied from compact films to open structures consisting of columnar microcrystallites. After that several studies have been published reporting a facile electrochemical route for the one-step fabrication of ZnO nanorods arrays, showing the effect of growth temperature, precursor concentration, substrate etching, and deposition time on the layer morphology and structure.[104,105] It is important to note that the processes described of electrodeposition are obtained at low temperatures in Zn ions aqueous solutions.

I.6.4.3 Hierarchical ZnO 3D structures

By combining the two structures previously described, hierarchical ZnO 3D architectures can be obtained. These structures consist of films made of ZnO nanorods embedded in a nanocrystalline nanoporous ZnO matrix. In 2010, Lincot and Yoshida have reported this original method for the electrochemical growth of ZnO nanocrystalline porous layers and hierarchical 3D nanostructures. The structures were designed by just playing on the growth conditions and without any use of template or additive in the aqueous deposition bath.[103] The structures were used in a preliminary test for prepraring dye-sensitized solar cell (DSSC), showing the interest and advantages of these nanostructures. Later, Pauporte and Guérin have presented the same strategy for the fabrication of DSSCs,[142] showing how the nanorods play several important beneficial roles in the presented structures. They allow the electrodeposition of thick nanoporous

ZnO films that immobilize a large amount of dye molecules, acting as preferential electron pathways for efficient charge collection, and due to their size, they increase light trapping in the photoelectrode.

Despite these promising results, this type of structure has never been used in catalysis. We used their strategy, changing now the dye molecule for a molecular catalyst. The resulting structures were used in the EC reduction of CO_2, showing interesting results, including improved catalytic activity compared to simple 2D catalytic structures.

I.7 Conclusion

In this first chapter, we have briefly presented the general context of this thesis. Starting from the energy context, we have highlighted the importance of proposing new strategies to improve current photoelectrochemical CO_2 reduction systems. We discussed the possible synergistic benefits of using molecular catalysts with photovoltaic material, to get highly efficient photoelectrodes able to reduce CO_2 into fuels in PEC conditions. The difficulty of such task becomes evident when looking at the limited number of reported molecular catalyst based photocathodes in the literature, their poor stabilities and in most of the cases low efficiencies. Furthermore, the majority of PEC CO_2 reports to date mainly use precious metal-based components. We described some of the surface immobilization methods proposed so far for molecule-driven photoelectrocatalysis, advantages and drawbacks where highlighted, giving an overview of the state of the art, laying the background to then describe the strategy we have used in this thesis work.

The molecular-based photoelectrodes designed and studied in this thesis aim to meet three criteria: the use of Earth-abundant catalyst, simple and inexpensive fabrication methods, and the ability to perform CO_2 reduction with simultaneous high efficiency, high selectivity and good stability.

To this end, the fabrication of a CIGS|catalyst|ZnO photoelectrode have been developed. We have given in this chapter an overview of the strategy used to make this possible, a more in-depth description and explanations will be presented in the following chapters, as well as the experiments carried out to evaluate the performance of these photoelectrodes, followed by a scientific discussion of the results obtained.

Chapter II

Experimental and analytical methods

II Experimental and analytical methods

II.1 Introduction

As introduced before, electrochemistry is one of the main tool for synthesis preparation performance measurement of electrodes and photoelectrodes coated with hybrid catalytic layers. The electrodeposition of hybrid nanostructured ZnO/organic films have been described before,[100,106,139] and it offers a wide range of possibilities in terms of creating electrodes material that can be used in catalysis or photocatalysis. The main goal of this thesis project is the fabrication of a highly efficient and selective photoelectrode for CO_2 reduction in PEC conditions.

We will describe in this chapter the various experimental setups for the electrodeposition of ZnO and ZnO|catalyst hybrid structures and the characterization techniques applied for these materials. However, keeping in mind that these ZnO hybrid structures will be finally incorporated as the window layers on a CIGS photoelectrode, we will also describe the experimental setup and conditions for the light-assisted electrodeposition of ZnO|catalyst hybrid layers, as well as the photovoltaic and electrochemical characterization techniques used for these photoelectrodes.

II.2 Experimental setups

II.2.1 Electrodeposition setup

The electrochemically grown films presented in this thesis have been electrodeposited using a classical three electrodes setup as shown in the figure II.1, in which the reference electrode is a Saturated Calomel Electrode (SCE) with a potential of +0.244 V vs. SHE at 25 °C. The counter electrode is a platinum wire or mesh. As working electrodes, we have used transparent conductive oxide coated glass, either FTO glass or ZnO:Al glass.

FTO glass was purchased from Solaronix, FTO substrates are cleaned ultrasonically in water, acetone and ethanol, activated in 45% HNO_3 for 2 min and finally rinsed with distilled water prior to the electrodeposition.

ZnO:Al substrates are 2 mm thick borosilicate or soda-lime glass covered by a transparent conductive zinc oxide aluminium doped (ZnO:Al) layer of 380 nm thick deposited either by Atomic Layer Deposition (ALD) or by sputtering,[143] and were prepared at IPVF. These layers present the same characteristics as the ZnO:Al window layers at a CIGS solar cell and are denoted AZO. The AZO coated glass substrates were ultrasonically sequentially cleaned in acetone, 2-propanol, and water each for 5 min. They were activated in a KOH solution (pH=10.5) for 2 min and finally rinsed with distilled water prior the electrodeposition.

In the electrochemical setup, the electrodes are connected to a potentiostat BioLogic Instruments® (model VSP) and controlled by the software EC-lab V10.19. The contact between the conductive substrate and the potentiostat is made with a small coating point of Gallium-Indium eutectic covered and connected with a copper tape from the surface of the substrate working electrode. Copper is isolated from the electrolyte by an electrochemical tape that delimits the active surface, as shown in Figure II.2.

The electrochemical cell used has also a bubbling system. Oxygen is bubbled into the solution 20 minutes prior each deposition and maintained during all the depositions. The temperature of the electrodeposition was controlled, according to the structure to be deposited, with a thermostated bath.

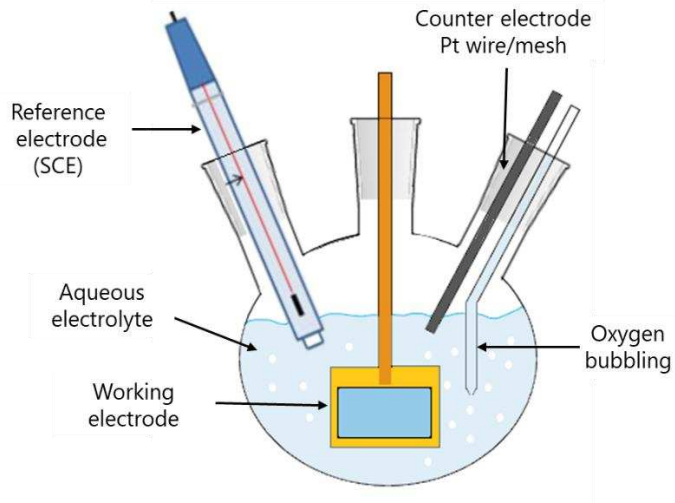

Figure II.1 Schematic representation of the experimental set-up used for the ZnO electrodeposition.

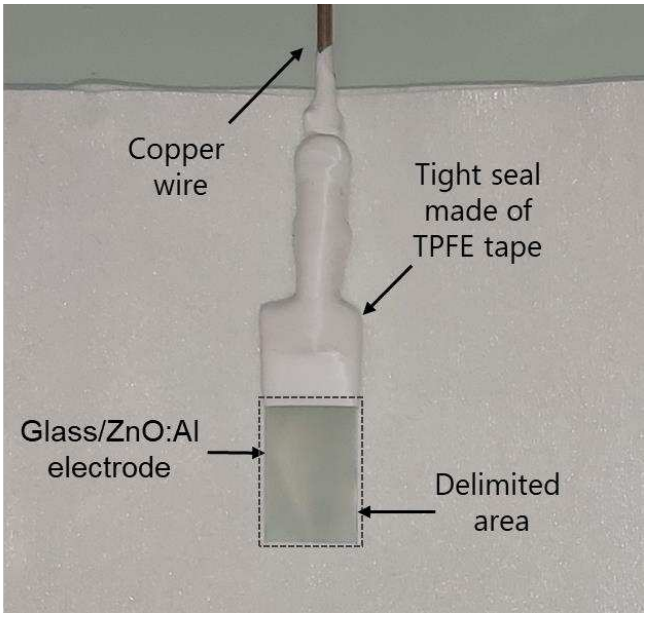

Figure II.2 Picture of a Glass ZnO:Al electrode connected to a copper wire. The electric contact is protected by a tight seal made of TPFE tape.

The deposition of thin films has been performed in potentiostatic mode: the electrode is held at a controlled potential for a given duration and the resulting current is recorded (chronoamperometry). Depending on the target ZnO structure, two different electrochemical cells were used. For the nanoporous structures, we have used 30 ml cell as shown in Figure II.3.

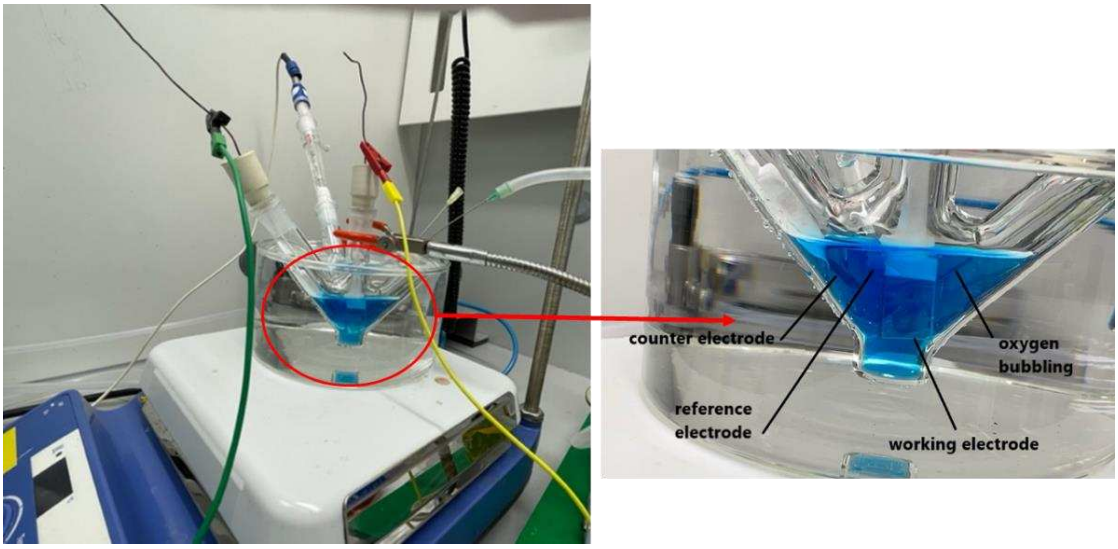

Figure II.3 Pictures of the experimental setup used for the electrodeposition of the ZnO nanoporous layers (NPS).

For the deposition of the ZnO nanorod arrays structures, we used a 1 L cell, as shown in Figure II.4.

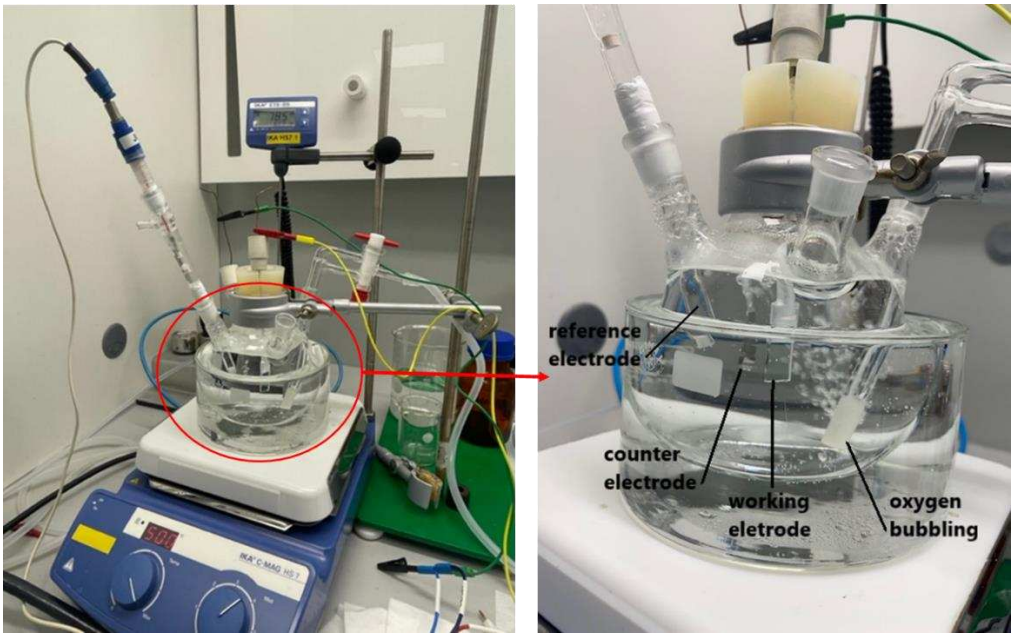

Figure II.4 Pictures of the experimental setup used for the electrodeposition of the ZnO nanorod arrays (ZNRs).

II.2.2 Light-assisted electrodeposition setup

The films deposited on the CIGS photoelectrodes presented in this thesis were prepared by a light assisted electrochemical process, referred as photo-electrodeposition in this manuscript. It corresponds to a three electrodes setup, as presented in Figure II.1. Irradiation was simulated with a 150-W xenon lamp from Oriel Instrument. UV light was filtered at wavelength below λ = 435 nm with a low-bandpass filter. A cell with a quartz window was used, allowing the light to penetrate into the solution, Figure II.5 and Figure II.7.

The contact between the CIGS photoelectrode and the potentiostat is made from the back contact molybdenum layer of the solar cell using a small coating point of Gallium-Indium eutectic covered and connected with a copper tape. Copper is isolated from the electrolyte by an TPFE tape, forming a tight seal, which also delimits the specific active area of the photoelectrode in contact with the electrolyte, as shown in Figure II.6.

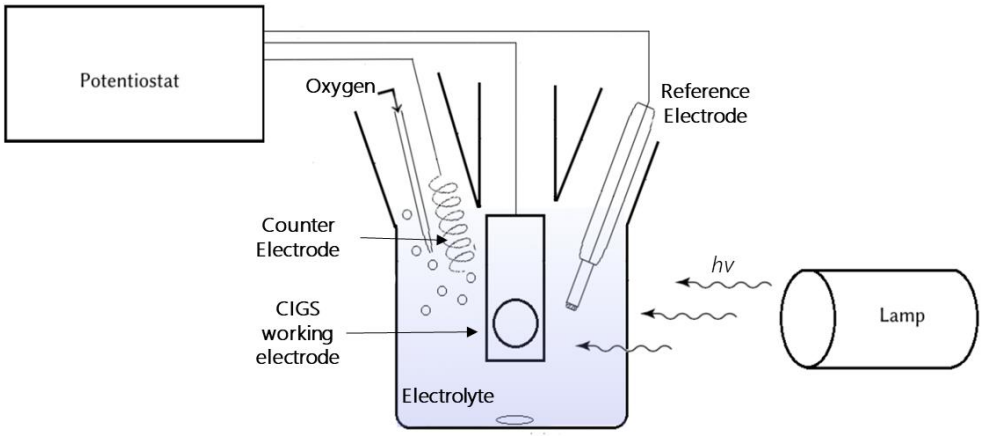

Figure II.5 Schematic representation of the experimental setup used for the light assisted electrochemical synthesis of ZnO nanostructures.

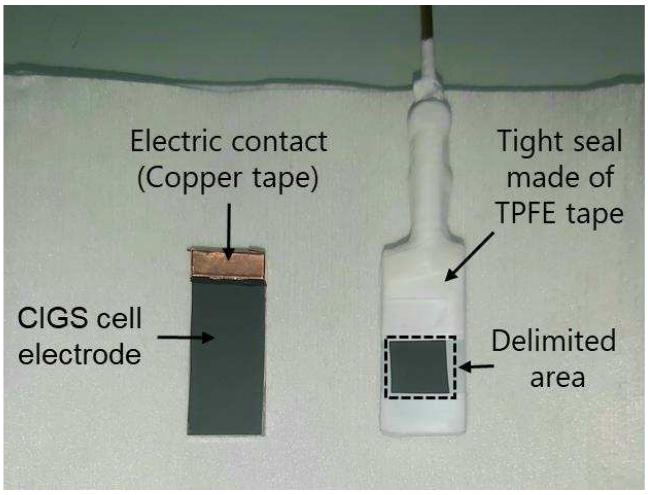

Figure II.6 Picture of a CIGS photoelectrode connected to a copper wire. The electric contact is protected by a tight seal made of TPFE tape.

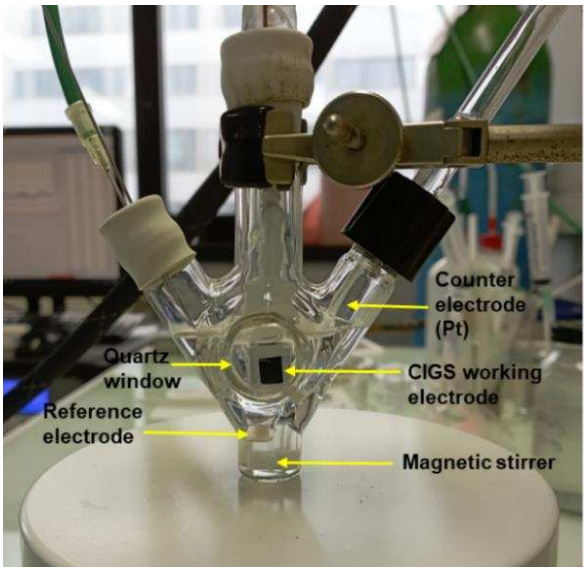

Figure II.7 Picture of the cell used for the light assisted electrochemical depositions.

II.2.3 Electrochemical (EC) and Photoelectrochemical (PEC) CO_2 reduction setup

The EC and PEC CO_2 reduction experiments were carried out in the same three electrodes setup described before (Figures II.5 and II.7), using the 30 ml cell. For the PEC experiments part of the light above 1000 nm was also filtered via a water tank filter to avoid electrolyte warmup, placed between the light source and the electrode. The PEC setup used is shown in Figure II.8.

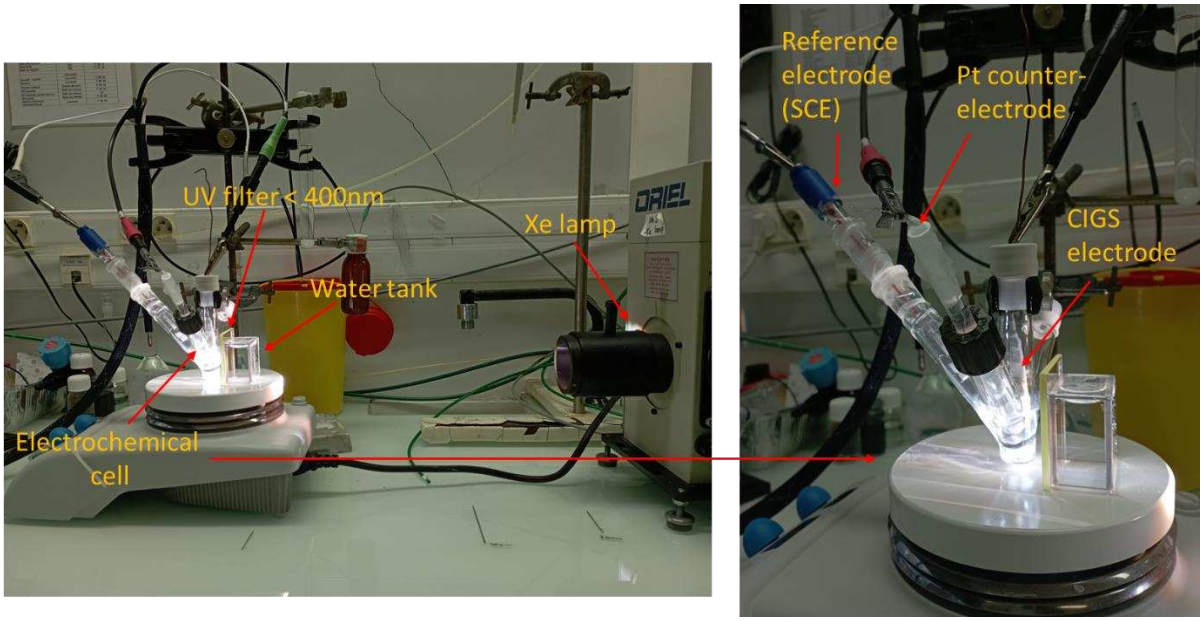

Figure II.8 Photography of the experimental setup used for electrochemical (EC) and photoelectrochemical (PEC) CO_2 reduction experiments. Images showing the electrochemical cell with the three electrodes setup, the UV light filter, the water tank filter and the Xe lamp.

The electrochemical cell shown in Figure II.8 includes a Saturated Calomel Electrode (SCE) used as reference electrode. The counter electrode is a platinum grid. As working electrode, we have used the CIGS photoelectrodes. For electrodeposition, the electrodes were connected to a potentiostat BioLogic Instruments® (model VSP) controlled by the software EC-lab V10.19. For EC and PEC CO_2 reduction experiments the electrodes were connected to either a potentiostat PARSTAT 4000 or PARSTAT 4000A from Princeton Applied Research.

II.3 Experimental details

II.3.1 Solvents

All the electrodeposition of ZnO structures were prepared in aqueous solutions. CO_2 reduction experiments where performed in acetonitrile, due to its large electrochemical stability window, meaning that it can be polarized at relatively negative or positive potentials without undergoing reduction or oxidation. In addition it is polar solvent, which allows for the dissolution of salts, and it shows high CO_2 solubility (314 mM at 25°C).[74] A source of proton is commonly added (acid) as a co-substrate, we have used water.

For ecological and industrial purposes, the use of water instead of organic solvents present strong advantages. Water is actually already widely used at the laboratory scale despite its narrower electrochemical window and lower CO_2 solubility. In this work we focused principally on using acetonitrile as solvent for the electrochemical CO_2 reduction experiments. This last offers a less corrosive environment for the photoelectrodes than the one in aqueous solutions. However, some preliminary experiments in aqueous solutions will be also presented in this manuscript.

II.3.2 Atmosphere

Electrodeposition and light-assisted electrodeposition were performed in oxygen saturated solution. The oxygen concentration in these last depends on the temperature used for each structure electrodeposited, 120 mM in water at 70 °C for the nanoporous layers and 87 mM in water at 80 °C[144] in the case of the nanorods arrays.

Electrolysis and photoelectrolysis experiments in CO_2 saturated solutions were performed under 1 atmosphere of pressure, resulting in a concentration of 34 mM in water and 314 mM in CH_3CN at 25°C.[145]

II.3.3 Illumination in light-assisted electrodeposition and photoelectrolysis experiments

At present, photovoltaic materials are generally tested under standard conditions developed by the American Society for Testing and Materials (ASTM) in conjunction with research and development laboratories for reporting comparable results. A laboratory testing is performed at the AM 1.5 (Air mass) Solar spectrum. At AM 1.5 condition, 1 sun is defined as equal to 100 mW cm^{-2}, it represents the annual average solar irradiance at mid-latitudes, taking into account 1.5 times the thickness of Earth's atmosphere normal to the surface.[146] In our case, both, light assisted electrodeposition and PEC CO_2 reduction experiments, presented in this manuscript, the light intensity from the halogen lamp was adjusted with a power meter at 100 mW cm^{-2}.

For the light-assisted electrodeposition, standard co-evaporated CIGS layers were deposited by classical three stage co-evaporation on glass/Mo substrates and completed by chemical bath deposited CdS and i-ZnO/ZnO:Al layers. The CIGS cell were provided by NICE Solar Energy GmbH.

II.3.4 Electrochemical baths

For each electrodeposition the chemicals were dissolved in Milli-Q pure water (18.2 MΩ.cm at 25°C). As it will be explained in the next chapter, ZnO geometry strongly depends on the electrochemical bath composition and potential applied. The bath composition and potential applied is described in table below (table II.1) in regard with the expected geometry of the layer and references are given for each condition.

Table II.1 Summary of the bath deposition conditions used for the electrodeposition.

Nanostructure	Substrate	Conditions	Reference
Nanoporous ZnO (NPS)	ZnO:Al-ALD ZnO:Al sputtered FTO	Oxygen saturated solution at 70° C, KCl 0.1 M, $ZnCl_2$ 5.0 mM, Catalyst 50 µM Applied potential – 1.0 V vs. SCE	[107]
	CIGS electrodes	Oxygen saturated solution at 70° C, KCl 0.1 M, $ZnCl_2$ 5.0 mM, Catalyst 50 µM Applied potential – 0.5 V vs. SCE, Light power 100mW cm^{-2}	This work
ZnO Nanorods (ZNRs)	ZnO:Al-ALD ZnO:Al sputtered FTO	Oxygen saturated solution at 80° C, KCl 0.1 M, $ZnCl_2$ 0.2 mM, Applied potential from -1.2 to -1.4 V vs. SCE	[103–105]

II.4 Characterisation techniques

In this section we will describe the techniques applied for the characterisation of the prepared electrodes and photoelectrodes.

II.4.1 Electrochemical characterization methods

II.4.1.1 Cyclic voltammetry measurements (CV)

This technique consists in sweeping forward and backward a window of potential from defined starting and ending values at a defined scan rate usually expressed in mV s^{-1}. The collected data is the current (i). A cyclic voltammogram shows the current (i), normally expressed as current density (j) in mA cm^{-2} as a function of the applied potential (V). This technique allows to:

- Determine the electrochemical domain of the substrates used as working electrode. Knowing the electrochemical domain allows to avoid cathodic decomposition during the electrodeposition processes or the catalytic tests.
- Determine the potential to be used for the deposition.
- Assess the catalytic activity of the electrodes.

Compare intensity and profile of catalytic currents under different experimental conditions.

II.4.1.2 Chopped light linear scan voltammetry

This technique is similar to CV with additional chopped light illumination flashing the sample. The collected data is the current as a function of the applied potential. A chopped light experiment allows to assess the photo current generated in the electrodes. This experiment has been performed to determine more precisely the potential domain in which a photocurrent is observed and to calculate the value of the photocurrent for a given potential value.

II.4.1.3 Controlled potential electrolysis/photoelectrolyis (CPE) or chronoamperommetry

These two terms refer to the same type of experiment were a fixed potential value is applied to an electrode and maintained for a determined period of time. According to the purposes of the experiment we will used one term or the other. Chronoamperommetry aims to record the current (i) as a function of time, whereas, in CPE the objective is to accumulate product of a reaction in the electrochemical cell in order to make a product analysis. Both information are of high relevance. The current (i) as a function of time provides valuable information related to the activity and the stability of the catalytic system, while product analysis provides information on its selectivity.

We will refer to chronoamperometry in the case of electrodeposition of the ZnO structures. For assessing electrodes in electrochemical CO_2R we will use the term CPE. Whereas, for assessing photoelectrodes in CO_2R under light illumination, we will use the term controlled potential photoelectrolysis.

II.4.1.4 Chopped light chronoamperometry

This method refers to experiment in which a fixed value of potential is applied to an electrode and maintained for a determined period of time while a chopped light

flashes the photoelectrode, providing valuable information related to the stability of the photocurrent generated by the sample.

II.4.2 Material characterizations

II.4.2.1 Structural analysis: X-ray diffraction (XRD)

XRD is a method that allows the identification of the crystalline structure of a material, the crystal preferred orientation and the crystallite size, by irradiating a sample with an incident monochromatic X-ray beam of wavelength λ at an angle θ. The atomic planes (of order *n*) and the lattice spacing *d* of the crystal cause this incident beam of X-rays to interfere with one another as they leave the crystal, which scatters the beam at angle 2θ and results in the measurement of an intensity pattern. Each position of the peaks corresponds to one crystalline lattice plane orientation, labelled by Miller indices (*h*,k,l).

The directions of the constructive interferences are given by Bragg's law:

$$2\mathrm{d}_{\mathrm{hkl}} \cdot \sin(\theta) = \mathrm{n} \cdot \lambda \quad \textbf{(eq. II.1)}$$

Where d_{hkl} is the spacing between diffracting planes (h,k,l), θ is the incident angle, n is the diffraction order and λ is the incident beam wavelength.

The structure of all the electrodeposited ZnO films of this thesis has been investigated by X-ray diffraction (XRD) under grazing incidence (GIXRD) conditions for crystallinity determination and phase detection. The analyses were performed both in a Bragg-Brentano configuration (θ-2θ) and grazing incidence X-ray diffraction (GIXRD) setups using an Empyrean (PANalytical) equipped with a copper anode (λ_{Cu-Ka2}= 0.15406 nm) and a Pixel detector. The analysis of the diffractograms has been performed using Highscore Plus software subtracting the copper $K\alpha_2$ signal.

II.4.2.2 Scanning electron microscopy (SEM)

SEM provides micro and nano scale information on morpohology at the electrode surface. In a SEM microscope, electrons with high energy are accelerated towards the sample surface from the filament source. The deflected and scattered electrons provide information on the surface topography. We have used SEM to identify the different nanostructures deposited in this work, their size, thickness and different morphologies. Thin-film morphologies were obtained using a Merlin VP Compact scanning electron microscope (SEM) provided by Zeiss, equipped with an energy dispersive X-Ray spectroscopy (EDS) detector from Bruker.

II.4.2.3 Energy Dispersive X-ray Spectroscopy (EDX)

This technique is used for chemical analysis of thin films. EDX is measured when the sample is exposed to high energy electrons resulting in the excitation of the atoms of the sample. A part of the core electrons either moves from the ground state to a higher energy level or is emitted leaving an electron hole. Then, two phenomena may occur: (i) an electron from an outer, higher energy shell falls back into this hole causing characteristic X-ray emission lines (EDX) or (ii) a second electron is emitted leading to Auger effect (only for light elements). Specific X-rays are released to fill the difference in energy between the higher-energy and the lower-energy shells of a given atom. Hence, the type of element and the approximate concentration of it into the layer can be obtained. EDX measurements allow to map the distribution and proportion of different atoms into the studied layer.

We have used EDX analysis to detect the presence and the distribution of the metallic centres of the molecular catalyst incorporated into the electrodeposited layers. The chemical analysis of samples was carried out using an energy dispersive X-ray (EDX) Zeiss Ultra 55.

II.4.2.4 X-ray Photoelectron Spectroscopy (XPS)

XPS is a surface-sensitive qualitative and quantitative chemical analysis technique used to determine the elemental composition, the chemical and electronic states and the

chemical environment of the elements on the surface of a sample. The X-ray beam irradiates the sample surface leading to the escape of electrons from the first 10-15 nm of the material. XPS spectra are obtained analysing the number of escaping electrons and their kinetic energy.

X-ray photoelectron spectrometer analyses were performed with a THERMO-VG ESCALAB 250 (RX source Al-K_α X-Ray (1486.6 eV)).

II.4.2.5 Inductively coupled plasma optical emission spectrometry (ICP–OES)

ICP is an analytical technique used to determine how much of certain elements are in a sample. The ICP-OES is based in the fact that atoms and ions can absorb energy to promote electrons from the ground state to an excited state. The source of energy is heat from an argon plasma that operates at ca. 8000 K. The ICP-OES principle relies on those excited atoms releasing light at specific wavelengths as they drop to a lower energy level. The amount of light released at each wavelength is proportional to the number of atoms or ions making the transition.

The electrodes and photoelectrodes studied in this thesis were analysed by ICP measurements for quantifying the amount of molecular catalyst incorporated into the electrodeposited layers, making possible to find the relationship between the thickness of the layers deposited and the concentration of catalyst inside. The electrodeposited layers were desorbed from the electrodes with a 69% HNO_3 solution. Solutions were then diluted to 2% HNO_3 and injected into ICP. ICAP 6300 Thermoelectron apparatus was used with detection of cobalt (238.8 nm band that is the most intense).

II.4.3 Optoelectronic materials characterization

II.4.3.1 Ultraviolet-visible (UV-vis) Spectrophotometry

The total transmission and absorption of the deposited films were measured using an Agilent Cary 5000 UV− vis−NIR spectrophotometer equipped with an Agilent diffuse reflectance accessory.

II.4.3.2 External Quantum Efficiency (EQE)

The Quantum Efficiency (QE) measurements evaluate the magnitude of current which will be produced when the cell is exposed to sunlight. The photogenerated current J_{ph} is closely related to the photon flux incident on the cell, and its dependence on the wavelength of light. Therefore, J_{SC} depends on the spectral distribution of the incident sunlight. Achieving high J_{SC} requires an important fraction of the incoming photons with an energy exceeding the electronic gap of the cell. In addition, each photon with sufficiently high energy should ideally be converted into an electron hole pair. The quantum efficiency (**QE**) indicates the probability of a photon of a given wavelength (λ) to create an electron-hole pair efficiently collected by the solar cell. It can be expressed using equation:

$$QE(\lambda) = \left(\frac{Jph(\lambda))}{(q\Phi 0(\lambda)}\right) \quad \textbf{(eq II.2)}$$

Where $J_{ph}(\lambda)$ is the photocurrent at the λ wavelength, q is the electron charge and $\Phi_0(\lambda)$ is the flow of incident photons at the λ wavelength.

The External Quantum Efficiency (EQE) is the ratio of the number of charge carriers collected by the solar cell by the number of incident photons. This parameter takes into account the optical losses effects such as the non-absorbed or the reflected light and electrical collection issues. The EQE were measured with an IQE200 Newport instrument (wavelength range 300 nm – 1300 nm). Figure II.9 illustrates the quantum efficiency (QE) of a crystalline silicon solar cell.

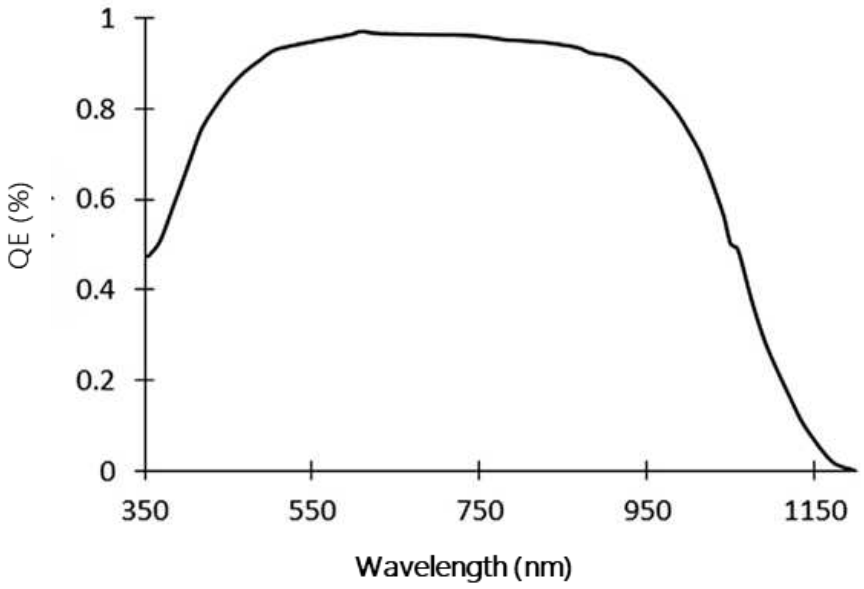

Figure II.9 Quantum efficiency (QE) of a crystalline silicon solar cell.

II.4.3.3 Current – Voltage characteristics (*J-V*)

Solar cell J-V curves were recorded under illumination using a solar simulator to obtain the efficiency (η), short circuit current (J_{SC}), open circuit voltage (V_{OC}), and fill factor (FF). J-V measurements of the CIGS solar cells & photoelectrodes were made by a 4 points probe connected to an Agilent voltage source. Light or dark measurements can be performed on this setup. For the measurements under illumination, the parameters used were AM1.5 spectra, with an irradiation power of 1000 W/m^2 on a Newport class AAA instrument. The measurements were performed at a controlled temperature of 25 °C by placing the samples on a temperature regulated surface.

II.4.4 CPE product analysis

For each reported electrolysis (in EC or PEC conditions), gas phase headspace was analysed by gas chromatography with a thermal conductivity detector (GC-TCD). In order to confirm that no liquid product was present, the liquid phase was analysed by Proton nuclear magnetic resonance (^{1}H NMR). In this manuscript, we will only focus on the gas phase product since our electrodes can only produce gas product. NMR was used once to verify that no liquid product was produced.

GC analyses of gas evolved in the headspace of the electrochemical cell during the electrolysis (H_2, O_2, N_2, CO, and CO_2) were conducted with an Agilent Technologies 7820A GC system equipped with a thermal conductivity detector and a capillary column (CARBOPLOT P7), with Argon as carrier gas. Products were quantified after separation through the column inside the GC via previously established calibration curves. Calibration for H_2 and CO were determined separately by injecting known volumes of pure gas. A typical gas chromatogram is shown in Figure II.10, it indicates the peaks of H_2, Air, CO and CO_2 detected from each analysis.

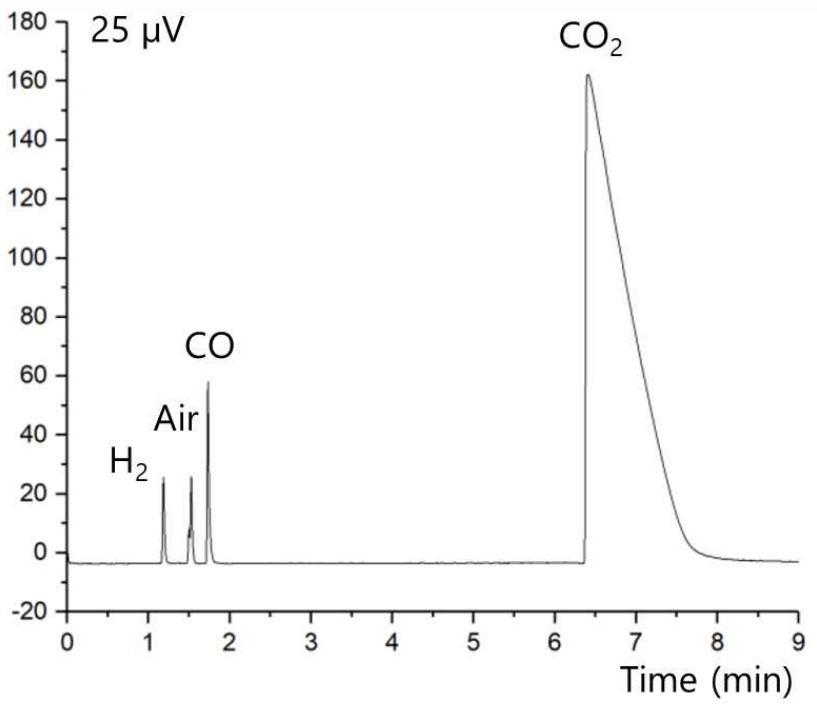

Figure II.10 Typical gas chromatogram of CO_2 reduction electrolysis/photoelectrolysis experiments.

II.5 Useful notions and performance indicators for PEC CO_2 reduction systems

We describe in this section notions concerning electrocatalysis in general that may be useful in the practical characterization of catalytic systems for the electrochemical reduction of CO_2, and that are widely used to compare CO_2RR systems.

It should be noted that the electrocatalytic metrics discussed in this manuscript are primarily based on the results of product quantification (e.g., gas chromatography).

II.5.1 Overpotential

As described before, an additional potential is needed to make the reaction happen with respect to standard redox potential of this reaction. To quantify this additional energy, we use the term overpotential denoted "η" defined in equation I.3. It corresponds to the absolute value of the difference between the applied potential at an electrode performing a given reaction (E), and the standard redox potential of this reaction ($E°_{\text{substrate/target product}}$). The Overpotential represents a high importance feature for benchmarking of electrochemical devices.[147]

$$\eta = \left|(E^{\circ}_{\text{substrate/target product}}) - E\right| \quad \textbf{(eq.II.3)}$$

II.5.2 Onset potential

This parameter refers to the working potential where the electrocatalytic current starts to rise up rapidly. It is complicated to define since sometimes it is difficult to determine the exact current onset point in particular when the capacitive current contribution is significant. As consequence, onset potential is frequently defined as the potential where the electrocatalytic current of a defined product reaches a given level (e.g., 0.1 mA cm^{-2}). This predefined level also varies from study to study, so that comparing onset potentials across the literature is only qualitative.

II.5.3 Turnover number (TON) and turnover frequency (TOF)

The parameters TON and TOF are used to quantify catalyst performance and reflect the rate at which a product is generated.[37] As classical definition, the turnover number, TON is the ratio between the total mol number of product (n_{product}) and the total mol number of catalyst molecules (n_{catalyst}) until the total deactivation of the catalyst/photoelectrode.[147] It reflects the intrinsic stability of an electrocatalyst and allows the comparison among different catalytic materials. It is challenging to calculate the TON value of most electrocatalysts due to the structural ambiguity of the active sites and the difficulty to precisely quantify them. Reports in literature often assume that, all the added catalyst effectively participates in the reaction. Thus derived TON values are

underestimated.[148] Calculations of TON and TOF are made considering the total amount of molecular catalyst added into the catalyst material.

$$\mathrm{TON} = \frac{n_{product}}{n_{catalyst\ in\ the\ film}} \quad \textbf{(eq. II.4)}$$

The TOF is then defined as the TON per unit of time. This value is simple an average value over the duration of the experiment. Strictly speaking, TOF is an instantaneous rate which could be evaluated at any time and typically over the course of a (photo)electrolysis due to the progressive degradation of the catalyst. Finally, the amount of electrochemically active catalyst in the film is decaying over time, so the TOF is changing with time (t). The TOF calculated here is a mean value over the course of the electrolysis.

$$\mathrm{TOF} = \frac{TON}{t} \quad \textbf{(eq. II.5)}$$

Where *t* is the reaction's time usually in seconds.

II.5.4 Faradaic Efficiency (FE)

The Faradaic efficiency (FE) represents the selectivity for a given product of the CO_2 reduction. FE is defined as the percentage of electrons consumed for the formation of a given product. It can be calculated by the equation:

$$\mathrm{FE} = \frac{e^{-} n_{product} F}{Q} \quad \textbf{(eq. II.6)}$$

Where e^- is the number of electrons transferred (e.g., = 2 for reduction of CO_2 to CO), n is the number of moles obtained for a desired product, F correspond to Faraday's constant (96,485 C mol^{-1}), while Q is the total charge passed during the experiment. The FE gives the conversion efficiency between electricity and products and reveals

what fraction of the charge is redirected to side products or parasitic reactions (e.g., solvent, electrode, and/or catalyst decomposition).[37]

II.5.5 Current density

The current density reflects the rate of the CO_2RR. When bulk or nanostructured materials are used as the electrocatalysts, active sites with unknown structures coexist.[12] Under these circumstances, the catalytic current density (*j*) is sometimes used to indicate the average activity of the catalyst. For practical simplicity to make comparison between diverse situations, this current is reported normalized by the geometrical surface of electrode and called current density, usually expressed in mA cm^2. The same term can refer to the actual current density plot as a function of time j(t) or to the average current density when a single value is given for a long term experiment. In this last case, j refers to the total charge passed during the experiment divided by the time of the experiment and the electrode surface.

II.5.6 Stability

The stability of an electrocatalytic CO_2RR system is another important performance indicator, it is commonly evaluated by conducting long term electrolysis under a constant applied potential or current density. Both current density and FE of the target product are recorded during the whole experiment to evaluate the catalytic stability. Following the product selectivity through the determination of FE is crucial during stability testing because current density on its own does not provide conclusive evidence on the stability of an electrocatalyst for CO_2 reduction due to the complexity of the products formed.[149]

II.5.7 Solar to fuel efficiency (STF)

Solar-to-fuel efficiency (STF) is the most well-known figure of merit of a whole PEC cell.[83,150,151] STF evaluates the total conversion of the incident light into the reduced products of the CO_2RR. It is use for reporting photocathode performances with more

rigour and standardisation, especially in terms of efficiency. In our case it is related to CO_2 reduction to CO. Solar-to-CO (STCO) efficiency was calculated according to the following equation:

$$\mathrm{STCO\%} = \frac{|\mathrm{J\ (mA\ cm^{-2})}| \times \mathrm{FE(\%)} \times (\Delta \mathrm{E^{\circ}} - \mathrm{E})}{\mathrm{P(mW\ cm^{-2}\ )}} \quad \textbf{(eq. II.7)}$$

Where, J is the photocurrent density, FE is the Faradaic efficiency towards CO, ΔE° is the thermodynamic energy stored in the CO_2 chemical fuel couple at 25 °C. Here, the equilibrium potential for oxygen evolution reaction (OER) occurring at the anode is 1.23 V vs. RHE, and the equilibrium potential for the CO_2 reduction half reaction occurring at cathode is 0.11 V vs. RHE. This approximation considers that no overpotential is required at the anode (a platinum electrode) and negligible ohmic loss. E is the applied bias (V vs RHE) and P is the incident light irradiance ($mW{\cdot}cm^{-2}$).[83]

Chapter III

ZnO hybrid catalytic nanostructures: synthesis and performance in EC CO_2 reduction

III ZnO hybrid catalytic nanostructures: synthesis and performance in EC CO_2 reduction

III.1 Introduction

In the first chapter we have described the typical CIGS heterojunction solar cell architecture and its properties. This chapter will focus on the window layer of the CIGS solar cells, namely the ZnO:Al layer. The use of ZnO as window layer meets the requirements to be used in solar cells (wide band gap, high conductivity). A ZnO layer acts as front contact, collecting electrons from the buffer layer while also allowing light to pass through to the absorber beneath. Typically, in a CIGS cell the bilayer of ZnO consists of a thin (≃100 nm) intrinsic ZnO layer and a thick (≃300 nm) *n-type* ZnO:Al layer. Before the deposition of the window layer, it is common to use an undoped high resistivity sputtered ZnO (*i*-ZnO). This additional buffer layer is typically used to make the *p-n* junction less sensitive to shunts, absorber material fluctuations or to protect it from sputter damage by energetic ions. The window layer of chalcopyrite-based solar cells is typically a degenerately doped semiconductor that functions as both an *n*-type partner in the *p-n* heterojunction and as transparent contact layer (TCO). Low resistivity and high transparency from the UV-visible region up to the absorber band gap in the near IR are obviously required. However, good matching of the electronic bands and lattice constants to the underlying absorber/buffer layers is also required for optimal performance. The most common TCO materials are SnO_2:F (FTO), In_2O_3:Sn (ITO), and highly aluminium doped ZnO (AZO). However, because FTO deposition requires temperatures higher than 200°C, it is not used in chalcopyrite-based devices. ITO and AZO can both be used, but AZO is the most commonly used material due to its lower material cost.[93]

ZnO presents excellent optical properties, low toxicity and is widely available. Among the specific benefits of ZnO, one can also highlight the ease with which it can be grown in high quality by solution routes and the possibility to prepare large range of nanostructures, such as nanorods, nanotubes, nanobelts. In fact, ZnO can be synthesized electrochemically from aqueous solutions of zinc salts. In 1996, Izaki et al.,[99] and Peulon et al.,[100,101] independently discovered methods to electrodeposit crystalline ZnO thin films from aqueous solution of zinc salts, employing cathodic reduction. Electrochemical deposition is simple and low-cost for the preparation of high quality ZnO.

Moreover, conformal films can be easily produced by electrodeposition on substrates with a complicated shape and the technique allows the design of complex nanostructures by combining and adjusting the growth conditions.[102–105]

The electrochemical growth of the ZnO also allows the loading of organic molecules during the film growth. In the end of the 90's Yoshida et al.[106] reported the electrochemical self-assembly of dye-modified ZnO thin films in a one-step process, by adding water-soluble dyes (Eosine) to the electrochemical bath containing $Zn(NO_3)_2$. They obtained coloured ZnO thin films with very different surface morphologies and crystallographic structures from the pure ZnO film. The loading of organic molecules into ZnO films was also attempted from an organic molecule and $ZnCl_2$ bath employing cathodic reduction of dissolved molecular oxygen precursor.[107,108] The presence of additives in the bath has a significant impact on the local growth mechanism and changes the shape of zinc oxide. In most cases, additives are incorporated into the deposit as hybrid organic-inorganic structures resulting in nanoporous interpenetrated hybrid materials. The use of an inorganic porous nanostructured matrix of ZnO allows not only the immobilisation of a large amount of the organic molecule but also the good accessibility of the complexes to the electrolytic solution.

Since CIGS cells are ended with a ZnO windows layer, that can be grown and modified via electrochemistry, our strategy was to incorporate a molecular catalyst into the ZnO inorganic matrix, resulting in a hybrid film with catalytic activity. By introducing the semiconductor material as the substrate to the reaction solution, co-catalyst nanostructures may heterogeneously nucleate and grow on its surface. The organic/inorganic interfaces formed in this way are generally very robust and can withstand higher mechanical stresses and protect the semiconductor from photocorrosion.[42]

We will show in this chapter the principles of the electrodeposition of ZnO process that we have chosen. We describe the formation of three different ZnO nanostructures: (i) a hybrid nanoporous layer (NPS), (ii) a nanorods arrays (ZNRs), and (iii) a 3D structures formed by the nanorods and the nanoporous layer (ZNRs+NPS). The results of a series of optimisation experiments, as well as the characterisation of these materials will be discussed. Finally, we present the performance and characterisation of these nanostructures in electrocatalytic CO_2 reduction presenting at the end a summary of the results obtained.

III.2 Principles of the electrodeposition of ZnO

Electrochemically ZnO can be growth from aqueous solutions of different zinc salts.[100,136] We have selected the ZnO electrochemical deposition method proposed by Peulon et al.,[100] which is carried out using $ZnCl_2$ and dissolved oxygen as a precursors. This method allows for cathodic electrodeposition of ZnO as well as controlled changes in film properties and morphology.

The ZnO films are deposited cathodically from a $ZnCl_2$ aqueous solution at a very low concentration (mM), in the presence of dissolved oxygen according to the overall reaction given in Equation III. 1.

$$Zn^{2+} + \frac{1}{2}O_2 + 2e^- \rightarrow ZnO \quad \textbf{(eq. III.1)} \qquad E°_{ZnO} = 0.88 \text{ V/NHE}$$

The standard potential of this reaction versus the normal hydrogen electrode is $E°_{ZnO}$= 0.88 V/NHE at pH 0. Meaning that, thermodynamically, deposition is possible by applying a cathodic potential to a conducting substrate, with a value lower than this value. Besides, the standard potential of metallic zinc deposition is around $E°_{Zn}$ = -0.76 V/NHE at pH 0 (Equation III.2).

$$Zn^{2+} + 2e^- \rightarrow Zn \quad \textbf{(eq. III.2)} \qquad E°_{Zn} = -0.76 \text{ V/NHE}$$

As a result, there is a large potential window for ZnO deposition between - 0.76 V and 0.88 V, with no deposition of metallic zinc.

The mechanism of the electrochemical deposition of zinc oxide occurs in two steps.[152] First, the reduction of oxygen leads to a generation of hydroxide ions according to equation III.3 with the standard potential E° = 0.401 V/NHE. The hydroxide ions are generated next to the electrode by electrochemical reduction, which locally increases the solution's pH and leads to the precipitation of the metallic oxide. The hydroxide ions react with Zn(II) species to precipitate ZnO following the equation III.4.

$$O_2 + 2H_2O + 4e^- \rightarrow 4OH^- \quad \textbf{(eq. III.3)} \qquad E° = 0.401\ V/NHE$$

$$Zn^{2+} + 2OH^- \rightarrow ZnO + H_2O \quad \textbf{(eq. III.4)}$$

Depending on the concentration of Zn^{2+} ions, deposition of ZnO can take place as continuous films, (at high concentrations of Zn^{2+}),[107] or nanorods (lower concentration of Zn^{2+}).[105] The addition of water-soluble molecular catalyst to the deposition bath can act not only as structure directing agent but also let their incorporation inside the non-porous ZnO layer. As a consequence, the morphology, the crystal size, and orientation of the deposited ZnO films are then significantly modified by the added molecule. The self-assembly of these mixed materials is governed not only by the chemical interaction between the ZnO surface and the molecular catalyst but also by the amount of adsorbed molecules. Depending on the molecule and its concentration, the ZnO growth will be partially quenched and pores will appear in the crystal, resulting in a nanoporous structure. That phenomena have been reported by Yoshida et al.[106,153] and Pauporté et al.,[107] using tetrasulfonated metallophthalocyanines molecules (metal = Ni, Co, Fe).

III.3 Electrodeposition of nanostructured ZnO layers

The use of nanostructured or high surface area electrodes can greatly enhances surfaces reactivity with a sizable fraction of the reactive sites available for catalysis. Moreover, owing to quantum confinement, the nanostructured architecture, can facilitate the movement of electrons and holes as well as it can enhance the transport properties related to phonons and pho-tons. The small size of nanostructured materials also increases the specific surface area and the surface-to-volume ratio. In this section we will present two kinds of ZnO structures prepared by electrodeposition. First, we will show the preparation of hybrid nanoporous layers (NPS) of ZnO and the CoPc3 molecular catalyst (Figure III.1.a). After that, we will describe the preparation of a more sophisticated ZnO nano-structures, a 3D ZnO hierarchical structure, made of ZnO nanorods arrays (Figure III.1.b) covered by a NPS layer (Figure III.1.c).

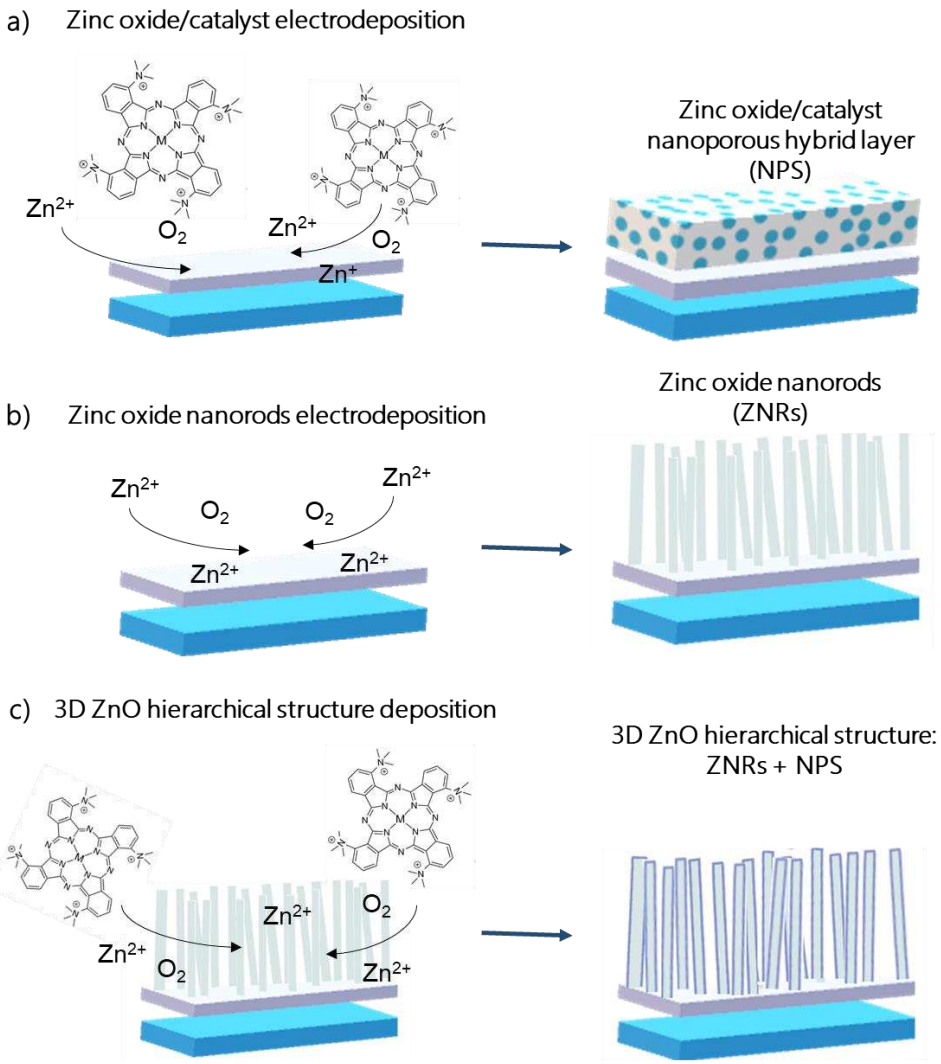

Figure III.1 Schematic representation of the three electrodeposited ZnO nanostructures presented in this manuscript. a) Hybrid ZnO|catalyst nanoporous structures (NPS). b) Zinc oxide nanorods arrays (ZNRs), used as substrate for the deposition of the 3D nanostructures. c) hierarchical 3D structures made of zinc oxide nanorod arrays coated by a hybrid ZnO|catalyst nanoporous layer (ZNRs + NPS).

III.3.1 Electrodeposition of hybrid nanoporous ZnO|catalyst (NPS)

III.3.1.1 Synthesis process

For this study, depositions have been performed on glass substrates coated by a 380 nm ZnO:Al layer deposited by atomic layer deposition. The electrodeposition of the zinc oxide/catalyst hybrid layers was carried out potentiostatically at -1.0 V vs SCE in

an aqueous solution containing 5.0 mM $ZnCl_2$, 0.1 M KCl and 50 µM of the water soluble molecular catalyst. Typically, an electrode with a surface 1 cm^2 is used in a 10 mL bath solution (see chapter II section II.3.4, Table II.1). The working electrode was fixed and the solution was stirred. The reference electrode (SCE) is set in a compartment containing the electrolytic solution in order to keep the electrode at room temperature and avoid fluctuation of the potential with the temperature. Temperature was maintained at 70°C. The deposition process was stopped when a fixed value of total charge transferred has been reached. The deposited films were rinsed with water, dried in air into an oven at 100° for 30 min, then stored at room temperature. In this section we will focus on the deposition of hybrid layers using CoPc3 as catalyst molecule.

III.3.1.2 Study of the electrochemical bath

Prior to each deposition the glass/ZnO:Al (AZO) substrates were characterized by cyclic voltammetry in the bath deposition solution in order to ensure a good electric contact and to study the stability of the substrate in the solution. In Figure III.2 we show the cyclic voltammetry of a glass/AZO electrode in a bath deposition solution before and after adding the 50 µM of the CoPc3 molecular catalyst. The scan starts at the 0 V and the potential is swept in the cathodic direction. The CV of the bath solution without the catalyst shows a slight increase of the cathodic current (-0.2 mA cm^{-2}) around -0.5 V. At this potential, the reduction of dissolved oxygen in the solution starts according to the following reaction:

$$O_2 + 2H_2O + 4e^- \rightarrow 4OH^-$$

The current density then starts increasing around -0.8 V. After this point, one can observe a steep increase of the current density reaching a value of -1.75 mA cm^{-2} at – 1.2 V. This is due to the hydrogen evolution reaction (HER) but also to the reduction of the Zn^{2+} ions. In fact, the reduction wave corresponding to Zn(II) ions reduction to metallic Zn is expected around -1.0 V vs. SCE.[101] Based on the equation:

$$Zn^{2+} + 2e^- \rightarrow Zn$$

In the reverse scan, an anodic peak appears around -1.0 V, corresponding to the oxidation of the Zn formed in the cathodic direction. Two reactions can be considered during the oxidation of zinc:

$$Zn^{2+} + 2e^- \rightarrow Zn \quad \text{or} \quad Zn^{2+} + 2OH^- \rightarrow ZnO + H_2O$$

Once the CoPc3 molecule is added two phenomena are observed. First, a shift in the potential of the oxygen reduction towards less negative potential, starting now around -0.2 V. Second, a large increase in the current density reached due to the fact that CoPc3 molecule can catalyse the oxygen reduction reaction,[154] (ca. -1 mA cm^{-2}).

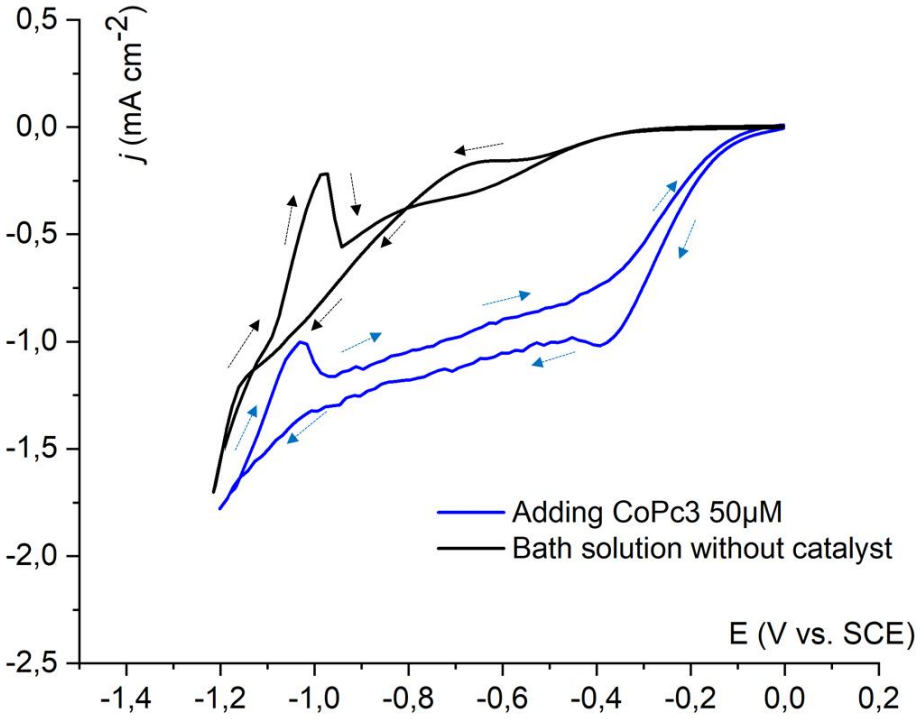

Figure III.2 Cyclic voltammograms of an AZO-ALD electrode into the bath deposition solution of the hybrid ZnO nanoporous layers (NPS) before (black) and after (blue) adding the CoPc3 molecule. CV from 0 to -1.2 V vs. SCE, at scan rate of 0.1 V s^{-1}. Electrode surface 1 cm^2. The arrows indicate the scan direction. The bath temperature is maintained at 70°C.

III.3.1.3 Electrodeposition process

Nanoporous structure were grown in the electrochemical bath described before (aqueous solution containing 5.0 mM $ZnCl_2$, 0.1 M KCl and 50 µM of the water soluble molecular catalyst). Figure III.3 displays current trace vs. time for the deposition of hybrid ZnO|CoPc3 layers onto an AZO electrode at -1.0 V vs. SCE and T = 70°C. The potential of -1.0 V vs. SCE was selected since it allows the layers to grow at the higher current density without reducing the Zn(II) ions into metallic Zinc. The current density increase slightly during the very first second of deposition before decreasing from -1 mA cm^{-2}

to -1.5 mA cm^{-2}. The trend of the deposition curve is characteristic of a tri-dimensional nucleation, in which grains nucleate in an instantaneous step and grow tri-dimensionally in such a way that the increase of the surface leads to an increase of the current density. Coalescence of the grain further lead to a decrease of the surface area and therefore to a decrease of the current density.[152]

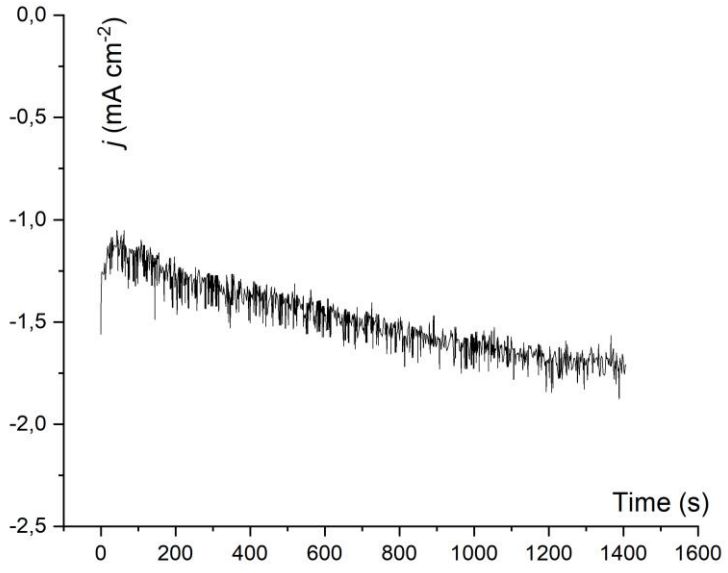

Figure III.3 Chronoamperometry curve during electrodeposition of a hybrid ZnO|CoPc3 nanoporous (NPS) layer on an AZO-ALD electrode at -1.0 V vs. SCE. 75°C and 500 rpm.

In the presence of water soluble CoPc3 catalyst, porous ZnO thin films are deposited. As observed on the SEM images (Figure III.4.a), addition of the molecular catalyst during the growth of ZnO seems to strongly affect the crystal growth mechanism of the ZnO, leading to a significantly higher surface area, resulting in a sponge like nanoporous structure. Furthermore, the nanoporous layers obtained present a crystalline structure as shown in Figure III.4.b. In this figure the X-ray diffraction patterns of the Atomic layer deposited (ALD) ZnO:Al substrate is compared with that of a ZnO|CoPc3 nanoporous layer (NPS). ALD ZnO:Al layer presents a mixed (100), (101) and (110) orientation indicating that the *c* axis of ZnO is mostly parallel to the substrate. The comparison of the X-ray diffraction patterns of ZnO|CoPc3 nanoporous layer with the ALD ZnO:Al substrate (Figures III.4.b black vs blue) show an increased peak intensity of the (002) planes for the nanoporous layer as well as appearance of (102) and (103) reflections. The nanoporous film is thus mainly oriented according to the (002) reflection

which correspond to the c-axis of the wurtzite type lattice. However, several other reflections such as (100), (101), (102), (110), (103) and (200) are also observed.

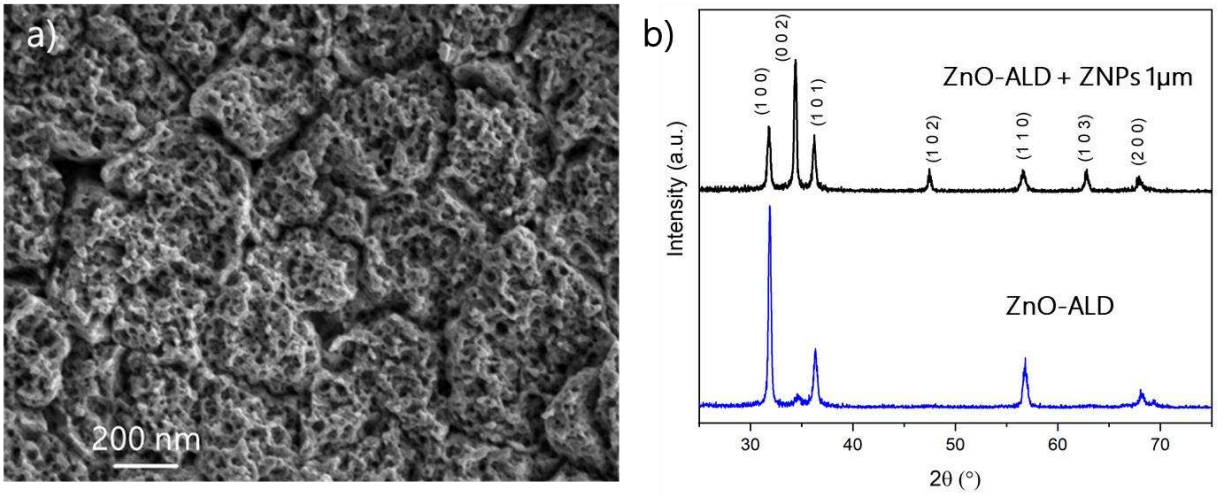

Figure III.4 a) Top view SEM image of an electrodeposited ZnO NPS layer, showing the nanoporous structure. b) GIXRD patterns of the AZO/ZnO NPS electrodes (black) and the AZO-ALD substrates (blue) at a glancing-incident angle ω = 3.0°.

III.3.1.4 Controlling the film thickness and catalyst concentration in the film

The effect of the charge transferred during the electrodeposition process on the thickness of the electrodeposited layers was studied by comparing different charge amounts transferred. Figure III.5 shows cross section SEM images of three ZnO|CoPc3 NPS layers deposited with 2, 3 and 4 C cm^{-2}. We can observe that the thickness of the electrodeposited layer increase linearly with the transferred charge during the whole process, allowing us to have a control of the thickness. However, we can also notice the difference in the morphologies obtained, it can be explained by the sensibility of the electrodeposition process.

Moreover, in order to confirm the incorporation of the molecular catalyst into the electrodeposited layers, ICP analyses were carried out on these samples. The results are presented in Figure III.6, showing that the concentration of the CoPc3 molecule in the layers is linearly correlated to the film thickness. Therefore, the amount of molecules encapsulated into the layer also depends on the transferred charge, permitting to control the encapsulated catalyst quantity.

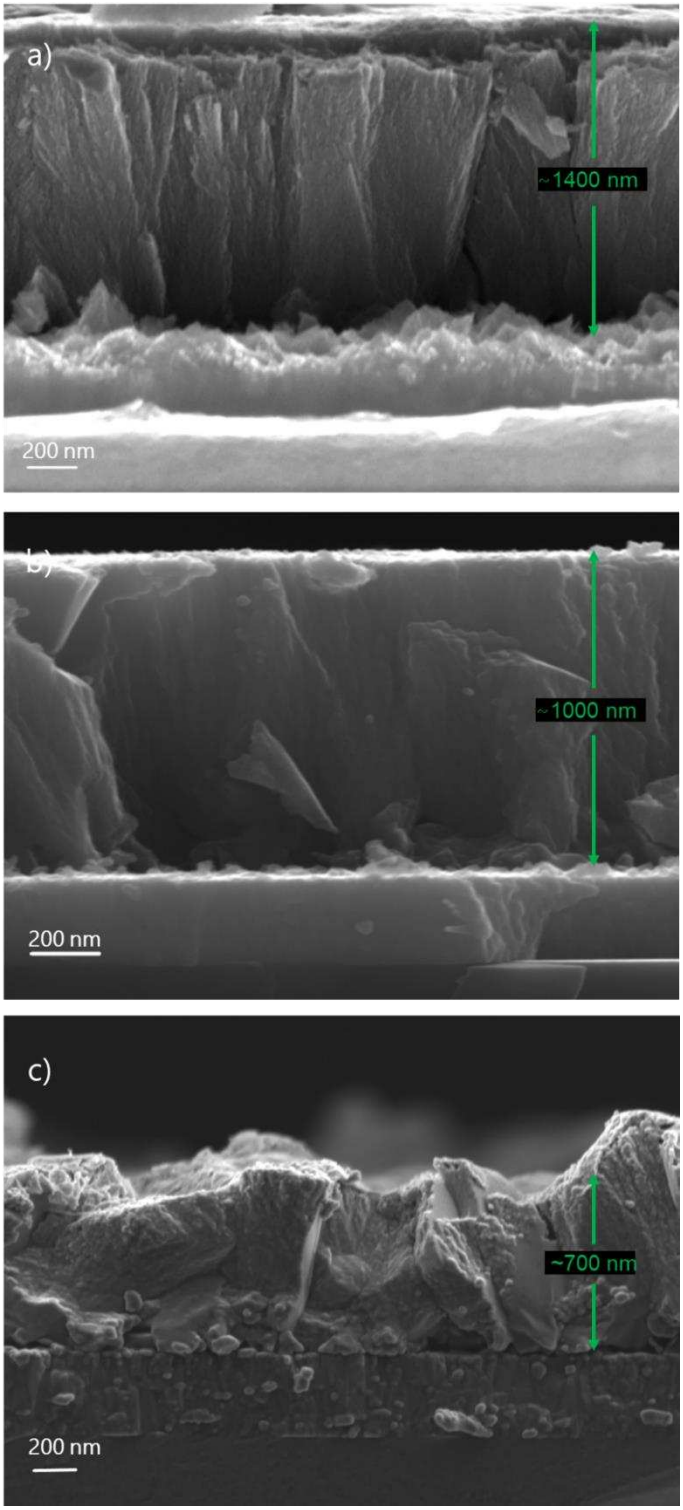

Figure III.5 Cross sectional SEM images of the electrodeposited ZnO|CoPc3 NP layers, showing the different thickness and morphologies obtained by variation of the charge transferred a) 2.0 b) 3.0 c) 4.0 C cm^{-2}.

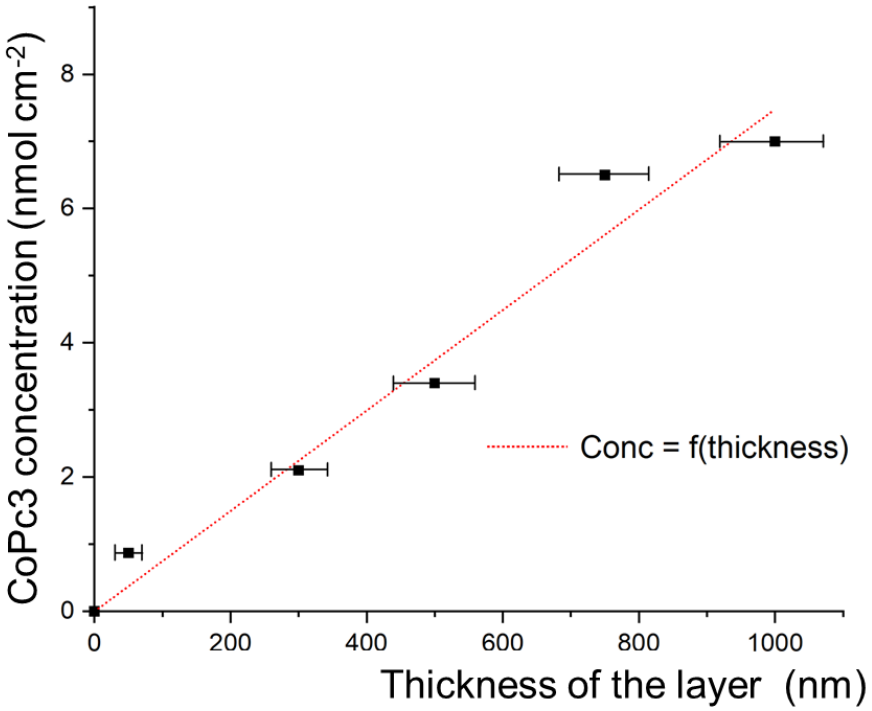

Figure III.6 Relation between the concentration of the CoPc3 molecules (obtained by ICP) into the ZnO NPS layers and the thickness of the layers measured by SEM. Linear fit of the catalyst's concentration as a function of the thickness of the layer (red dashed line).

The absorbance of the layers was measured by UV-vis spectroscopy. Figure III.7.a shows the absorption spectra of the CoPc3 molecule in an aqueous solution, with wel defined peaks, attributed to Q and Soret bands: a weak Q band (transition to the first excited state (LUMO)) in the visible region, around 600 - 700 nm and an intense Soret band due to an electron dipole movement that allows π-π* transitions (transition to the second excited state) around 350 nm range.[155,156] In Figure III.7.b spectra obtained for different thickness of ZnO|CoPc3 NPS layers are presented. The absorbance peak shown by the ZnO NPS samples at 658 nm lays at the same wavelength than the absorbance peak of the molecule in solution. Furthermore, increase of the sample absorbance is observed with the thickness, meaning that increase of the layer thickness leads to incorporation of more catalyst molecules (dependence was found to be linear). Figure III.7.c shows the concentration of CoPc3 molecules into the ZnO NPS layers measured by ICP as a function of the layer thickness and as a function of the absorbance at 658 nm. Both, absorbance and concentration variations follow the same linear trend confirming the incorporation of CoPc3 catalysts inside the nanoporous ZnO layers. The concentration of molecular catalyst in the films was 0.7, 2.1, 3.4, 6.5 and 7.1 nmol cm^{-2} for thicknesses of 50, 300, 530, 780 and 1000 nm respectively.

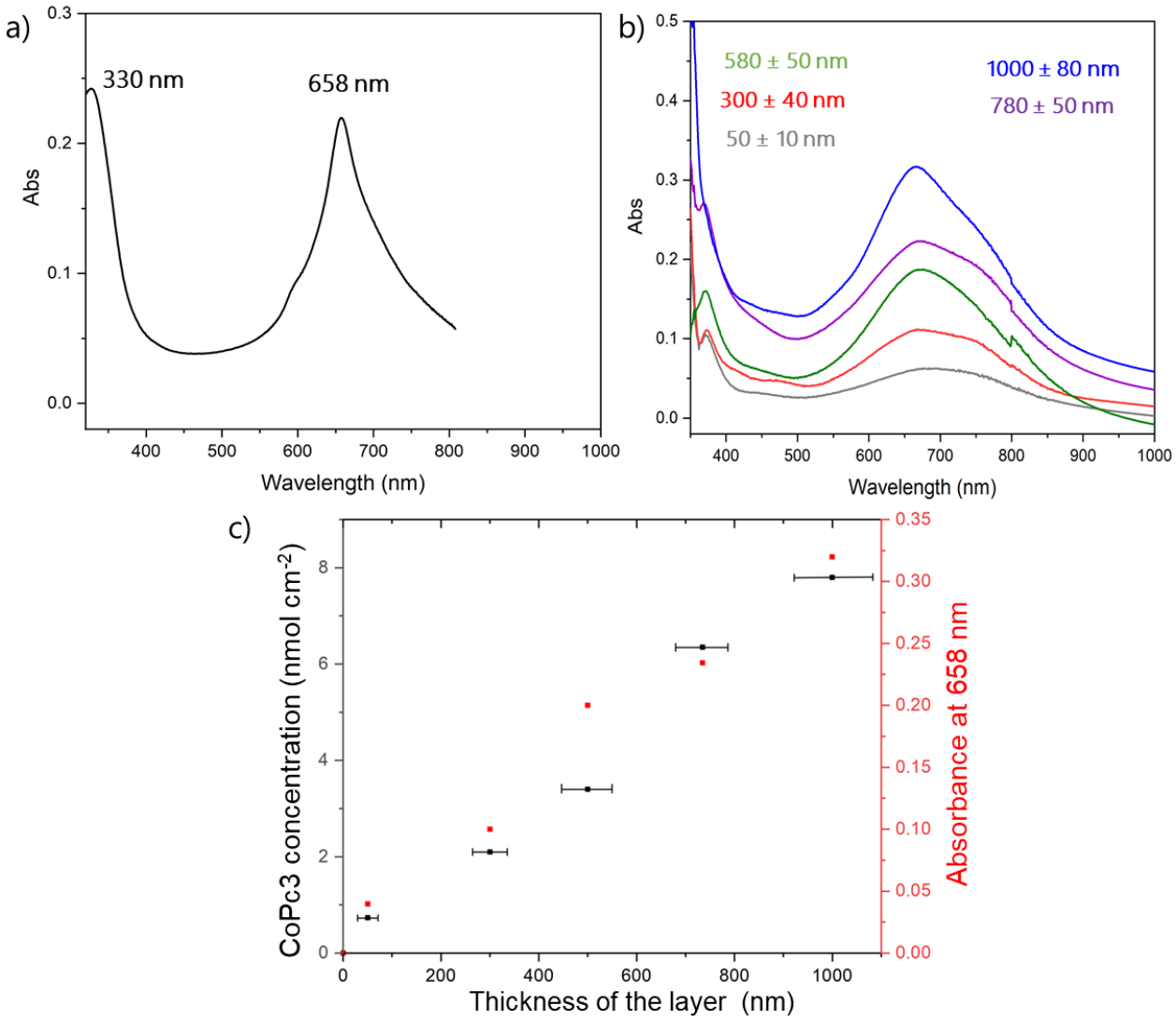

Figure III.7 UV-vis absorption spectra of: a) the CoPc3 molecular catalyst in a water solution 0.5 µM b) the electrodeposited hybrid nanoporous NPS layers incorporating the CoPc3 molecular catalyst, for thicknesses of 50, 300, 530, 780 and 1000 nm. c) Concentration of CoPc3 molecules (expressed in nmol per cm^2 of the electrode surface) into the ZnO NPS layers measured by ICP as a function of the thickness of the layer and compared to the absorbance of the same samples at the wavelength of 658 nm.

III.3.1.5 Distribution of the catalyst molecules into the ZnO nanoporous films

After assessing the presence of molecular catalysts into the electrodeposited NPS layer, dispersion and distribution of the catalyst into the layers was investigated by EDX. Figure III.8 shows EDX-mapping measurement on a ZnO NPS electrode (1 µm thick). The images show signals from the O, Zn, Cl atoms of the ZnO matrix, but also

signals from Co, definitively proving the presence of the catalyst and its incorporation into the film during the electrodeposition. Additionally, mapping of Co element revealed the absence of cobalt aggregate, suggesting a homogeneous distribution of the catalyst inside the oxide.

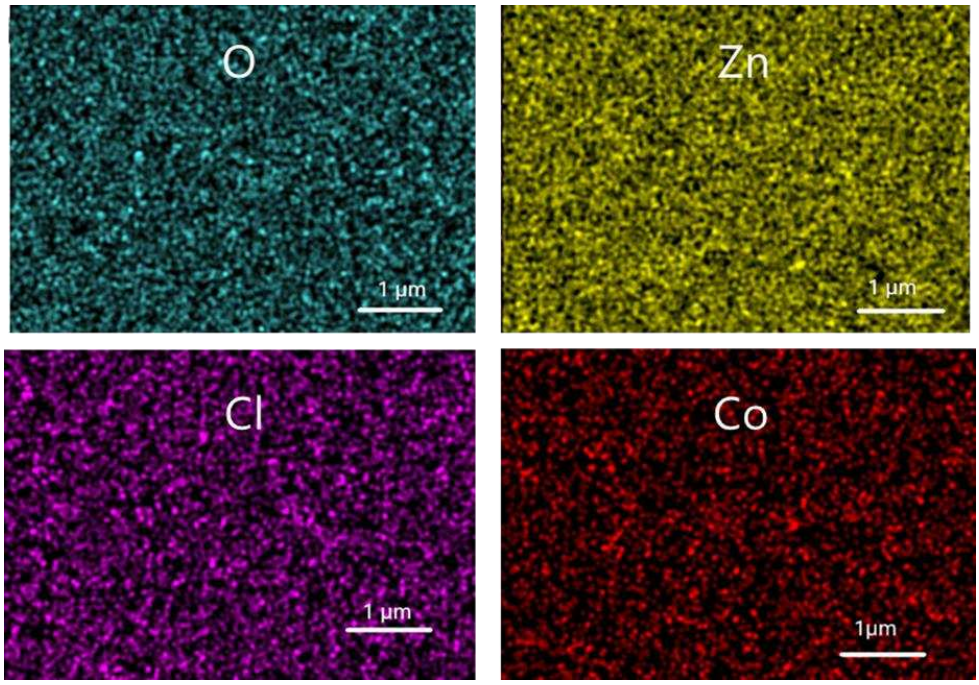

Figure III.8 EDX-mapping measurement on a ZnO|catalyst NPS layer (1 µm thick).

III.3.1.6 Further confirmations of the catalyst incorporation into the NPS layers

The encapsulated CoPc3 molecule was also monitored by XPS analysis. Figure III.9.a and FigureIII.9.b we compared the Co 2p and N 1s signals, of pure CoPc3 molecule with ZnO|CoPc3 NPS layer and a blank ZnO layers without adding the molecular catalyst. For ZnO|CoPc3 NPS layer it revealed two peaks corresponding to Co2p signals indicative of a Co^{2+} oxidation state, a main peak $2p_{3/2}$ at 780 eV and secondary peak $2p_{1/2}$ at 796 eV[157] (Figure III.9.a). Figure III.9.b shows the detected signals from nitrogen on the surface of the ZnO|CoPc3 NPS electrodes. Signals for N1s at 398.8 eV in the NPS sample corresponding to the characteristic binding energy of the pyridinic N complexing a cobalt atom in Cobalt phthalocyanines (CoPc) (BE = 399.3 eV).[157] This peak reflects the configuration of the CoN_4 center, a Co^{2+} ion with four equivalent nitrogens. Furthermore, a small N1s peak, centered at 402.5 eV is observed which is typically

assigned to N–O bonds.[158] This could imply an interaction between the N atoms of the CoPc3 molecule and the O atoms of the ZnO.

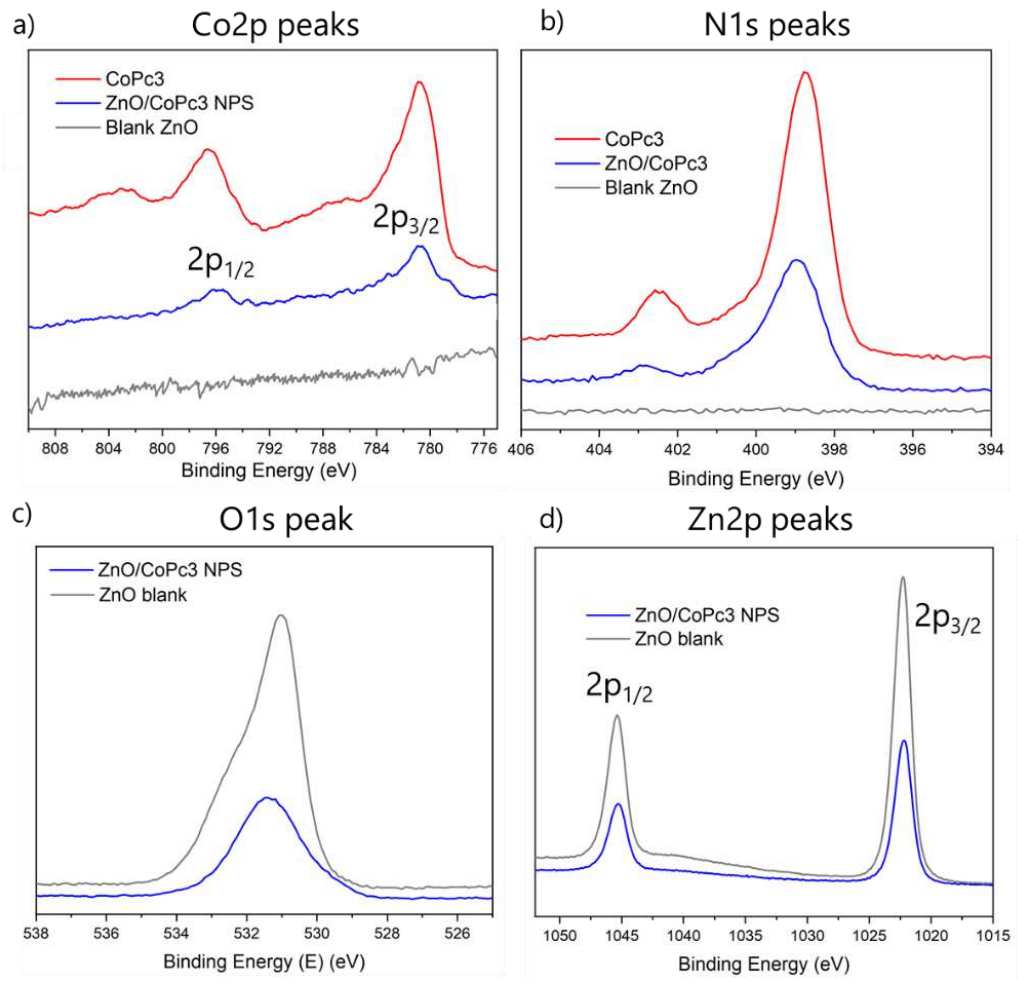

Figure III.9 a) Co 2p and b) N 1s, c) O 1s and d) Zn 2p XPS spectra a ZnO|CoPc3 NPS layer. Co 2p and N 1s spectra of the CoPc3 molecule are shown in a) and b) respectively. All the spectra compared with a ZnO blank sample deposited without adding the molecular catalyst.

In order to have a better understanding of the interactions between the molecular catalyst and the inorganic ZnO matrix in Figure III.9 c & d the O 1s and Zn 2p XPS spectra of a ZnO|CoPc3 NPS layer were compared to the blank ZnO layers. As observed, the peaks do not show shift in the binding energy values before and after the incorporation of the molecular catalyst. Therefore, no conclusions can be drawn from these results, further analyses must be done.

Moreover, infrared spectroscopy analyses were performed on the 1 µm ZnO NPS samples. Figure III.10 shows the spectra obtained by attenuated total reflectance infrared spectroscopy (ATR-IR) analysis of the CoPc3 molecule, a ZnO|CoPc3 NPS sample and a blank sample of ZnO. The CoPc3 molecule spectrum, (Figure III.10.c) shows a strong adsorption at ~1607 cm^{-1} corresponding to the C-N-C bending vibration. The pyrrole C–C stretching tied-up peak is displayed at 1321 cm^{-1}. The bands at ~1393, ~1490, ~1520 cm^{-1} are assigned to the aromatic ring stretching vibration. The metal to ligand (M–N) vibration of CoPc3 is observed at ~911 cm^{-1}. The absorptions present at ~1090 and ~1121 cm^{-1} are due to C–N stretching and C–H in-plane bending vibrations of CoPc3 respectively.[159] The adsorption peaks a at 2895 and 2980 cm^{-1} can be attributed to the C-H stretching vibration of the CH_3 from the trimethylammonium groups.[160] The comparison of the spectra of the hybrid ZnO|CoPc3 NPS (Figure III.10.b) with that of the CoPc3 molecule (Figure III.10.c) reveals a similarity in fingerprint regions between CoPc3 powder and CoPc3 loaded into the ZnO NPS structure. This add evidence that the catalyst is well incorporated into the electrodeposited layer. Moreover, we can observe the metal to ligand (M–N) vibration of CoPc3 at ~910 cm^{-1}, a peak around 1080 cm^{-1} from C–N stretching bending vibrations, a peak at 1393 cm^{-1} assigned to aromatic ring stretching vibrations which matches perfectly with the one detected from the CoPc3 sample. The peaks from the CH_3 groups at ~2895 and ~2986 cm^{-1} confirm complex structural preservation upon incorporation in the ZnO nanoporous layers.

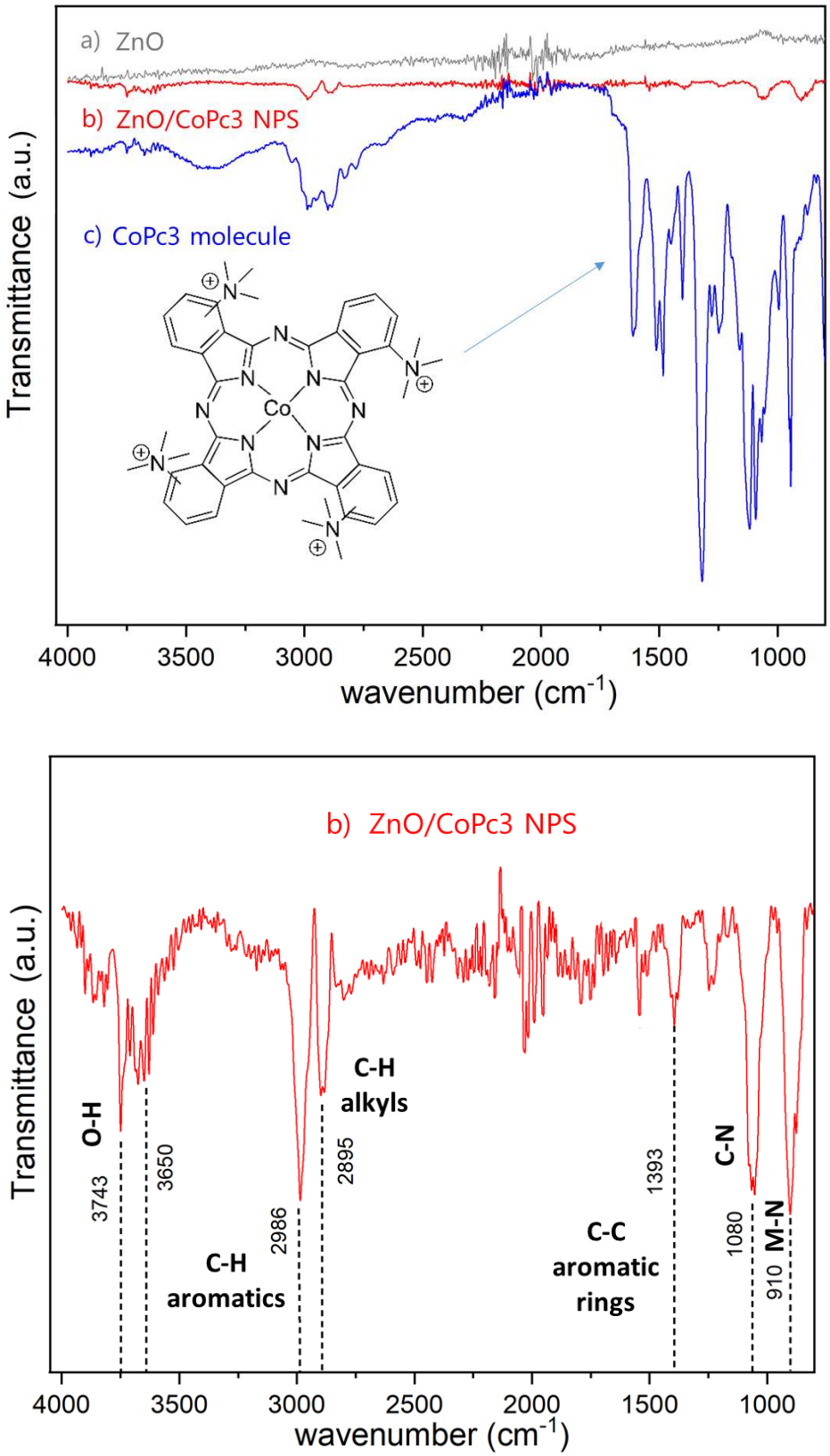

Figure III.10 Top: ATR–IR spectra of a) pure ZnO electrodeposited sample, b) ZnO|CoPc3 NPS 1 µm c) CoPc3 molecule. Bottom: enlarged spectra of the ZnO|CoPc3 NPS sample.

III.3.2 Zinc oxide nanorods arrays (ZNRs)

III.3.2.1 Growth of ZnO nanorods arrays

Among various nanostructures that can be obtained by electrodeposition of ZnO, nanorods are the most investigated. Studies on the influence of the potential of deposition, temperature of the electrolyte and concentration of zinc precursor have been extensively reported.[101,104,105,142,161] Based on these studies, we set the deposition parameters. The deposition of the nanorods arrays was carried out potentiostatically in an aqueous solution containing a low concentration of Zn^{2+} ions. In order to assess the impact of the substrat on the orientation of nanorods three different substrat were used: Glass/FTO, Glass/ZnO:Al deposited by ALD & Glass/ZnO:Al deposited by sputtering.

Typically, a 0.2 mM $ZnCl_2$, 0.1 M KCl aqueous solution was saturated with oxygen for 20 min prior to the deposition and the same gas flow was maintained during all the proces. The working electrode was fixed and the solution was stirred at 800 rpm using a magnetic stirrer. The temperature was maintained at 80°C. The deposition process was stopped when the total required charge was reached. The deposited films were rinsed with water and dried in air at 100°C. When the deposition was made on ZnO:Al substrates, it was carried out potentiostatically at-1.4 V vs SCE, whereas for the FTO substrates the applied potential was -1.0 V vs. SCE.

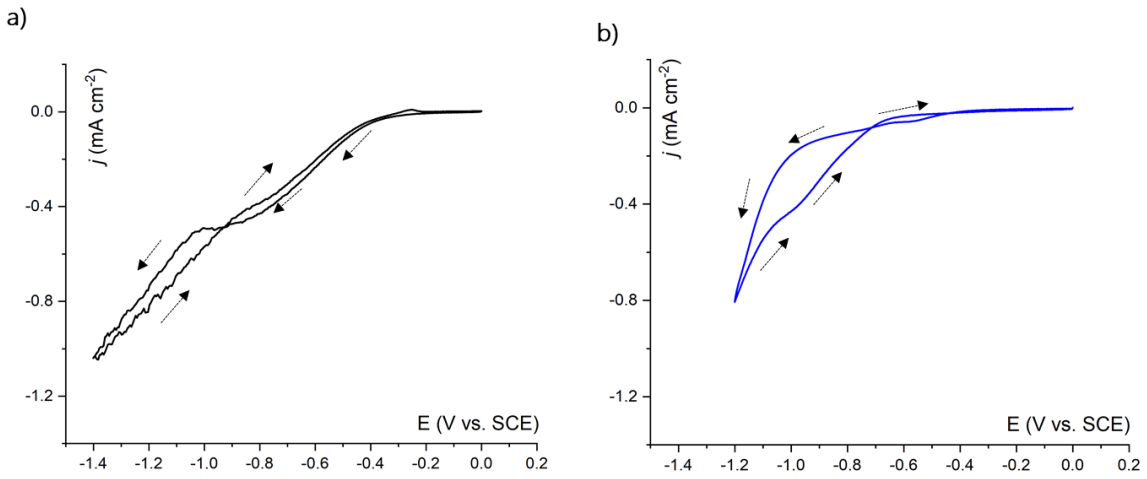

Figure III.11 Cyclic voltammograms of: a) an AZO-ALD electrode and b) a FTO electrode into the ZnO nanorods bath deposition solution. Registered at scan rate 0.1 V s^{-1}. Electrode surface 1 cm^2.

In Figure III.11 a) and b), the forward and reverse scans of AZO (ZnO:Al) and FTO substrates in the deposition bath are reported. In the bath deposition solution for ZnO nanorods (Figure III.11) with a [Zn^{2+}] concentration of 0.2 mM is different compare to the one obtained in the bath for the nanoporous ZnO structure([Zn^{2+}] concentration of 5mM, Figure III.2). In the case of the nanorods' bath, because of a quite low concentration of Zn^{2+} ions, we could not detect the oxidation peak of metallic Zn (around -1.0 V vs SCE). The scan starts at the 0 V and the potential is swept in the cathodic direction. The CV shows an increase of the cathodic current around -0.5 V due to the oxygen reduction. The current density then starts increasing around -0.9 V due to the HER. No peak was detected in the reverse scan.

III.3.2.2 Effect of the substrate on the ZnO nanorods morphology

As mentioned before, three different substrates were used for the growth of nanorods: glass/FTO, glass/Sputtered-AZO, and glass/AZO-deposited by Atomic layer deposition (ALD). The objective is to synthesize tunable ZnO nanorods with a high exposed surface that can be used to improve the catalytic activity of the material by containing more catalytic centers than a flat surface.

It is well known that the crystalline structure of the substrate impact directly the orientation of nanorods. For this thesis, the final purpose of the ZnO nanorods arrays is to be used in the deposition of Hierarchical ZnO 3D structures. Figure III.12 compared the chronoamperometry curve of ZnO nanorod on FTO, sputtered ZnO:Al and ZnO:Al- ALD layers. The current densities appear relatively stable and similar to each other. The current density decreases in the first minutes of deposition before reaching a stable current density around -1,5 $mA.cm^{-2}$ for sputtered ZnO:Al layers and -2$mA.cm^{-2}$ for FTO and AZO-ALD. We can also detect a difference in the current density of the FTO substrate compared to the one shown by the AZO in the first five minutes of deposition: On the AZO substrates, the formation of ZnO nanorods begins quickly while it takes longer on the FTO substrates. As a result, the FTO substrates take longer to reach a steady current value.

The increase of the current density that occurs throughout the deposition is generally attributed to growth of nanowires that increase the developed surface. The current density value of the curve tends to slightly increase on time due to the increase of the surface of the electrode when the nanorods start growing. The deposition parameters

have been chosen in regard to the large literature in this topic. We focused only on the morphologic aspects.

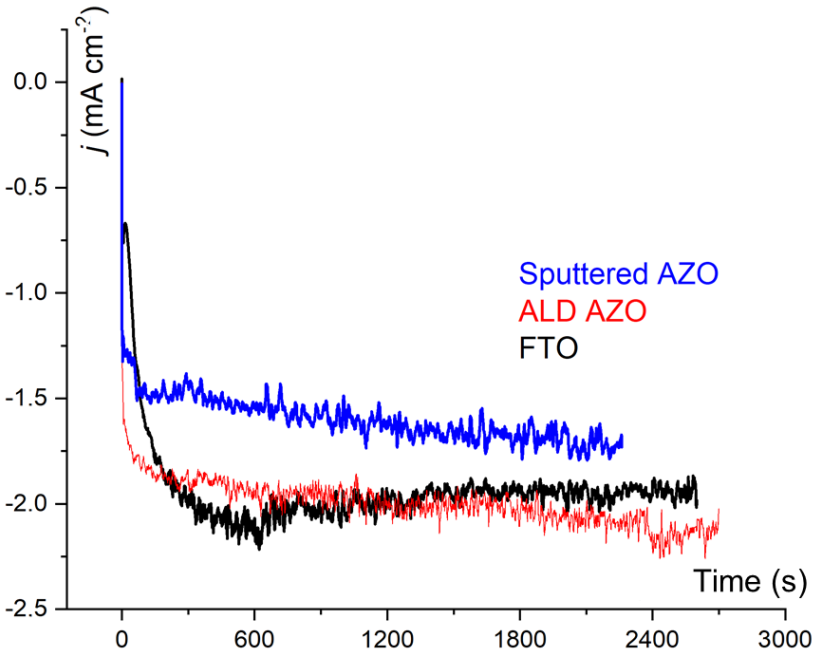

Figure III.12 Comparison of current densities transient curves of ZnO nanorods deposited on FTO, AZO-ALD and Sputtered AZO using an electrochemical bath containing 0.1 M KCl and 0.2 mM $ZnCl_2$ electrolyte at T= 80°C.

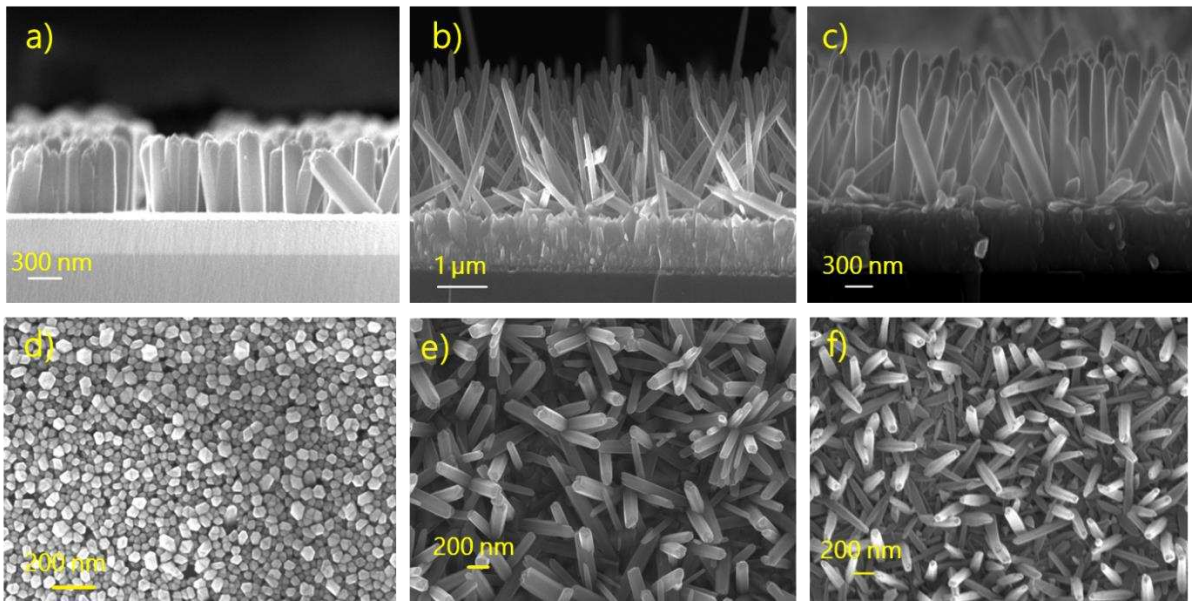

Figure III.13 Cross sectional and top view SEM images of ZnO nanorods deposited at 80°C in 0.1 M KCl for 10 C cm^{-2} at: a,d) AZO sputtered substrate, b,e) FTO and c,f) AZO-ALD. Comparison between the different morphologies obtained as a function of the substrate.

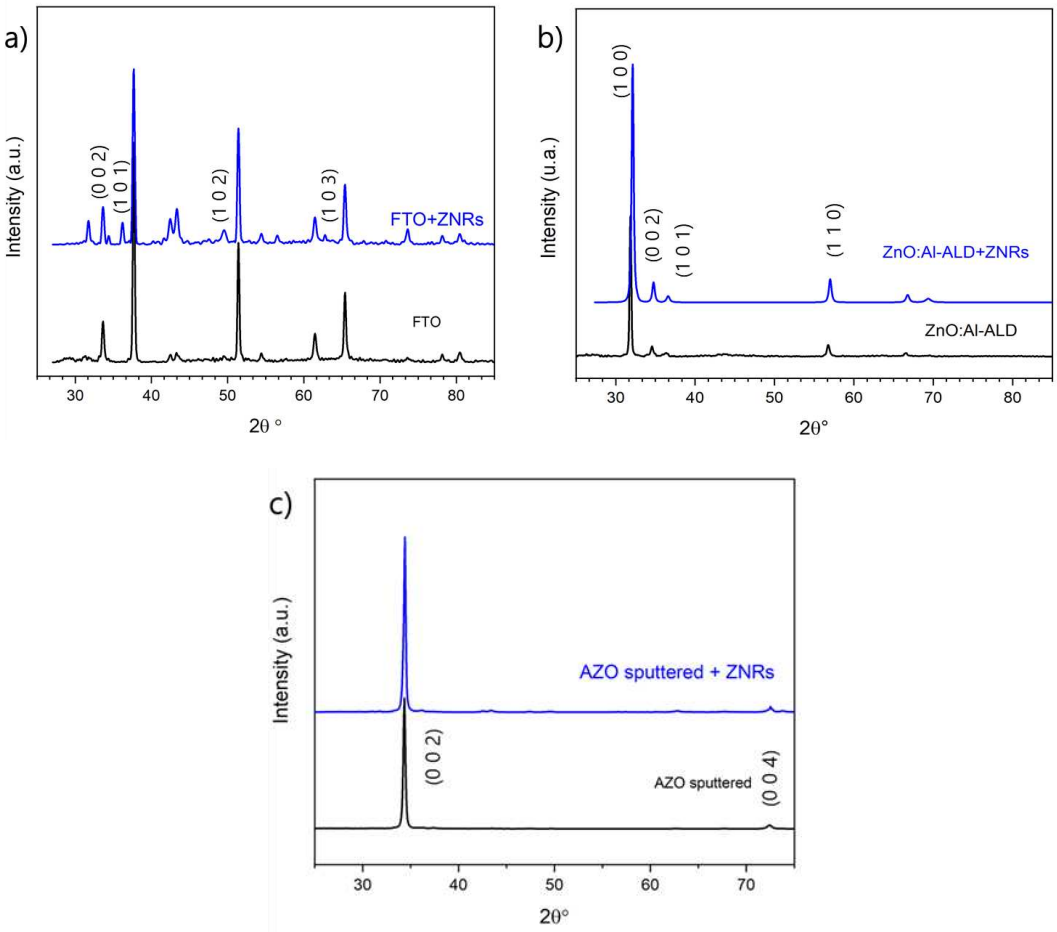

Figure III.14 XRD bragg-brentano patterns of a) FTO substrate b) ZnO:Al – ALD c) ZnO:Al sputtered, before and after the deposition of the nanorods (ZNRs).

Figure III.14 shows large scan XRD diffraction under Bragg–Brentano conditions measurement made on each sample. Depending on the substrate, the ZnO nanorods are differently orientated. The films deposited on sputtered ZnO:Al (Figure III.14.c) show the ZnO structure oriented only along the (002) and (004) directions and no other reflections are visible as for the bare substrate. This is confirmed by SEM images (Figure III. 13 a,d) where the nanorods are highly vertically oriented along the c axis with a diameter of around 60 nm. This is attributed both to a lattice match and a shared crystalline orientation between the film and the substrate.

When the growth of ZnO NRs is carried out on FTO or ZnO:Al-ALD substrates, it results in non-vertically oriented NRs (Figure III. 13.b and 13.c). On FTO substrates the nanorods seems to be randomly orientated as confirmed by the XRD measurements in Figure III.14.a. However, for AZO-ALD substrate, the ZnO nanorods preserve the structure of the substrate with the presence of (100) and (110) peaks (fig. III.14.b). These peaks indicate that for both the substrate and the electrodeposited nanorods the c axis is parallel to the substrate. Moreover, it seems that the density of NRs deposited in this

substrates decreases compared to the density of NRs on sputtered AZO substrates (Figure. III. 13.d and Figure III.I3.f). Nanorods in AZO-ALD are thinner and longer compared to the ones grown in AZO sputtered substrates. These results are in line with previously reported studies.[104]

The impact of the orientation of nanorods on optical properties has also been studied. Nano-structuration of window layers in solar cells can impact the light scattering and thus enhance the absorption of light in thin absorber layers. Since our final goal is to deposit this kind of nanostructures on top of a CIGS solar cell, we have investigated optical properties, as illustrate in Figure III.15.

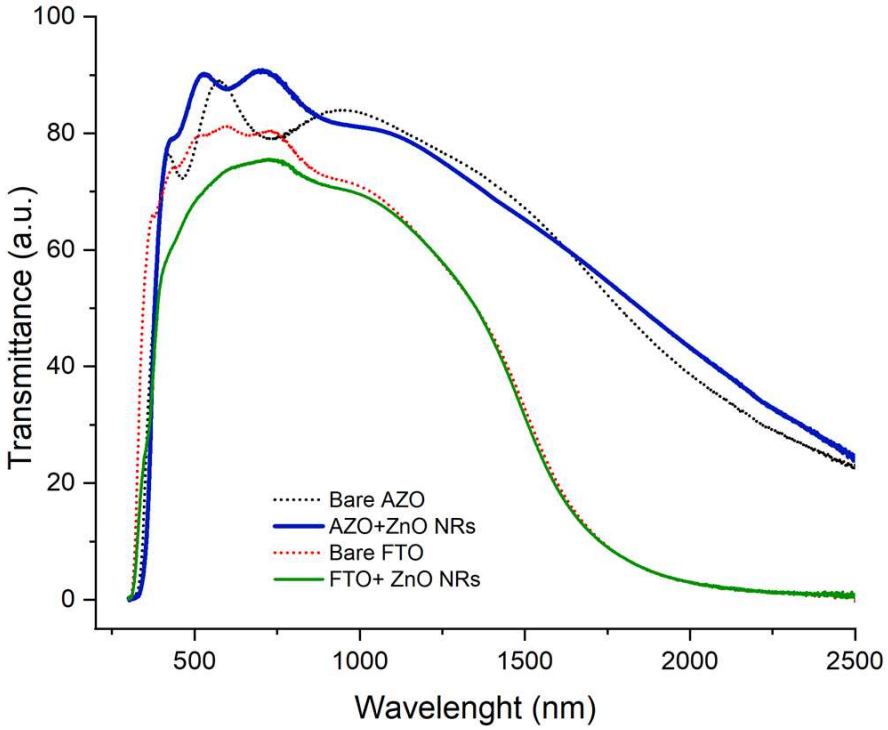

Figure III.15 Transmittance spectra in the UV-Visible and near infrared range for ZnO NRs electrodeposited in AZO and FTO substrates.

Comparison between a bare AZO layer deposited by ALD and ZnO NRs deposited on it shows that after the deposition of the NRs, the transmittance is improved in the visible range mainly between 400 and 800 nm. Decrease of interference fringes on transmission spectra confirms the anti-reflecting effects of nanorods. Anti-reflection coating (ARC) is already widely used as technique to increase the proportion of the

incident light entering in solar cells. It is commonly known that transparent conductive oxides (TCO) nanorods can present high light scattering properties.[104,162]

On the contrary, in the case of the FTO samples, the transmission decreases from ~82% transmission to ~74% in the visible range (between 400 and 800 nm). The reason for this decrease could be the enhanced diffusion in this wavelength range, trapping the light in the nanostructures. These data illustrate the impact of the orientation of nanorods on the optical properties.

III.3.2.3 Controlling the length of the ZnO nanorods (ZNRs)

In this section, we investigate the effect of the transferred charge density on the length and diameters of the nanorod arrays. We show here the result obtained for depositions on AZO-ALD substrates, as illustrate in Figure III.16.

Table III.1 summarizes the evolution of the length and diameter of nanorods as a function of the charge density. The length of the nanorods increases linearly with the charge. It is interesting to note that the charge transferred also slightly impact the diameter of nanorods, which increases from 60 nm for C = 1 C cm^{-2} to 90 nm for C = 10 C cm^{-2}.

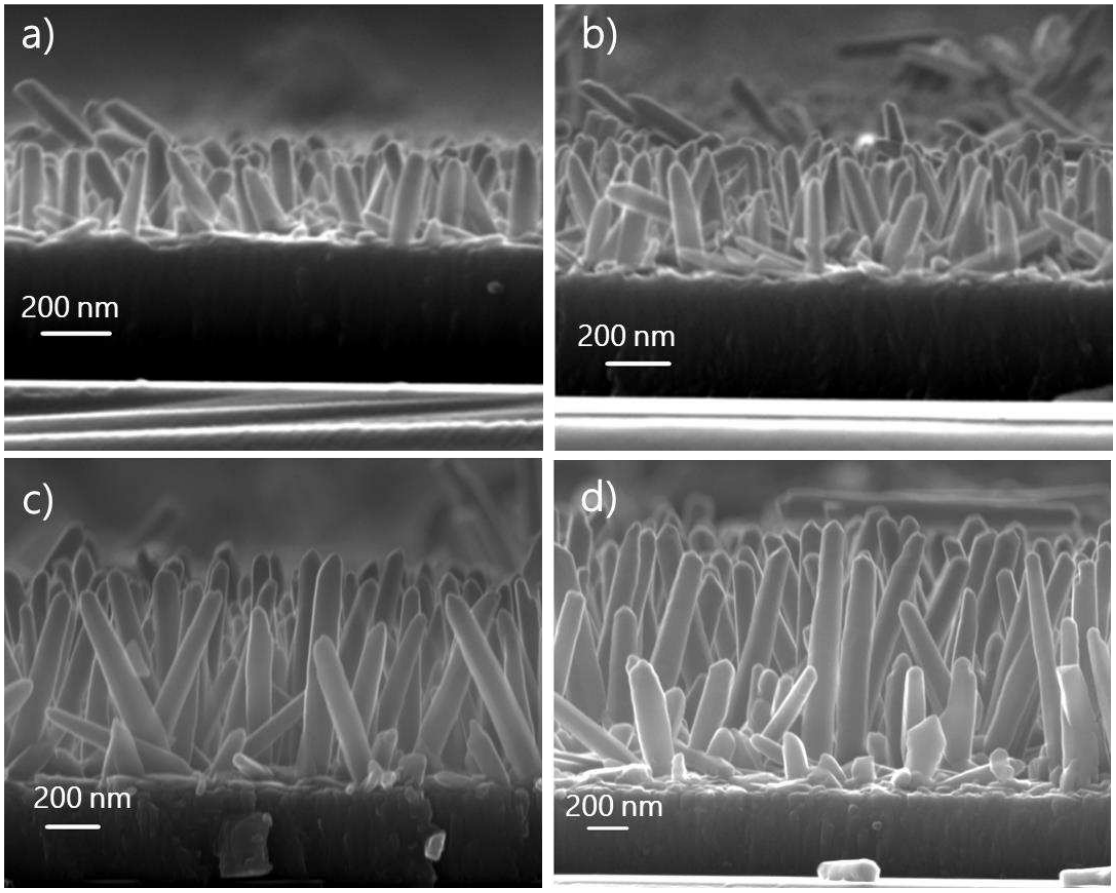

Figure III.16 Cross sectional SEM images of ZnO nanorods deposited at 80°C in 0.1M KCl for a total charge transferred of a) 2.5, b) 3, c) 6 and d) 10 C cm^{-2}.

Table III.1 Geometrical parameters of the ZnO NRs deposited on AZO-ALD substrates

Charge transferred (C cm^{-2})	**Length (nm)**	**Diameter (nm)**
1	150-200	~60
2.5	300-350	~60
3	400-500	~70
5	550-600	~70
6	750-850	~80
10	1200-1300	~80

III.3.3 Hierarchical ZnO 3D structures grown by electrodeposition

III.3.3.1 Building the 3D structures

Hierarchical 3D structures were designed by depositing a nanoporous ZnO|CoPc3 thin layer on a ZnO nanorod network, as shown in Figure III.1.c (see page 81). In this way, we will combine the advantages of both structures. The ZnO nanorods enhance the electronic transport properties and optical properties, while offering a higher active surface. Whereas, adding the hybrid layer containing a catalyst will provide an improvement of the catalytic activity of the electrode towards the CO_2RR.

First an array of metal oxide nanorods is deposited as described in the section III.3.2.1. We have chosen to prepare the 3D structures on ZnO NRs 1 µm, which can offer a high surface area to growth the ZnO|catalyst nanoporous layer. These electrodes were then used as working electrode for the deposition of the NPS layers, following the same procedure as described before in the section III.3.1.1. It led to a structure composed of zinc oxide nanorods surrounded by a nanoporous metal oxide/catalyst layer, obtained by a two-step cathodic electrodeposition.

Figure III.17 displays the current trace vs. time for the two step deposition of the 3D ZnO structures. The first step (Figure III.17.a-black) corresponds to the deposition of the ZNRs. After that, the electrodes with the ZNRs were introduced in the bath containing the molecular catalyst (CoPc3) to carry out the second deposition step (Figure III.17.b-red).

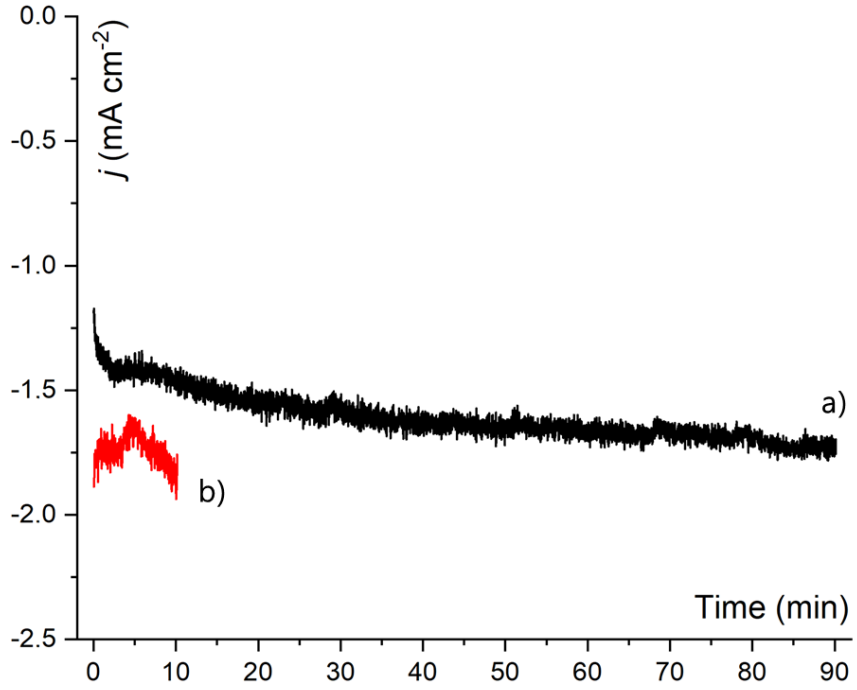

Figure III.17 Chronoamperometry curves during electrodeposition of (a) ZnO nanorods (E = -1.4 V vs. SCE). (b) a thin hybrid ZnO|CoPc3 NPs layer on the ZnO nanorods electrode (E = -1.0 V vs. SCE).

III.3.3.2 Optimization of the 3D structures deposition process

The coating process of the ZnO NRs by a hybrid nanoporous layer (NPS) was further optimized to be able to prepare electrodes that conserve the nanorods structure. While the deposition of ZnO NRs and the dependence of the deposition parameters on their characteristics is a relatively well-known process, only two works report the coating of ZnO NRs with a new electrodeposited layer for the creation of a 3D nanostructured layer.[103,142] In Figure II.18 we present the SEM images obtained from some of the prepared hierarchical ZnO 3D structures.

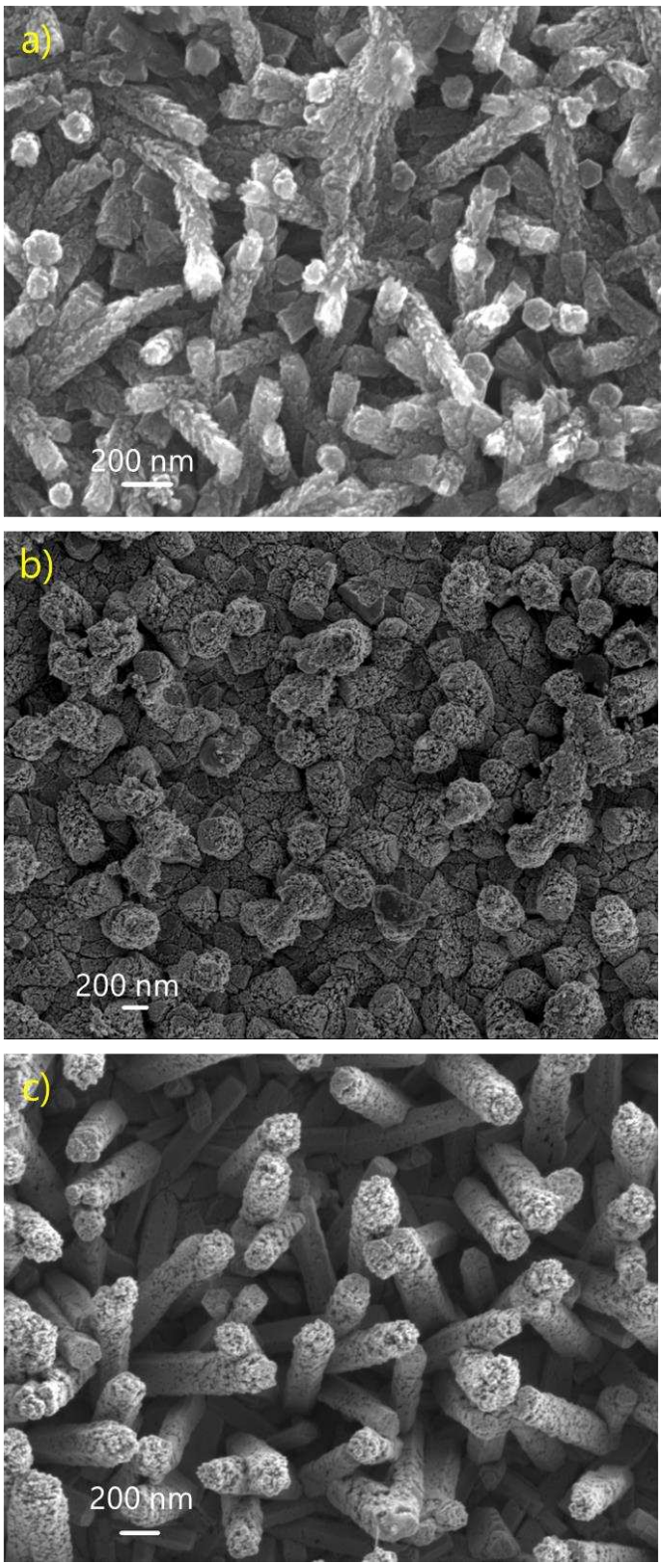

Figure III.18 Top view SEM images of ZNRs deposited on AZO:Al-ALD substrates and covered by a ZnO|CoPc3 NPs layer. Deposition of the NPS layer for different charge densities: a) 0.3, b) 1.0, c) 0.5 C cm^{-2}.

Covering ZnO NRs arrays with NPs layer has been achieved by varying the total charge transferred during the electrodeposition. We show in Figure III.18.a a ZnO NRs electrode that has been covered by a NPs layer with a total charge of 0.3 C cm^{-2} (about 3 minutes). In this case, the deposition of the NPs layer did not lead to complete coverage of the nanorods. The image in Figure III.18-b shows a ZnO NRs electrode that has been covered by a total charge transferred of 1 C cm^{-2} (about 12 minutes). In these conditions too much NPs layer is deposited covering the NRs completely, until almost losing the nanorods structure. Finally, after several experiments we have reached the best deposition parameters to obtain a 3D hierarchical nanostructure in which ZnO nanorods are covered by a very thin ZnO|CoPc3 NPs layer as shown in Figure III.18.c. For that, the charge density should be close to 0.5 C cm^{-2} (about 5 minutes).

III.3.4 Summary

In this work, electrodeposited ZnO is used as a matrix for incorporation of molecular catalysts. Three different nanostructures have been described and prepared. Two of these nanostructured layers have been developed and combined with a molecular catalyst: nanoporous structure (NPS) presenting a sponge-like structure at a nanoscale level, and 3D nano-structure made of a nanoporous ZnO|CoPc3 structure (NPS) grown on zinc oxide nanorods (ZNRs). Figures III.19 & III.20 show the grazing incidence X-ray diffraction (GIXRD) patterns and SEM images of these different nanostructures.

In Figure III.19, we compare the X-ray diffraction patterns (GIXRD) of the atomic layer deposited ZnO:Al substrate with those of a ZnO|CoPc3 nanoporous layer (NPS), pure ZnO nanorods (ZNRs), and a hybrid 3D structure of ZnO nanorods covered by ~20 nm ZnO|CoPc3 nanoporous layer (ZNRs+NPS). For all these layers, the diffraction patterns match the standard diffraction patterns of the hexagonal wurtzite ZnO crystal structure (JCPDS-36-1451).[163]

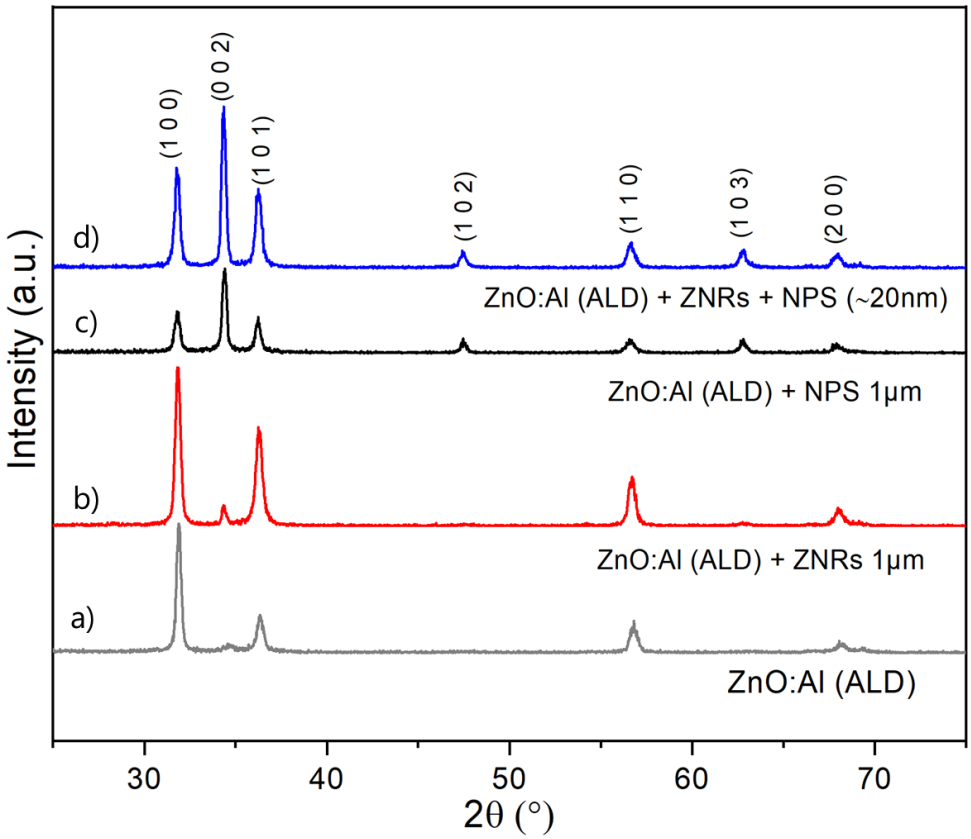

Figure III.19. GIXRD patterns at a glancing-incident angle ω = 3.0°of a) ALD ZnO:Al substrate, b) ZNR 1 µm grown on ALD ZnO:Al substrate, c) NPs ZnO|CoPc3 grown on ALD ZnO:Al substrate and d) ZnO nanorods covered by ZnO|CoPc3 nanoporous layer (ZNRs+NPS)

ALD ZnO:Al layer presents a mixed (100), (101) and (110) orientation indicating that the *c* axis of ZnO is mostly parallel to the substrate (Figure III.19.a). When ZnO NRs are grown on this substrate, it results in non-vertical random oriented NRs as observed on SEM images (Figures III.20.c-d) presenting the same crystalline orientation and diffraction plans than the substrate (Figures III.19.b). In the presence of water soluble CoPc3 catalyst, porous but still crystalline ZnO semiconductor thin films are deposited (Figures III.20.a-b). As observed in SEM images, addition of the molecular catalyst during the growth of ZnO seems to strongly affect the crystal growth mechanism of the ZnO, leading to a significantly higher surface area when compared to pure ZnO films formed without addition of the molecular catalyst.

The comparison of the X-ray diffraction patterns of CoPc3/ZnO nanoporous layer with the ALD ZnO:Al substrate (Figures III.19. a and c respectively) show an increased peak intensity of the (002) planes for the nanoporous layer. This means that the ZnO crystallites tend to be self-oriented with their c-axis being perpendicular with the substrate

plane when the CoPc3 molecule is added to the electrodeposition bath. Such preferential orientation is very often seen for ZnO layers, as the (002) crystal face is the densest and the most stable thermodynamically.

Interestingly, the same preferred orientation is obtained when CoPc3/ZnO is grown on ZnO nanowire hybrid thin film (Figure III.19.d), for which the most intense peak remains the (002). This confirm that, when CoPc3 is added to the deposition bath, nanoporous layers whatever the substrate orientation tends to self-organize with a preferential c-axis orientation along (002) plane. For these layers, SEM pictures show a hierarchical structure composed by a hybrid CoPc3/ZnO coat surrounding the nanorods (Figures III.20.e-f).

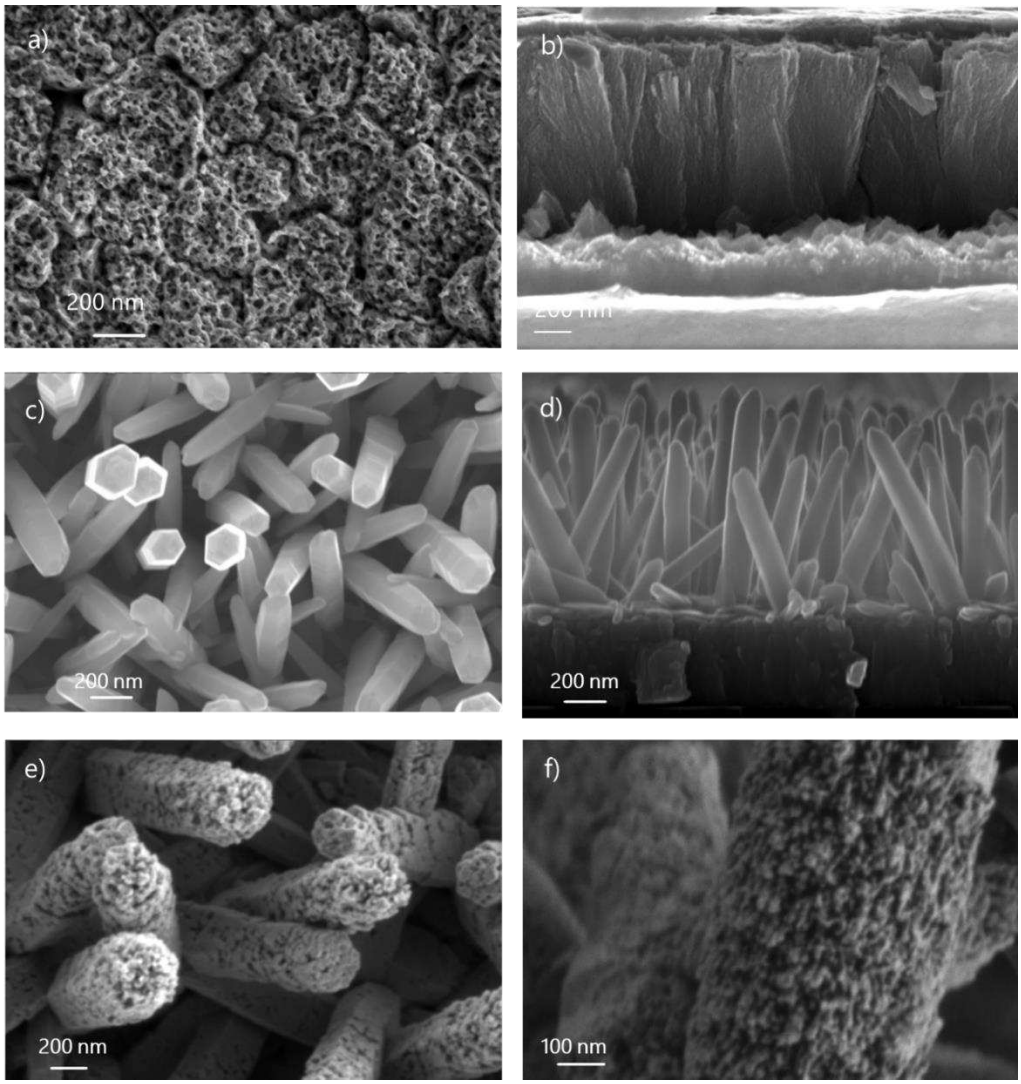

Figure III.20 Top view and cross sectional SEM images of the different ZnO nanostructures presented in this work: a,b) NPS, c,d) ZnO NRs, e,f) ZNRs covered by a thin NPS layer. All layers electrodeposited on ALD-deposited AZO substrate.

In Figure III.21.a, optical transmission curves obtained for these three different ZnO nanostructures are presented and compared to the absorbance of an aqueous solution of the pure CoPc3 molecule (50 µM). In the visible range, the transparency of ZnO nanorods (ZNR) are near 90%. The impact on the total transmission of the incorporation of the CoPc3 molecule into the nanaporous ZnO layers (ZnO NPS) becomes clear between 525 and 1000 nm, with a decrease from ~97% transmission to ~55% between 665 et 700 nm for a ZnO NPS layer 1 µm thick. This decrease in transmittance is clearly related to the CoPc3 incorporated into the ZnO nonporous layers. CoPc3 presents an absorption peak around 665 nm which can explain the reduction of transmission of the nano-porous electrodes down to 53% around this wavelength. The transmission is highly improved (>75%) by using hierarchical structure ZnO (ZNRs+NPS) thanks to the very low amount of catalyst incorporated in the layer.

The concentration of encapsulated CoPc3 within NPS ZnO layers have been measured by ICP. Figure III.21.b shows a linear increase of the CoPc3 concentration into the film from 0.8 to 7.1 nmol cm^{-2}, with an increase of NPS ZnO thickness from 50 to 1000 nm. The absorbance of these layers at 665 nm follows the same linear trend, confirming the incorporation of CoPc3 catalysts inside the nanoporous ZnO layers. Concerning the 3D ZNR (1 µm) + NPS (20 nm) layers, the ICP analysis shows a concentration of around 0.73 nmol cm^{-2} of CoPc3 in the films, ten times less than in the 1 µm thick nano-porous layers.

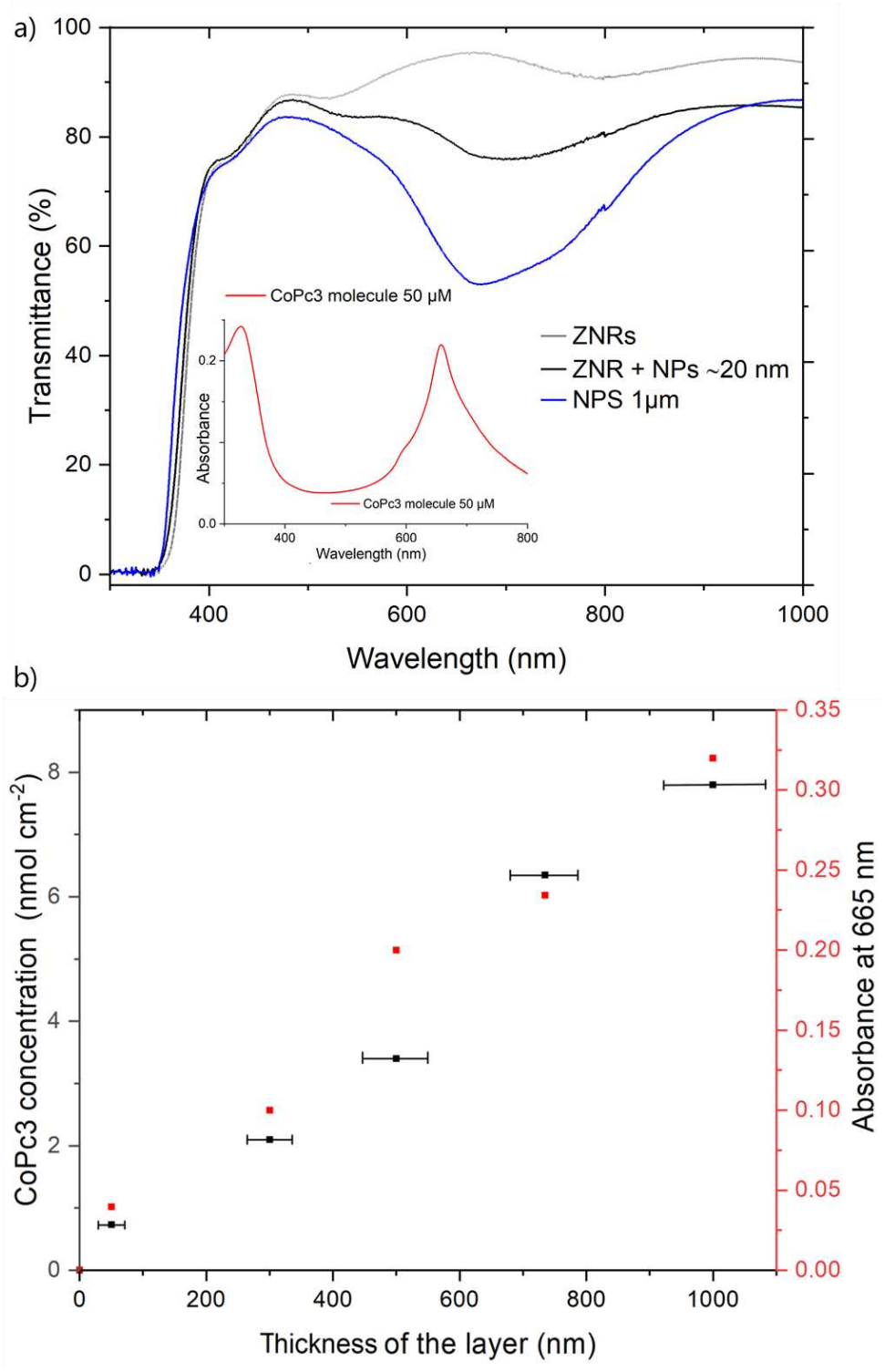

Figure III.21 a) Optical transmission of electrodeposited ZnO NRs, ZnO NPS (1 µm) and ZnO ZNR+NPS (deposited on ALD- ZnO:Al substrate) compared to the absorbance of an aqueous solution CoPc3 50 µM. b) Concentration of CoPc3 molecules in the ZnO NPS layers measured by ICP and absorbance of the same samples at the wavelength of 655 nm as a function of the thickness of the layer.

III.4 Performance of the ZnO nanostructures in the electrochemical CO_2RR

III.4.1 Electrochemical CO_2 reduction using hybrid nanoporous ZnO|catalyst layers (NPS)

The catalytic activity of the ZnO NPS electrodes was first explored by cyclic voltammetry (CV) in a solution acetonitrile (CH_3CN) containing 0.6 M H_2O and 0.1 M tetrabutylammonium hexafluorophosphate ($TBAPF_6$) as support electrolyte saturated, first under Ar and then after CO_2 saturation. Figure III.22 shows the behaviour of an AZO+ZnO|CoPc3 NPS electrode.

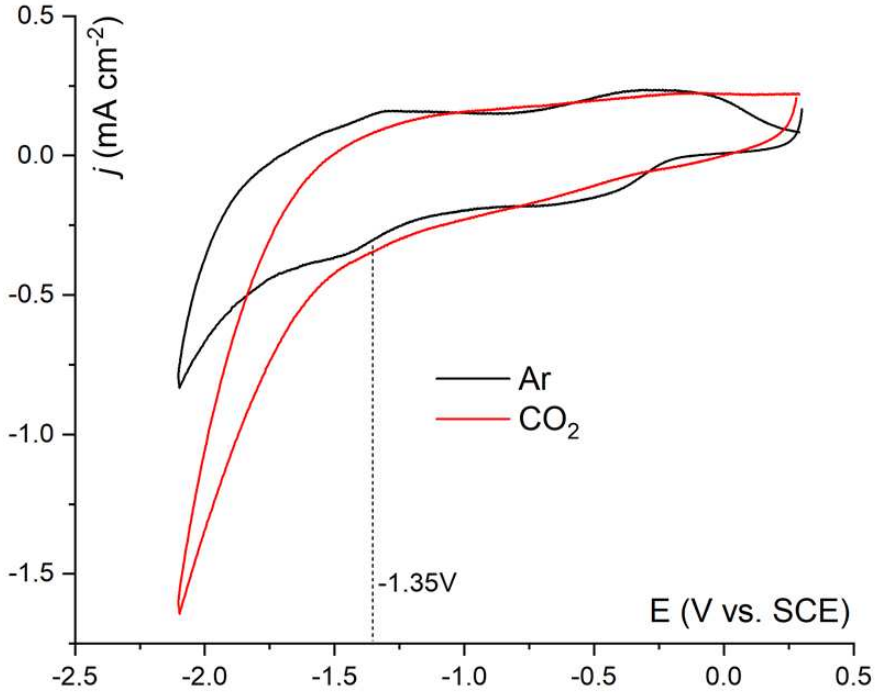

Figure III.22 CVs in CH_3CN solution with 0.1 M TBAPF6 and 0.44 M H_2O with an AZO ALD electrode covered with a ZnO|CoPc3 NPS layer 1 µm thick. Surface of the electrodes 0.5 cm^{-2}. Scan rate: 0.1 V s^{-1}.

CV in the Ar saturated solution shows two reversible peaks around -0.5 and -1.35 V vs SCE. These could be attributed to the reduction of the cobalt metal center of the CoPc3 molecule, passing from Co(II) to Co(I) state. Upon CO_2 saturation a large increase of the current occurs at potentials more negative than −1.5 V vs. SCE. This current can be attributed to the CO_2 reduction, meaning that ZnO|CoPc3 NPS electrodes are electrochemically accessible to the substrate (CO_2) and able to react with it.

III.4.1.1 Enhancing the catalytic response of the electrodes

Addition of Lewis and Brønsted acids has been shown to boost CO_2RR.[147] As an example phenol has been shown to accelerate CO2 protonation and clivage leading to CO formation.[164]

In this study we have used water as a weak Brønsted acid and studied its impact on the performance of the ZnO|CoPc3 NPS electrodes. For that three different concentration of water were used (0.33 M, 0.44 M and 0.67 M). As observed in Figure III.23, the increase of the concentration of H_2O into the acetonitrile solution results in significant current enhancement, and also on lowering the onset potential of the CO_2 reduction reaction, from -1.8 V vs. SCE with 0.33 M H_2O to -1.6 V vs. SCE with 0.67 M H_2O.

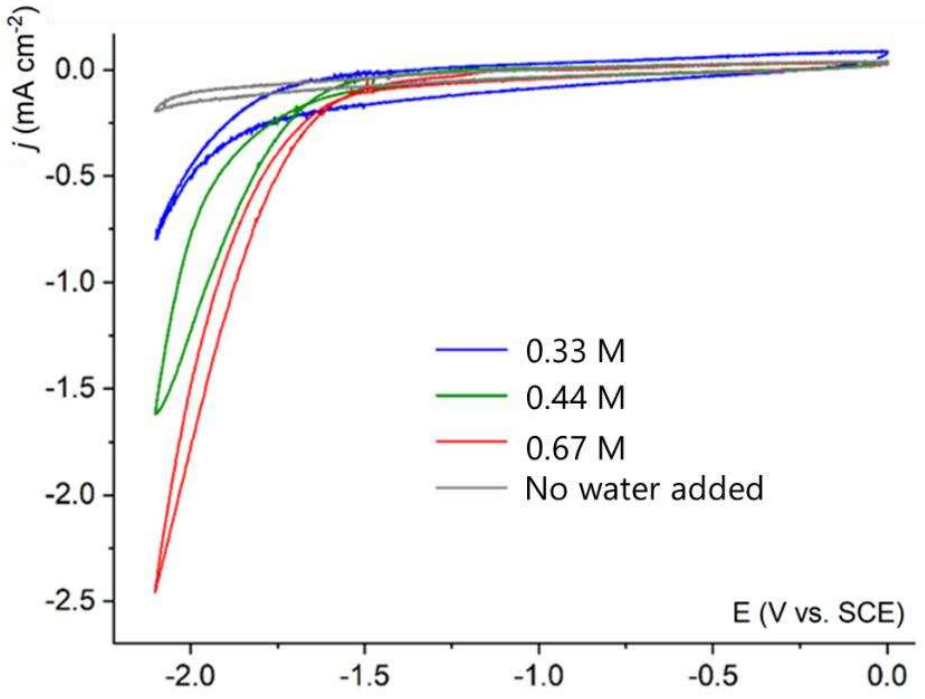

Figure III.23 Cyclic voltammograms of a ZnO|CoPc3 NPS layer (1 µm thick) electrode in CH_3CN solution with 0.1 M $TBAPF_6$, CO_2 saturated. Surface of the electrode: 0.5 cm^{-2}. Scan rate: 0.1 V s^{-1}.

As the highest current density is obtained for a water concentration of 0.67 M. For the experiments that we will show later we will use this water concentration of 0.67 M.

Adding more water (>0.7 M) did not show a considerably impact on the current density reached, instead it has promoted a faster degradation of the photoelectrodes.

The Figure III.24 shows the effect of the thickness of the NPS layers on the electrochemistry response. Increasing the thickness of the NPS layers allows to reach higher current densities: layers of 50 nm, 530 and 1000 nm led to current densities of ca. -0.5, -1.4 and -2.0 mA cm^{-2} respectively. The fact that the current density increases with the layer thickness suggests that it is dependent on the active surface area of the electrode as well as the amount of catalyst into the layers. We can note that in a layer 1 µm thick the current density reached at high negative potential (e.g. -2.1 V vs SCE) is higher than in a 530 nm layer (-1.48 and -2.07 mA cm^{-2}, respectively). However, at less negative potential, e.g. -1.5 V vs SCE, the 1 µm thick layer shows a negligible current density whereas the layer 530 nm thick already provides an important increase in current density. It could be explained by a slow charge transport (high resistivity) through the thick layer that necessitate to apply highly negative potential to efficiently reduce the catalytic centers into their active form.

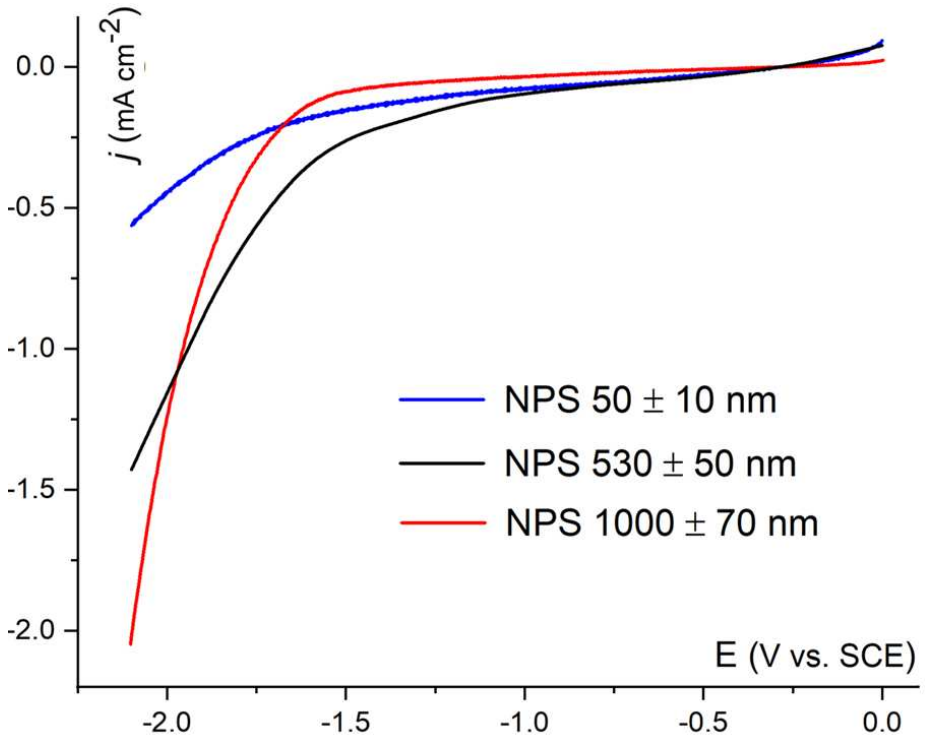

Figure III.24 Linear voltammograms of ZnO|CoPc3 NPS electrodes in CH_3CN solution with 0.1 M $TBAPF_6$ and 0.67 M H_2O, CO_2 saturated. Electrode surface: 0.5 cm^{-2}. Scan rate: 0.1 V s^{-1}.

III.4.1.2 Controlled potential electrolysis of CO_2 using ZnO NPS layers

Controlled potential electrolysis (CPE) experiments were performed using ZnO|CoPc3 NPS electrodes (Figure III.25). It allows us to explore the effect of increasing the thickness of the electrodeposited layer on the catalytic activity and the CO selectivity. Figure III.25 shows the evolution of the current density for CO production during CPE at -2.1 V vs. SCE in CH_3CN solution with 0.1 M $TBAPF_6$ and 0.67 M H_2O, for three different thickesses of ZnO|CoPc3 NPS layers (50 ±10 nm, 530 ±50 nm and 1000 ±70 nm respectively), a pure ZnO nanoporous layer and the CoPc3 molecule in homogeneous conditions. We can notice that the current density increases (in absolute value) with the thickness of the NPS layer, indicating that at least until 1 µm, the CoPc3 molecules incorporated into the ZnO nanoporous matrix are accessible and can react to produce CO. Moreover, these results confirm that the CoPc3 catalyst is well dispersed and distributed throughout the thickness of the layer and not just on the oxide surface. The ZnO|CoPc3 electrodes used in this experiments have shown a good stability for 45 minutes of CPE experiments (Figure III.25 c-d). During the first 10 minutes of CPE the current gradually increases until it reaches a steady-state value staying stable until the end of the experiment. This behaviour could be due to the porosity of our layers, it takes some time for the substrate (CO_2) and co-substrate (protons) to fill and reach all the porosity of the layer, at the beginning just a fraction of the porosity is accessible, then progressively, the CO_2 molecules reach all the catalytic sites accessible into the film. Additionally, charge transport through the film may be also a limiting factor.

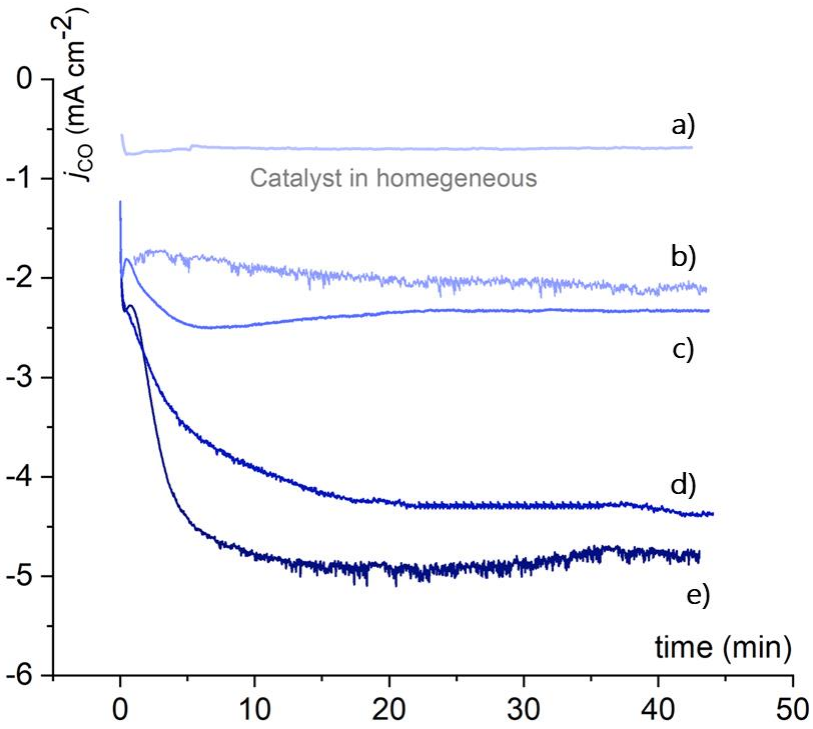

Figure III.25 CPE at -2.1 V vs. SCE in a CO_2 saturated CH_3CN solution with 0.1 M $TBAPF_6$ and 0.67 M H_2O of: a) CoPc3 molecule under homogeneous conditions, at a concentration of 50 mM b) a AZO-ALD/ZnO porous layer without catalyst (1 µm thickness). Compared with AZO-ALD electrodes covered with a ZnO|CoPc3 NPS layer of c) 50±10 nm d) 530±50 nm e) 1000±70 nm.

In Figure III.25.b we show the CPE result obtained using an AZO electrode covered with a layer of pure ZnO nanoporous (1 µm). From this result we can illustrate the property of the ZnO to reduce CO_2 to CO, as mentioned before. However, this ZnO nanoporous layer led to a current density of ca. -2 mA cm^{-2}, whereas, the hybrid ZnO|CoPc3 NPS layer has shown a significantly enhancement of the current density reaching values of ca. -5 mA cm^{-2}. There is thus a huge improvement in the catalytic activity of the electrodeposited oxide layer upon incorporation of the CoPc3 molecule.

The presence of a small amount of molecules into the oxide layers, not only led to an increase of the current density but also significantly improves the selectivity of the reaction. It was confirmed by gas chromatography analysis of the gas products during the CPE experiments, as shown in Table III.3 (see page 117). If we compare entries 2 and 5 of the table, CO selectivity is increased from 73.7% to 98.9%. We can conclude for these results that there is a large contribution in the catalytic activity from the molecular catalyst in synergy with the ZnO matrix which provides a favourable hydrophobic environment to the catalyst. Additionally, the presence of Zn ions in the oxide may

play a role of Lewis acid sites, helping CO_2 binding at the Co centres and weakening also C-O bend which is favourable to cleavage, as demonstrated by Saveant et al., in reduction of CO_2 to CO with Fe(II) porphyrins in the presence of Mg^{2+}.[165] The presence of a hard electrophile such as Mg^{2+} dramatically improves the rate of the reaction.

Besides, entries 3,4 and 6, show that upon increasing the thickness of the layer the current densities increase (in absolute value) from -2.45, to -3.37 and -5.5 mA cm^{-2}. However, looking at the turnover frequency (TOF) we can observe that it decreases when the thickness of the layer increases, meaning that the catalysis occurs faster in oxide thin layers. It may result from both slow charge transport through the oxide layer when the thickness is large and from diffusion limitations of the substrate and protons in the material.

III.4.1.3 Preliminary investigation of NPS layers with different catalyst molecules for EC CO_2 reduction

In addition to the CoPc3 molecule, preliminary experiments were performed with electrodes containing hybrid nanoporous layers of Zinc oxide with two other different molecular catalysts; a Porphyrin Cobalt complex and a Nickel phthalocyanine complex, both bearing sulphonated groups. AZO-ALD electrodes were coated by a NPS layer containing these molecules, following the procedure described in section III.3.1.1. These electrodes were then studied and compared with the ones prepared with the CoPc3 catalysts in EC CO_2 reduction. All the samples compared in this section present a ZnO|catalyst layer 1 µm thick.

The UV-vis transmittance spectra of the prepared electrodes are shown in Figure III.26. NPS layers of ZnO|CoPc3 present an absorbance peak between 600 – 800 nm (Figure III.26.a) with a low transmittance of 60%, while NPS ZnO/NiTSPc sample presents the higher absorbance, especially in the region of 500 – 800 nm (Figure III.26.b) and thus a low transmittance, as low as 20%. Finally, the NPS ZnO/CoTSPP sample present a large peak of absorbance around 400 - 450 nm, with a transmittance close to 10% (Figure III.26.c). These UV-vis spectra indicate the presence of the molecular catalyst in the electrodeposited NPS layers.

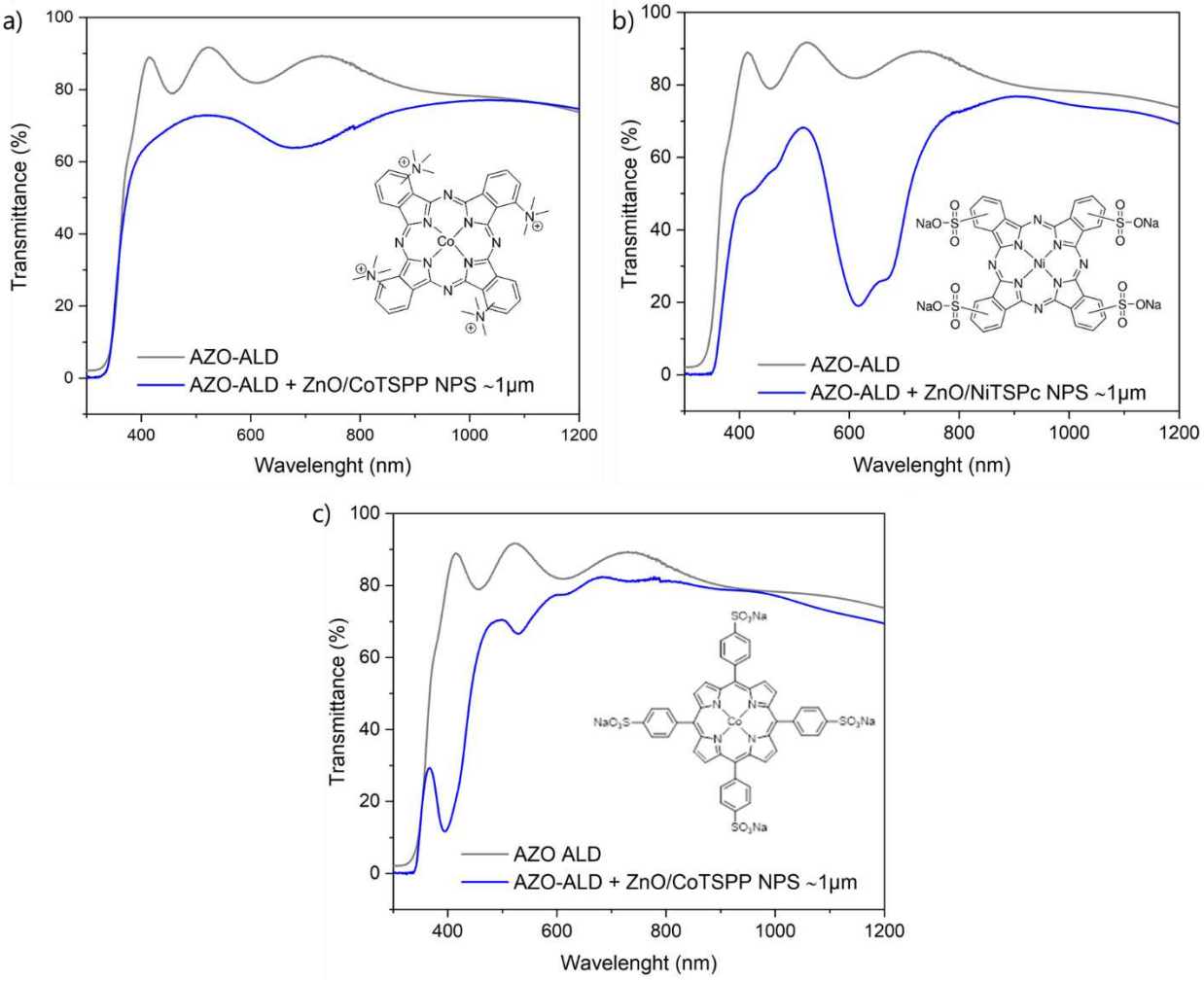

Figure III.26 UV-vis transmittance spectra of ZnO NPS layers (1 µm thick) incorporating a: a) CoPc3, b) NiTSPc, d) CoTSPP. The structure of each catalyst is shown.

Controlled potential electrolysis (CPE) experiments were performed using the presented NPS electrodes (Figure III.27). Remarkably, the current density reached by these electrodes was similar, with mean values of -1.85, -1.75 and -1.71 mA cm^{-2} for ZnO|CoPc3, ZnO|CoTSPP and ZnO|NiTSPP electrodes respectively. Gas chromatography analyses of the gas reaction products were performed for each CPE experiment, in order quantify the selectivity of each catalyst molecule in the CO_2 reduction performance. The results of these analysis are shown in Table III.2. They clearly illustrate the favourable effect of the zinc oxide matrix in providing favourable environment for high selective CO_2 reduction (hydrophobicity, porosity, assistance/synergy thanks to the presence of the Zn ions). It also shows that encapsulation of many type of catalyst could be envisioned, with variation of both the metal and the ligand, opening many possibilities.

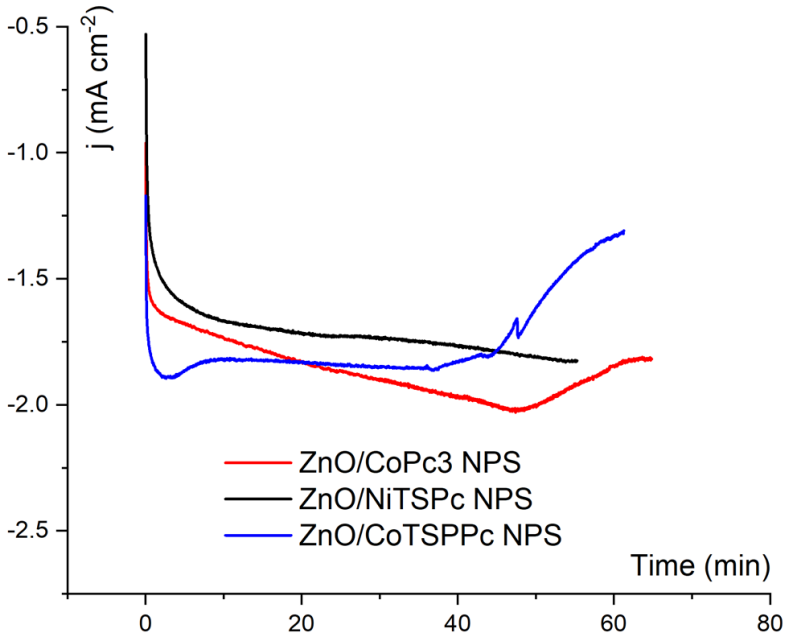

Figure III.27 CPE recorded at -2.1 V vs. SCE in a CO_2 saturated CH_3CN solution with 0.1 M $TBAPF_6$ and 0.44 M H_2O for AZO-ALD electrodes covered with NPS layers (1 µm thick) of: ZnO|CoPc3 (red), ZnO/NiTSPc (black) and ZnO/CoTSPP (blue)

Table III.2 Comparative data of performance of the ZnO nanoporous electrodes with different catalyst during a 60 minutes electrolysis experiments at -2.1 V vs. SCE in CO_2-saturated CH_3CN solution containing 0.1 M $TBAPF_6$ and 0.44 M H_2O.

Sample	Faradaic Efficiency			Selectivity	
	FE CO	FE H_2	FE total	CO	H2
ZnO|NiTSPc	103.0%	3.4%	106.4%	**96.8%**	3.2%
ZnO|CoTSPP	97.1%	3.1%	100.2%	**96.9%**	3.1%
ZnO|CoPc3	95.6%	6.9%	102.6%	**93.3%**	6.7%

A slightly difference in the CO selectivity was obtained. In terms of stability, the electrodes ZnO|NiTSpc and ZnO|CoPc3 have shown a stable current density during the CPE experiments. Whereas the ZnO|CoTSPP electrode has shown an important decrease in the current density (in absolute value) from -1.7 mA cm^{-2} to -1.25 mA cm^{-2} after 40 minutes CPE experiment.

Regarding the UV-vis transmittance characteristics (figure III.26), for NiTSPP electrodes, although having excellent EC CO_2 reduction efficiency, present significant visible-range absorption, making them unattractive for applications in photovoltaic. In contrast with the ZnO|CoTSPP and ZnO|CoPc3 which have shown both a good catalytic response and a high visible light transmittance, making them interesting to be assembled to solar cells.

III.4.2 Catalytic activity of hierarchical ZnO 3D structures (ZnO NRs + NPS) for EC CO_2 reduction

The catalytic activity of the ZnO 3D structures electrodes was explored first by cyclic voltammetry (CV) in CH_3CN solution saturated with Ar and CO_2. Furthermore, controlled potential electrolysis (CPE) experiments were also performed. We show the results of these experiments in Figure III.28.

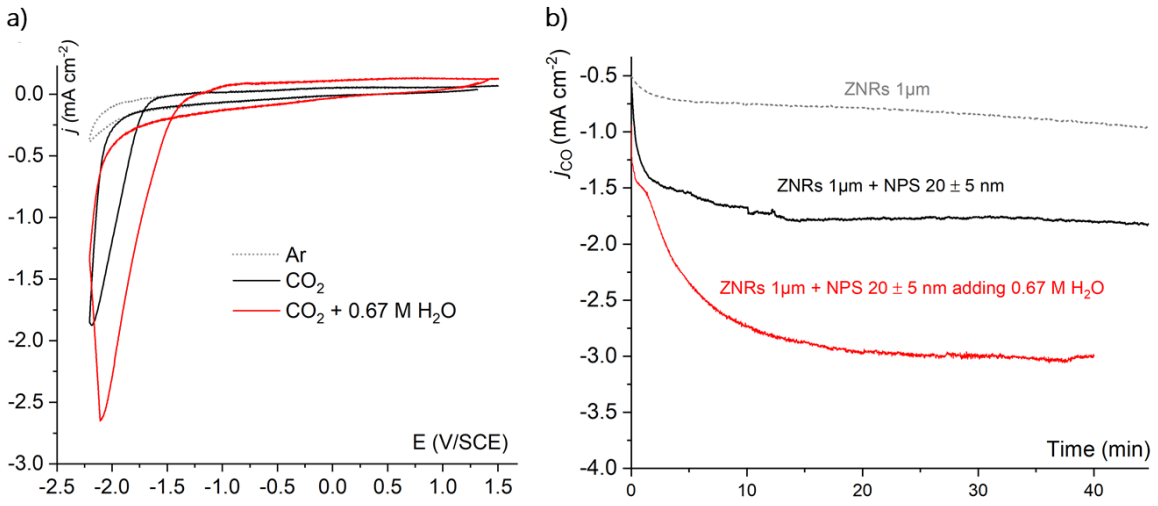

Figure III.28 a) Cyclic voltammograms of 3D nanostructured electrode made by ZNR (1 µm thick) + NPS (20 nm) in CH_3CN solution with 0.1 M $TBAPF_6$. Surface of the electrodes 0.5 cm^{-2}. Scan rate 0.1 V s^{-1}. b) CPE at E = -2.1 V vs. SCE of the same ZNR + NPS electrode, before and after adding water (black and red respectively), compare to a ZNR (1 µm thick) electrode without the NPS layer (grey).

From the CVs in the Figure III.28.a, one can see a large increase of the catalytic current that occurs at potentials more negative than −1.85 V vs. SCE in CO_2 saturated solution.

Furthermore, when water, is added this catalytic wave is enhanced reaching current values as high as -2.5 mA cm^{-2}, similar to the one reached by a ZnO|CoPc3 NPS layer with 1 µm thickness (Figure III.23, page 107), in which we have incorporated a concentration of CoPc3 almost ten times higher than in the 3D structure (7 nmol cm^{-2} vs 0.73 nmol cm^{-2} respectively). Taking advantage of the large surface area provided by the nanorods, we are able to reduce considerably the amount of catalyst while maintaining good catalytic performance. Using a blank ZNRs electrode, without catalyst, electrolysis of CO_2 led to low current densities (ca. 0.8 mA cm^{-2}) and low CO selectivity 73.5 % (Table III.3, entry 6). When the ZNR are covered by a thin ZnO|catalyst layer, forming the 3D hierarchical structure, the electrodes thus show an important enhancement in current density, reaching values of ca. -1.75 mA cm^{-2} (Fig. III.28.b, black line). Furthermore, we can observe a significantly positive effect of adding water as a proton source in the solution. The current density reached is then almost twice higher than without a proton source (-3.0 mA cm^{-2} vs -1.75 mA cm^{-2}) leading to a high selectivity (96%, Table III.3, entry 7). In addition, the 3D structure electrode (ZNR 1 µm thick + NPS 20 nm) used in these experiments have shown a good stability across a 45-minute period of CPE experiment.

III.4.3 Comparison of the CO_2 reduction performance of the ZnO nanostructures

After assessing the catalytic activity in CO_2RR of the two ZnO structures prepared in this work, it is interesting to compare them in order to determine which configuration offers the best performance. Figure III.29 shows the CPE experiments of an electrode with a ZnO|CoPc3 NPS thin layer (50 nm) versus a 3D nanostructured electrode (ZNR 1 µm thick + NPS 20 nm), both containing a close amount of incorporated molecular catalyst, 0.85 nmol cm^{-2} and 0.73 nmol cm^{-2} respectively.

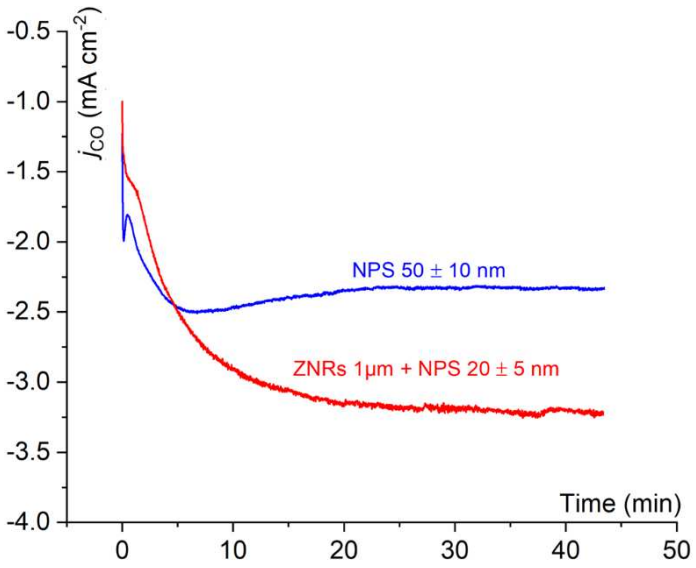

Figure III.29 CPE recorded at -2.1 V vs. SCE in CH_3CN solution with 0.1 M $TBAPF_6$ and 0.67 M H_2O, of a ZnO|CoPc3 NPS layer 50 nm thick electrode (blue) and a ZNR (1 µm thick) + NPS (20 nm) electrode, with close catalyst loading, 0.85 nmol cm^{-2} and 0.73 nmol cm^{-2} respectively.

The current density for CO formation reached with the NPS structure was as high as -2.5 mA cm^{-2} (Fig. III.29, blue line) while the current density with the 3D structure electrode was higher, showing values of ca. -3.4 mA cm^{-2} (Fig. III.29, red line). This last electrode also led to a higher TOF (11.7 s^{-1}) as compare to the NPS structure (7.3 s^{-1}), meaning that the CO production is fast with these two electrodes (table III.3, see page 117). From these results, we can conclude that combining good electronic transport properties and the high exposed surface of the ZnO nanorods with a hybrid layer that presents a catalyst with good intrinsic catalytic activity results in an enhancement of the catalytic performance towards the CO_2RR. However, these results, both, the ones from NPS structures and 3D structures, are in themselves, remarkable despite the high overpotential employed, since electrochemical catalysis of CO_2 reduction with this ZnO hybrid material have not precedent.

III.4.4 Summary of the catalytic CO_2 reduction performance

A summary of the catalytic performance of the different ZnO structures is presented Table III.3. The poor catalytic activity of the CoPc3 in homogeneous conditions (Table III.3, entry 1) reflects high overpotential, low product selectivity, low TON and TOF. It is well know that the cobalt phthalocyanine under homogeneous conditions is not

among the best catalysts so far reported.[166] However, upon incorporation of CoPc3 molecule into ZnO nanoporous structures, a remarkable enhancement of the electro-catalytic activity for CO_2 reduction is obtained, with selective reduction of CO_2 to CO > 95% (entries 3, 4 and 5) in CH_3CN solution. This effect could be attributed to the particular environment created by ZnO porous matrix and the immobilized catalyst that facilitates reaction of CO_2 with the active sites, and to a synergic effect between the catalytic activity of the ZnO and the molecular catalyst, as already noted. We also present the catalytic performance of 3D ZnO nanostructures (entry 6-7). We compare there an electrode with a network of ZnO nanorods (ZNRs), to an electrode based on the same ZNRs covered with a thin ZnO|CoPc3 NPS layer. The results show how the combination of a 3D structure (with very good electronic properties) with the hybrid catalytic NPS layer results in an enhancement of the catalytic performance, using a very small amount of molecular catalyst (<1 nmol).

Table III.3 Comparative data of performance of the different ZnO nanostructures catalytic materials during a 45 minutes electrolysis experiments at a bias potential of -2.1 V vs. SCE in CO_2-saturated CH_3CN solution containing 0.1 M $TBAPF_6$ and 0.67 M H_2O.

Sample	Catalyst amount	Current density (mA cm^{-2})	Total FE	Selectivity		TON	TOF (s^{-1})
				%CO	%H2		
[1]Catalyst in homogeneous conditions	0.5 mM	-0.35	98.1	60.8	39.2	0.93	0.001
[2]Blank ZnO-NPS 1000 nm	0	-2.04	99.0	73.7	26.3	-	-
[3] ZnO|CoPc3 NPS 50 ± 10 nm	0.81 nmol	-2.45	98.6	97.4	2.6	18387	9.6
[4] ZnO|CoPc3 NPS 500 ± 50 nm	1.86 nmol	-3.37	99.6	98.4	1.6	9283	4.9
[5] ZnO|CoPc3 NPS 1000 ± 70 nm	2.80 nmol	-5.0	97.1	98.9	1.1	8280	4.4
[6]ZNRs 1 μm	0	0.75	98.0	73.5	26.5	-	-
[7]ZNRs 1 μm + NPS 20 nm	0.75 nmol	-2.90	91.0	96.7	3.3	22242	11.7

III.5 Conclusions

In this chapter, we have designed and optimized hybrid zinc oxide electrodes incorporating a molecular catalyst. These electrodes present a significant visible light transmission, enabling their application in photovoltaics devices. Our strategy allows to incorporate a very low amount of molecular catalyst into the electrodes, leading to high catalytic activity towards CO_2 reduction. Moreover, it was shown that it is easy to change the molecular catalysts and incorporate different catalysts as soon as these latest are soluble in the electrochemical bath used for the electrodeposition of the hybrid ZnO NPS layers.

Different ZnO structures were presented as well as their characterizations and performance for electrochemical CO_2 reduction. The incorporation of the molecular catalysts was demonstrated by different techniques (UV-vis, ICP, XPS). The accessibility and catalytic activity of the electrodeposited layers was confirmed by the CPE experiments. The hybrid structures presented in this manuscript have shown a high CO selectivity (>90%) and reached high current densities for CO_2 reduction in an organic solvent, values from -2.4 mA cm^{-2} up to large current densities ca. -5.0 mA cm^{-2}, obtained after a series of optimizations of the electrodes.

Chapter IV

Hybrid ZnO nanoporous structures assembled at CIGS photoelectrodes – PEC CO_2 reduction

IV Hybrid ZnO nanoporous structures assembled at CIGS photoelectrodes – PEC CO_2 reduction

IV.1 Introduction

Encouraged by the good results obtained in the EC CO_2RR experiments with the hybrid ZnO|CoPc3 structures, and aiming to create a highly efficient and selective photoelectrode for PEC CO_2 reduction, we have used CIGS solar cell photoelectrodes as substrate to grow these hybrid catalytic layers. As described in chapter I, CIGS solar cells possess a ZnO:Al window layer as front contact, this latter can be modified by electrochemistry using the strategy presented in chapter III, resulting in the addition of a catalytic activity to the CIGS photoelectrode.

In this chapter, we present the process of incorporation of the hybrid ZnO catalytic active layer on a CIGS cell by electrodeposition, creating a photoelectrode with a catalytic activity towards CO_2RR. We will describe and present the light assisted electrochemical process used to growth the catalytic layer on the photoelectrode and their structural and photovoltaics characterization. Then, we will present and discuss the results obtained by using this modified CIGS photoelectrodes in a PEC system to reduce CO_2 to CO. The impact of different experimental conditions on the photo-electrocatalytic performances of the system will be also discussed in this chapter. The best results obtained so far will be shown, discussed and compared with the state-of-the-art.

IV.2 Light-assisted electrodeposition of ZnO layers on CIGS cells

In the previous chapter, hybrid nanostructures were grown by co-electrodepositing ZnO and a water soluble molecular catalyst. In the case of a semiconductor based material, as the CIGS, the growth of the layer is achieved by photoelectrochemistry, that means, including interactions between semiconductors and light in an electrochemical system.

In a CIGS cell, the p-type semiconductor CIGS and the n-type semiconductor CdS in contact form a *p-n* junction as described in chapter I. This assembly is photo-sensitive and constitutes the heart of the solar cell. When a CIGS photoelectrode is dipped into

the electrolyte solution, the electrochemical potential (E_F) is not uniform across the surface. Electron flow will occur at the semiconductor−electrolyte interface to minimize the difference in the Gibbs free energy of the two different phases, that flow of charge causes a band bending within the semiconductor. The net result is that $E_F = E_{F\ redox}$. Since the whole system is at in equilibrium, then the Fermi level must be constant throughout the electrolyte and the photoelectrode. Upon illumination, the populations of electrons in both the conduction band and valence band are altered; this phenomenon is illustrated in Figure IV.1. Incoming photons will generate electron-hole pairs in the CIGS, with electrons in the conduction band and holes in the valence band. The direction of the electric field across the *p–n* junction interface, between CIGS/CdS (inside the CIGS cell) is such that electrons are swept away from the p-type absorber to the *n-type* buffer layer and transported through the n-type ZnO to the surface. Electrons arriving at the photoelectrode-electrolyte interface are consumed in the electrochemical reactions of ZnO formation, and the growth of the ZnO nanoporous layers starts.

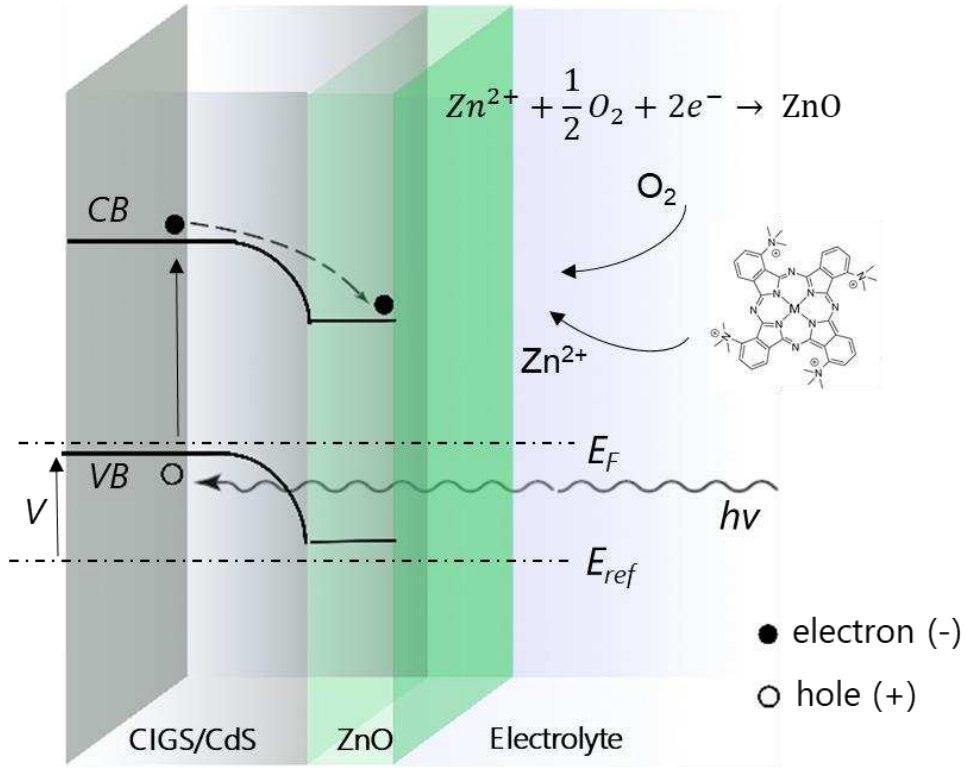

Figure IV.1 Schematic representation of the light-assisted electrodeposition of the zinc oxide nanoporous layers (NPS) on CIGS cells electrodes. An incident photon generates an electron-hole pair and the applied potential drives the electrons towards the CIGS surface, where ZnO is formed.

The ZnO NPS structure is electrodeposited under the conditions described in Chapter III (aqueous solution containing 5.0 mM $ZnCl_2$, 0.1 M KCl and 50 µM of the water soluble molecular catalyst), under illumination. Hence, adding the effect of the light, hybrid ZnO|CoPc3 layer grows on top of CIGS solar cell, adding to this last a high catalytic activity for CO_2RR.

IV.2.1 Incorporation of Hybrid ZnO nanoporous layers on a CIGS photoelectrode

The light assisted electrodeposition of the zinc oxide/catalyst hybrid layers was carried out potentiostatically at -0.5 V vs SCE in an aqueous solution containing 5.0 mM $ZnCl_2$, 0.1 M KCl and 50 µM of the water soluble Cobalt phthalocyanine molecule (CoPc3). Irradiation was simulated with a 150-W xenon lamp from Oriel Instrument, using a light power of 100 mW cm^{-2}. The procedure followed for the electrodepositions is the same as described in chapter III. In this case, a potential of -0.5 V vs. SCE is applied. This latter is less negative that the one used in chapter III (-1.0 V vs. SCE). The difference is due to the photovoltage generated in the CIGS cell under illumination.

The effect of the total charge transferred during the photoelectrodeposition on the thickness of the layers was investigated. By varying the deposition time and the total charge transferred, several thicknesses were obtained.

IV.3 Characterizations of the modified CIGS photoelectrodes

IV.3.1 Material characterizations

Photo-electrodeposited ZnO|CoPc3 NPS with sponge-like structure at a nanoscale level, incorporating the CoPc3 molecular catalyst were grown on CIGS photoelectrodes. Figure IV.2 shows a typical SEM image of one of the prepared photoelectrodes in which we can differentiate each layer of the CIGS solar cell as well as the electrodeposited hybrid nanoporous layer.

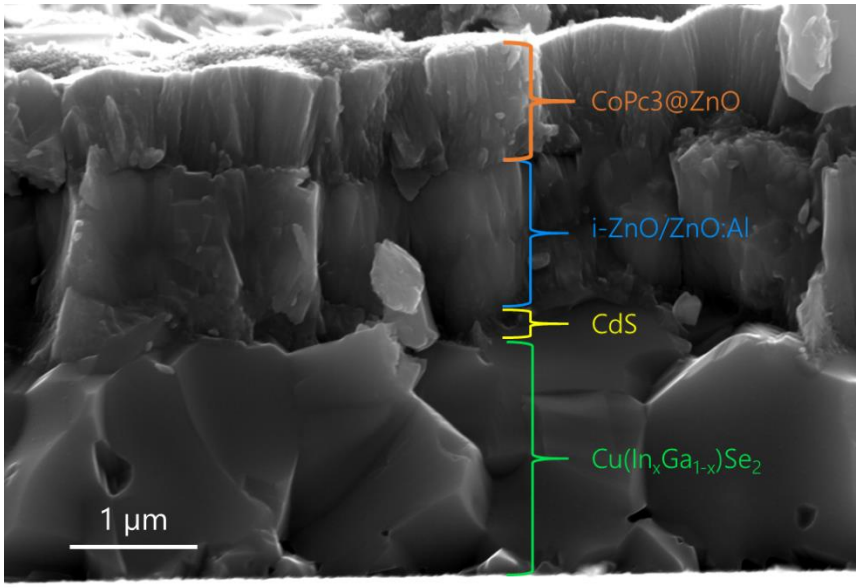

Figure IV.2 Cross-sectional SEM image of a modified CIGS/CdS/ZnO/AZO photoelectrode, showing a nanoporous hybrid layer ZnO|CoPc3 (NPS) grown on top of the solar cell by phototoelectrodeposition.

In order to verify if this layer possess a nanoporous structure similar to the one obtained with the electrodeposited layer shown in chapter III, SEM images from the surface of an AZO+ZnO|CoPc3 electrode were compared with a CIGS/CdS/ZnO/AZO+ZnO|CoPc3 photoelectrode in Figure IV.3.

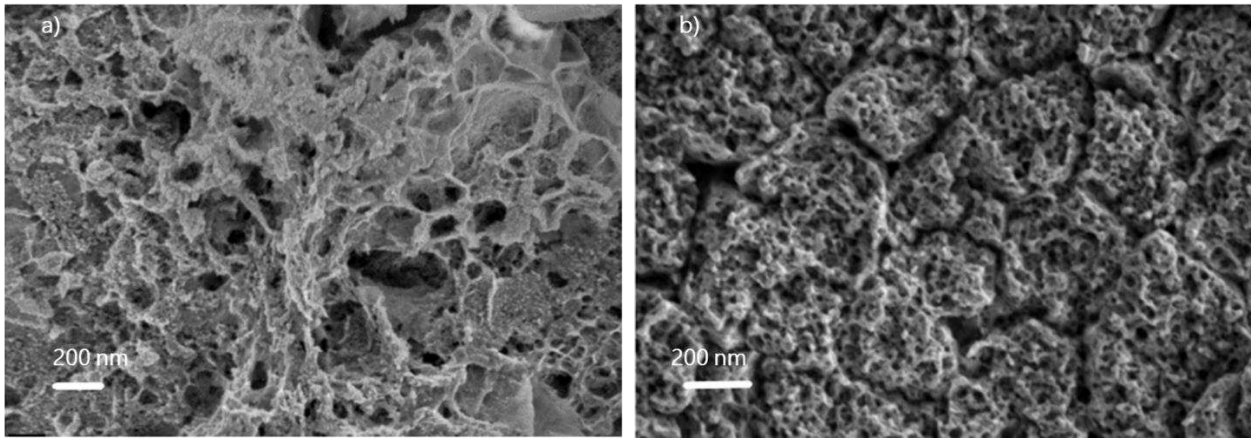

Figure IV.3 SEM image of the surface of: a) a modified CIGS/CdS/ZnO/AZO+ZnO|CoPc3 photoelectrode. b) an AZO+ZnO|CoPc3 electrode.

From the images above, we can notice that a nanoporous layer is also formed when the ZnO|CoPc3 NPS layer are grown on CIGS photoelectrodes.

The effect of the charge transferred during the light-assisted electrodeposition on the thickness of the electrodeposited layers as well as the concentration of catalyst was then studied. Figure IV.4 shows cross section SEM images of several CIGS photoelectrodes with ZnO|CoPc3 NPS layer on top, where the charge transferred was varied between 0.5 and 4.0 C cm^{-2} giving layers with thickness between 0.3 µm to 1.2 µm. The ICP results are shown and compare with the thickness of the layers as a function of charge transferred in Figure IV.5. As observed in Figures IV.4 and IV.5, the thickness of the electrodeposited layer is almost linearly increasing when the charge transferred increases. This allows us to have a precise control of the thickness.

Moreover, ICP analyses carried out on these samples show that the amount of molecules encapsulated into the layer depends also on the transferred charge. The concentration of the CoPc3 molecule also varies linearly upon increasing the thickness of the nanoporous layers. Such behavior allows us to control the quantity of catalyst that we aim to incorporate in our electrodes.

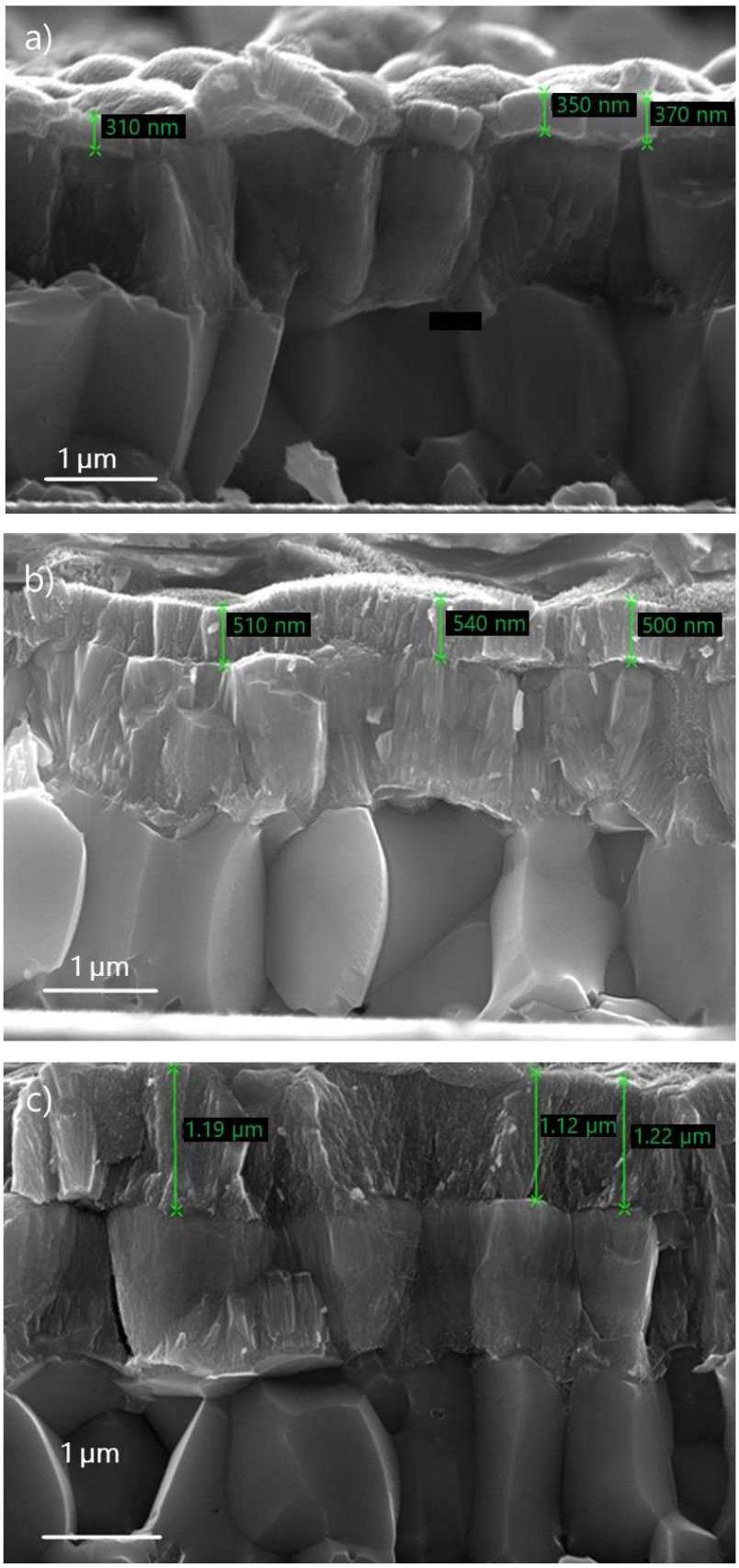

Figure IV.4 Cross sectional SEM images of the modified CIGS/CdS/ZnO/AZO electrodes upon adding a ZnO|CoPc3 NP layers. Photoelectrodes show the different thickness of the NPS layer obtained by variation of the charge transferred a) 0.5 b) 1.0 c) 4.0 C cm^{-2}.

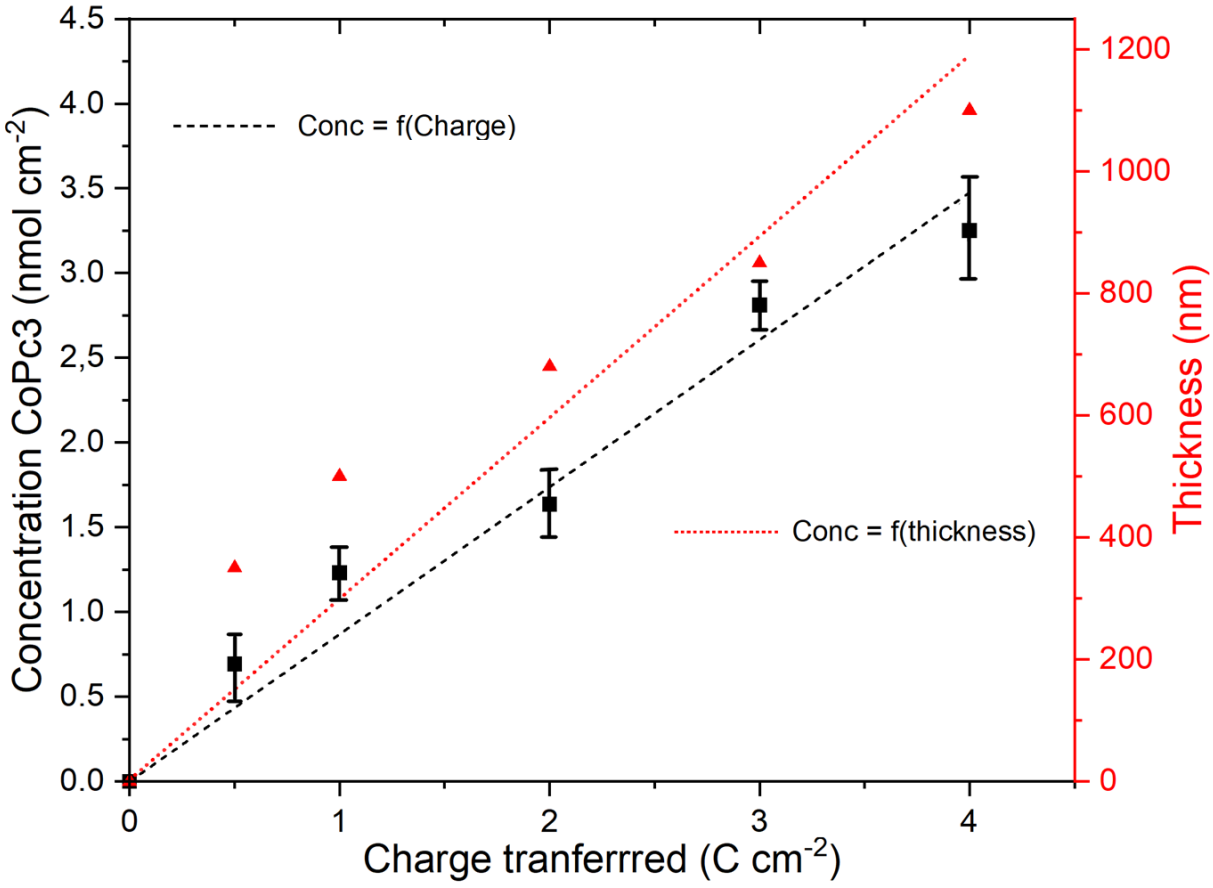

Figure IV.5 Concentration of the CoPc3 molecule into the ZnO|CoPc3 NPS films calculated from ICP analysis. Thickness of the deposited ZnO|CoPc3 NPS layers measured from the SEM images.

The films deposited on CIGS electrodes can incorporate a very small quantity of the CoPc3 molecule, as the concentrations found into the film are in the order of nano-moles per square centimeter (between 0.5 and 3.7 nmol cm^{-2}). This concentration remains in the same range that the ones found in the ZnO NPS films described in chapter III. Catalyst amount changes linearly with respect to the thickness of the deposited layer. The concentration of catalyst into the films shown here can be compared with the concentration of some photoelectrodes reported in the literature in which a molecular catalyst is incorporated to the photoelectrode by covalent immobilization on the surface by the mean of anchoring groups. For a NPS layer 800 nm thick, after catalyst dissolution, ICP–OES measurements indicate a catalyst loading of 3.2 ± 0.5 nmol cm^{-2}. This concentration is comparable with previously reported data on a CIGS photoelectrode of 3 ± 1 nmol cm^{-2} for a cobalt quaterpyridine complex with phosphonic acid anchoring group (CIGS photoelectrode covered by a TiO_2 layer).[29] However, these

concentration values are lower than previously reported data 24 ± 2 nmol cm^{-2} for a cobalt phthalocyanine bearing phosphonic acid anchoring groups on a mesoporous TiO_2 layer deposited on a p-type silicon (Si) photoelectrode.[26]

IV.3.2 Photovoltaic characterizations

The impact of the thickness of the hybrid ZnO|CoPc3 layer at the surface of the CIGS solar cells was investigated by measuring their current-voltage characteristics under an illumination of 1 sun (1000 Wm^{-2} AM 1.5 G). The best values of efficiency, fill factor, open circuit voltage V_{OC} and short circuit current density J_{SC} recorded after J-V measurements are reported in table IV.1. The Figure IV.6 shows the J-V curves of the samples modified by a ZnO|CoPc3 layer compared with a non-modified CIGS cell.

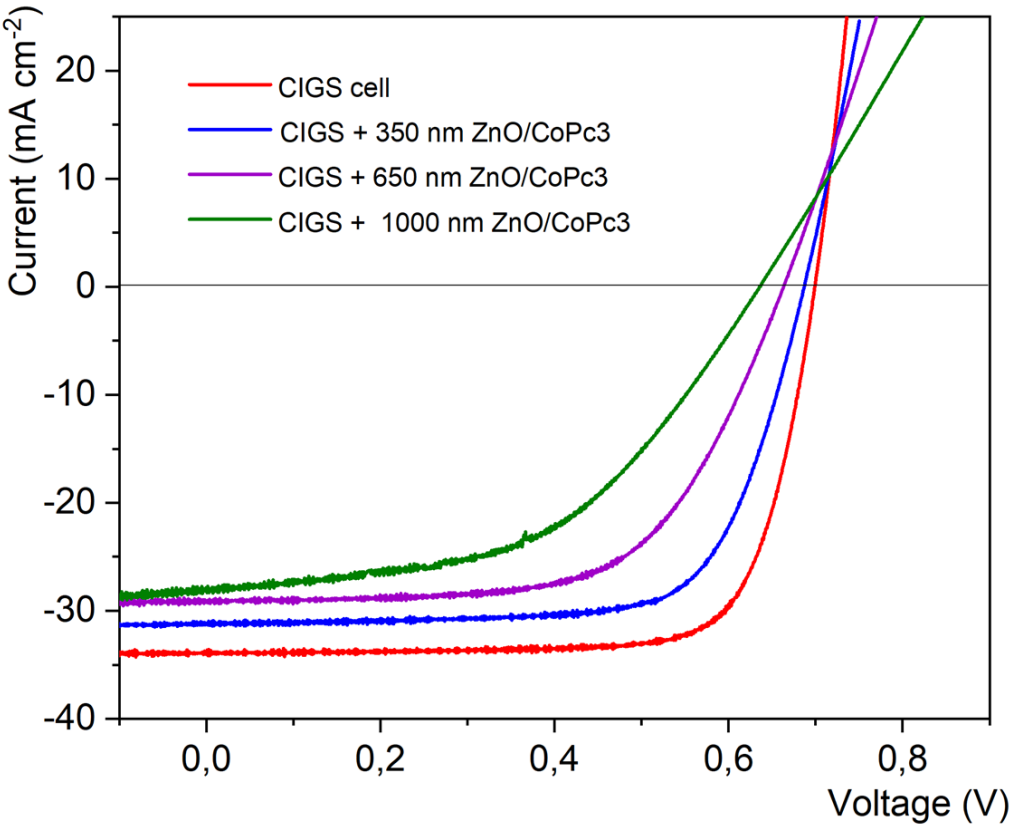

Figure IV.6 Comparison of J-V characteristics for CIGS cells covered with ZnO|CoPc3 NPS layers of different thicknesses.

Table IV.1 J-V parameters of the modified CIGS cells.

Sample	J_{sc} (mA cm^{-2})	V_{oc} (mV)	FF (%)	η (%)
CIGS cell	33.9	698	75	17.8
CIGS + ZnO|CoPc3 350 nm	31.4	685	71	15.8
CIGS + ZnO|CoPc3 600 nm	29.3	663	67	12.1
CIGS + ZnO|CoPc3 1000 nm	27.2	633	67	9.0

The increase of the thickness of the hybrid layer affects all the parameters of the CIGS solar cell. With the increase of the thickness of the ZnO|CoPc3 layers up to 1000 nm the J_{SC} of the layer decreases from 33.9 mA.cm^{-2} to 27.2 mA.cm^{-2}, the fill factor from 75% to 67% and the V_{OC} from 698 mV to 633 mV. Thus while the non-modified CIGS cell present an efficiency of 17.8% the modified CIGS cells present an efficiency of 15.8, 12.1 and 9.0 % when the ZnO|CoPc3 NPS layers thicknesses are 350, 600 or 1000 nm respectively. The decrease of the J_{SC} could be mainly due to the decrease of the transmission of these nanoporous layers in the visible range of wavelength as we have observed in Chapter III (see section III.3.1.4, page 86).

To confirm this hypothesis, EQE measurements have been also performed on these samples and reported in Figure IV.7. In these measurements we can observe that the modified samples show a deeper loss in the visible wavelength part of the EQE curve with the increase of the thickness of the nanoporous layers. In fact, when the thickness of nanoporous layers increases from 300 nm to 1000 nm, the EQE decreases in the wavelength region of incident photons with energies between 550 and 850 nm. That corresponds to the CoPc3 absorbance region (Figure III.7, chapter III section 3.1.4) with a peak around 665 nm, which can explain the reduction of the number of electrons produced in this wavelength region.

From these results, we can conclude that the added nanoporous layers present an absorbance that can become important if the layer becomes too thick, preventing photons to pass through it and go to the CIGS absorber, leading to the decrease of J_{SC}.

Besides, adding a new layer to the CIGS stack add a new interface that generates losses in electron transport and facilitates recombination. In addition, since the hybrid layer

can incorporate some CoPc3 molecules, it results in an increase of the resistance of the window layer, affecting the FF and efficiency of the cell.

As a result, a compromise must be found in order to maintain both the layers' high catalytic effect and the solar cell's good performance. The added hybrid layer must be thin enough to allow light to pass through it without exhibiting significant absorbance, but it must also contain a sufficient amount of catalyst to confer catalytic activity to the device. These results lead to the conclusion that the hybrid layer added to the solar cell must be thin, less than 350 nm, to avoid a considerable decrease in efficiency while maintaining the catalytic properties.

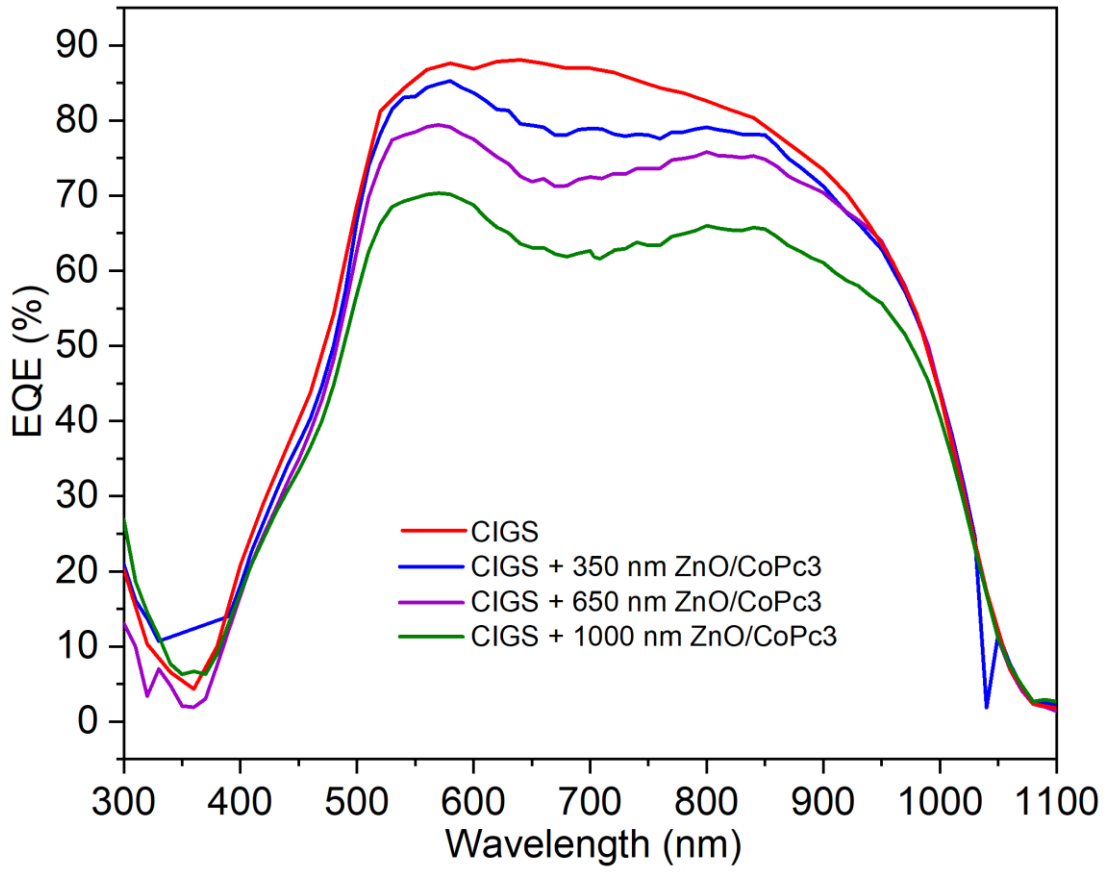

Figure IV.7 EQE response of the modified cells, compare with a non-modified CIGS cell.

Following several studies and tests, we selected ZnO|CoPc3 layers with 350 nm in all the next experiments, in order to obtain CIGS devices capable of performing PEC CO_2 reduction at a high photovoltaic efficiency.

IV.4 PEC CO_2 reduction using modified CIGS cells

In this section we investigate the photoelectrochemical characterizations and the PEC CO_2 reduction results obtained by a system in which a multilayer device based on Cu(In,Ga)Se_2 (CIGS) and a cobalt phathalocyanine catalyst (Figure IV.8) was used as photocathode, demonstrating photoelectrocatalytic activity with high selectivity for CO_2 reduction to CO.

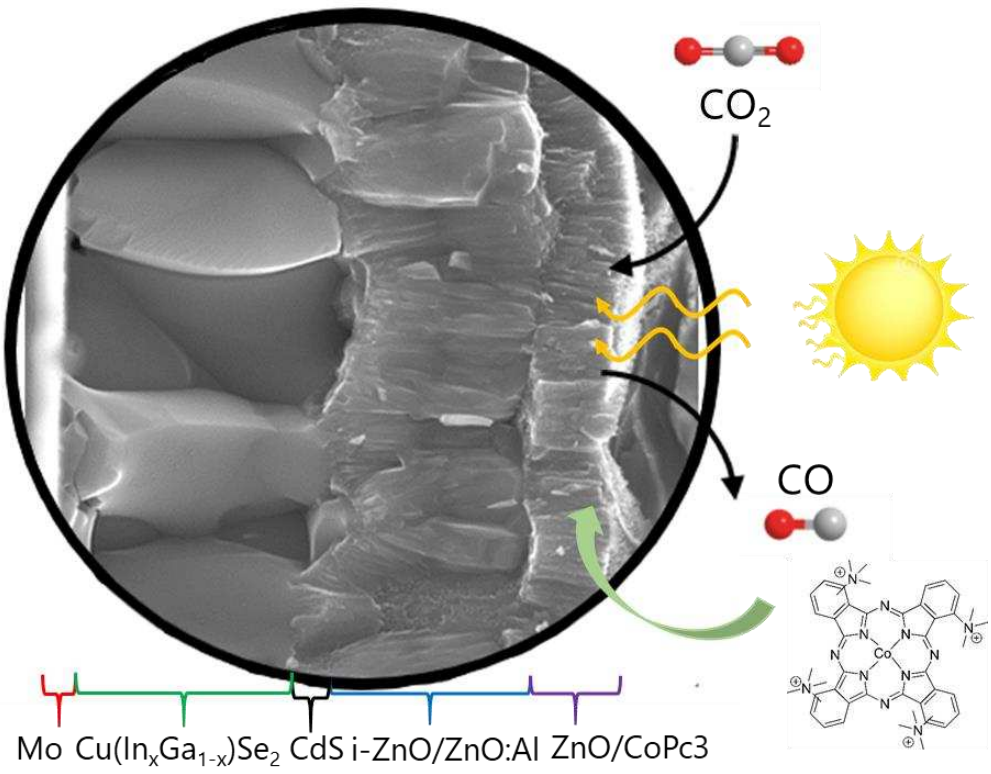

Figure IV.8 Schematic representation of the photoelectrochemical CO_2 reduction process involving modified CIGS photocathodes covered with a ZnO|CoPc3 hybrid layer.

Upon illumination, incoming photons generate electron-hole pairs in the CIGS. Electrons are transported through the layers until reaching the NPS layer. Electrons arriving at the NPS layer are directed to the molecular catalyst, allowing it to perform the electrochemical reaction of reduction of CO_2. The process is illustrated in Figure IV.9.

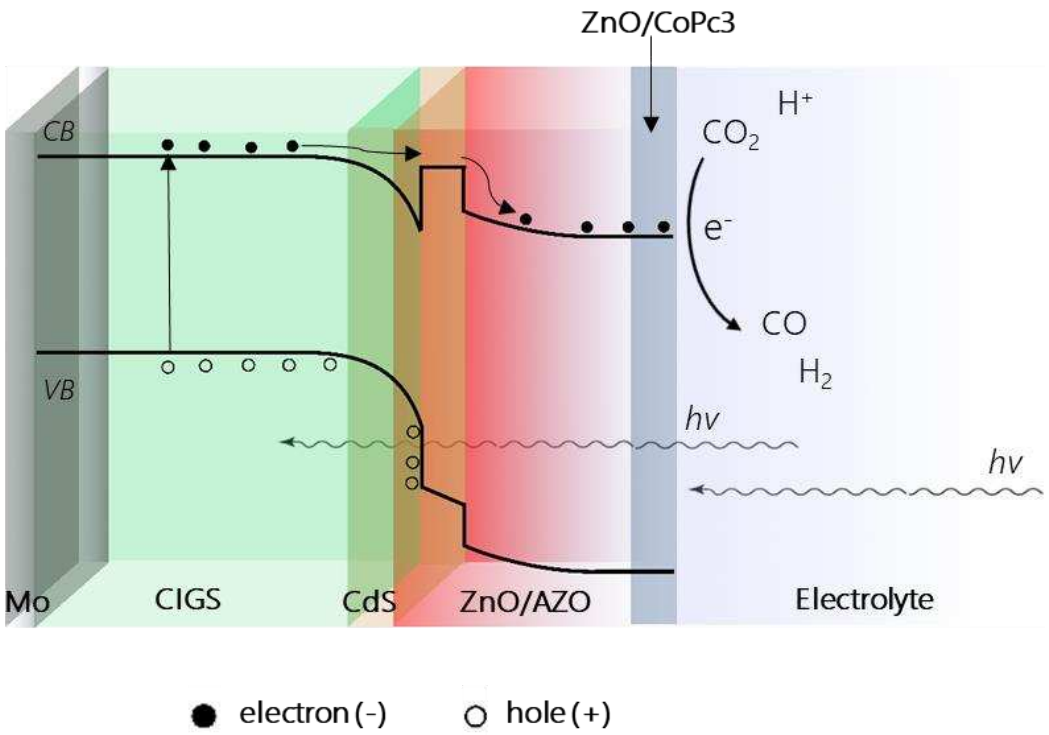

Figure IV.9 Schematic representation of a CIGS/CdS/ZnO/AZO photoelectrode covered with a ZnO|CoPc3 layer (PEC CO_2 reduction system).

IV.4.1 Electrochemical characterizations

To explore the CO_2 reduction activity of the modified CIGS device, photoelectrochemical experiments were carried out using the conditions studied in the EC experiments shown in chapter III: acetonitrile solution containing 0.1 M of $TBAPF_6$ and 1% H_2O. (chapter III, section 4.1.1). The solution was saturated with either argon or CO_2. First, we have studied the photoelectrochemical behaviour of a non-modified CIGS photoelectrode by linear scan voltammetry (Figure IV.10).

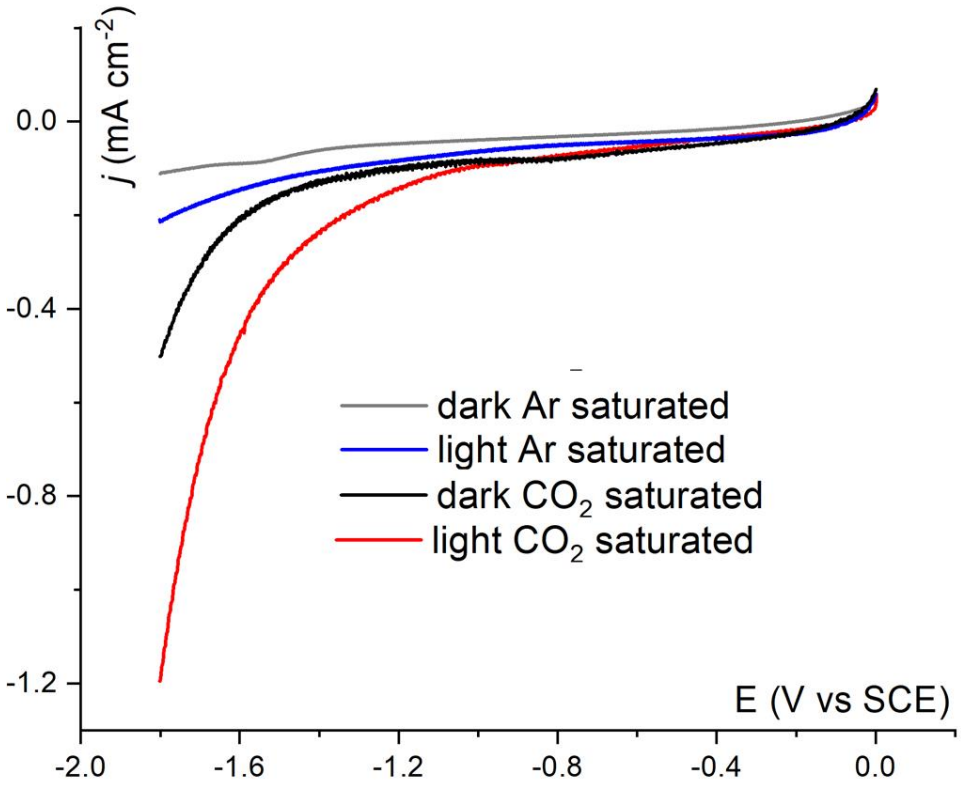

Figure IV.10 Linear scan voltammograms of a CIGS/CdS/ZnO/AZO photoelectrode in the dark and under illumination (100 mW cm^{-2}) in CO_2 or Ar saturated CH_3CN with 0.1 M $TBAPF_6$ and 1 % H_2O solution. Scan rate: 20 mV s^{-1}. Electrode surface 0.5 cm^{-2}.

As shown in the voltammograms curves (Figure IV.10), the CIGS/CdS/ZnO/AZO photoelectrode does not produce obvious cathodic current when the solution is saturated with Argon. There is a small current produced under illumination ca. -0.2 mA cm^{-2} at -1.8 V vs. SCE, that can be attributed to the hydrogen evolution reaction. When CO_2 is added, the cathodic current starts increasing in the dark after applying a large bias around -1.6 V vs. SCE. This cathodic current, shown in the black trace, probably comes from the reduction reaction of the CO_2 molecule with the AZO top layer of the CIGS solar cell, since ZnO has been demonstrated to have a catalytic activity in CO_2 reduction to CO.[110–113] In addition, it has been also reported that CIGS cell can by itself reduce CO_2 to CO.[30]

Under illumination, the photocathode begins to produce photocurrent as early as -1.3 V vs SCE, suggesting a smaller overpotential (kinetic barrier) for CO_2 reduction. With increasing bias, the photocurrent at the CIGS photocathode reaches high current density of ca. -1.2 mA cm^{-2} at -1.8 V vs. SCE. This photocurrent should be attributed to

the combination effects including the charge carrier separation created at the *p-n* junction of the solar cell, a probably fast charge transfers between the CIGS cell layers and fast CO_2 reduction rate at the catalytic sites. However, this current density is still poor compared to the expectations based on the known performance of CIGS as a photoabsorber (J_{SC}~30 mA cm^{-2}).

In Figure IV.11 we compare the photoelectrochemical behaviour of a non-modified CIGS/CdS/AZO photoelectrode with the CIGS/CdS/AZO photoelectrodes covered with a ZnO|CoPc3 NPS layer in order to show the improvement in PEC CO_2 reduction.

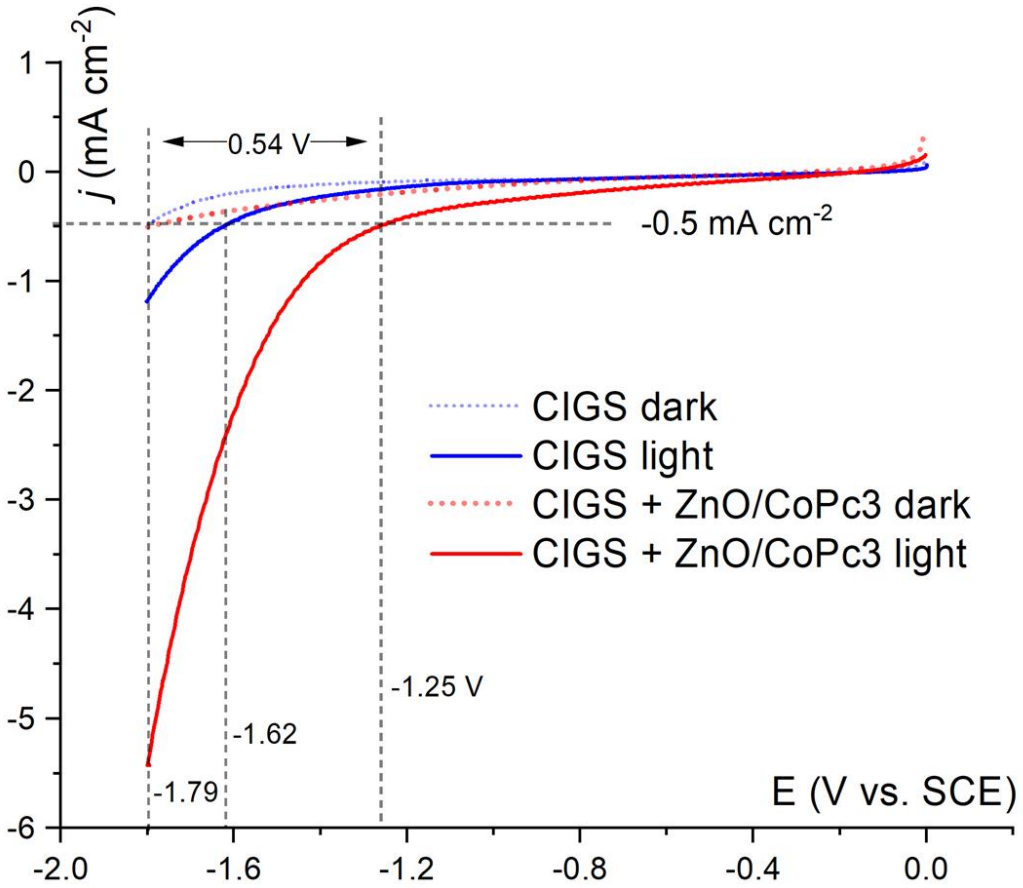

Figure IV.11 Linear scan voltammograms of a CIGS/CdS/ZnO/AZO photoelectrode and a CIGS/CdS/ZnO/AZO+ZnO|CoPc3 (350 nm) in the dark and under illumination (100 mW cm^{-2}) in CO_2 saturated CH_3CN with 0.1 M $TBAPF_6$ and 1 % H_2O solution. Scan rate: 20 mV s^{-1}. Electrode surface: 0.5 cm^{-2}.

A large improvement in the catalytic activity is obtained when the hybrid ZnO|CoPc3 layer is added onto CIGS photoelectrodes. The voltammograms curves in Figure IV.11

show how under illumination the cathodic current of a CIGS/CdS/ZnO/AZO+ZnO|CoPc3 electrode (red line) starts increasing considerably as early as -1.25 V vs. SCE (taking arbitrary a current density of -0.5 mA cm^{-2} as reference), as compared with a non-modified CIGS (blue line) in which the same current density is reached with a high overpotential of -1.62 V vs. SCE.

Furthermore, with increasing bias, the photocurrent of the CIGS cell electrode (CIGS/CdS/ZnO/AZO) reaches a current density of ca. -1.2 mA cm^{-2} at -1.8 V vs. SCE. (Fig. IV.11 blue trace), while the CIGS/CdS/ZnO/AZO+ZnO|CoPc3 electrode produce an important increase of the current produced, with high current density of ca. -5.5 mA cm^{-2} at -1.8 V vs. SCE. The addition of a ZnO nanoporous layer with a molecular catalyst on top of the solar cell affect positively the catalytic response of the CIGS/CdS/ZnO/AZO photoelectrode. Upon illumination the CIGS/CdS/ZnO/AZO+ ZnO|CoPc3 present a photovoltage of ca. 0.54 V, this value corresponds to the V_{OC} delivered by the CIGS cell (table IV.1).

This difference between the current density value of (-5.5 mA cm^{-2}) reached with the modified CIGS electrode compare with the one reached by the CIGS cell photoelectrode (-1.2 mA cm^{-2}) at the same potential, shows the enhancement of the system by the incorporation of a hybrid ZnO molecular catalyst layer, despite the loss in efficiency that the CIGS cell can suffer after the modification (see table IV.1). Even if a small part of the incident light is absorbed by the CoPc3 molecules into the last layer, most of the photons can pass through and reach the CIGS/CdS *p-n* junction generating electrons that are transported to the catalytic centers of the hybrid layer.

Linear scan voltammetry experiments also revealed a strong cathodic current response of CIGS/CdS/ZnO/AZO+ZnO|CoPc3 electrodes, when the solution is CO_2 saturated (-5.5 mA cm^{-2}) compared to a weaker current response when it is Argon saturated (-1.6 mA cm^{-2}), clearly demonstrating that the current flow is used for carbon dioxide reduction (Figure IV.12). The current observed in the absence of CO_2 (under Ar saturation) could be attributed to the addition of hydrogen evolution reaction (HER) and the reduction of the ZnO|CoPc3 layer itself.

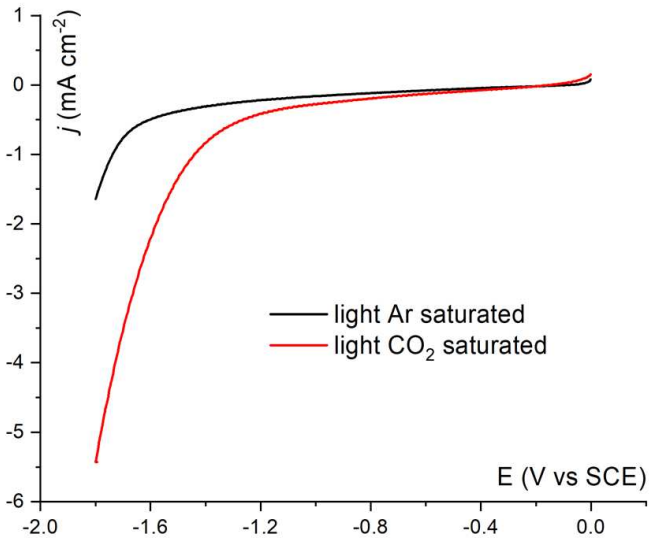

Figure IV.12 Linear scan voltammograms of a CIGS/CdS/ZnO/AZO+ZnO|CoPc3 (350 nm) photoelectrode under illumination (100 mW cm^{-2}) in CO_2 or Argon saturated CH_3CN with 0.1 M $TBAPF_6$ and 1 % H_2O solution. Scan rate 20 mV s^{-1}. Electrode surface: 0.5 cm^{-2}.

In order to verify the continued photoactivity of the CIGS device, chopped illumination chronoamperometry experiments, where the light source was interrupted for 3 seconds have been performed in CO_2 saturated solution (Figure IV.13).

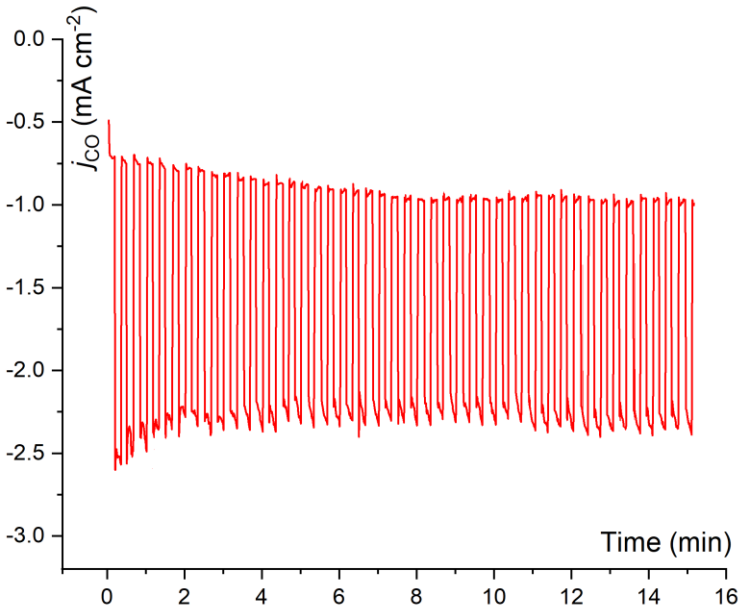

Figure IV.13 Chopped light chronoamperometry of a CIGS/CdS/ZnO/AZO+ ZnO|CoPc3 (350 nm) photoelectrode under illumination (100 mW cm^{-2}) in CO_2 saturated CH_3CN 0.1 M $TBAPF_6$ 1 % H_2O solution. Electrode surface: 0.5 cm^{-2}. Potential applied: -1.5 V vs. SCE.

The operating current of the modified solar cell device under chopped light illumination at -1.5 V vs. SCE, revealed a strong and stable with time photocurrent response up to -2.5 mA cm^{-2}. The photocurrent (difference between dark and illuminated current) is close to -1.6 mA cm^{-2} during the first minutes, after that, we can notice a slightly increase of the dark current, reducing the photocurrent, reaching now a value of -1.3 mA cm^{-2}. The current under illumination slightly decrease (in absolute value) during the first 2 minutes reaching a mean value of -2.35 mA cm^{-2} and remains so during the rest of the experiment. This behaviour confirms the continued photoactivity of the modified photoelectrode. It indicates the generation of true photocurrent, rather than corrosion processes which would manifest as an large increase in the dark current.[167]

The effect of the light power on the photocurrent of the modified CIGS electrodes in the PEC CO_2 system was also studied, in order to evaluate the relationship between incoming photon flow and generated photocurrent.

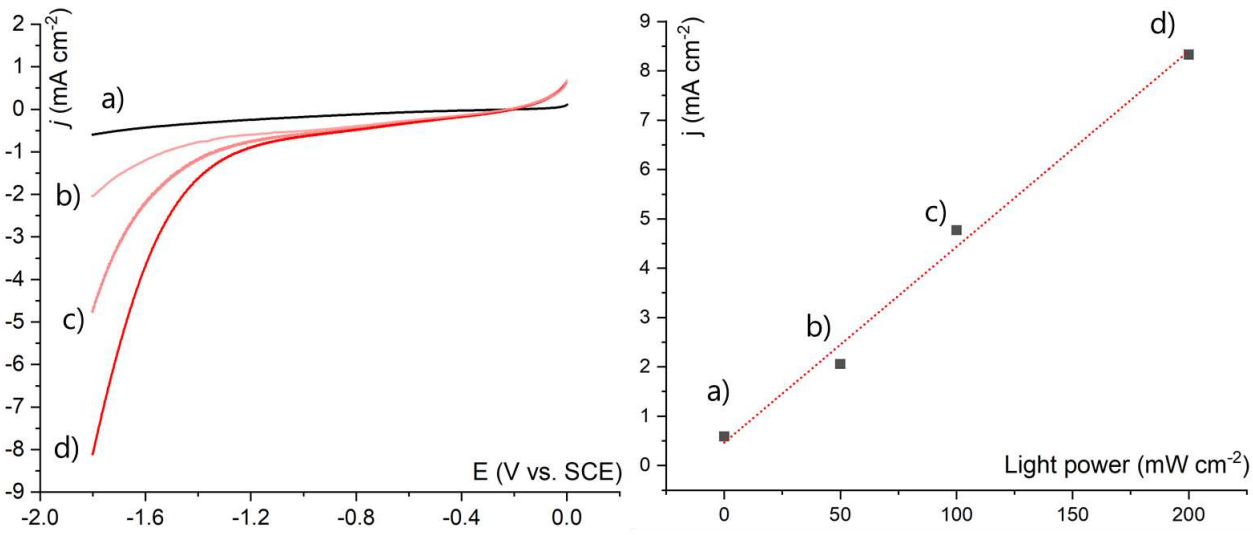

Figure IV.14 Left: linear scan voltammograms of a CIGS/CdS/ZnO/AZO+ZnO|CoPc3 (350 nm) photoelectrode in dark a). under illumination: b) 50 mW cm^{-2}, c) 100 mW cm^{-2} d) 200 mW cm^{-2}. in CO_2 saturated CH_3CN with 0.1 M $TBAPF_6$ and 1 % H_2O solution. Electrode surface: 0.5 cm^{-2}. Right: Current density as a function of the light power, measured at -1.8 V vs. SCE.

The Figure IV.14 shows how the current density varies with the light power (varied between 50 mW cm^{-2} and 200 mW cm^{-2}). Increasing the light intensity produce a much sharper increase in the current density magnitude, reaching current densities up to ca. -8 mA cm^{-2} under a power of 200 mW cm^{-2}. As observed on Figure IV.14-right, the

increase of the current density presents a linear dependence with the light power intensity. This is the expected behaviour of a solar cell in good conditions, that means that the device modified with the ZnO|CoPc3 layer still present a good photovoltaic response after the light-assisted electrodeposition process of deposition of the hybrid layer. Moreover, increasing the light power produces a higher photovoltage, resulting in a shift of the overpotential for the CO_2 reduction reaction. If a current of -1 mA cm^{-2} is taken as a reference, this current value is obtained at a potential of -1.25 V vs SCE when the sample is illuminated with a power of 200 mW cm^{-2}, compared to a potential of -1.34 V vs. SCE under 100 mW cm^{-2} and a potential of -1.51 V vs SCE at 50 mW cm^{-2}. The increase in light intensity affects both the current density and decreases the overpotential.

Finally, that the current density is proportional to the light intensity indicates that the catalysis is not limited by the catalysts reaching CO_2 by diffusion process, but rather by the flux of photons being absorbed and converted into electron-hole pairs.

IV.4.2 Photoelectrolysis experiments

IV.4.2.1 Impact of the thickness of the ZnO|CoPc3 layer in the PEC performance

The influence of the thickness of the hybrid ZnO|CoPc3 layer on top of CIGS solar cells was then further investigated. The Figure IV.15 shows the current density measured during photoelectrolysis experiments, for samples covered by a ZnO|CoPc3 350 nm (blue) and 1000 nm (red) layer compared with a non-modified CIGS solar cell (grey) at a constant potential of -1.5 V vs. SCE. The potential was chosen from the linear scan voltammetry experiments shown before (Figure IV.12). At –1.5 V vs SCE, the modified CIGS/CdS/ZnO/AZO+ZnO|CoPc3 show a current density between -1.5 and -2.0 mA cm^{-2}. These values are higher than the most high found in the literature in similar PEC CO_2 reduction systems, as the reported FTO/Au/Cu2O/AZO/TiO2/m-TiO2 + rhenium complex photoelectrode that can reduce CO_2 to CO under illumination at -1.52 V vs SCE (1.9 V vs. Fc/Fc+) reaching a current density of -1.75 mA cm^{-2}, in the same electrolyte solution.[22]

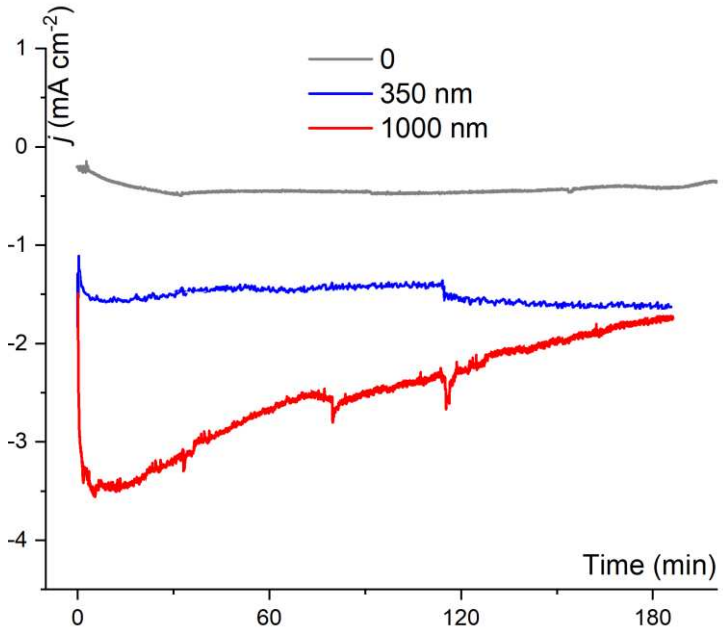

Figure IV.15 Photo-electrolysis experiments registered at -1.5 V vs. SCE. using CIGS/CdS/ZnO/AZO+ZnO|CoPc3 photoelectrodes in CO_2 saturated CH_3CN with 0.1 M $TBAPF_6$ and 1 % H_2O solution. Electrode surface: 0.5 cm^{-2}. Light power: 100 mW cm^{-2}.

The incorporation of a ZnO|CoPc3 layer on top of the CIGS cell, not only produces an increase of the current density during PEC CO_2 reduction, but also improves the selectivity of the reaction, as confirmed by gas chromatography analysis (Figure IV.16).

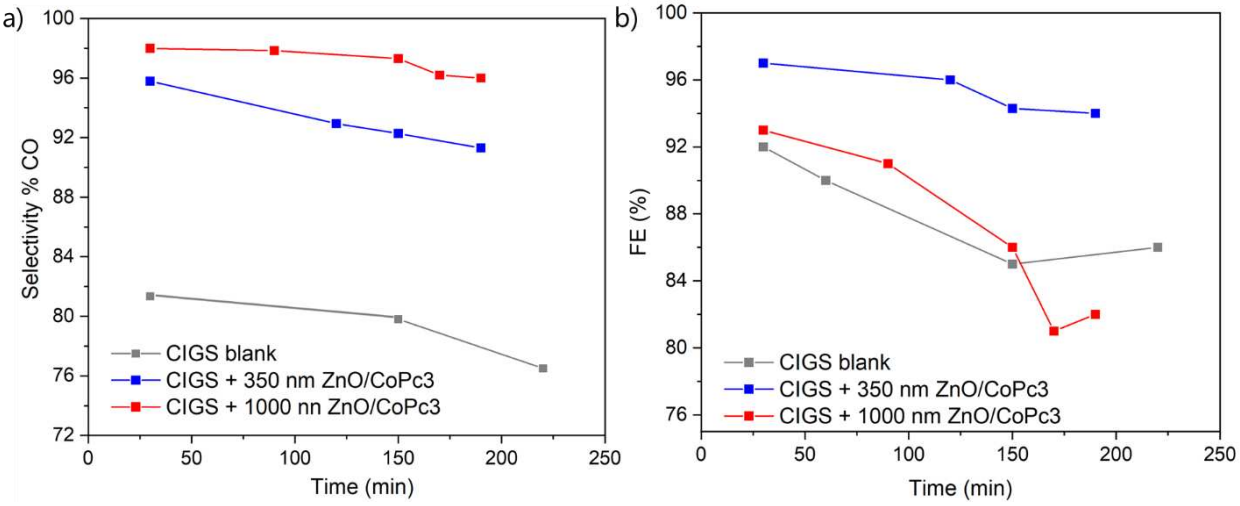

Figure IV.16 a) CO selectivity and b) Faradaic efficiency calculated from gas chromatography quantification of products (CO, H_2).

When long-term photoelectrocatalysis experiment, up to 3 hours, were carried out at a bias potential of −1.5 V vs. SCE, the current density varies with the thickness of the ZnO|CoPc3 layers. For a CIGS cell covered with a ZnO|CoPc3 layer 350 nm thick the current shows a good stability along the 3 h electrolysis (Fig. IV.15 blue trace), with a CO selectivity that ranges from 96% to 92% at the end of the experiment, only obtaining 8% of H_2 as the by-product (Fig. IV.16.a blue). For this sample, the Faradaic efficiency stays around 95% during the whole experiment (Fig. IV.16.b blue). For a CIGS cell covered with a thicker ZnO|CoPc3 layer (1000 nm) the current density was unstable, after 20 minutes it starts to decrease (in absolute value) from -3.5 mA cm^{-2} continuously up to -1.6 mA cm^{-2} at the end of the experiment (Fig. IV.15 red). However, this sample still showed a high CO selectivity of 97% after 3 h electrolysis (Fig. IV.16.a red). Nevertheless, the Faradaic efficiency decreases considerably, from 93% to a final value of 82% (Fig. IV.16.b red). It be explained by catalyst leaching from the electrode, and/or degradation of the ZnO layers. Nonetheless, it is remarkable that such a high selectivity for CO production could be obtained for several hours with a fully integrated device, at small overpotential for systems working in organic solvents.

The Figure IV.15 also shows the results obtained using a non-modified CIGS cell. The current shows by the CIGS cell present a good stability along the 3 hours photoelectrolysis, at a very low current density (-0.5 mA cm^{-2}, Figure IV.15 grey). We can see that without the nanoporous layer, the CO selectivity is low (ca. 80%, Figure IV.16.a).

These results lead us to conclude that a thin Zn/CoPc3 layer (≤ 350 nm) is well suited to confer to the CIGS photoelectrode high catalytic activity. Such photoelectrode has shown the best stability in PEC conditions maintaining a high selectivity (> 90%) at a current density of -1.5 mA cm^{-2}, while using a small amount of molecular catalyst (ca. 1.5 nmol cm^{-2}).

The results reported in this section added to the results obtained from the J-V characteristics (table IV.1) and EQE (fig. IV.7), allow us to conclude that incorporation of thin hybrid ZnO|catalyst layers on top of a CIGS photoelectrode resulted in significant improved performances in PEC CO_2 reduction, leading to a high photovoltaic efficiency. For next experiments, we selected electrodes CIGS/CdS/ZnO/AZO covered with ZnO|CoPc3 layers ~350 nm thick.

IV.4.2.2 Improving the stability of the CIGS modified electrodes in PEC conditions

Whit this optimal configuration for our photoelectrocatalytic device, we started to vary the PEC conditions in order to improve the performance of the photoelectrodes, in particular its stability.

Long-term photoelectrocatalysis experiments were carried out at different potentials. The Figure IV.17 shows the current density obtained during a long-term (5 hours) photoelectrolysis experiment at an applied potential of -1.5 V vs. SCE. Current density remained stable during the first 3 h electrolysis, then started decreasing (in absolute value) from a mean value of -1.65 mA cm^{-2} to -1.15 mA cm^{-2}. The CO selectivity was high (>94%) even after 5 h electrolysis experiment. As demonstrated before, the high selectivity of the systems comes from the presence of the molecular catalyst into the hybrid layers. This indicates that the catalyst is still present and active inside the layer. The degradation of the photoelectrodes could thus come from the cathodic degradation of the ZnO layer itself.

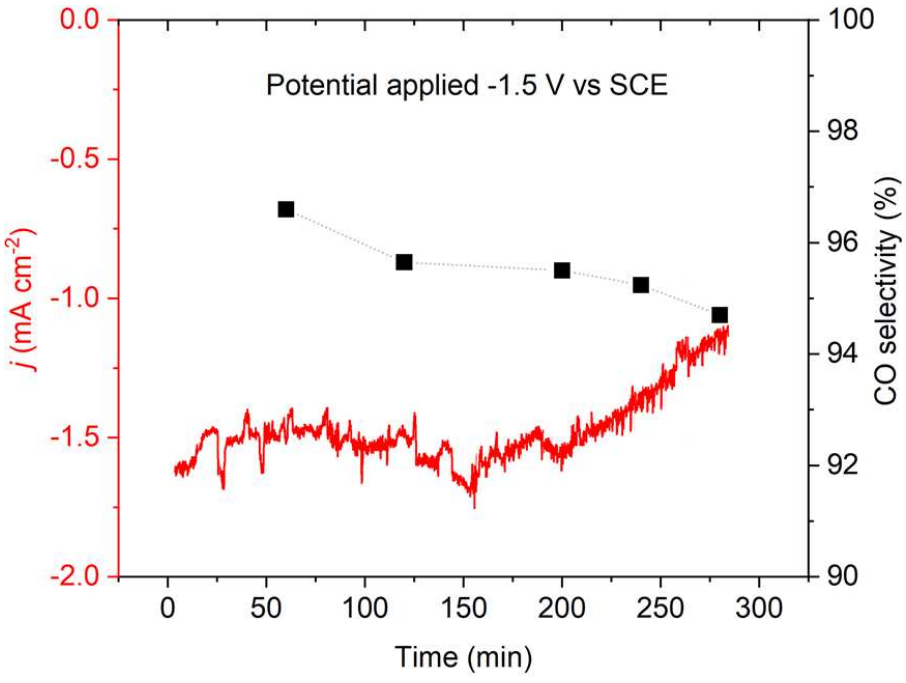

Figure IV.17 Long-term photoelectrocatalysis experiment registered at -1.5 V vs. SCE. using CIGS/CdS/ZnO/AZO+ZnO|CoPc3 (350 nm) photoelectrodes in CO_2 saturated CH_3CN with 0.1 M $TBAPF_6$ and 1 % H_2O solution. Electrode surface: 0.5 cm^{-2}. Light power: 100 mW cm^{-2}.

In order to further improve the stability of photoelectrode during the PEC CO_2 reduction, we decide then to apply a less negative potential. Figure IV.18 shows the current density during a photoelectrolysis experiment at an applied potential of -1.45 V vs. SCE, for 20 hours.

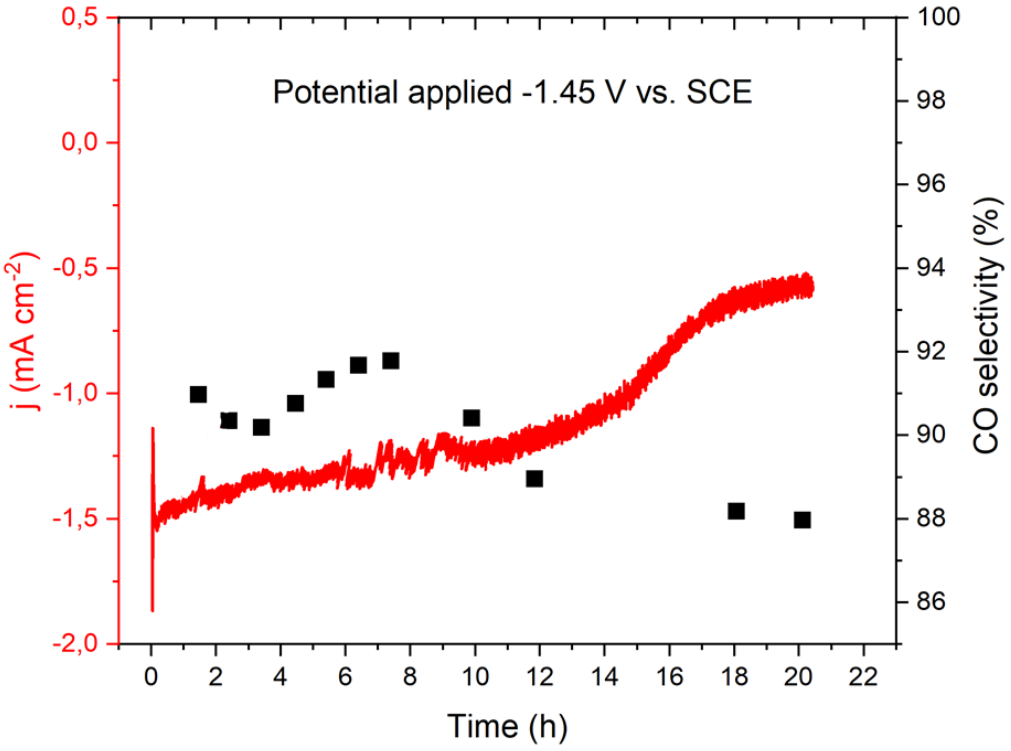

Figure IV.18 Long-term photoelectrocatalysis experiment registered at -1.45 V vs. SCE. using CIGS/CdS/ZnO/AZO+ZnO|CoPc3 (350 nm) photoelectrodes in CO_2 saturated CH_3CN with 0.1 M $TBAPF_6$ and 1 % H_2O solution. Electrode surface: 0.5 cm^{-2}. Light power: 100 mW cm^{-2}.

The current density during the photoelectrolysis experiment remains relatively stable during the first 10 hours, with only a slight decrease (in absolute value) in its slop, from -1.5 to -1.37 mA cm^{-2}. After this time, the decrease in current becomes more pronounced, as observed in the curve. Finally, after 15 hours, there is a new change in the slop of the current density curve. The current density decreases faster, reaching -0.5 mA cm^{-2}. After that, the electrode stopped working. The CO selectivity was around 92% during the first 10 hours, then it decreases to a final value of 88%.

A slight increase in the applied potential, can thus improve the stability of the photoelectrodes, with current densities larger than -1 mA cm^{-2} for at least 10 hours. This is an important step forward for this fully integrated photoelectrode, which can operate

in PEC conditions with high selectivity and low overpotential. We performed an additional PEC CO_2 reduction experiment, fixing a constant current value of -2 mA cm^{-2}.

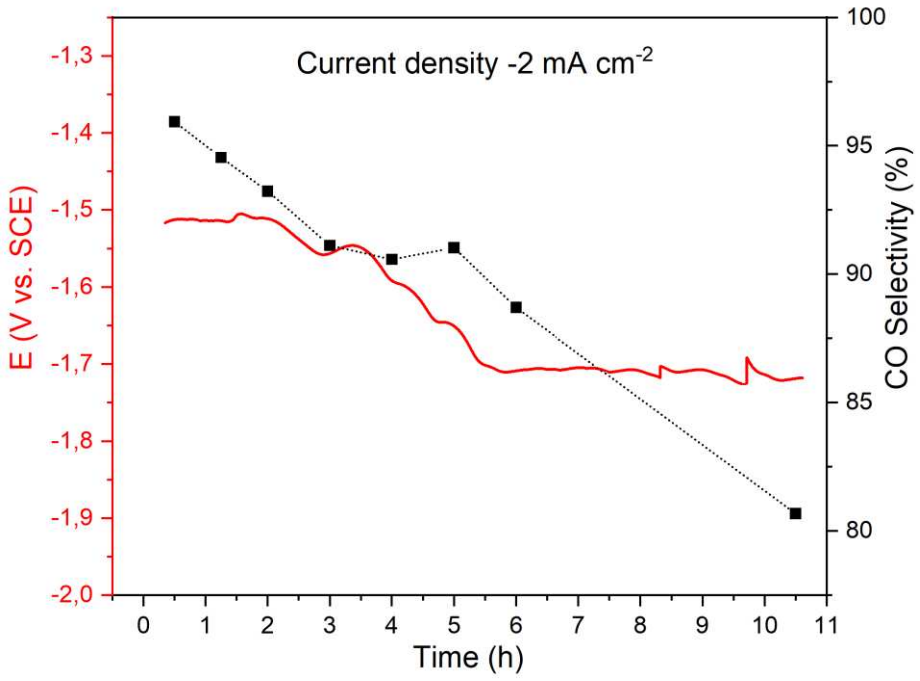

Figure IV.19 Photoelectrolysis experiment registered during a Chronopotentiometry with a current held at -2 mA cm^{-2}, using CIGS/CdS/ZnO/AZO+ZnO|CoPc3 (350 nm) photoelectrodes in CO_2 saturated CH_3CN with 0.1 M $TBAPF_6$ and 1 % H_2O solution. Electrode surface: 0.5 cm^{-2}. Light power: 100 mW cm^{-2}.

As observed, up to 2h the system works at a potential around -1.55 V vs SCE. After that, the potential starts increasing (in absolute value) and reaches after 5.5 h a value of -1.7 V vs. SCE. This last potential value remains stable until the end of the experiment. Regarding the selectivity, it decreases during the whole experiment. However, the selectivity remains higher than 90% during the first 5.5 h photoelectrolysis, after that it dropped down to 80%. High negative potentials promote the hydrogen evolution reaction, making the system less selective toward CO production.

So far, 10 hours of stability was obtained for CO production at 92% selectivity with a partial current density of ca. -1.25 mA cm^{-2}.

IV.4.2.3 High current densities PEC CO_2 reduction system

In chapter III, we have shown how the addition of a proton source into the electrolyte solution enhances the catalytic performance of the ZnO|CoPc3 hybrid layers. For our study, we used water as a proton source in the CH_3CN solution. In this study, concentration of water has been increased from 1% up to 2%. The Figure IV.20.a shows the linear scan voltammetry of a CIGS modified electrode under chopped light in an electrolyte containing 1.5% H_2O. The CIGS/CdS/ZnO/AZO+ZnO|CoPc3 photoelectrode produce a little cathodic current when the solution is saturated with Argon. It can be attributed to the hydrogen evolution reaction, which reaches values around -3.8 mA cm^{-2} at -2.1 V vs. SCE, due to the significant proton content. When CO_2 is added, the cathodic current starts increasing fast. A photocurrent density of ca. -13 mA cm^{-2} was measured at -2.1 V vs. SCE. This high photocurrent is attributed to combined effects including high light harvesting efficiency of CIGS, fast charge transport between the CIGS cell layers and the catalytic centers of the hybrid layer, and fast CO_2 reduction rate at the catalytic sites, enhance by the presence of a higher concentration of protons in the solution. The photogenerated current (difference between dark and illuminated current) is as high as 7 mA cm^{-2}. Upon increasing the water concentration up to 2% (Figure IV.20.b) current densities were enhanced, with a maximum values of ca. -16 mA cm^{-2} at -2.1V vs. SCE. The photogenerated current was measured to be as high as ca. -10 mA cm^{-2}.

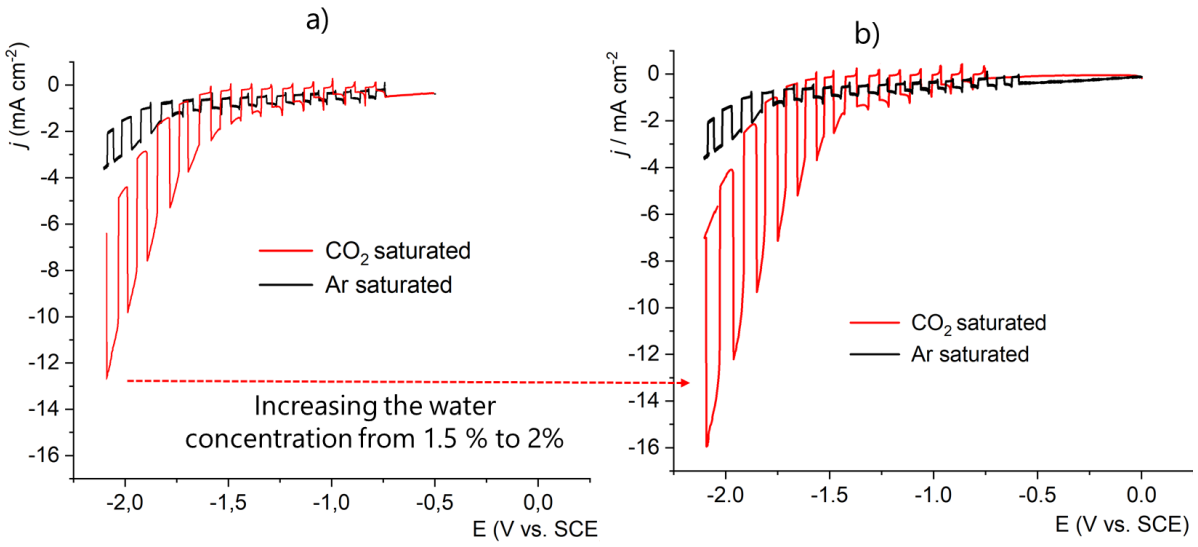

Figure IV.20 Linear scan chopped light voltammograms of a CIGS/CdS/ZnO/AZO+ZnO|CoPc3 (350 nm) photoelectrodes in CO_2 saturated CH_3CN with 0.1 M $TBAPF_6$ adding: a) 1.5% H_2O and b) 2 % H_2O, in the solution. Electrode surface: 0.5 cm^{-2}. Light power: 100 mW cm^{-2}.

This addition of 2% water allows to reach the best performance in terms of current density. Adding more water (> 2%) did not show a significant effect on the current density, instead it promoted a higher production of hydrogen and a faster degradation of the photoelectrodes.

Figure IV.21 shows the current density of a long-term (4.5 h) photoelectrolysis experiment in a CH_3CN with 0.1 M $TBAPF_6$ and 2 % H_2O at an applied potential of -1.5 V vs. SCE. This experiment shows a current density of around -4 mA cm^{-2}. This last remains stable for the first 4 h of photoelectrolysis. After this time, the reduction current begins to decrease (in absolute value) until the photoelectrode stops working. The increased proton concentration allowed the system to generate current densities that are twice as large as those obtained before (1% H_2O). Under these new conditions, CO selectivity appears to be unaffected, since a high value of 94% was reached. The system lost in lifetime (4.5 h) compared to the experiments shown before (10 h at -1.45 V vs. SCE, in the presence of 1% added water). However, this has been compensated by a significant increase in the current density for CO production (3.8 mA cm^{-2} vs 1.25 mA cm^{-2} respectively for J_{CO}).

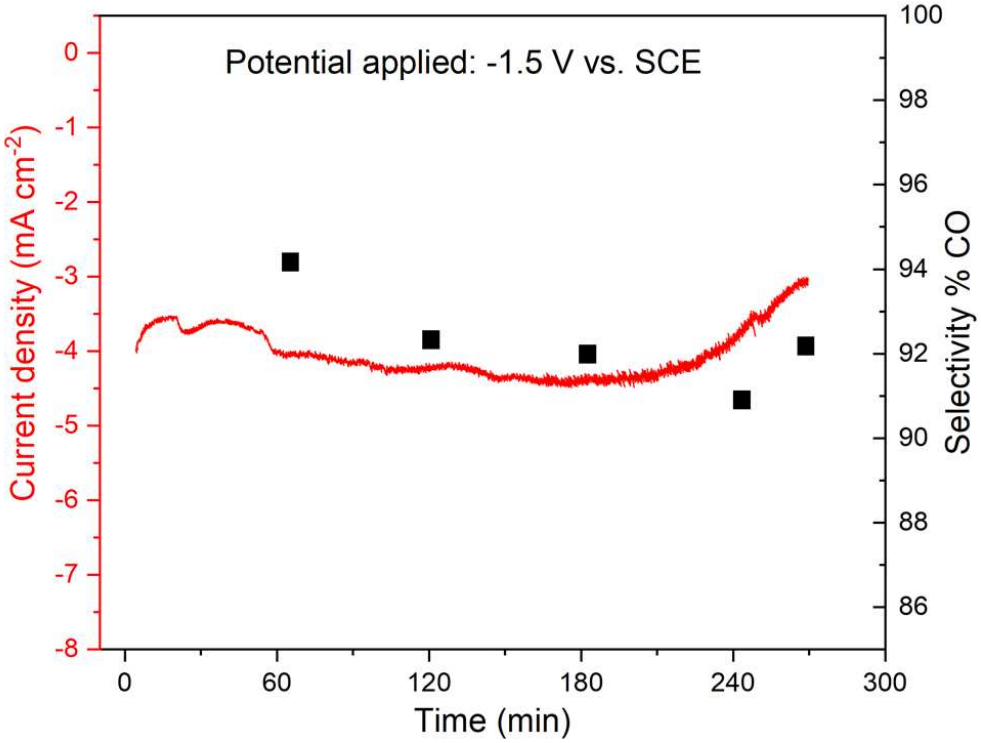

Figure IV.21 Long-term photoelectrocatalysis experiment at E = -1.5 V vs. SCE. using a CIGS/CdS/ZnO/AZO+ZnO|CoPc3 (350 nm) photoelectrode in CO_2 saturated CH_3CN with 0.1 M $TBAPF_6$ and 2 % H_2O solution. Electrode surface: 0.5 cm^{-2}. Light power: 100 mW cm^{-2}.

In order to assess the behaviour of a photoelectrode at higher current densities (> 4 mA cm^{-2}), a photoelectrolysis experiment was performed at a high current density of -7 mA cm^{-2} (Figure IV.22), using the best structure of our device i.e. CIGS/CdS/ZnO/AZO+ZnO|CoPc3 (350 nm) in the best electrolyte conditions, i.e. CO_2 saturated CH_3CN with 0.1 M $TBAPF_6$ and 2 % H_2O solution. Such high current density was maintained for 3 hours photoelectrolysis. The potential requires to reach this high current density value started around -1.55 V vs. SCE and progressively increases (in absolute value) to ca. -1.70 V vs. SCE. After that, the potential continuously increased to -1.75 at the end of the experiment. The system was able to produce -7 mA cm^{-2} under these conditions with a mean selectivity of ca. 92%, corresponding to a partial current density for CO production J_{CO} of ca. -6.5 mA cm^{-2}, achieving a solar-to-CO conversion (STCO) of 0.75 %.

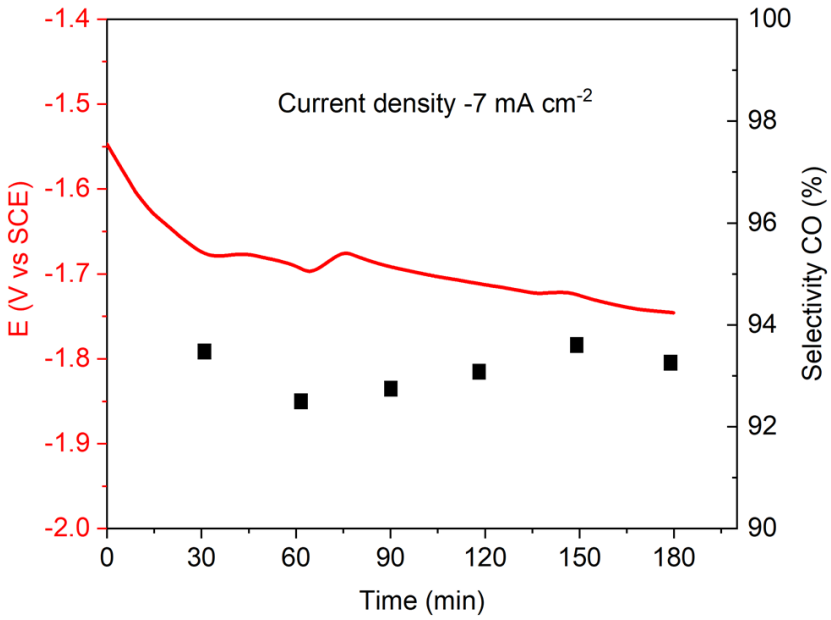

Figure IV.22 Chronopotentiometry experiment with a current held at -7 mA cm^{-2}, using a CIGS/CdS/ZnO/AZO+ZnO|CoPc3 (350 nm) photoelectrode in CO_2 saturated CH_3CN with 0.1 M $TBAPF_6$ and 2 % H_2O solution. Electrode surface: 0.5 cm^{-2}. Light power: 100 mW cm^{-2}.

IV.4.3 PEC performance in aqueous solution: Preliminary study

In addition to the previous experiments shown before, we tested the modified CIGS photoelectrodes in a $KHCO_3$ aqueous solution. Working in aqueous solution presents a challenge for the photocathode because the metal oxide layer degrades faster in

aqueous solutions that in organic media, and this phenomenon is accelerated when negative potentials are applied. The potentials in this section are expressed in V vs. RHE, the values are obtained using the following equation:

$$\mathrm{E(vs.\,RHE)} = \mathrm{E(vs.\,SCE)} + 0.242 + 0.059 * \mathrm{pH} \qquad \textbf{(Eq. IV.1)}$$

The Figure. IV.23.a shows the cyclic voltammetry of a CIGS/CdS/ZnO/AZO+ZnO|CoPc3 (350 nm) photoelectrode in 0.1 M $KHCO_3$ Ar or CO_2 saturated aqueous solution (pH 6.8) under illumination. The voltammograms under CO_2 atmosphere revealed a current density that appears at an onset potential around 0.1 V vs. RHE. The current density reaches values as high as -1.35 mA cm^{-2} at an applied potential of -0.18 V vs. RHE.

Furthermore, the effect of the light power on the photocurrent was studied. Figure IV.23.b shows how the current density increases with the light power (variations between 80 mW cm^{-2} and 300 mW cm^{-2}). The increase of the light intensity, as expected, leads to an increase of the current density, with greater light intensity producing a much sharper increase in current density. This behaviour is similar to the results obtained in experiments in an organic solvent. Showing that the CIGS cell modified by a ZnO|CoPc3 layer continues to exhibit a strong photovoltaic response. Moreover, increasing the light power produce a higher photovoltage, resulting in a shift of the overpotential for the CO_2 reduction reaction towards more positive potentials.

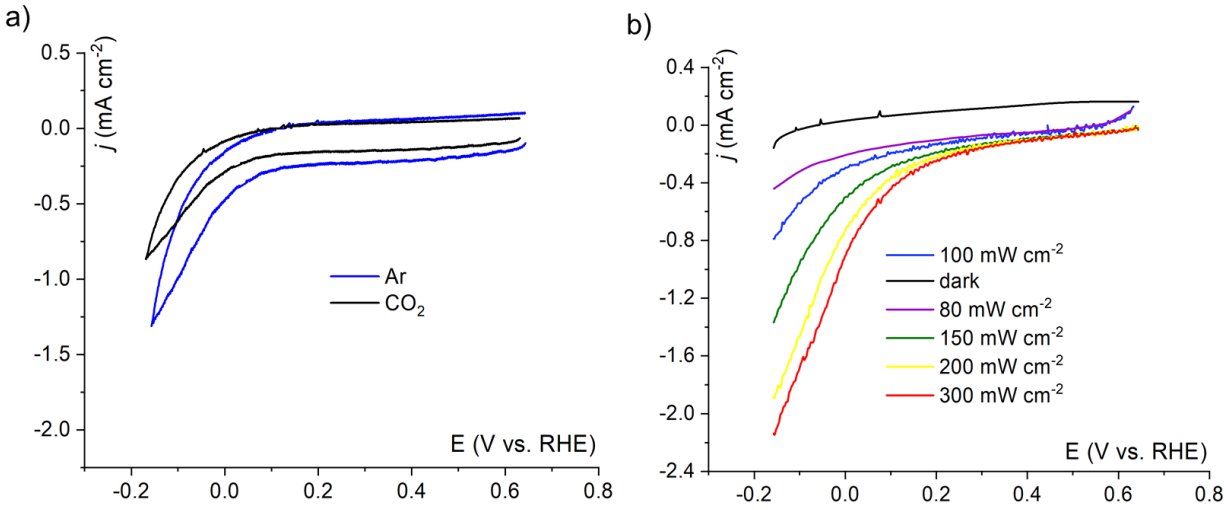

Figure IV.23 a) Cyclic voltammograms in PEC conditions for a CIGS/CdS/ZnO/AZO+ZnO|CoPc3 (350 nm) photoelectrode in 0.1 M $KHCO_3$ solution, saturated with argon (black) or CO_2 (blue). Light power: 100 mW cm^{-2}. Scan rate: 100 mV s^{-1}. b) linear scan voltammetry of the modified CIGS electrode as a function of the light power. Scan rate: 20 mV s^{-1}. Electrode surface: 0.5 cm^{-2}.

Linear sweep voltammetry under chopped illumination in 0.1 M $KHCO_3$ CO_2 saturated solution (Fig. IV.24) revealed a photoresponse with an onset potential of ca. 0.1 V vs. RHE. This represents a small overpotential value for a CO_2 reduction system, comparable to the value reported recently of 0.2 V vs. RHE, in a similar system, by Pati et al.[29] This overpotential value is possible thanks to the photovoltage delivered by the photoelectrode combined with the high catalytic activity of the hybrid layer ZnO|CoPc3.

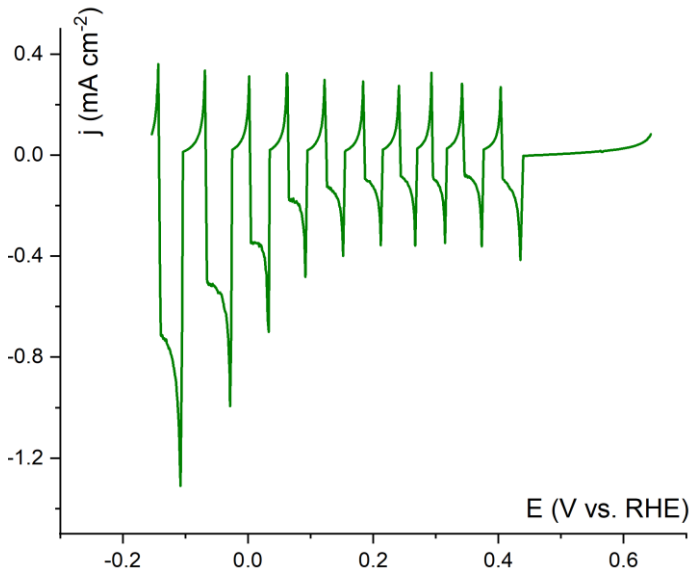

Figure IV.24 a) LSV in PEC conditions at a CIGS/CdS/ZnO/AZO+ ZnO|CoPc3 (350nm) photoelectrode in 0.1 M $KHCO_3$ saturated with CO_2 under chopped light irradiation. Scan rate was 20 mV s^{-1}.

An average current density of -0.85 mA cm^2 was recorded during a 2 hours photoelectrolysis experiment at an applied potential of 0.057 V vs. RHE (Figure IV.25). With a slight decay from the maximum current value reached of -1.1 mA cm^{-2} to a value of -0.7 mA cm^{-2} at the end of the experiment. Some fluctuation in the current density were observed over the whole experiment, keeping the stability at least for 2h. A CO selectivity of 87% was obtained with only 13% of H_2 produced as by-product.

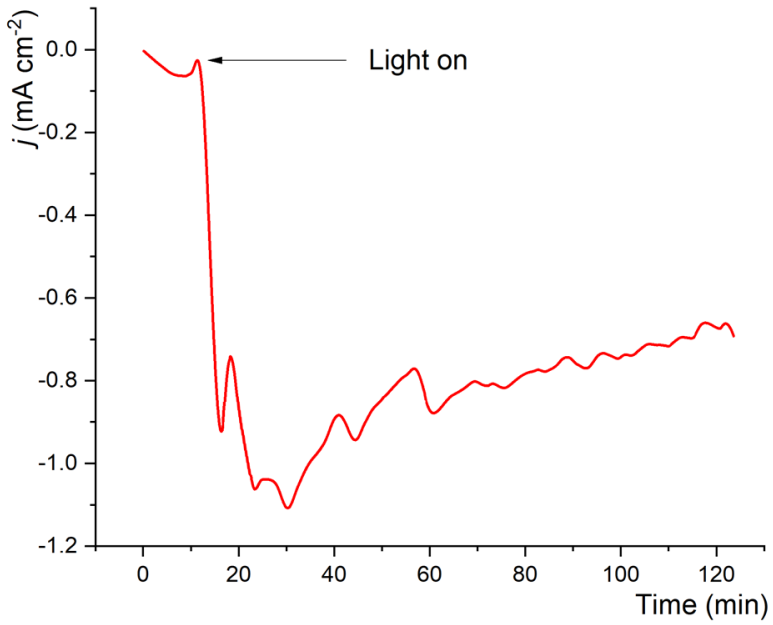

Figure IV.25 Long-term photoelectrolysis registered at an applied potential of −0.057 V vs. RHE for a CIGS/CdS/ZnO/AZO+ZnO|CoPc3 (350 nm) photoelectrode in 0.1 M $KHCO_3$ solution, saturated with CO_2.

Results obtained in aqueous media are really encouraging. The use of water instead of organic solvents present strong advantages for ecological and industrial purposes,. We show here only one preliminary study, there is still a long way for improvement of these photoelectrodes in aqueous solution. However, under these conditions the CIGS/CdS/ZnO/AZO+ZnO|CoPc3 electrode achieves a solar-to-CO conversion (STCO) of 1.1 %. The results presented here are comparable and competitive with those found in the literature, as we will show and discuss in the next section (IV.4.4).

IV.4.4 Benchmark of the PEC performance of our modified CIGS with the state of the art

The findings of this thesis, based on the preparation and implementation of a photo-electrode for the photoelectrochemical reduction of carbon dioxide, consisting of the electrochemically growth ZnO|CoPc3 layer on CIGS solar cell, are compared with the works found in the literature in the following table.

Table IV.2 EC and PEC performance of some (photo)electrodes for CO_2 conversion to CO.

Catalytic Electrode material	Reaction conditions	Potential applied	Performance	ref
1. $Cu_3(BTC)_2$ MOF coating Cu_2O/ITO	(a) CH_3CN 0.1 $TBAPF_6$ In EC	-1.97 V vs. Fc^+/Fc	FE 95% -0.4 mA cm^{-2}	83
	(b) CH_3CN 0.1 $TBAPF_6$ In PEC AM 1.5G illumination	-2.07 V vs. Fc^+/Fc	-0.8 mA cm^{-2} solar-to-CO reaches 0.83%	
2. FTO/Au/Cu2O/AZO/TiO2/ m-TiO2 + rhenium complex	(a) CH_3CN 0.1 $TBAPF_6$ in EC	-2.1 V vs. Fc^+/Fc	FE 80 - 95% No info about the current density	22
	(b) CH_3CN 0.1 $TBAPF_6$ In PEC AM 1.5G illumination 15 min experiment	-1.9 V vs. Fc^+/Fc	-1.75 mA cm^{-2} FE 80 - 95%	
3. CIGS/CdS/ZnO/AZO photo-electrode	0.1 M $KHCO_3$ In PEC AM 1.5 G illumination	-0.2 V vs. RHE	-4.8 mA cm^{-2} 99.3% FE CO_2 to CO	30
4. CIGS/CdS/ZnO/AZO coated by a Co-qPyH|f-TiO2|	0.1 M $KHCO_3$ CO_2 sat. (pH = 6.8) In PEC 100 mW/cm2	-0.06 V vs. RHE	-0.81 mA cm^{-2} 89% FE selectivity CO 97% 2 h experiment	29
5. ZnO|CoPc3 hybrid layers	CH_3CN 0.1 $TBAPF_6$ 0.8 M H_2O In EC	-2.38 V vs. Fc^+/Fc	**-5 mA cm^{-2} 97% FE selectivity CO 98%**	This work
6. ZnO|CoPc3 coating a CIGS solar cell	0.1 M $KHCO_3$ CO_2 sat. (pH = 6.8) In PEC 100 mW/cm2	-0.057 V vs. RHE	**-0.85 mA cm^{-2} 99% FE selectivity CO 87% 2 h experiment solar-to-CO reaches 1.1%**	This work
7. ZnO|CoPc3 coating a CIGS solar cell	(a) CH_3CN 0.1 $TBAPF_6$ 2% v/v H_2O In PEC 100 mW/cm2	-2.08 V vs. Fc^+/Fc	**-7.0 mA cm^{-2} 90 %FE selectivity CO 93% 3 h experiment solar-to-CO reaches 0.75%**	This work
	(b) CH_3CN 0.1 $TBAPF_6$ 1 % v/v H_2O In PEC 100 mW cm2	-1.83 V vs. Fc^+/Fc	**-1.25 mA cm^{-2} selectivity CO 90% 10 h experiment**	This work
	(c) CH_3CN 0.1 $TBAPF_6$ 2% v/v H_2O In PEC 100 mW/cm2	-1.88 V vs. Fc^+/Fc	**-4.0 mA cm^{-2} FE 98% . selectivity CO 93% 4 h experiment**	This work

As the SCE electrode is not a standard reference for a non-aqueous system, the recorded potentials vs SCE were converted to E vs Fc/Fc+ by the following equation: E(vs Fc/Fc+) = E(vs SCE) – E°(Fc/Fc+), where the Fc/Fc+ potential vs SCE is measured as 0.380 V in acetonitrile.

Comparing PEC CO_2 reduction systems is not an easy task. Several factors need to be taken into account. The majority of the reported PEC systems were implemented in aqueous solutions, and the photoelectrode material may differ in composition or structure between one report to another. The amount of catalyst incorporated into the photoelectrode can also vary, as well as the bias potential and time for photoelectrolysis. The table presented summarizes the results of a few of the most recently reported EC and PEC systems that have features in common or comparable to our system, such as the solvent and the photoelectrode material.

Table IV.2 entries 1 and 2 refer to Cu_2O photo absorbers, instead of CIGS, but working in the same solvent (CH_3CN). EC and PEC systems are reported. These systems present quite low current densities even using a precious metal (Re) complex, with a maximum value reported of -1.75 mA cm^{-2} at -1.9 V vs. Fc/Fc^+ bias potential, compared to our system, this current density remains less than a half of the current density reached by our CIGS/CdS/ZnO/AZO+ZnO|CoPc3 photocathode in very similar PEC conditions, which can reach current densities from -4.0 up to -7.0 mA cm^{-2} (entry 7a and 7c) at -1.88 and -2.08 V vs. Fc/Fc^+ bias potential, respectively.

The high selectivity of our hybrid layers, either deposited on a conductive substrate (working in EC conditions), or deposited on a photoelectrode (PEC conditions), compares favourably with other state-of-the-art photocathodes.

Furthermore, we compare our preliminary results in aqueous solution (entry 6) with two PEC systems from literature (entries 3 and 4) in which the photoelectrode material is the same used in this thesis, a CIGS solar cell. These results were indeed obtained under different conditions; the PEC experiments were carried out at different applied potentials -0.2 and -0.06 V vs. RHE, reaching current densities of -4.8.0 mA cm^{-2} and 0.81 mA cm^{-2}, respectively. We can notice that the performance (current density, stability, selectivity) reached by our PEC system is comparable with the one reached by the previous PEC system presented by the LEM laboratory (entry 4).[29] In our preliminary results, a small enhancement was reached in the current density reached (-0.85 mA $cm^{-}2$) at a slightly more positive bias potential (compare entries 4 and 6).

IV.5 Conclusions

The results presented in this section illustrate an efficient hybrid photoelectrode consisting of the electrochemically growth ZnO|CoPc3 layer on CIGS solar cell photoelectrodes for the photoelectrochemical carbon dioxide reduction. The developed CIGS/CdS/ZnO/AZO+ZnO|CoPc3 device afforded selective CO formation from CO_2 with high current density (up to −7.0 mA cm^{-2} at −1.7 V vs SCE under visible light irradiation). The excellent performance of the device can be explained by a combination of the excellent catalytic properties of the hybrid layer formed by the ZnO and the CoPc3 molecular catalyst, and by the combined effects including high light harvesting efficiency of CIGS, fast charge transport between the CIGS cell layers, allowing electron to reach the catalytic centers into the last layer, and fast CO_2 reduction rate at the catalytic sites. To the best of our knowledge, this work represents the first demonstration where a CIGS electrode has been successfully used for CO_2 photoelectrocatalytic reduction in an organic solvent.

We demonstrated that for improving the catalytic performance of the modified CIGS photoelectrodes, various parameters such as, the thickness of the hybrid nanoporous layer, the amount of protons in the electrolyte, and the reaction potential must be optimized in parallel. These improvements led to the first CIGS device incorporating a molecular catalyst via a method other than covalent immobilization of catalyst on the surface of electrodes, demonstrating photoelectrocatalytic activity for the reduction of CO_2 to CO, with 93% of product selectivity.

We took into account the best conditions to add a catalytic layer to the device while affecting its photovoltaic efficiency the least. We concluded that the incorporation of a thin hybrid layer of around 350 nm was sufficient to make our device catalytically active and efficient.

The findings shown here lead to the development of better-performing photocathode for CO_2 reduction. The system may still be significantly improved with a higher catalyst loading, using a different catalyst molecule able to reduce CO_2 to other product than CO, with strategy such as nanostructuration of the last oxide layer. Eventually, it could also be possible to add a different metal oxide matrix (a doped ZnO, ITO) for the incorporation of the catalyst into the last layer of the device. We could also think in a further improvement of the system by combining the catalytic hybrid layer with other light absorbing materials. This suggests a large scope for further improvement. This

work not only puts forward a promising strategy for designing advanced performance photoelectrodes, but also opens up a large scope of possibilities for the design of new different photoelectrodes.

Chapter V

General conclusions and perspectives

V Conclusions and perspectives

V.1 Key findings

The purpose of this thesis was to synergistically combine the fields of materials for photovoltaics and molecular catalysis by developing versatile transparent & conductive nano-structured electrodes integrating earth abundant molecular catalysts and adaptable to Cu(In,Ga)Se_2 based solar cells for photo-electro-reduction of CO_2.

The development of an assembly strategy for introducing the molecular catalyst inside the transparent conducting electrodes was a critical factor in the preparation of transparent and nanostructured photoelectrodes with high catalytic efficiencies. As a proof of concept, these multifunctional window layers were integrated and tested at the front contact of highly efficient Cu(In,Ga)Se_2 solar cells.

First, we develop an inorganic/organic hybrid layers, including zinc oxide and a molecular catalyst, with a catalytic activity toward the electrochemical CO_2 reduction reaction. A one-step electrochemical method was used for that, in which ZnO layers were electrodeposited in aerated solutions from a metal salt precursor in the presence of a soluble catalyst. This leads to concomitantly encapsulate the molecular catalyst inside the oxide layer. The one-step electrodeposition method enables the preparation of electrodes containing a very low amount of molecular catalyst while still providing good catalytic activity towards CO_2 reduction.

Three electrodeposited nanostructured window layers have been mainly explored**:** metal oxide/catalyst hybrid nanoporous structure (NPS) with sponge-like structure at a nanoscale level, Nanorod ZnO structures (ZNR); and multiscale 3D hierarchical structures based on the nanoporous ZnO structure NPS grown on ZNRs.

For the nanoporous structure (NPS), we showed that it is possible to precisely control the thickness of the oxide layer (from a few tens of nm to a micrometer) and the concentration of the catalyst, by varying the deposition time. The incorporation of the molecular catalysts was demonstrated by different techniques (UV-vis, ICP, XPS, ATR-IR and EDX-mapping). It appears that molecular catalysts are homogeneously dispersed in the metal oxide matrix. The accessibility and catalytic activity of the electrodeposited layers was confirmed by linear/cyclic voltammetry and CPE experiments. We showed that there is a contribution in the catalytic activity from both the ZnO matrix

and the molecular catalyst, with the latter offering a high selectivity towards CO production.

Furthermore, we discovered that adding a small amount of water to the acetonitrile up to 0.67 M (2%) results in an increase in current density and a 250 mV decrease in the over potential of the CO_2 reduction. In these conditions, increasing the thickness of the nanoporous layers allows to reach higher current densities up to -5.0 mA cm^{-2} for a 1 µm thick with a bias potential of -2.1 V vs SCE in acetonitrile solution, while achieving a CO selectivity of 98%.

Once the system optimized, several molecular catalysts (Co, Ni) based on derivatives of porphyrin and/or phthalocyanines have been integrated to the nanostructured layer resulting in hybrid layers with similar selectivity and catalytic efficiencies.

Finally, we showed that by combining nanoporous ZnO structure (NPS) grown on nanoroad ZnO layers it is possible to reach for a bias potential of -2.1 V vs SCE, current densities up to -3 mA cm^{-2} for only 20 nm of nanoporous layer.

In a 2nd step, using a light assisted electrodeposition process, these functional window layers were integrated to the surface of high efficiency CIGS-based solar cells. A strong emphasis has been placed on the modification of the window layers and understanding the impact of the hybrid nanostructure morphology and composition on light absorption in the CIGS solar cells. The developed CIGS/CdS/ZnO/AZO/ZnO|catalyst showed current density up to −7 mA cm^{-2} at −1.7 V vs SCE under visible light irradiation in acetonitrile solution, with CO selectivity >92%.

The performance of the modified CIGS photoelectrodes in PEC CO_2 reduction in aqueous solutions was also investigated. Preliminary experiments have shown that CIGS/CdS/ZnO/AZO/ZnO|catalyst electrodes can effectively reduce CO_2 to CO, with an average current density of -0.85 mA cm^{-2} at -0.057 V vs. RHE and a 87% CO selectivity.

This study is the first to describe a CIGS cell as a constituent of a molecular-based photocathode CO_2 reduction in an organic solvent that exhibit outstanding CO_2 PEC reduction performance (high selectivity and good stability) and high photocurrent under illumination. In particular, our study resulted in the first CIGS device incorporating a molecular catalyst via a method other than covalent immobilization on the surface. In addition, we have also explored the performance of our devices in a PEC CO_2 reduction system in water, obtaining very encouraging results which open up a number of possibilities for further improvement.

V.2 Experimental perspectives

As a proof-of-concept, we showed that it is possible to functionalize the window layers of high efficiency CIGS based solar cells. Moreover, the highly electrochemically active nature of the molecules through the zinc oxide layer have been shown. While these results are very promising, further optimization of their stability is missing, as well as, the possibility of integrating the best multifunctional window layers with other single junction or tandem high efficiency solar cells in terms of compatibility and performance such as Perovskites, tandem Si/perovskite or tandem CIGS/perovskite based solar cells.

- **Study of the degradation of the ZnO|catalyst hybrid layers – Improvement of the long term stability**

Long term electrolysis experiments presented in the previous section have evidenced a drawback of the hybrid ZnO|catalyst layers. CO_2 electrolysis experiments at an applied potential of -2.1 V vs. SCE did not last more than one hour. For a better understanding of the degradation mechanism, a series of deeper studies need to be made. Currently, some analyses (XPS, ICP, etc.) are planned to be perform with ZnO|catalyst electrodes after electrolysis, in order in order to determine possible degradation pathways. Low stability could come from a degradation of the ZnO matrix at such negative potential (-2.1 vs SCE) but also from a possible leak of the catalyst from the layer to the electrolyte solution.

The improvement of the stability of the proposed hybrid layers could be achieved by doping the inorganic matrix with metal ions such Cu^{2+}, Ni^{2+}, Al^{3+} or Ti^{4+}. That could be made by adding the ions in the bath deposition solution used for the growth of the hybrid layers. Furthermore, the presence of these metals in the layer may improve the layer's catalytic activity.

- **Catalysis beyond CO production**

As a general idea, it would be possible to incorporate catalysts (e.g. molecular complex, nanoparticles) able to drive CO_2 reduction beyond two electron process, thereby producing other fuel molecules (e.g. methanol, methane).

- **Exploring different PV materials**

Since the proposed metal-oxide|catalyst layers present high transmittance in the visible range, other semiconductor materials such as p-Silicon, GaP or tandem solar cells could be used to replace CIGS absorbers, resulting in photoelectrodes for PEC reduction of CO_2 with higher photovoltage or higher current densities.

VI References

1. North, M. "What is CO2? Thermodynamics, Basic Reactions and Physical Chemistry." Carbon Dioxide Utilisation. *Elsevier*, 2015. pp. 3–17.
2. Xu, Q., Xia, Z., et al. "Recent advances in solar-driven CO2 reduction over g-C3N4-based photocatalysts," *Carbon Energy,* 2022;1–43.
3. Blunden, J. and D. S. Arndt, Eds., 2019: State of the Climate in 2018. Bull. *Amer. Meteor. Soc*., 100 (9), Si–S305, doi:10.1175/2019BAMSStateoftheClimate.1.
4. Kim, J., and Kwon, E. E. "Photoconversion of carbon dioxide into fuels using semiconductors," *Journal of CO2 Utilization*, V. 33, 2019, pp. 72–82.
5. Li, T.-T., Mei, Y., Li, H., et al. "Highly Selective and Active Electrochemical Reduction of CO_2 to CO on a Polymeric Co(II) Phthalocyanine@Graphitic Carbon Nitride Nanosheet–Carbon Nanotube Composite," *Inorganic Chemistry*, V. 59, No. 19, 2020, pp. 14184–92.
6. Halmann, M. "Photoelectrochemical reduction of aqueous carbon dioxide on p-type gallium phosphide in liquid junction solar cells," *Nature*, V. 275, No. 5676, 1978, pp. 115–6.
7. Li, D., Yang, K., Lian, J., et al. "Powering the World with Solar Fuels from Photoelectrochemical CO_2 Reduction: Basic Principles and Recent Advances," *Advanced Energy Materials*, 2022, p. 2201070.
8. Chang, X., Wang, T., Yang, P., et al. "The Development of Cocatalysts for Photoelectrochemical CO_2 Reduction," *Advanced Materials*, V. 31, No. 31, 2019, p. 1804710.
9. Olivo, A., Zanardo, D., Ghedini, E., et al. "Solar Fuels by Heterogeneous Photocatalysis: From Understanding Chemical Bases to Process Development," *Chem Engineering*, V. 2, No. 3, 2018, p. 42.
10. Hannah Ritchie and Max Roser and Pablo Rosado. "CO_2 and Greenhouse Gas Emissions," 2020.
11. Jiang, Z., Xiao, T., Kuznetsov, V. L., et al. "Turning carbon dioxide into fuel," *Philosophical Transactions of the Royal Society A: Mathematical, Physical and Engineering Sciences*, V. 368, No. 1923, 2010, pp. 3343–64.
12. IEA (2021), World Energy Outlook 2021, IEA, Paris https://www.iea.org/reports/world-energy-outlook-2021
13. Jones, W. D. "Carbon Capture and Conversion," *Journal of the American Chemical Society*, V. 142, No. 11, 2020, pp. 4955–7.
14. Consoli, C. P., and Wildgust, N. "Current Status of Global Storage Resources," *Energy Procedia*, V. 114, 2017, pp. 4623–8.
15. Robert, M. "Running the Clock: CO_2 Catalysis in the Age of Anthropocene," *ACS Energy Letters*, V. 1, No. 1, 2016, pp. 281–2.
16. Xu, S., and Carter, E. A. "Theoretical Insights into Heterogeneous (Photo)electrochemical CO_2 Reduction," *Chemical Reviews*, V. 119, No. 11, 2019, pp. 6631–69.
17. Listorti, A., Durrant, J., and Barber, J. "Solar to fuel," *Nature Materials*, V. 8, No. 12, 2009, pp. 929–30.

18. Li, Z., Feng, J., Yan, S., et al. "Solar fuel production: Strategies and new opportunities with nanostructures," *Nano Today*, V. 10, No. 4, 2015, pp. 468–86.
19. Lewis, N. S., and Nocera, D. G. "Powering the planet: Chemical challenges in solar energy utilization," *Proceedings of the National Academy of Sciences*, V. 103, No. 43, 2006, pp. 15729–35.
20. Spitler, M. T., Modestino, M. A., Deutsch, T. G., et al. "Practical challenges in the development of photoelectrochemical solar fuels production," *Sustainable Energy & Fuels*, V. 4, No. 3, 2020, pp. 985–95.
21. White, J. L., Baruch, M. F., Pander, J. E., et al. "Light-Driven Heterogeneous Reduction of Carbon Dioxide: Photocatalysts and Photoelectrodes," *Chemical Reviews*, V. 115, No. 23, 2015, pp. 12888–935.
22. Schreier, M., Luo, J., Gao, P., et al. "Covalent Immobilization of a Molecular Catalyst on Cu $_2$ O Photocathodes for CO $_2$ Reduction," *Journal of the American Chemical Society*, V. 138, No. 6, 2016, pp. 1938–46.
23. Paracchino, A., Laporte, V., Sivula, K., et al. "Highly active oxide photocathode for photoelectrochemical water reduction," *Nature Materials*, V. 10, No. 6, 2011, pp. 456–61.
24. Li, C., Wang, T., Liu, B., et al. "Photoelectrochemical CO $_2$ reduction to adjustable syngas on grain-boundary-mediated a-Si/TiO $_2$ /Au photocathodes with low onset potentials," *Energy & Environmental Science*, V. 12, No. 3, 2019, pp. 923–8.
25. Gurudayal, G., Beeman, J. W., Bullock, J., et al. "Si photocathode with Ag-supported dendritic Cu catalyst for CO $_2$ reduction," *Energy & Environmental Science*, V. 12, No. 3, 2019, pp. 1068–77.
26. Roy, S., Miller, M., Warnan, J., et al. "Electrocatalytic and Solar-Driven Reduction of Aqueous CO $_2$ with Molecular Cobalt Phthalocyanine–Metal Oxide Hybrid Materials," *ACS Catalysis*, V. 11, No. 3, 2021, pp. 1868–76.
27. Zhou, B., Kong, X., Vanka, S., et al. "A GaN:Sn nanoarchitecture integrated on a silicon platform for converting CO $_2$ to HCOOH by photoelectrocatalysis," *Energy & Environmental Science*, V. 12, No. 9, 2019, pp. 2842–8.
28. Liu, G., Narangari, P. R., Trinh, Q. T., et al. "Manipulating Intermediates at the Au–TiO $_2$ Interface over InP Nanopillar Array for Photoelectrochemical CO $_2$ Reduction," *ACS Catalysis*, V. 11, No. 18, 2021, pp. 11416–28.
29. Pati, P. B., Wang, R., Boutin, E., et al. "Photocathode functionalized with a molecular cobalt catalyst for selective carbon dioxide reduction in water," *Nature Communications*, V. 11, No. 1, 2020, p. 3499.
30. Hu, Z., Gong, J., Ye, Z., et al. "Cu(In,Ga)Se2 for selective and efficient photoelectrochemical conversion of CO2 into CO," *Journal of Catalysis*, V. 384, 2020, pp. 88–95.
31. Kim, J. H., Hansora, D., Sharma, P., et al. "Toward practical solar hydrogen production – an artificial photosynthetic leaf-to-farm challenge," *Chem Soc Rev*, 2019, p. 65.

32. Tran, P. D., Wong, L. H., Barber, J., et al. "Recent advances in hybrid photocatalysts for solar fuel production," *Energy & Environmental Science*, V. 5, No. 3, 2012, p. 5902.
33. Kumar, B., Llorente, M., Froehlich, J., et al. "Photochemical and Photoelectrochemical Reduction of CO_2," *Annual Review of Physical Chemistry*, V. 63, No. 1, 2012, pp. 541–69.
34. Montoya, J. H., Seitz, L. C., Chakthranont, P., et al. "Materials for solar fuels and chemicals," *Nature Materials*, V. 16, No. 1, 2017, pp. 70–81.
35. Ardo, S., Fernandez Rivas, D., Modestino, M. A., et al. "Pathways to electrochemical solar-hydrogen technologies," *Energy & Environmental Science*, V. 11, No. 10, 2018, pp. 2768–83.
36. Boutin, E., Merakeb, L., Ma, B., et al. "Molecular catalysis of CO_2 reduction: recent advances and perspectives in electrochemical and light-driven processes with selected Fe, Ni and Co aza macrocyclic and polypyridine complexes," *Chemical Society Reviews*, V. 49, No. 16, 2020, pp. 5772–809.
37. Dalle, K. E., Warnan, J., Leung, J. J., et al. "Electro- and Solar-Driven Fuel Synthesis with First Row Transition Metal Complexes," *Chemical Reviews*, V. 119, No. 4, 2019, pp. 2752–875.
38. Takeda, H., Cometto, C., Ishitani, O., et al. "Electrons, Photons, Protons and Earth-Abundant Metal Complexes for Molecular Catalysis of CO_2 Reduction," *ACS Catalysis*, V. 7, No. 1, 2017, pp. 70–88.
39. Leung, C.-F., and Ho, P.-Y. "Molecular Catalysis for Utilizing CO2 in Fuel Electro-Generation and in Chemical Feedstock," *Catalysts*, V. 9, No. 9, 2019, p. 760.
40. Pang, H., Masuda, T., Ye, J. "Semiconductor-Based Photoelectrochemical Conversion of Carbon Dioxide" *Chem. Asian J.* 2018, 13. pp. 127 - 142
41. Garcia Osorio, D. A., Neri, G., and Cowan, A. J. "Hybrid Photocathodes for Carbon Dioxide Reduction: Interfaces for Charge Separation and Selective Catalysis," *ChemPhotoChem*, V. 5, No. 7, 2021, pp. 595–610.
42. Ding, P., Jiang, T., Han, N., et al. "Photocathode engineering for efficient photoelectrochemical CO2 reduction," *Materials Today Nano*, V. 10, 2020, p. 100077.
46. Brian, C., O.J, M., Srinivasan, S., "Electrochemistry in transition: From the 20th to the 21 century" *Plenum Press.* 1992. pp 381 - 396
44. Zheng, Y., Zhang, W., Li, Y., et al. "Energy related CO2 conversion and utilization: Advanced materials/nanomaterials, reaction mechanisms and technologies," *Nano Energy*, V. 40, 2017, pp. 512–39.
48. Surdhar, P. S., Mezyk, S. P., and Armstrong, D. A. "Reduction Potential of the 'COP-Radical Anion in Aqueous Solutions," Vol. 93. N° 8. 1989. p 3361.
46. Kumar, A., Hasija, V., Sudhaik, A., et al. "Artificial leaf for light-driven CO2 reduction: Basic concepts, advanced structures and selective solar-to-chemical products," *Chemical Engineering Journal*, V. 430, 2022, p. 133031.
47. Costentin, C., Robert, M., Savéant, J.-M., et al. "Efficient and selective molecular catalyst for the CO_2 -to-CO electrochemical conversion in water," *Proceedings of the National Academy of Sciences*, V. 112, No. 22, 2015, pp. 6882–6.

48. Kinzel, N. W., Werlé, C., and Leitner, W. "Transition Metal Complexes as Catalysts for the Electroconversion of CO_2: An Organometallic Perspective," *Angewandte Chemie International Edition*, 2021, p. anie.202006988.
49. Li, M., Garg, S., Chang, X., et al. "Toward Excellence of Transition Metal-Based Catalysts for CO_2 Electrochemical Reduction: An Overview of Strategies and Rationales," *Small Methods*, V. 4, No. 7, 2020, p. 2000033.
50. Choi, J., Wagner, P., Jalili, R., et al. "A Porphyrin/Graphene Framework: A Highly Efficient and Robust Electrocatalyst for Carbon Dioxide Reduction," *Adv. Energy Mater.*, 2018, p. 14.
51. Tatin, A., Comminges, C., Kokoh, B., et al. "Efficient electrolyzer for CO_2 splitting in neutral water using earth-abundant materials," *Proceedings of the National Academy of Sciences*, V. 113, No. 20, 2016, pp. 5526–9.
52. Maurin, A., and Robert, M. "Noncovalent Immobilization of a Molecular Iron-Based Electrocatalyst on Carbon Electrodes for Selective, Efficient CO_2 -to-CO Conversion in Water," *Journal of the American Chemical Society*, V. 138, No. 8, 2016, pp. 2492–5.
53. Costentin, C., Robert, M., Savéant, J.-M., et al. "Efficient and selective molecular catalyst for the CO_2 -to-CO electrochemical conversion in water," *Proceedings of the National Academy of Sciences*, V. 112, No. 22, 2015, pp. 6882–6.
54. Wang, M., Chen, L., Lau, T.-C., et al. "A Hybrid Co Quaterpyridine Complex/Carbon Nanotube Catalytic Material for CO_2 Reduction in Water," *Angewandte Chemie International Edition*, V. 57, No. 26, 2018, pp. 7769–73.
55. Wang, M., Torbensen, K., Salvatore, D., et al. "CO2 electrochemical catalytic reduction with a highly active cobalt phthalocyanine," *Nature Communications*, V. 10, No. 1, 2019, p. 3602.
56. Zhang, X., Wu, Z., Zhang, X., et al. "Highly selective and active CO2 reduction electrocatalysts based on cobalt phthalocyanine/carbon nanotube hybrid structures," *Nature Communications*, V. 8, No. 1, 2017, p. 14675.
57. Choi, J., Wagner, P., Gambhir, S., et al. "Steric Modification of a Cobalt Phthalocyanine/Graphene Catalyst To Give Enhanced and Stable Electrochemical CO_2 Reduction to CO," *ACS Energy Letters*, V. 4, No. 3, 2019, pp. 666–72.
58. Chen, C. "Enhanced CO2 electroreduction via interaction of dangling S bonds and Co sites in cobalt phthalocyanine/ZnIn2S4 hybrids," *Chemical Science*, 2019, p. 5.
59. Bonin, J., Maurin, A., and Robert, M. "Molecular catalysis of the electrochemical and photochemical reduction of CO2 with Fe and Co metal based complexes. Recent advances," *Coordination Chemistry Reviews*, V. 334, 2017, pp. 184–98.
60. Chen, L., Guo, Z., Wei, X.-G., et al. "Molecular Catalysis of the Electrochemical and Photochemical Reduction of CO_2 with Earth-Abundant Metal Complexes. Selective Production of CO vs HCOOH by Switching of the Metal Center," *Journal of the American Chemical Society*, V. 137, No. 34, 2015, pp. 10918–21.

61. Boutin, E., Wang, M., Lin, J. C., et al. "Aqueous Electrochemical Reduction of Carbon Dioxide and Carbon Monoxide into Methanol with Cobalt Phthalocyanine," *Angewandte Chemie International Edition*, V. 58, No. 45, 2019, pp. 16172–6.
62. Rao, H., Lim, C.-H., Bonin, J., et al. "Visible-Light-Driven Conversion of CO_2 to CH_4 with an Organic Sensitizer and an Iron Porphyrin Catalyst," *Journal of the American Chemical Society*, V. 140, No. 51, 2018, pp. 17830–4.
63. de la Torre, G., Vázquez, P., Agulló-López, F., et al. "Role of Structural Factors in the Nonlinear Optical Properties of Phthalocyanines and Related Compounds," *Chemical Reviews*, V. 104, No. 9, 2004, pp. 3723–50.
64. Martínez-Díaz, M. V., de la Torre, G., and Torres, T. "Lighting porphyrins and phthalocyanines for molecular photovoltaics," *Chemical Communications*, V. 46, No. 38, 2010, p. 7090.
65. Materna, K. L., Crabtree, R. H., and Brudvig, G. W. "Anchoring groups for photocatalytic water oxidation on metal oxide surfaces," *Chemical Society Reviews*, V. 46, No. 20, 2017, pp. 6099–110.
66. Martini, L. A., Moore, G. F., Milot, R. L., et al. "Modular Assembly of High-Potential Zinc Porphyrin Photosensitizers Attached to TiO_2 with a Series of Anchoring Groups," *The Journal of Physical Chemistry C*, V. 117, No. 28, 2013, pp. 14526–33.
67. Pujari, S. P., Scheres, L., Marcelis, A. T. M., et al. "Covalent Surface Modification of Oxide Surfaces," *Angewandte Chemie International Edition*, V. 53, No. 25, 2014, pp. 6322–56.
68. Brennan, B. J., Llansola Portolés, M. J., Liddell, P. A., et al. "Comparison of silatrane, phosphonic acid, and carboxylic acid functional groups for attachment of porphyrin sensitizers to TiO2 in photoelectrochemical cells," *Physical Chemistry Chemical Physics*, V. 15, No. 39, 2013, p. 16605.
69. McNamara, W. R., Snoeberger III, R. C., Li, G., et al. "Hydroxamate anchors for water-stable attachment to TiO2 nanoparticles," *Energy & Environmental Science*, V. 2, No. 11, 2009, p. 1173.
70. Materna, K. L., Jiang, J., Crabtree, R. H., et al. "Silatrane Anchors for Metal Oxide Surfaces: Optimization for Potential Photocatalytic and Electrocatalytic Applications," *ACS Applied Materials & Interfaces*, V. 11, No. 6, 2019, pp. 5602–9.
71. Gong, L., Yin, H., Nie, C., et al. "Influence of Anchoring Groups on the Charge Transfer and Performance of p-Si/TiO_2/Cobaloxime Hybrid Photocathodes for Photoelectrochemical H_2 Production," *ACS Applied Materials & Interfaces*, V. 11, No. 37, 2019, pp. 34010–9.
72. Jiang, J., Spies, J. A., Swierk, J. R., et al. "Direct Interfacial Electron Transfer from High-Potential Porphyrins into Semiconductor Surfaces: A Comparison of Linkers and Anchoring Groups," *The Journal of Physical Chemistry C*, V. 122, No. 25, 2018, pp. 13529–39.
73. Yang, H., Wang, X., Hu, Q., et al. "Recent Progress in Self-Supported Catalysts for CO_2 Electrochemical Reduction," *Small Methods*, V. 4, No. 6, 2020, p. 1900826.
74. Bard, A. J., and Faulkner, L. R. "Electrochemical methods: fundamentals and applications," 2nd ed, New York, Wiley, 2001, 833 pp.

75. Bard, A. J., ed. "Encyclopedia of Electrochemistry: Online," 1st edition, Wiley, 2007.
76. Arai, T., Sato, S., Uemura, K., et al. "Photoelectrochemical reduction of CO2 in water under visible-light irradiation by a p-type InP photocathode modified with an electropolymerized ruthenium complexw," 2010, p. 3.
77. Arai, T., Tajima, S., Sato, S., et al. "Selective CO2 conversion to formate in water using a CZTS photocathode modified with a ruthenium complex polymerwz," 2011, p. 4.
78. Sekizawa, K., Sato, S., Arai, T., et al. "Solar-Driven Photocatalytic CO_2 Reduction in Water Utilizing a Ruthenium Complex Catalyst on p-Type Fe_2O_3 with a Multi-heterojunction," *ACS Catalysis*, V. 8, No. 2, 2018, pp. 1405–16.
79. Liu, J., Shi, H., Shen, Q., et al. "Efficiently photoelectrocatalyze CO 2 to methanol using Ru(II)-pyridyl complex covalently bonded on TiO 2 nanotube arrays," *Applied Catalysis B: Environmental*, V. 210, 2017, pp. 368–78.
80. Alenezi, K., Ibrahim, S. K., Li, P., et al. "Solar Fuels: Photoelectrosynthesis of CO from CO_2 at p-Type Si using Fe Porphyrin Electrocatalysts," *Chemistry - A European Journal*, V. 19, No. 40, 2013, pp. 13522–7.
81. Torralba-Peñalver, E., Luo, Y., Compain, J.-D., et al. "Selective Catalytic Electro-reduction of CO_2 at Silicon Nanowires (SiNWs) Photocathodes Using Non-Noble Metal-Based Manganese Carbonyl Bipyridyl Molecular Catalysts in Solution and Grafted onto SiNWs," *ACS Catalysis*, V. 5, No. 10, 2015, pp. 6138–47.
82. He, D., Jin, T., Li, W., et al. "Photoelectrochemical CO_2 Reduction by a Molecular Cobalt(II) Catalyst on Planar and Nanostructured Si Surfaces," *Chemistry - A European Journal*, V. 22, No. 37, 2016, pp. 13064–7.
83. Deng, X., Li, R., Wu, S., et al. "Metal–Organic Framework Coating Enhances the Performance of Cu_2O in Photoelectrochemical CO_2 Reduction," *Journal of the American Chemical Society*, V. 141, No. 27, 2019, pp. 10924–9.
84. Powalla, M., Paetel, S., Ahlswede, E., et al. "Thin-film solar cells exceeding 22% solar cell efficiency: An overview on CdTe-, $Cu(In,Ga)Se_2$ -, and perovskite-based materials," *Applied Physics Reviews*, V. 5, No. 4, 2018, p. 041602.
85. Riverola, A., Vossier, A., and Chemisana, D. "Fundamentals of solar cells." Nanomaterials for Solar Cell Applications. Elsevier, 2019. pp. 3–33.
86. Soga, T. "Fundamentals of Solar Cell." Nanostructured Materials for Solar Energy Conversion. Elsevier, 2006. pp. 3–43.
87. Markvart, T., and Castañer, L. "Semiconductor Materials and Modelling." Practical Handbook of Photovoltaics. Elsevier, 2012. pp. 33–62.
88. Kazmerski, L. L., White, F. R., and Morgan, G. K. "Thin-film $CuInSe_2$ /CdS heterojunction solar cells," *Applied Physics Letters*, V. 29, No. 4, 1976, pp. 268–70.
89. Ramanujam, J., and Singh, U. P. "Copper indium gallium selenide based solar cells – a review," *Energy & Environmental Science*, V. 10, No. 6, 2017, pp. 1306–19.
90. Saji, V. S., Choi, I.-H., and Lee, C.-W. "Progress in electrodeposited absorber layer for CuIn(1−x)GaxSe2 (CIGS) solar cells," *Solar Energy*, V. 85, No. 11, 2011, pp. 2666–78.

91. Mohan, R., and Paulose, R. "Brief Review on Copper Indium Gallium Diselenide (CIGS) Solar Cells." In: Yang, X.-Y., ed. Photoenergy and Thin Film Materials. Hoboken, NJ, USA, John Wiley & Sons, Inc., 2019. pp. 157–92.
92. Mufti, N., Amrillah, T., Taufiq, A., et al. "Review of CIGS-based solar cells manufacturing by structural engineering," *Solar Energy*, V. 207, 2020, pp. 1146–57.
93. Ramanujam, J., and Singh, U. P. "Copper indium gallium selenide based solar cells – a review," *Energy & Environmental Science*, V. 10, No. 6, 2017, pp. 1306–19.
94. Rau, U., and Schock, H. W. "Cu(In,Ga)Se2 Thin-Film Solar Cells." Practical Handbook of Photovoltaics. Elsevier, 2012. pp. 323–71.
95. Lincot, D., and Guillemoles, J.-F. "Cellules solaires en couches minces à base de CuInSe $_2$," *Reflets de la physique*, No. 5, 2007, pp. 16–9.
96. Rau, U., and Schock, H. W. "Cu(In,Ga)Se2 Thin-Film Solar Cells." Practical Handbook of Photovoltaics. Elsevier, 2012. pp. 323–71.
97. Singh, U. P., and Patra, S. P. "Progress in Polycrystalline Thin-Film Cu(In,Ga) Se 2 Solar Cells," *International Journal of Photoenergy*, V. 2010, 2010, pp. 1–19.
98. Ghosh, A. "Fenestration integrated BIPV (FIPV): A review," *Solar Energy*, V. 237, 2022, pp. 213–30.
102. Izaki, M., and Omi, T. "Transparent zinc oxide films prepared by electrochemical reaction," *Appl. Phys. Lett.* 1996 68, 2439
100. Peulon, S., and Lincot, D. "Cathodic electrodeposition from aqueous solution of dense or open-structured zinc oxide films," *Advanced Materials*, V. 8, No. 2, 1996, pp. 166–70.
101. Pauporté, Th., and Lincot, D. "Heteroepitaxial electrodeposition of zinc oxide films on gallium nitride," *Applied Physics Letters*, V. 75, No. 24, 1999, pp. 3817–9.
102. Yoshida, T., and Minoura, H. "Electrochemical Self-Assembly of Dye-Modified Zinc Oxide Thin Films," *Adv. Mater.*, No. 16, 2000, p. 4.
103. Haller, S., Suguira, T., Lincot, D., et al. "Design of a hierarchical structure of ZnO by electrochemistry for ZnO-based dye-sensitized solar cells: Design of a hierarchical structure of ZnO by electrochemistry," *physica status solidi (a)*, V. 207, No. 10, 2010, pp. 2252–7.
104. Jehl, Z., Rousset, J., Donsanti, F., et al. "Electrodeposition of ZnO nanorod arrays on ZnO substrate with tunable orientation and optical properties," *Nanotechnology*, V. 21, No. 39, 2010, p. 395603.
105. Pauporté, Th., Bataille, G., Joulaud, L., et al. "Well-Aligned ZnO Nanowire Arrays Prepared by Seed-Layer-Free Electrodeposition and Their Cassie−Wenzel Transition after Hydrophobization," *The Journal of Physical Chemistry C*, V. 114, No. 1, 2010, pp. 194–202.
106. Yoshida, T., Tochimoto, M., Schlettwein, D., et al. "Self-Assembly of Zinc Oxide Thin Films Modified with Tetrasulfonated Metallophthalocyanines by One-Step Electrodeposition," *Chemistry of Materials*, V. 11, No. 10, 1999, pp. 2657–67.
107. Pauporté, T., Bedioui, F., and Lincot, D. "Nanostructured zinc oxide–chromophore hybrid films with multicolored electrochromic properties," *J. Mater. Chem.*, V. 15, No. 15, 2005, pp. 1552–9.

108. Yoshida, T., Terada, K., Schlettwein, D., et al. "Electrochemical Self-Assembly of Nanoporous ZnO/Eosin Y Thin Films and Their Sensitized Photoelectrochemical Performance," *Adv. Mater.*, No. 16, 2000, p. 4.
109. Kołodziejczak-Radzimska, A., and Jesionowski, T. "Zinc Oxide—From Synthesis to Application: A Review," *Materials*, V. 7, No. 4, 2014, pp. 2833–81.
110. Zhao, Y., Liu, N., Zhou, S., et al. "Two-dimensional ZnO for the selective photoreduction of CO $_2$," *Journal of Materials Chemistry A*, V. 7, No. 27, 2019, pp. 16294–303.
111. Jiang, X., Cai, F., Gao, D., et al. "Electrocatalytic reduction of carbon dioxide over reduced nanoporous zinc oxide," *Electrochemistry Communications*, V. 68, 2016, pp. 67–70.
112. Geng, Z., Kong, X., Chen, W., et al. "Oxygen Vacancies in ZnO Nanosheets Enhance CO $_2$ Electrochemical Reduction to CO," *Angewandte Chemie*, V. 130, No. 21, 2018, pp. 6162–7.
113. Luo, W., Zhang, Q., Zhang, J., et al. "Electrochemical reconstruction of ZnO for selective reduction of CO2 to CO," *Applied Catalysis B: Environmental*, V. 273, 2020, p. 119060.
114. Liu, C.-F., Lu, Y.-J., and Hu, C.-C. "Effects of Anions and pH on the Stability of ZnO Nanorods for Photoelectrochemical Water Splitting," *ACS Omega*, V. 3, No. 3, 2018, pp. 3429–39.
119. Labat, F., et al. "First Principles Modeling of Eosin-Loaded ZnO Films: A Step toward the Understanding of Dye-Sensitized Solar Cell Performances" *J. AM. Chem. Soc*. 2009. 131, 14290 - 14298.
116. Rahman, F. "Zinc oxide light-emitting diodes: a review," *Optical Engineering*, V. 58, No. 01, 2019, p. 1.
117. Cebulla, R., Wendt, R., and Ellmer, K. "Al-doped zinc oxide films deposited by simultaneous rf and dc excitation of a magnetron plasma: Relationships between plasma parameters and structural and electrical film properties," *Journal of Applied Physics*, V. 83, No. 2, 1998, pp. 1087–95.
118. Assunção, V., Fortunato, E., Marques, A., et al. "Influence of the deposition pressure on the properties of transparent and conductive ZnO:Ga thin-film produced by r.f. sputtering at room temperature," *Thin Solid Films*, V. 427, Nos. 1–2, 2003, pp. 401–5.
119. Jie, J., Wang, G., Han, X., et al. "Indium-doped zinc oxide nanobelts," *Chemical Physics Letters*, V. 387, Nos. 4–6, 2004, pp. 466–70.
120. Sun, Y., Chen, L., Bao, Y., et al. "The Applications of Morphology Controlled ZnO in Catalysis," *Catalysts*, V. 6, No. 12, 2016, p. 188.
121. Kelly, S. R., Shi, X., Back, S., et al. "ZnO As an Active and Selective Catalyst for Electrochemical Water Oxidation to Hydrogen Peroxide," *ACS Catalysis*, V. 9, No. 5, 2019, pp. 4593–9.
122. Nguyen, D. L. T., Jee, M. S., Won, D. H., et al. "Selective CO $_2$ Reduction on Zinc Electrocatalyst: The Effect of Zinc Oxidation State Induced by Pretreatment Environment," *ACS Sustainable Chemistry & Engineering*, V. 5, No. 12, 2017, pp. 11377–86.

123. Liu, K., Wang, J., Shi, M., et al. "Simultaneous Achieving of High Faradaic Efficiency and CO Partial Current Density for CO_2 Reduction via Robust, Noble-Metal-Free Zn Nanosheets with Favorable Adsorption Energy," *Advanced Energy Materials*, V. 9, No. 21, 2019, p. 1900276.
124. Han, K., Ngene, P., and Jongh, P. "Structure Dependent Product Selectivity for CO_2 Electroreduction on ZnO Derived Catalysts," *ChemCatChem*, V. 13, No. 8, 2021, pp. 1998–2004.
125. Xiang, Q., Li, F., Wang, J., et al. "Heterostructure of ZnO Nanosheets/Zn with a Highly Enhanced Edge Surface for Efficient CO_2 Electrochemical Reduction to CO," *ACS Applied Materials & Interfaces*, V. 13, No. 9, 2021, pp. 10837–44.
126. Zong, X., Jin, Y., Li, Y., et al. "Morphology-controllable ZnO catalysts enriched with oxygen-vacancies for boosting CO2 electroreduction to CO," *Journal of CO2 Utilization*, V. 61, 2022, p. 102051.
127. Xin, C., Hu, M., Wang, K., et al. "Significant Enhancement of Photocatalytic Reduction of CO_2 with H_2O over ZnO by the Formation of Basic Zinc Carbonate," *Langmuir*, V. 33, No. 27, 2017, pp. 6667–76.
128. Jang, H. J., Yang, J. H., Maeng, J. Y., et al. "Photoelectrochemical CO2 Reduction Products Over Sandwiched Hybrid Ga2O3:ZnO/Indium/ZnO Nanorods," *Frontiers in Chemistry*, V. 10, 2022, p. 814766.
129. Zhang, L., Li, N., Jiu, H., et al. "ZnO-reduced graphene oxide nanocomposites as efficient photocatalysts for photocatalytic reduction of CO2," *Ceramics International*, V. 41, No. 5, 2015, pp. 6256–62.
130. Taunk, P. B., Das, R., Bisen, D. P., et al. "Synthesis and optical properties of chemical bath deposited ZnO thin film," *Karbala International Journal of Modern Science*, V. 1, No. 3, 2015, pp. 159–65.
131. Sánchez-Martín, S., Olaizola, S. M., Castaño, E., et al. "Study of deposition parameters and growth kinetics of ZnO deposited by aerosol assisted chemical vapor deposition," *RSC Advances*, V. 11, No. 30, 2021, pp. 18493–9.
132. Tynell, T., and Karppinen, M. "Atomic layer deposition of ZnO: a review," *Semiconductor Science and Technology*, V. 29, No. 4, 2014, p. 043001.
133. Khan, M. I., Bhatti, K. A., Qindeel, R., et al. "Characterizations of multilayer ZnO thin films deposited by sol-gel spin coating technique," *Results in Physics*, V. 7, 2017, pp. 651–5.
134. Dang, W. L., Fu, Y. Q., Luo, J. K., et al. "Deposition and characterization of sputtered ZnO films," *Superlattices and Microstructures*, V. 42, Nos. 1–6, 2007, pp. 89–93.
139. Nozik, A.J. "Photoelectrochemical cells" *Philosophical Transactions of the Royal Society of London*. 1980. A 295, 453-470.
136. Izaki, M., and Omi, T. "Transparent zinc oxide films prepared by electrochemical reaction," *Applied Physics Letters*, V. 68, No. 17, 1996, pp. 2439–40.
137. Michaelis, E., Wöhrle, D., Rathousky, J., et al. "Electrodeposition of porous zinc oxide electrodes in the presence of sodium laurylsulfate," *Thin Solid Films*, V. 497, Nos. 1–2, 2006, pp. 163–9.

142. Yoshida, T., Pauporte, T., Lincot, D., et al. "Cathodic Electrodeposition of ZnO/Eosin Y Hybrid Thin Films from Oxygen-Saturated Aqueous Solution of ZnCl2 and Eosin Y," *Journal of The Electrochemical Society*, 2003. 150 (9), C608-C615.
139. Pauporté, T., Yoshida, T., Cortès, R., et al. "Electrochemical Growth of Epitaxial Eosin/ZnO Hybrid Films," *The Journal of Physical Chemistry B*, V. 107, No. 37, 2003, pp. 10077–82.
140. Yoshida, T., Zhang, J., Komatsu, D., et al. "Electrodeposition of Inorganic/Organic Hybrid Thin Films," *Advanced Functional Materials*, V. 19, No. 1, 2009, pp. 17–43.
141. Pauporté, T., and Rathouský, J. "Electrodeposited Mesoporous ZnO Thin Films as Efficient Photocatalysts for the Degradation of Dye Pollutants," *The Journal of Physical Chemistry C*, V. 111, No. 21, 2007, pp. 7639–44.
142. Guérin, V.-M., and Pauporté, T. "From nanowires to hierarchical structures of template-free electrodeposited ZnO for efficient dye -sensitized solar cells," *Energy & Environmental Science*, V. 4, No. 8, 2011, pp. 2971–9.
143. Le Tulzo, H., Schneider, N., Lincot, D., et al. "Toward an all-Atomic Layer Deposition (ALD) process for Cu(In,Ga)(S,Se)2 (CIGS)-type solar cell," *Solar Energy Materials and Solar Cells*, V. 200, 2019, p. 109965.
144. Xing, W., Yin, M., Lv, Q., et al. "Oxygen Solubility, Diffusion Coefficient, and Solution Viscosity." Rotating Electrode Methods and Oxygen Reduction Electrocatalysts. Elsevier, 2014. pp. 1–31.
145. König, M., Vaes, J., Klemm, E., et al. "Solvents and Supporting Electrolytes in the Electrocatalytic Reduction of CO2," *iScience*, V. 19, 2019, pp. 135–60.
146. Mazzio, K. A., and Luscombe, C. K. "The future of organic photovoltaics," *Chemical Society Reviews*, V. 44, No. 1, 2015, pp. 78–90.
147. Costentin, C., Robert, M., and Savéant, J.-M. "Catalysis of the electrochemical reduction of carbon dioxide," *Chem. Soc. Rev.*, V. 42, No. 6, 2013, pp. 2423–36.
148. Wu, J., Huang, Y., Ye, W., et al. "CO $_2$ Reduction: From the Electrochemical to Photochemical Approach," *Advanced Science*, V. 4, No. 11, 2017, p. 1700194.
149. Zhang, X., Guo, S.-X., Gandionco, K. A., et al. "Electrocatalytic carbon dioxide reduction: from fundamental principles to catalyst design," *Materials Today Advances*, V. 7, 2020, p. 100074.
150. Kalamaras, E., Maroto-Valer, M. M., Shao, M., et al. "Solar carbon fuel via photoelectrochemistry," *Catalysis Today*, V. 317, 2018, pp. 56–75.
151. Cheng, W.-H., Richter, M. H., Sullivan, I., et al. "CO $_2$ Reduction to CO with 19% Efficiency in a Solar-Driven Gas Diffusion Electrode Flow Cell under Outdoor Solar Illumination," *ACS Energy Letters*, V. 5, No. 2, 2020, pp. 470–6.
153. Peulon, S., and Lincot, D. "Mechanistic Study of Cathodic Elecfrodeposition of Zinc Oxide and Zinc Hydroxychioride Films from Oxygenated Aqueous Zinc Chloride Solutions," J. Electrochem. Soc. 1998. Vol. 145, N° 3
154. Yoshida, T., Pauporte, T., Lincot, D., et al. "Cathodic Electrodeposition of ZnO/Eosin Y Hybrid Thin Films from Oxygen-Saturated Aqueous Solution of ZnCl2 and Eosin Y," *Journal of The Electrochemical Society*, 2003. 150 (9), C608-C615.

154. Zagal, J., Páez, M., Tanaka, A. A., et al. "Electrocatalytic activity of metal phthalocyanines for oxygen reduction," *Journal of Electroanalytical Chemistry*, V. 339, Nos. 1–2, 1992, pp. 13–30.
156. "Calogero et al. "Vegetable-based dye-sensitized solar cells" Chem. Soc. Rev. 2015. 44, 3244-3294
157. Staicu, A., Pascu, A., Nuta, A., et al. "Studies about phthalocyanine photosensitizers to be used in photodynamic therapy " *Romanian Reports in Physycs*. 2013. Vol. 65, N° 3, pp 1032-1051.
158. Hochst, H., Goldmann, A., Hufner, S., Malter, H."X-Ray Photoelectron Valence Band Studies on Phthalocyanine Compounds" *Phys. Stat. sol.* 1976. (b) 76, 559.
158. Hellgren, N., Guo, J., Luo, Y., et al. "Electronic structure of carbon nitride thin films studied by X-ray spectroscopy techniques," *Thin Solid Films*, V. 471, Nos. 1–2, 2005, pp. 19–34.
159. Neelgund, G. M., and Oki, A. "Cobalt Phthalocyanine-Sensitized Graphene–ZnO Composite: An Efficient Near-Infrared-Active Photothermal Agent," *ACS Omega*, V. 4, No. 3, 2019, pp. 5696–704.
160. Kong, M. J., Lee, S. S., Lyubovitsky, J., et al. "Infrared spectroscopy of methyl groups on silicon," *Chemical Physics Letters*, V. 263, Nos. 1–2, 1996, pp. 1–7.
161. Haller, S., Rousset, J., Renou, G., et al. "Electrodeposition of nanoporous ZnO on Al-doped ZnO leading to a highly organized structure for integration in Dye Sensitized Solar Cells," *EPJ Photovoltaics*, V. 2, 2011, p. 20401.
162. Aé, L., Kieven, D., Chen, J., et al. "ZnO nanorod arrays as an antireflective coating for Cu(In,Ga)Se $_2$ thin film solar cells," *Progress in Photovoltaics: Research and Applications*, V. 18, No. 3, 2010, pp. 209–13.
163. Basnet, P., Samanta, D., Inakhunbi Chanu, T., et al. "Assessment of synthesis approaches for tuning the photocatalytic property of ZnO nanoparticles," *SN Applied Sciences*, V. 1, No. 6, 2019, p. 633.
164. Costentin, C., Drouet, S., Robert, M., et al. "Turnover Numbers, Turnover Frequencies, and Overpotential in Molecular Catalysis of Electrochemical Reactions. Cyclic Voltammetry and Preparative-Scale Electrolysis," *Journal of the American Chemical Society*, V. 134, No. 27, 2012, pp. 11235–42.
165. Hammouche, M., Lexa, D., Momenteau, M., et al. "Chemical catalysis of electrochemical reactions. Homogeneous catalysis of the electrochemical reduction of carbon dioxide by iron('0') porphyrins. Role of the addition of magnesium cations," *Journal of the American Chemical Society*, V. 113, No. 22, 1991, pp. 8455–66.
166. Hu, X.-M., Rønne, M. H., Pedersen, S. U., et al. "Enhanced Catalytic Activity of Cobalt Porphyrin in CO $_2$ Electroreduction upon Immobilization on Carbon Materials," *Angewandte Chemie International Edition*, V. 56, No. 23, 2017, pp. 6468–72.
167. Schreier, M., Gao, P., Mayer, M. T., et al. "Efficient and selective carbon dioxide reduction on low cost protected Cu $_2$ O photocathodes using a molecular catalyst," *Energy & Environmental Science*, V. 8, No. 3, 2015, pp. 855–61.